The Evaluation of Microneedle Performance on a Representative *In Vitro* Skin Model

Kikelomo Vanessa Moronkeji

School of Engineering

University of Liverpool

A thesis submitted for the degree of

Doctor of Philosophy

May 2017

Acknowledgements

A PhD is like going on a journey of a thousand days that culminates at a final destination. As with any journey, there have been many individuals along the way that have helped to make the process as seamless as possible, though I must add that it has been fraught with challenges. It is them that I must now thank and truly show my gratitude for their support.

I would like to acknowledge the Centre for Global Eco-Innovation in conjunction with the European Regional Development Fund and Renephra Ltd for their financial facilitation of this project and therefore affording me the opportunity to undertake this PhD.

I would like to thank my primary supervisor, Dr Riaz Akhtar for his knowledge, diligence, calmness and openness. I really admire his work ethics and have learnt so much from him over the past four years. I must thank Professor Ahmed Elsheikh, my secondary supervisor for ensuring that there was order and structure in our large team that made up the Biomechanical Engineering Group. I would like to thank Professor Eithne Comerford who taught me how to hold the scalpel knife in order to harvest pig skin. Thanks to Dr Rob Birch who assisted with the early impact tests, which was a struggle to setup. He was so patient with me and I was at his door numerous times for him to help resolve a problem with either the oscilloscope readings or the accelerometer. Thanks to Mr Derek Neary for his technical assistance in the middle through to the latter stages of my testing, he was always so gracious and willing to help with whatever device that I could think up to make my experimental setup function better. I would also like to thank Mr Steve Bode for his support with my experimental setup. I would like to acknowledge Mr John Curran, Mr Jiji Mathew and the rest of the team in the workshop for helping to make the components that went with my experimental setup. I would also like to thank Mr Lee Moore at the Veterinary Teaching Suite for sourcing the neonatal pigs and providing access to his facilities at my convenience.

At Renephra, I would like to thank Dr Simon Todd for his technical expertise in guiding the direction of my project during the early days, when I was such a novice. I would also like to thank Dr Idalia Dawidowska for her expertise as a clinician particularly in explaining pitting and non-pitting oedema and finally I would also like to thank Dr Mark Rahn for his insight on the few occasions we had meetings together.

I would like to thank Dr Matt Fulton for his project management of the Centre for Global Eco-Innovation team and making sure that all the researchers were looked after and to Mr Doug McInnes, thank you for all your efforts in purchasing the materials and equipment needed for my project, as well as regularly chasing for time-sheets.

I would like to thank Dr Tom McDonald for his help with SEM imaging of my microneedles, who was gracious and always willing to help. I would also like to thank Dr Steve Barrett for writing the ImageSXM software code, which I used for my work on image analysis. I must thank Mr Dave Atkinson, who has been such a wonderful support and always willing to help. He gave me access to his labs, particularly the fume cupboards for all the super-cooling of isopentane in liquid nitrogen in order to preserve my skin samples whenever I needed. I cannot forget to thank Ms Marion Pope for her help in sectioning and staining my microneedle perforated skin samples. I would like to thank Ms Gemma Charlesworth for showing me how to section and stain my tissue samples, wax embed some of them and prepare PFA solution. To my colleagues, Rosti, Charlie, Sherif, Junjie, Mars, Zhuola, Brendan, Akram and Ahmed in Ocular and Biomaterial and Biomechanics Group, thank you so much for your support.

Thank you Dr Sunday Adelaja for giving me the nudge to pursue this PhD, I have gained such invaluable knowledge and skills these last four years. Thank you Mary Cliff and Cath Cliff for your support, you are my extended family. I appreciate them for all those times that I

was either stuck in the lab or on the motorway and could not make it in time to pick my daughter from after school club. I could always count on them, in my desperate time to pick her up for me and they were always so jolly about it. For me, that was a great stress relief, knowing that I could rely on them to care for my precious child.

I would like to thank my husband, Damola for his support. He heard my frustrations and encouraged me to keep going. He made many sacrifices too, by having to leave work impromptu numerous times when I was stuck on campus trying to finish my testing, or sample preservation. I would like to thank him for his patience and understanding and I cannot say it enough how much I love and appreciate him. I would also like to thank my daughter, Imisi, who has such a cheerful disposition. She missed many parties because mummy had to read numerous journals in order to complete a PhD related task. I will make it up to her and I would like to thank her for being so understanding and not throwing her "toys out of the cot". I would like to thank my son, Olumakin for being such a joyful baby because from babyhood to now being a toddler, he has had to share me with my thesis write-up. I must thank my parents, my daddy, who is retired but would come up to Burnley whenever required to help with babysitting in the first year of my studies, when my daughter was poorly and could not go to nursery. He has been such a great help and I cannot thank him enough. Thank you mummy, who has been such an encouragement to me and I thank her for her insight. I would also like to thank my brothers and sister for their support and encouragement. It definitely takes a community to complete a PhD. And finally, thank you Eledumare for helping me see this PhD to fruition.

Dedication

I dedicate this thesis to my dearest cousin, Dr Johnson Ayodele Olorunfemi, who passed away on 29th September 2014. You were the reason I decided to undertake this PhD, which would have been a promising fluid overload management therapy to your health battles with kidney disease. I had hoped that you would be a beneficiary of Renephra's Trandermal Fluid Removal technology once it became commercially available. Sadly, it was not to be. Nonetheless it is my hope that millions of people suffering from fluid overload or oedema due to kidney or heart disease will benefit from this technology.

RIP

Abstract

The skin is an extremely complex organ and its natural function is to act as a barrier by restricting the entry of foreign substances as well as preventing the loss of water and other fluids. Transdermal microneedle arrays provide a minimally invasive means of delivering drugs into the body via the skin. The challenge to effective microneedle penetration is to bypass the inherent elasticity of the stratum corneum, the skin's uppermost layer. The advent of microneedle technology is promising and numerous studies have been conducted on its applications to skin, with most of the work centred on skin models that have inadequate underlying substrates to support skin.

In this thesis, a representative experimental model of skin was developed accounting for mechanical contributions from subcutaneous layers comprising tissue fluid and muscle mimics in order to characterise skin's interaction with microneedles *in vitro*. Neonatal porcine skin from the abdominal and back regions, several concentrations of porcine-derived gelatine gels acted as the subcutaneous tissue fluid mimic and Perma-Gel®, a type of polymer used in ballistics testing was the muscle mimic. These layers of biological material made up the representative *in vitro* skin model. Micromechanical tests using a dynamic nanoindentation technique was conducted on the individual layers that made up the skin model in order to establish their mechanical characteristics such as elastic modulus, shear storage modulus, shear loss modulus and loss factor. The average elastic modulus was 24.49 ± 5.47 kPa for abdominal skin and 45.89 ± 9.61 kPa for back skin; for the gelatine gels at 67%, 80% and 88%, it was 63.11 ± 6.23 kPa, 34.56 ± 3.16 kPa and 11.3 ± 1.64 kPa respectively; the Perma-Gel® exhibited the highest elastic modulus of 80.73 ± 2.67 kPa in the skin model. The overall mechanical behaviour of these layers in the skin model contributed to its interaction with microneedles.

Two types of polymethylmethacrylate microneedles were used for the work in this thesis i.e. Design 1 and Design 2; the microneedles varied in height, needle density, base diameter and interspacing. Design 1 and 2 microneedles were applied to the skin model using a custom-made impact test setup system. The results of the initial tests using Design 1 microneedles on back skin model at 88% gelatine gel concentration demonstrated that optimal penetration was achieved with 9.33 ± 2.76 N insertion force and at an insertion velocity of 2.96 ms^{-1}. Methylene blue, histology staining and quantitative image analysis were used to analyse microneedle perforation quality. The microneedle penetration studies using Design 1 microneedles were reproducible and laid out the optimal conditions for the tests that involved the Design 2 microneedles on abdominal and back skin models at all gelatine gel concentrations. The mechanical properties for the skin models influenced the outcome of the penetration tests, as smaller deformations occurred within the stiffer back skin model as compared to the abdominal skin model. It was also found that for the impact test setup, microneedle geometry in terms of projections did not play a significant role in how microneedles interfaced with skin, as other parameters such as the insertion force and insertion velocity were more paramount.

Further tests were carried out using a clinical applicator provided by Renephra in order to compare results of their *in vivo* studies with the *in vitro* work carried out in this thesis. Although the insertion force produced by the clinical applicator was 2–7 times the magnitude of the insertion produced by the impact applicator, reproducible penetration of skin occurred. A comparison study was carried out on the clinical applicator and the impact applicator and it was found that the impact applicator was the preferred approach for microneedle application to skin because more effective microneedle penetration of skin could be achieved at a relatively low insertion force and a low insertion velocity as compared to the clinical applicator.

List of Publications

A. Papers and Book Chapter

[1] Moronkeji, K., Todd, S., Dawidowska, I., Barrett, S. D. and Akhtar, R. (2016) 'The Role of Subcutaneous Tissue Stiffness on Microneedle Performance in a Representative *In Vitro* Model of Skin', In: *Journal of Controlled Release*.

[2] Moronkeji, K., Todd, S., Dawidowska, I., and Akhtar, R. (2015) '*In Vitro* Quantification of Optimal Impact Properties for Microneedle Penetration', pp. 39-49 In: *Proceedings of Society of Experimental Mechanics 2015 Annual Conference and Exposition on Experimental and Applied Mechanics*.

[3] Moronkeji, K. and Akhtar, R. (2015) 'Mechanical Properties of Aging Human Skin', pp. 237-263, In: *Mechanical Properties of Aging Soft Tissues*. Editors: Derby, B., Akhtar, R. (Eds), Springer International Publishing.

B. International Conference Presentations

[1] Oral Presentation: '*In Vitro* Quantification of Optimal Impact Properties for Microneedle Penetration into Skin', *SEM 2015 12th International Annual Conference & Exposition on Experimental and Applied Mechanics, Costa Mesa, CA, USA* (8–11th June 2015).

[2] Oral Presentation: 'Overcoming the Stratum Corneum Barrier for Microneedle Application', *26th Annual Conference of the European Society for Biomaterials, Liverpool, UK* (31st August–3rd September 2014).

[3] Poster Presentation: 'Impact Testing of Skin: Overcoming the Stratum Corneum Barrier for Microneedle Application', *5th International Conference on Mechanics of Biomaterials and Tissues, Sitges, Spain* (8–12th December 2013).

Contents

List of Figures

List of Tables

Abbreviations

ANOVA	Analysis of Variance
BCM	Body Composition Monitor
CKD	Chronic Kidney Disease
CMFT	Manchester Royal Infirmary
GFR	Glomerular Filtration Rate
HCI	Hydrochloric acid
HD	Haemodialysis
IMS	Industrial Methylated Spirit
ISF	Interstitial Fluid
ns	Not Significant
PBS	Phosphate Buffered Sulphate
PE	Penetration Efficiency
PEEK	PolyEtherEtherKetone
PMMA	PolyMethylMethAcrylate
RRT	Renal Replacement Therapy
SD	Standard Deviation
TEWL	TransEpidermal Water Loss
TFR	Transdermal Fluid Removal
UTS	Ultimate Tensile Strength
XMT	X-ray Micro Computed Tomography

Chapter 1

1. Introduction

1.1 General Introduction

There are a number of diseases like kidney failure, heart failure that lead to a build-up of fluid and oedema in the body. Fluid overload assessment therapies, which are mentioned in more detail in Section 1.2.1 and fluid overload management, mentioned in greater detail in Section 1.2.2 have advantages and disadvantages to their use, however, to improve patient prognosis and long-term recovery, the development of technologies that maintain the fluid volume level as close to the normal body fluid of the patient is necessary (Elsayed and Stack, 2015). Hence, Renephra Ltd is developing a novel approach using microneedles to address the issue of fluid overload, which involves a minimally invasive means of accessing the interstitial fluid (ISF) in the skin. This new approach involves the slow removal of fluids and toxins from the body. Renephra's technology would be sympathetic towards the environment as it does not require water usage, minimal power required to operate, is portable (Wang et al., 2005) and will therefore not contribute to the carbon footprint. Outside the UK, the technology will have a significant potential in developing countries with weak healthcare infrastructure and inability to implement energy-intensive and costly medical interventions (Wang et al., 2005). The aim of this project was to understand the insertion parameters required to obtain optimal insertion of microneedles into skin in order to facilitate fluid removal. The proposed novel solution is covered in Section 1.3.

1.2 The Effects of Fluid Overload and Oedema

The accumulation of fluid around the lungs, the heart and pericardium or the abdominal cavity and subcutaneous tissues can cause peripheral oedema because abnormal levels of

fluid can move from the intravascular space and build-up in the interstitial space (Lo Gullo et al., 2015). Therefore, oedema can be defined as a substantial swelling caused by a build-up of ISF (Ely et al., 2006). The build-up of ISF takes place in the pleural, pericardial and peritoneal spaces and subcutaneous tissue planes (Lo Gullo et al., 2015).

Within the interstitial space, there is transportable free fluid like water, collagen, elastin and gel-like ground substances. The combination of these components influence the mechanical behaviour of tissues (Guyton et al., 1971). In oedematous tissue, the interstitial spaces contain an abnormally high quantity of fluid, which affects its mechanical characteristics. This excess fluid creates stress and strain within the collagen and elastin fibres in the skin and diminishes the elasticity of the tissue and lowers the viscosity in ground substance (Guyton et al., 1971). Moreover, the severity and speed at which oedema develops affects the structural and mechanical integrity of the tissue (Guyton et al., 1971). Oedema in skin can be described as subcutaneous pitting or subcutaneous non-pitting oedema. The glycosaminoglycan content in healthy tissue enables it to produce a high resistance to displacement of ISF (Levick, 1987). To establish whether a patient has subcutaneous pitting oedema, a finger is pressed to the area of skin with swelling for 10 seconds, which leaves a dent. The dent will slowly fill back in, with the skin returning to its original state (Renephra, 2015). For subcutaneous non-pitting oedema however, after depressing the area affected by swelling, no dent is observed in the skin. Subcutaneous non-pitting oedema is usually hard and can be attributed to fibrous or fatty tissue growth (Bates et al., 1994).

Furthermore, fluid overload in the interstitial space can be caused by liver failure, renal failure, heart failure, protein loss, dietary noncompliance (Cho and Atwood, 2002) or drug induced (Singh et al., 2007). Some of the medical symptoms of fluid overload are weight gain (Nesto et al., 2003), oedema (Ely et al., 2006), loud snoring (Ely et al., 2006), sleep apnoea (Parker, 2003) or shortness of breath (Flores and Rider, 2016).

Fluid overload can be used as a biomarker for indicating heart failure in patients (Chin et al., 2014). A significant proportion of hospital admissions for heart failure are due to fluid overload (Peacock et al., 2009) and findings by Adams et al. indicated that the manifestations of peripheral oedema occurred in 66% of hospitalised patients with heart failure (Adams et al., 2005). Furthermore, globally heart failure is a common occurrence (Mendez and Cowie, 2001) that increasingly affects an ageing population (McMurray and Stewart, 2000). Despite the reduction in the number of deaths caused by cardiovascular disease, the frequency of heart failure however is on the rise (Gibbs et al., 1998) and the long-term prospects of recovery poor (Croft et al., 1999). Additionally, heart failure poses a major economic burden, with it accounting for 1–2% of health care expenditure in the UK and some developed countries (Berry et al., 2001). The health care expenditure for heart failure in the UK is a combination of direct and indirect cost, which is circa £1.12 Billion (Cook et al., 2014). In his study, Sutton (1990) projected that hospital admissions for heart failure would be between 100 000 to 200 000 admissions annually (Sutton, 1990). Over a decade later, Stewart et al. reported 140 000 hospital admissions (Stewart et al., 2002).

Fluid overload is also linked with mortality or cardiovascular morbidity in patients with advanced Chronic Kidney Disease (CKD) (Tsai et al., 2015). The rates of prevalence of CKD appear to be increasing globally and are likely to increase further as a consequence of ageing populations and the increased prevalence of Type II diabetes mellitus (Hamer and El-Nahas, 2006). CKD is characterised depending on the stage at which the disease has progressed to (see Table 1 for definitions). The Glomerular Filtration Rate (GFR), which is a measure of the amount of blood that passes through the glomerulus, the filtering unit of the kidney each minute falls as the disease progresses (Kerr, 2012). Fatality could occur within a few months of a patient reaching CKD stage 5 if untreated. Ferrario et al. demonstrated how fluid overload coupled with factors such as hyper-sympathetic activity, which include increased

heart rate, increased respiration, increased blood pressure, perspiration and elevated body temperature are connected with increased risk of cardiovascular mortality in CKD stage 5 patients (Ferrario et al., 2014).

Table 1 Definition and stages of CKD (Adapted from Kerr, 2012).

CKD stage	GFR (ml/min/1.73 m^2)	Description
1	≥90	Normal or increased GFR, but with other evidence of kidney damage
2	60 – 89	Slight decrease in GFR, with other evidence of kidney damage
3A	45 – 59	Moderate decrease in GFR, with or without other evidence of kidney damage
3B	30 – 44	
4	15 – 29	Severe decrease in GFR, with or without other evidence of kidney damage
5	<15	CKD stage 5

Previous studies showed that 6–8.5% of adults in England have CKD stages 3–5 and that the number of patients being treated for CKD stage 5 had risen by 35% in five years, with the highest level of incidence among the elderly. Furthermore, in 2009/10, 1.81 million people were recorded as having CKD stages 3–5 in the UK (Kerr et al., 2012). The overall annual cost of CKD in the UK is estimated at £1.44 to £1.45 Billion (Kerr, 2012). In the UK alone, 7000 patients a year progress to CKD stage 5 (Morton et al., 2010). Once kidney function has declined to CKD stage 5, Renal Replacement Therapy (RRT), such as kidney replacement or dialysis treatment becomes necessary.

Lymphoedema is a chronic condition characterised by oedema and typically occurs in one or more limbs and in some instances involving the trunk, head or genital area (Moffatt et al., 2003). It is a serious complication resulting from treatments for cancer and as such there is no

proven drug treatment for it (Moffatt et al., 2003). Hence, novel fluid removal treatments, such as Renephra's device would be extremely beneficial for lymphoedema patients.

There are a number of treatment therapies available for assessing and managing fluid overload and a brief overview is discussed in the next section.

1.2.1 Overview of current fluid overload assessment methodologies

Despite significant developments in science, there remains a significant barrier in dispensing effective treatment options for fluid overload. Furthermore, the clinical evaluation of fluid overload caused by cardiac failure is expensive and challenging (Frank Peacock and Soto, 2010). Moreover, as heart failure predominantly affects the ageing population (adults over 75 years old), this means that clinical trials of potential assessment or treatment therapies are often performed on younger, healthier subjects and as such the outcomes of these endeavours may not be applicable (Kitzman and Rich, 2010; Rich et al., 2016).

Measuring a patient's dry weight is a potential assessment solution for fluid overload. The accurate estimation of dry weight is necessary in reaching a state of normal body fluid; this is because the symptoms of hypervolemia exhibit inadequately low sensitivity rates (Frank Peacock and Soto, 2010). There are issues however surrounding the optimal approach of assessing dry weight and using this approach on its own could lead to a patient's demise.

Another approach is thermo-dilution, which is the measurement of the quantity of extravascular lung water present in the lung. This method has not gained significant popularity due to clinicians' reluctance in depending solely on lung water measurements (Brown et al., 2009).

Body Composition Monitor (BCM) is a well-known method of fluid overload assessment. BCM measures the hydration levels in CKD patients (Hung et al., 2014). It works because of

the ability of high-frequency current to pass through the total body water. On the contrary, this is not the case with low-frequency current, which cannot bypass the cell membranes and it therefore passes through the extracellular water (Moissl et al., 2006). A disadvantage to the BCM is that it cannot distinguish between increased extracellular fluid volume resulting from increased intravascular volume as opposed to increased interstitial volume (Tsai et al., 2015). BCM can be used as an assessment tool in detecting patients with CKD stages 3–5 (Hung et al., 2014).

A variation to BCM is the Bioimpedance Vector Analysis (BIVA). BIVA also assesses tissue hydration and some of its benefits are that it is a non-invasive, uncomplicated to use and a reproducible way of evaluating hydration levels and body composition of patients on dialysis (Onofriescu et al., 2014).

A novel way of evaluating fluid overload is conducting a post-mortem coherence tomography of the dead patient. Unfortunately, a disadvantage to this approach is that it is challenging to distinguish between fluid overload in a post-mortem coherence tomography compared to a pre-mortem coherence tomography. Moreover, the likelihood and accuracy of fluid estimation in the interstitial space can be utilised in the evaluation of fluid overload in pre-mortem conditions (Lo Gullo et al., 2015).

1.2.2 Overview of current fluid overload management therapies

Poor patient response to diuretics is linked to advanced heart failure, renal damage, diabetes and can act as a primary indicator for re-admitting a patient to hospital and mortality (Valente et al., 2014). Intravenous diuretics in large doses can be administered to some diuretics resistant patients (Costanzo et al., 2005). However, diuretics does not improve the clinical outcomes (Bart, 2009) and some of the adverse effects of intravenous diuretics are skin reaction, interstitial nephritis and hearing loss to name a few (Brater, 1998). Furthermore,

studies have shown that diuretic resistance develops in some heart failure patients (Kramer et al., 1999).

Dialysis is a machine-assisted blood filtration technique that removes waste and excess fluid from the blood in a dialyser. It requires surgical intervention, whereby a doctor creates permanent access to the blood stream, via the arm or thigh (Roth et al., 2012). Dialysis is an invasive treatment option for acute renal failure and has grown to become the leading rescue therapy for patients with CKD stage 5, without which would lead to a patient's imminent demise (Cavalli et al., 2010). For patients on dialysis, fluid overload is a common occurrence as well as other risk factors such as hypertension, left ventricular hypertrophy and death due to cardiac failure (Kalantar-Zadeh et al., 2009; Seibert et al., 2013). Antlanger et al. suggests that achieving a state of normal body fluid volume is key for maintaining the well-being of patients on dialysis (Antlanger et al., 2013). A drawback to dialysis is that it is related to poor long term clinical outcomes, high risk of death (Bleyer et al., 1999), expensive (Feest et al., 2004), is also one of the most water and power intensive of all healthcare therapies and disregards the environmental impact it creates (Agar, 2012).

This project aims to conduct a fundamental study on microneedles interaction with skin for the purpose of advancing Renephra's novel device. Microneedle technology is discussed in more detail in Section 2.5.

1.3 Proposed Novel Solution for Fluid Overload Relief

The novel medical device is for the relief of fluid overload, which should reduce the amount of oedema and lead to improved patient well-being. Fluid overload is associated with kidney and heart failure diseases (Peacock et al., 2009; Tsai et al., 2015), which affects a significant proportion of patients who are unresponsive to diuretic treatment (Valente et al., 2014). Consequently, the patients need hospitalisation for intravenous diuretics (Costanzo et al.,

2005) and in extreme cases requires the invasive dialysis treatment option (Grassmann et al., 2005).

1.3.1 Access to interstitial fluid via skin

One of the health challenges associated with heart and kidney disease is the onset of oedema. Removing ISF from skin in oedematous patients instead of blood via dialysis is feasible because blood and ISF are dynamic and interconnected compartments hence, fluid and toxins are shared between compartments (Ebah, 2012). Thus, extracting the ISF from skin eliminates the surgical intervention required to access the blood. The challenge however is overcoming the uppermost layer of skin (stratum corneum), which is designed to act as a barrier to prevent foreign objects from gaining entry and fluid loss by the body. A suitable device for bypassing the barrier characteristics of the stratum corneum, the skin's uppermost layer are microneedle arrays.

1.3.2 Microneedle arrays to breach skin's barrier

Microneedles are suitable to breach the stratum corneum in order to access the ISF in skin's epidermal layer, dermal layer and fluid located subcutaneously. Microneedle arrays for transdermal drug delivery purposes were first patented by Gerstel and Place in 1976 (Gerstel and Place, 1976). It was not until the advancements in the micro-fabrication industry in the 1990s however that the devices could be manufactured and tested (Henry et al., 1998). To date, microneedles are primarily used for drug delivery (Kim et al., 2012). Renephra has therefore found an innovative use for microneedles for the purpose of ISF extraction and the anticipation is for this approach to be used at a commercial level.

1.3.3 Transdermal Fluid Removal technology

The first generation Transdermal Fluid Removal (TFR) technology for fluid extraction was a combination of a hollow microneedle array with a fluid capturing hydrogel pouch able to

absorb large capacities of fluid. When the microneedle array is inserted into skin, the fluid is drawn up the microneedles by capillary action and captured by the hydrogel pouch. The initial application of the microneedle array to skin was by manual approach and then later with a spring-driven applicator. The preliminary study using human subjects highlighted that TFR required further development to make it a suitable device for managing fluid overload (Renephra, 2012). In particular, the unreliability and unpredictability associated with manual application of microneedles such as, dependence on fluid pressure and the inability to quantify insertion force demonstrated the limitations with this approach. Furthermore, the spring-driven microneedle applicator was also a crude way of controlling the insertion force or insertion velocity.

Ebah (2012) demonstrated the feasibility of TFR technology on 6 healthy volunteers and 37 CKD patients attending renal clinics or wards at Manchester Royal Infirmary (CMFT). ISF was extracted from 68.8% of patients, where successful microneedle penetration occurred and showed that microneedles caused no pain or bleeding in over 95% of applications (Ebah, 2012). Ebah (2012) also noted that CKD patients had raised interstitial pressures and ISF volumes compared to healthy subjects. The raised level of interstitial pressure in CKD patients with obvious oedema is a combination of a build-up of interstitial compartment fluid volume, pre-existing oedema and tissue mechanical characteristics. In addition, Ebah (2012) noted that the time taken for oedema to refill the depressed area could be a significant parameter in the clinical assessment of oedema.

The latest generation of the device uses microneedles to access fluid located in the epidermis/dermis and negative pressure used to extract fluid from skin and subdermis. The microneedle array is applied to the skin using an applicator. Once applied, it is removed after several seconds and microchannels are created in the top layers of the skin allowing for fluid to flow. Negative pressure is then applied to remove excess ISF and collect it in a canister

attached to a pump. Fig. 1 illustrates the possible concept of the look of the device. Renephra intends that the final product would be a wearable technology that could be self-administered by the patient or carer.

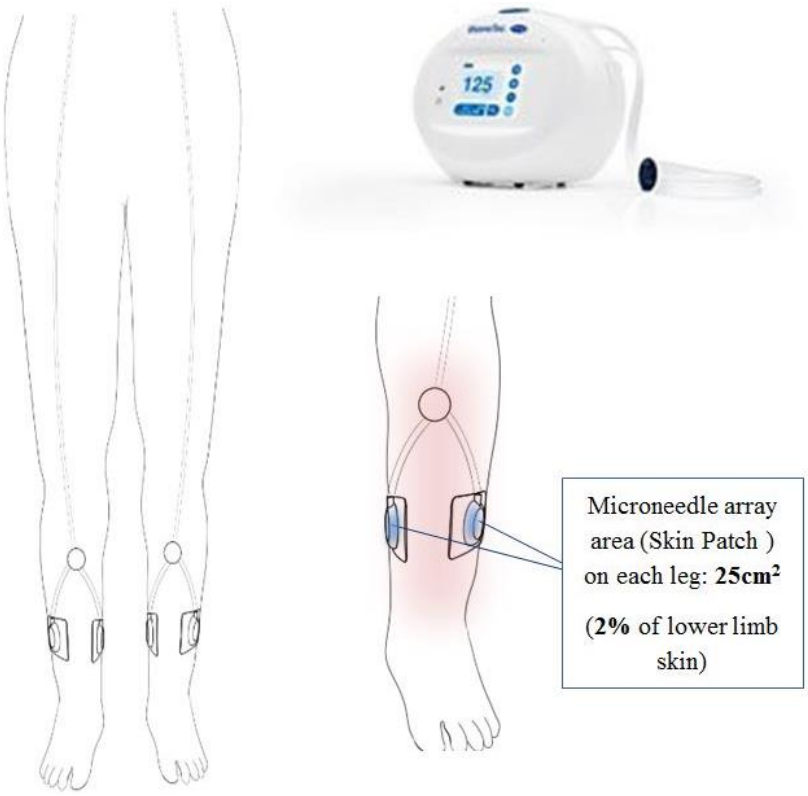

Figure 1 Renephra's wearable transdermal microneedle fluid overload relief technology.

As swelling resulting from fluid retention can occur all over the body or only in one part of the body (Levick, 1987), which is why current treatment therapies like dialysis have created access to the bloodstream via the arm or the thigh for the removal of blood including fluid and toxins and the replacement with clean oxygenated blood or using diuretics for the removal of excess fluid in the body irrespective of where the oedema is located. For example fluid overload, in heart failure patients was pulmonary oedema (Cotter et al., 2008) and in kidney failure patients was lower-extremity oedema and pulmonary oedema (Kalantar-Zadeh et al., 2009). Furthermore, as blood and ISF are dynamic and interconnected compartments, this means that fluid and toxins are shared between compartments (Ebah, 2012). Hence the device could potentially be used on various sites on the body. The work in this thesis focused

on two anatomical regions of neonatal porcine skin i.e. the abdominal tissue and back tissue due to their differences in thickness and stiffness. The physiological properties of neonatal porcine skin are similar to human skin (Lo Presti et al., 2012) and the stiffness is within the range of values for the stiffness of human tissue (Groves, 2011).

The device will use technology developed by Renephra Ltd where the skin is pierced with a small cluster of microneedles. More recent studies by Renephra demonstrated that following the bypass of the stratum corneum by microneedle intervention, this fluid is readily accessible. Using microneedles and negative pressure, the fluid extraction rates of 2 $ml/cm^2/hr$ were achieved along with fluid volume extracted, which was > 5 ml in patients with severe oedema. The fluid extraction process lasted over four hours, with approximately 60 ml of fluid removed over 7 cm^2 small surface area in some patients. The extracted fluid volume increased linearly with time ($r=0.24$, $p=0.008$). This indicates that an appropriate microneedle surface area of 50 cm^2 used for a period of 8 hours could result in the extraction of up to 800 ml and could be potentially clinically significant. Furthermore, clinicians estimate that a significant volume for such a device will be between 250 and 1000 ml per day (Renephra, 2015).

Fig. 2 shows the most recent progress with the proposed TFR technology, using a clinical applicator that comprises a spring and hammer driven mechanism (Renephra, 2015). The proposed device removes excess fluid from the body via the skin. A vacuum chamber is then placed over the microneedle perforated site to draw up liquid, which is collected in a canister. The images show the successful extraction of ISF from a patient in a clinical research at the CMFT. The potential device if developed would be a huge benefit to thousands of patients in the UK and hundreds of thousands globally. It would enable patients take advantage of a home/community based, minimally invasive, bloodless and self-administered fluid removal

therapy to manage fluid overload symptoms, improve outcomes and quality of life whilst preventing hospitalisations and thus potentially reducing costs to the National Health Service.

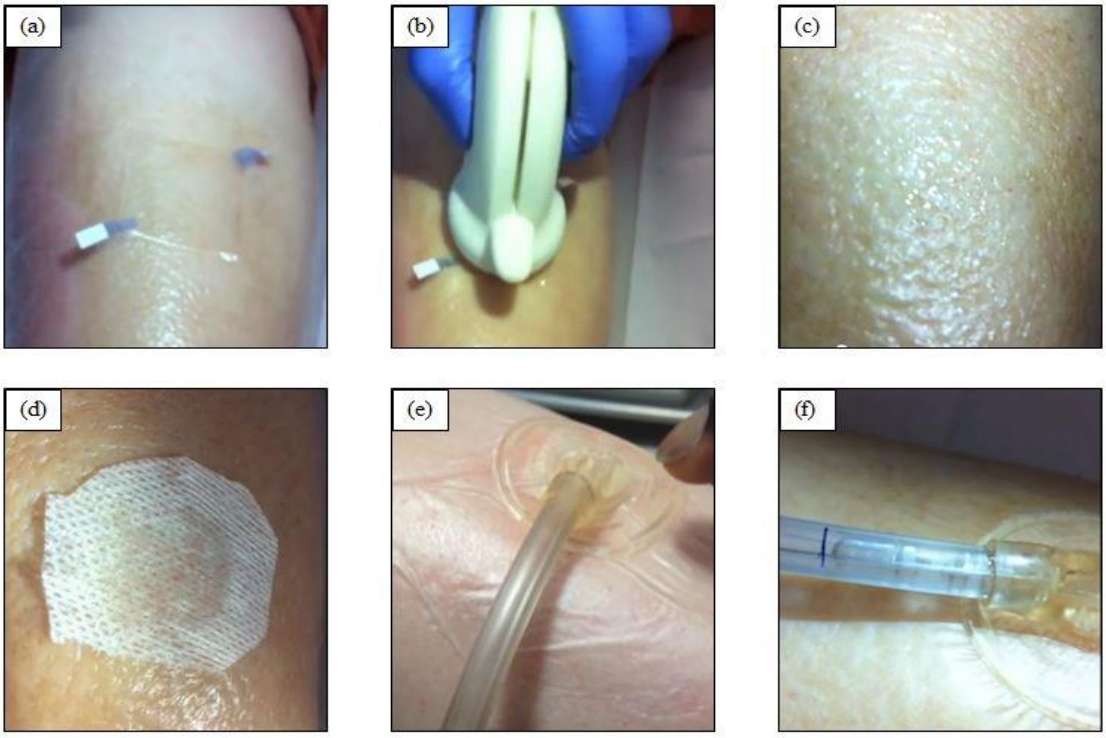

Figure 2 The Transdermal Fluid Removal technology (a) microneedle placed on patient, (b) clinical applicator used to insert microneedles into skin, (c) skin after microneedle treatment with no bleeding or lasting damage to skin (d) gauze placed on skin to absorb some of the ISF, (e) fluid extraction using negative pressure therapy and (f) extracted fluid passing through tube.

Fluid overload or oedema due to heart failure or kidney failure affects an ageing population and as such it is important to understand how skin's subcutaneous layer is affected by the ageing process. The subcutaneous tissue is diminished in some regions of the body such as the face, shins, hands and feet, whilst in other regions such as the abdomen in men and the thighs in women, it is increased (Fenske and Lober, 1986). Furthermore, in adults, the deep dermis or subcutaneous tissues is composed of several layers of fat separated by connective tissue septa (Ryan, 1995). Some adipose tissue in the subcutaneous layer actually extends into the dermis (Ryan, 1995). Dermal echogenicity indicates the distribution of fluid in the dermis. For intradermal echogenicity, there was a pattern in the different types of oedema implying that localisation of fluid varies in the dermis, from sub-epidermal

(lipodermatosclerosis), uniform (lymphoedema), to deep dermal (heart failure) (Gniadecka, 1996). Furthermore, magnetic resonance imaging showed that water content is particularly increased in the sub-epidermal layer of aged skin and decreased echogenicity (Gniadecka et al., 1994). Decreased echogenicity may also be attributed to changes in the collagen fibre arrangement (Gniadecka et al., 1994). The work in this thesis focused on a skin model that comprised a full thickness skin sample, a subcutaneous mimic of varying water content concentration and a muscle mimic. There are many limitations with developing an *in vitro* model of skin that can adequately mimic the *in vivo* behaviour of oedematous skin, however, in future; fluid could be injected into a membrane placed within the subcutaneous layer of the *in vitro* model.

1.4 Research Project Plan

This research programme will build on Renephra's background Intellectual Property and early stage TFR technology by conducting comprehensive experimental studies focusing on the biomechanical interaction of the microneedle device with skin. CMFT's preliminary study using human subjects however, has identified several areas where the technology needs further development to make it a robust fluid overload management treatment therapy.

1.4.1 Aims and Objectives

The overall aim of this project was to determine quantitatively the parameters for repeatable and reproducible insertion of microneedles into skin. The specific objectives were:

The first objective was to conduct an experimental analysis of the mechanical properties of skin. This involved the determination of an ideal skin model and micromechanical characterisation of each of the layers in the skin model and their contribution to the overall properties of the skin.

The second objective was to develop an *in vitro* impact applicator system for microneedles to quantify the optimal insertion force and insertion velocity. This involved the use of three types of microneedles to determine the optimum system for skin penetration.

The third objective was to determine the insertion force from the clinical applicator used in CMFT study. The results from the clinical applicator study were compared with the results of the impact applicator study.

The fourth objective was to assess the perforated skin model through various image analysis techniques. This involved the visual examination of the perforated skin following staining and analysis of the histology images of breach area created in skin with microneedles.

Chapter 2

2. Literature Review

2.1 Introduction

This section will detail the relevant literature. It will provide an overview of skin and its mechanical properties. In addition, it will also review and discuss various types of microneedle devices, microneedle applicators, mechanics of skin penetration and techniques for imaging perforated skin.

2.2 The Anatomy of Skin

Skin is the largest organ of the human body and covers a surface area of between 1.5–2 m^2 and functions as a regulator of heat and water loss from the body (Pegoraro et al., 2012). The large surface area of skin offers ideal and multiple sites to administer therapeutic compounds for both local and systemic actions. Furthermore, due to skin's highly efficient self-repairing barrier, it is designed to keep the internal organs protected and prevent foreign matter from entering the body. *In vivo*, skin is in a process of continually regenerating itself and provides immunological and histological reactions to external insults such as infection, temperature extremes, dehydration and mechanical trauma (Williams, 2004).

The skin is composed of three primary layers, which are the epidermis, dermis and hypodermis (Pegoraro et al., 2012) as represented schematically in Fig. 3.

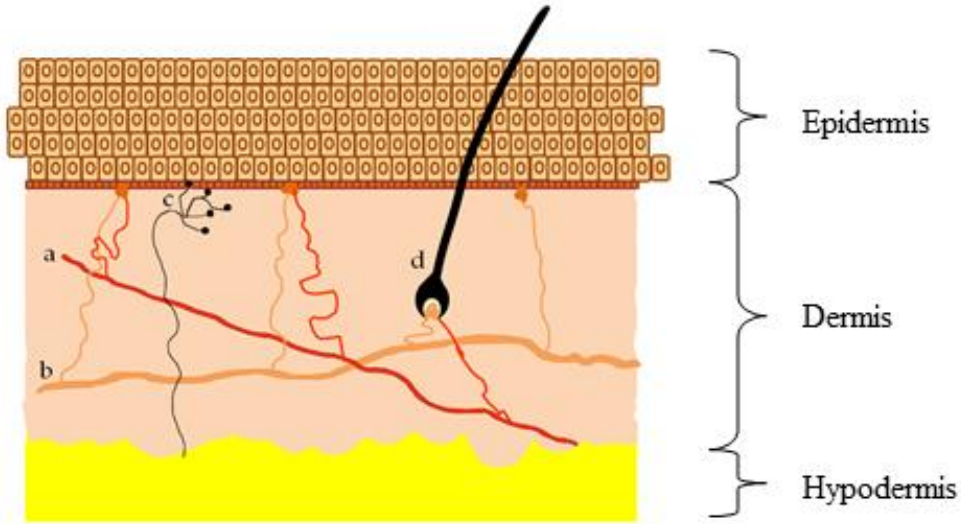

Figure 3 Schematic diagram showing skin layers: hypodermis, dermis and epidermis. (a) represents blood vessels, (b) lymph vessels, (c) nerve endings and (d) hair follicles. Sweat glands and sense receptors have not been shown in the figure.

2.2.1 Epidermis

The epidermis is in constant interaction with the environment and can be considered as being composed of four or five individual layers (Pegoraro et al., 2012) and is illustrated in Fig. 4.

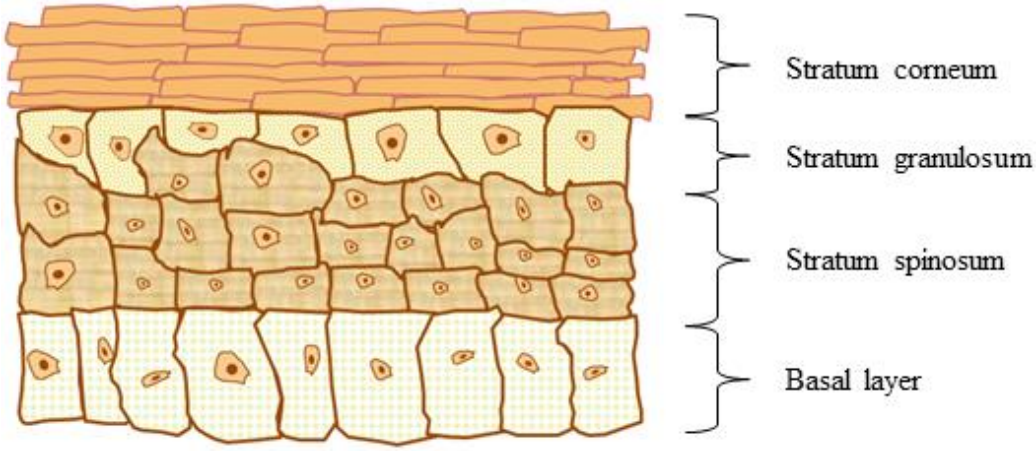

Figure 4 Schematic diagram showing the layers of the epidermis: stratum corneum, stratum granulosum, stratum spinosum and the basal layer.

The outermost layer of the epidermis, the stratum corneum is in direct contact with thermal, mechanical and chemical insults to which the body is exposed (Wilkes and Wildnauer, 1973). It is 10–20 μm thick and is made up of 10–30 thin layers of dead keratinocytes (Pegoraro et al., 2012). The dead layer of keratinised tissue varies in thickness depending on anatomical

site. The keratinisation process leads to the development of fibrous protein, which forms up to 50% of the stratum corneum layer and contributes substantially to its mechanical behaviour (Wilkes and Wildnauer, 1973). In the basal layer, the keratinocytes multiply through cell division and undergo multiple stages of differentiation in becoming corneocytes as they travel towards the skin surface. The thickness of each corneocyte is about 500 nm and 40–50 μm in diameter (Elias, 1983). Furthermore, it has been observed that the thickness of the epidermal layer can increase significantly as a result of oedematous state (Chao et al., 2012). Oedema refers to the swelling of tissue that results from excessive accumulation of ISF in tissue, which alters the skin's properties and is prevalent in patients with heart failure.

2.2.2 Dermis

The dermal layer lies between the epidermis and subcutaneous tissues that consists of connective tissue. It is separated into two layers, which are the papillary region that is adjacent to the epidermis and the reticular dermis, which comprises a deeper thicker area (James et al., 2006). The dermis is 0.9–1.3 mm and varies depending on region (Lasagni and Seidenari, 1995). The dermis also houses the blood vessels, lymph vessels, nerve endings with few myelinated fibres, sense receptors, hair follicles, sebaceous glands and sweat glands. The dermis provides the overall mechanical support for skin as well as supplying the epidermis with nutrients since it does not contain blood vessels (Pegoraro et al., 2012).

2.2.3 Hypodermis

The hypodermis also known as the subcutaneous tissue is the deepest layer of the skin. The subcutaneous fatty tissue can be divided into the superficial adipose layer, which contains small, tightly packed fat lobules within the septa and the deep adipose layer containing large, irregular and disorganised fat lobules. The deep adipose layer is also connected to the muscle. The thickness of the adipose layer is fairly consistent throughout the body and this differs

from the deep adipose layer, where there are variations with respect to anatomical site (Markman and Barton, 1987). The subcutaneous layers play an important role in the mechanical properties of skin. In the body, subcutaneous adipose tissue contributes to skin deformation during loading and load transfer from skin to deeper layers (Geerligs et al., 2010a). The main functions of the subcutaneous layer are insulation and shock absorption. Its abundance in collagen and fat means that it acts as an energy reservoir (Pegoraro et al., 2012).

2.3 The Mechanical Characteristics of Skin

There is increased interest in the mechanical behaviour of skin due to the development of micro-devices for drug delivery into the upper layers of skin (Crichton et al., 2013). Skin provides a mechanical defence and acts as a chemical barrier, limiting infiltration by foreign substances (Hendriks, 2005). It is subjected to pre-stress and exhibits anisotropic (Lanir and Fung, 1974; Fung, 1993), non-linear (Barbenel and Evans, 1977) and viscoelastic (Agache et al., 1980; Khatyr et al., 2004) characteristics. These mechanical characteristics are influenced by elastin, proteoglycan, collagen and ISF (Lanir and Fung, 1974; Oomens et al., 1987) and also differs due to age (Daly and Odland, 1979; Leveque et al., 1980), anatomical site (Sandby-Moller et al., 2003) and level of hydration (Tagami et al., 1980). Although the overall mechanical behaviour of skin is dominated by the dermal layers, the influence of the stratum corneum on the global behaviour of skin cannot be ignored (De Rigal and Leveque, 1985; Hendriks, 2005). The general behaviour of the stratum corneum is highly influenced by environmental properties such as temperature and relative humidity, both *in vivo* and *in vitro* (Hendriks, 2005). In addition, mechanical disturbances to the stratum corneum are used to highlight metabolic activities in order to preserve its barrier function (Yuan and Verma, 2006).

Early research demonstrated that skin is non-linear, viscoelastic and anisotropic (Veronda and Westmann, 1970). The viscoelastic property of skin means that the mechanical response to loading involves both a viscous component associated with hysteresis or energy dissipation and an elastic component associated with energy storage, as shown in Fig. 5. The stratum corneum is the stiffest of the skin's layers and is therefore the least extendable under applied load. It also exhibits less viscoelasticity and pre-conditioning behaviour compared to the other layers but still maintains a non-linear stress-strain relationship under applied load.

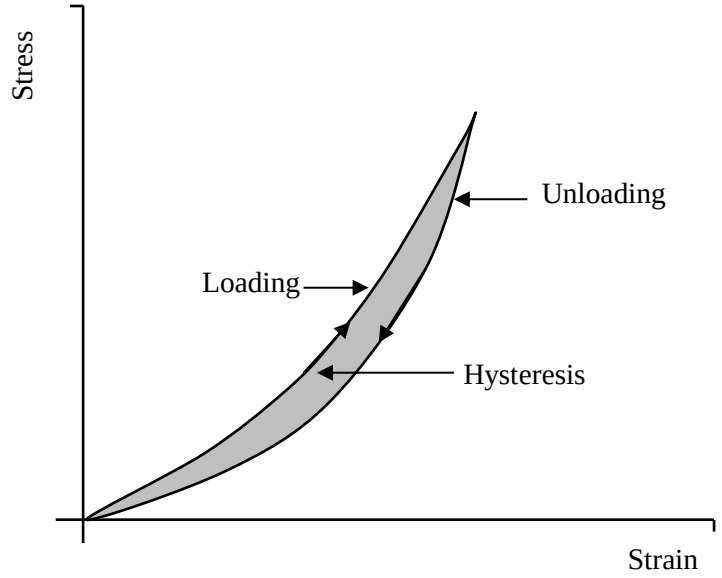

Figure 5 Hysteresis as observed in the stress-strain behaviour of a viscoelastic material during cyclic loading.

An observation made by Agache et al. for a strain–time curve showed that if a load was applied to skin, the curve obtained could be split into three parts. The first part corresponded to a purely elastic deformation, the second part of variable creep corresponded to the viscoelastic phase and the third corresponded to a constant creep phase (Agache et al., 1980; Khatyr et al., 2004). The typical stress-strain curve of human skin showed a gross re-alignment of the collagen fibres in the direction of extension in phase 1, while phase 3 illustrated the stress-strain characteristics of aligned collagen fibres. Phase 2 demonstrated the progressive alignment within the dermis. The tangent AB gave a measure of the elastic

modulus of the fully aligned collagen fibres. The intercept A at tangent AB indicated the strain required to align the collagen fibres in the direction of loading and is therefore a measure of the extensibility of the skin in that direction (Gibson et al., 1968).

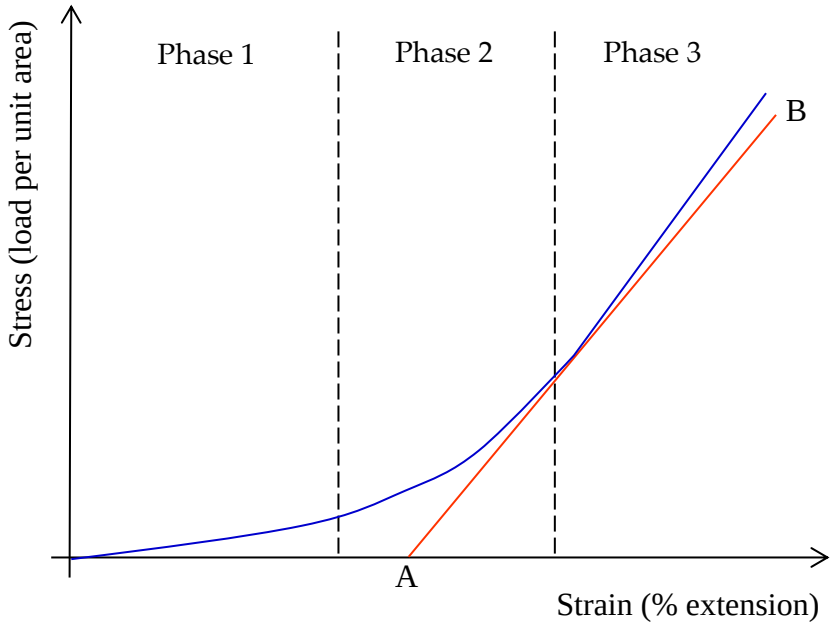

Figure 6 Typical stress-strain relation for skin in uniaxial tension obtained at a constant rate. The curve is subdivided into three sections in accordance with the mechanism of deformation. (Figure adapted from (Gibson et al., 1968)).

An important component of soft tissue is its fibrous structure and in particular, the arrangement of its collagen fibres. These fibres have a significant influence on the mechanical properties of the tissue and provide its anisotropic characteristics (Ogden, 2009). The mechanical behaviour of human skin differs across anatomical site and from person to person. The anisotropy of skin and the fact that it is locally orthotropic was reported by Langer (1861), who observed that circular holes punched in the skin of cadavers relaxed into elliptical shapes. He drew lines (subsequently called Langer lines) through the principal axes of the elliptic cut-outs, which approximate the direction of collagen bundles within the skin (Khatyr et al., 2004). According to Leveque et al., the viscoelastic behaviour of skin and the relative quantity of components such as collagen, elastin and ground substance influence the way in which skin is deformed.

It has been established in the literature that skin is in tension in the natural "relaxed" state' *in vivo* (Alexander and Cook, 1977; Holt and Evans, 2009), thereby making accurate predictions of the mechanical behaviour of the skin challenging (Wilkes et al., 1973). Additionally, skin elastic tension is lower in childhood and higher adulthood; however, it declines in old age (Kirk and Kvorning, 1949).

In order to measure the biomechanical properties of skin, the techniques and interpretation of two distinct categories of *in vitro* and *in vivo* methodologies must be considered.

2.3.1 *In vitro* techniques

In vitro testing contributes significantly to the characterisation of skin and developing constitutive models to understand its mechanical behaviour. The advantages of experimental testing *in vitro* skin sections is that it is relatively inexpensive, ethical considerations play a minor role in obtaining samples and the test results can be used as an indicator for *in vivo* tests. The disadvantages however are that the skin sections are treated in isolation away from its normal setting and as such is not connected to surrounding tissue, nutrients or blood supply. This makes replicating skin's *in vivo* behaviour with *in vitro* techniques challenging. Typically, *in vitro* techniques can be used to define three mechanical properties of soft tissue, which are its elastic modulus, creep and breaking strains (Edwards and Marks, 1995). Furthermore, *in vitro* techniques test property rather than function (Edwards and Marks, 1995). Generally, *in vitro* tests are performed on excised strips of skin from deceased or biopsy samples from living human subjects.

As the various techniques of *in vitro* testing have already been extensively covered in other literature e.g. Moronkeji and Akhtar (2015), only a brief overview of uniaxial tensile and indentation tests are provided in this section.

2.3.1.1 Uniaxial tensile tests

Uniaxial testing is easily one of the most accessible methods of mechanically testing skin. It has been used over the last 50 years to determine the material behaviour of skin *in vitro*. Previous studies by Ridge and Wright on strips of biopsy and autopsy skin demonstrated the relationship between the properties of skin and the alignment of collagen fibres (Ridge and Wright, 1966). Later, tests by Dunn and Silver (1983) showed the extensibility of skin, which reached an engineering strain of 100% and that the difference between the maximum elastic modulus for constant strain rate tests was 1.59 MPa ± 47% and 3.16 MPa ± 62% for the stress-relaxation tests (Dunn and Silver, 1983). A typical stress-strain curve is shown in Fig. 7, the different phases have been previously described in Section 2.3.

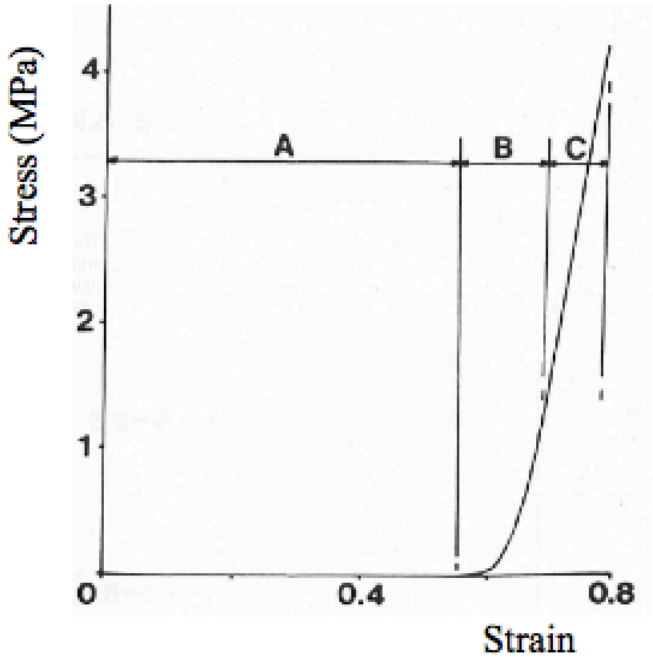

Figure 7 Stress-strain curve of skin obtained from the abdominal region of a 45 year old female subject (Daly and Odland, 1979). The graph shows the skin's profile as nonlinear with its mechanical behaviour falling into 3 different categories (where A = phase 1, B = phase 2 and C = phase 3).

2.3.1.2 Indentation tests

Within biomechanics and biomaterials characterisation, indentation has become a feasible technique for the local mechanical evaluation of tissue. For *in vitro* characterisation of skin biomechanics, indentation testing is a valuable technique. This is because it offers the

opportunity to determine the mechanical properties of very localised regions of skin compared to *in vivo* methods (Ebenstein and Pruitt, 2004).

Some examples of indentation tests of skin include its use to characterise the micromechanical properties of murine skin (Kendall et al., 2007), porcine skin (Jee and Komvopoulos, 2014) and stratum corneum samples of human skin (Pailler-Mattei et al., 2007b). The spatial resolution of the indentation measurements can be controlled by changing the indenter tip size. For example, Geerligs et al. used a 500 μm radius tip to characterise *ex vivo* abdominal skin obtained from patients undergoing abdominoplasty surgery (Geerligs et al., 2011). Their aim was to characterise the entire epidermis (stratum corneum and epidermis) rather than to assess a specific, localised region of the skin. In contrast, using a small tip (1–10 μm) results in very local properties being determined, particularly as the diameter of each corneocyte (40–50 μm) is larger than a small tip (Elias, 1983; Pailler-Mattei et al., 2007a).

Furthermore, Crichton et al. demonstrated that the mechanical characteristics of skin are influenced by the diameter of the probe used for indentation. Their work showed that the elastic modulus reduces with increased probe size and the data has been presented in Table 2. They suggest that the larger diameter probes are likely to cause a larger skin deflection before puncture and that the smaller probes will require greater structural integrity to bear the greater skin stiffness and forces. It was also postulated that the variation of elastic modulus with diameter of the probe may have been due to an aspect of stress-distribution within the skin by the stratum corneum and viable epidermis. The viable epidermis comprises the remaining layers that make up the epidermis and serve to regularly renew the stratum corneum (Prausnitz and Langer, 2008).

Table 2 Average elastic modulus of each probe size for nanoindentation tests performed on mice ears (Reproduced from (Crichton et al., 2013)).

Probe Size (μm)	Elastic Modulus, Mean ± SD (MPa)
0.5	29.70 ± 21.26
1.0	11.15 ± 4.90
2.5	8.19 ± 5.26
5.0	3.26 ± 2.01
10.0	1.31 ± 0.80
20.0	0.86 ± 0.44

The stress-strain curve in Fig. 8 depicts the locations along the curve where the elastic modulus or ultimate tensile strength (UTS) was taken for each study in Table 4.

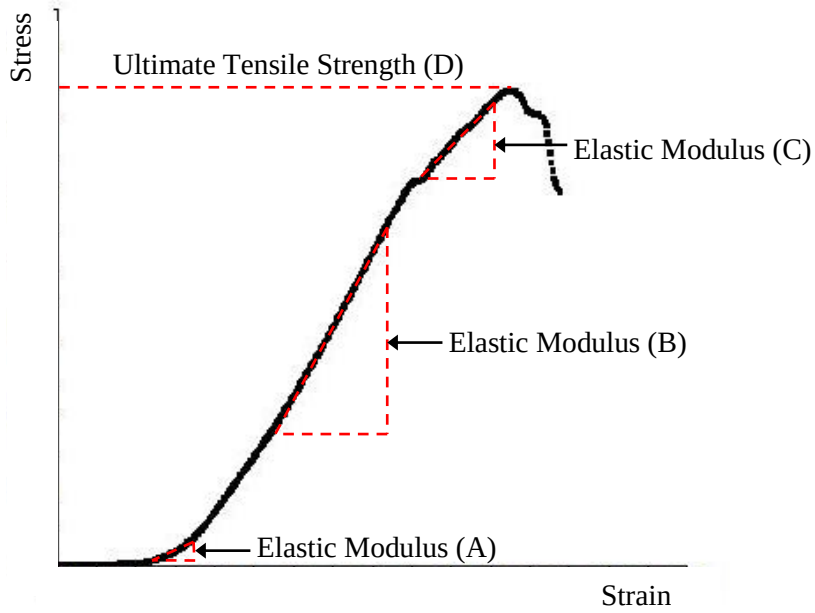

Figure 8 The stress–strain curve illustrating an abdominal porcine skin sample under uniaxial loading (Reproduced from (Zak et al., 2011)).

Table 3 presents a summary of the *in vitro* tests for human and porcine skin using indentation and tension methodologies. The table demonstrates that skin site, orientation and test approach influence the results of the mechanical characterisation of skin.

Table 3 Average elastic modulus for *in vitro* tests of human and porcine skin. In cases, where the elastic modulus has not been reported, the UTS values have been used and is denoted by *.

Experimental Technique	Elastic Modulus / UTS* (MPa)	Location on Stress / Strain Curve	Skin Site	Skin Details	Orientation	References
Tension	83.3± 34.9	B	Back	Human	Perpendicular Parallel 45 degrees	(Ni Annaidh et al., 2012)
	(2.50 ± 2.10)	B	Abdomen	Porcine	Parallel	(Zak et al., 2011)
	(7.17 ± 2.84)		Back			
	3 ± 1.5*	D	Forehead	Human	Perpendicular	(Jacquemoud et al., 2007)
	5–1000* 1–25 *	D	Stratum corneum		Parallel Perpendicular	(Wu et al., 2006)
Indentation	0.6	-	Abdomen (*ex vivo*)	Human	-	(Geerligs et al., 2011)
	0.0085		Dermal equivalents			(Zahouani et al., 2009)
	100–1000		Various			(Wilkes and Wildnauer, 1973)

Ni Annaidh et al. reported significant variations in the mechanical properties between samples of human skin from the back region at different orientations in terms of elastic modulus and the maximum tensile strength. In contrast, there were comparable results at ultimate failure and this was attributed to the interplay between orientation and skin site. Tests on abdominal and back neonatal porcine skin produced different values of elastic modulus (Zak et al., 2011), indicating that the back skin with the higher elastic modulus is stiffer than the abdominal skin. Zahouani et al. used dermal equivalents, which were made

from human fibroblasts put on a dermal substrate to demonstrate the contributions of the dermis and their results were comparable with the *in vivo* study of indentation tests on the volar forearm (see Table 4). Generally, the outcome of the mechanical characterisation of skin demonstrates how skin region, test approach, indenter type and size influence the results of the elastic modulus.

2.3.2 *In vivo* techniques

In vivo tests are useful because it provides information of how the skin reacts to the application of external forces such as compression and indentation on the body (Edwards and Marks, 1995). Several non-invasive techniques have been developed for measuring the mechanical properties of skin *in vivo*. The values obtained from these techniques are mainly descriptive (Hendriks et al., 2003a) and as Pailler-Mattei et al. demonstrated the large variation of elastic modulus for skin is profoundly influenced by the technique used (Pailler-Mattei et al., 2008).

Attempts have been made more recently to develop indentation testing as a tool for determining the *in vivo* properties of skin in a more quantitative manner (Pailler-Mattei et al., 2008a). Indentation tests involve the application of a known load (Bader and Bowker, 1983), or displacement to the skin, where the elastic modulus and other parameters are determined using contact mechanics models. In addition, uniaxial tensile testing on skin *in vivo*, also provides useful mechanical data as demonstrated by Meijer et al., whereby a tension test device was developed where pads were attached to human skin to induce deformation (Meijer et al., 1999).

As the various techniques of *in vivo* testing have already been extensively covered in other literature (Moronkeji and Akhtar, 2015), this section is a brief overview of the outcome of previous indentation studies and have been presented in Table 4. Nachman and Franklin

(2016) conducted indentation tests on the volar forearm of a healthy subject and obtained the reduced elastic modulus. Their results were comparable to the outcome of the indentation tests by Pailler et al. When their results were compared to reduced elastic modulus in the study by Groves (2011), the outcome was a significant difference. This wide variation in the reduced elastic moduli may be attributed to the size of the indenter head, where a large indenter head produces a low reduced elastic modulus, whilst a small indenter head produces a high value. Furthermore, Groves (2011) used two geometrically different indenter heads of varying sizes. It was observed that the reduced elastic modulus for the spherical indenter on skin was lower than that of the cylindrical indenter. Thus, the variation in the values for the reduced elastic modulus is typical for biological material; however, the characterisation of the mechanical properties of skin is also influenced by indenter size and type.

Table 4 Comparison of published elastic modulus results on the volar forearm of human skin using indentation methods *in vivo*.

Indenter	Elastic Modulus (kPa)	Reduced Elastic Modulus (kPa)	References
Spherical (R = 2 mm)	-	8.9–9.7	(Nachman and Franklin, 2016)
Spherical (R = 3.175 mm)	-	9.5	(Pailler-Mattéi and Zahouani, 2006)
Conical		12.5	(Pailler-Mattei et al., 2008)
Spherical (R = 3.175 mm)		8.3	(Zahouani et al., 2009)
Spherical (R = 0.7938 mm)	39.64 ± 10.19	47.19	(Groves, 2011)
Cylinder (R = 0.25 mm)	65.86 ± 13.37	78.41	

2.4 *In Vitro* Biomechanical Experiment on Skin and its Sub-layers

In this section, the different experimental tissues and materials that have been used to biomechanically represent human skin are reviewed.

2.4.1 The skin mimic

Murine and porcine skins have been used increasingly in the literature as a substitute for human skin. According to Fourtanier and Berrebi (1989), neonatal porcine skin is a superior model for human skin in terms of hair sparseness and physical properties (Fourtanier and Berrebi, 1989); hence, neonatal porcine skin is preferred over tissue from older pigs. Neonatal porcine skin also exhibits close biomechanical properties to human skin (Shergold et al., 2006) and is readily available. Donnelly et al. also used neonatal porcine skin for their microneedle application studies due to these reasons (Donnelly et al., 2010). Furthermore, as mentioned in the previous section, Zak et al. carried out uniaxial tests on neonatal porcine skin and documented the elastic modulus for various skin locations.

The literature also suggests that murine skin behaves similar to human skin for microneedle penetration studies (Kochhar et al., 2013b). There is an apparent difference in biomechanical behaviour for murine skin compared to human skin *ex vivo*. This is because under low loads human skin undergoes more extension than murine skin (Groves et al., 2013). Also, murine skin is thinner than human skin (Ding et al., 2009) with a significantly thinner epidermal layer (Li et al., 2015). It is therefore important that these factors are taken into consideration. Crichton et al. also stated that the mechanical behaviour of mice skin was comparable to human skin and cited the similarity in their results with indentation test results carried out by Geerligs et al. on frozen human tissue (Geerligs et al., 2011). Geerligs et al. used an *ex vivo* abdominal human tissue and reported that the elastic modulus of the stratum corneum (2.6 ±

0.6 MPa) was greater than the epidermis (1.1 ± 0.2 MPa). They also showed that a reduction in the stiffness of the viable epidermis causes an increase in indentation depth.

Zahouani et al. showed that the dermis made a significant contribution to skin because of its load bearing capabilities and reported the importance of a full thickness skin sample (Zahouani et al., 2009). Other work demonstrated the similarity in stiffness between dermal equivalents and the volar forearm (Pailler-Mattéi and Zahouani, 2006; Pailler-Mattei et al., 2008), which indicated that during *in vivo* tests, the mechanical contribution from the dermis was prominent. Furthermore, it is easier to penetrate the human epidermis without the dermal layer (Li et al., 2015). Pailler-Mattei et al. *ex vivo* tests on the stratum corneum layer only, yielded a low elastic modulus (7–8 kPa) as compared to the result of the indentation test on abdominal tissue shown in Table 3.

Based on the literature, neonatal porcine skin appears to be a more suitable substitute compared to murine skin because of its similarities to human skin in terms of its mechanical behaviour and physiological structure (Fourtanier and Berrebi, 1989; Shergold et al., 2006).

2.4.2 The subcutaneous mimic

As previously stated, the subcutaneous layers play a vital role in the mechanical properties of skin. The thickness of the subcutaneous layer varies between 5.0–15.0 mm in the elderly (Renephra, 2012). Using an ultrasound indentation system, Zheng et al. reported that the effective elastic modulus of the subcutaneous tissue of the forearm increased from 14.0 ± 5.0 kPa to 58.8 ± 1.7 kPa during contraction of the muscles. This indicated that soft tissues increase in stiffness as the corresponding muscles contract (Zheng et al., 1999).

As early as 1912, Schade (1912) discovered that there was a significant difference in behaviour of normal tissue compared to oedematous tissue, as the time required for the skin to return to its initial condition following the removal of a weight took longer for the

oedematous tissue (Schade, 1912). Using the same approach, Kirk and Kvorning (1949) demonstrated the contrast between young and old subjects. Following the removal of a weight on the skin, the indentation was greater in the young subjects compared to the old subjects and there was an almost instantaneous recovery of the skin to its original state in young subjects compared to the old subjects (Kirk and Kvorning, 1949). In their study, Radhakrishnan et al. demonstrated that acute intestinal oedema causes a decrease in tissue stiffness (Radhakrishnan et al., 2007). Therefore, tissue stiffness is influenced by fluid content. Furthermore, Guyton et al. carried out an extensive study on ISF pressure (Guyton et al., 1971), where he recorded the pressures for the various kinds of oedema and ISF (see Table 5).

Table 5 The interstitial fluid pressures as they relate to oedema (Guyton et al., 1971).

Fluid Content	Pressure (mmHg)	Pressure (kPa)
Subcutaneous pitting oedema	0 – 6	0 – 0.8
Subcutaneous pitting oedema following fluid injection in tissues	15 – 20	2.0 – 2.67
Non-pitting oedema	12 – 15	1.6 – 2.0

In tissue engineering applications, gelatine gel is often used as a mimic for natural tissues (Ahearne et al., 2005), as it can be used to simulate the viscosity and density of living human tissue and therefore, acts as a good representation for human tissue (Kwon and Subhash, 2010). Awad et al. demonstrated that the collagenous material present in gelatine gel provided its stiffness and mechanical strength (Awad et al., 2004). Mridha and Odman, (1985) and Mridha et al. used two mechanical techniques to determine the mechanical behaviour of subcutaneous pitting oedema. Their first technique, the mechanical impedance method is a semi-quantitative method that describes the inertial, elastic and frictional properties of tissues subjected to external deformation. Mridha and Odman (1985)

demonstrated the difference in mechanical impedance of subcutaneous oedematous tissues compared to normal tissue. A compression was applied to gelatine gel concentrations of 80%, 84%, 88%, 92% & 96% water content by weight and the static force was measured from the resulting deformation of the gelatine gel. They observed that softer structures, such as high water content gelatine gels and subcutaneous pitting oedema tissues had lower mechanical impedance compared to non-pitting oedema, which exhibited higher mechanical impedance. The water content in the gelatine gels highly influenced the outcome of the mechanical impedance tests (Mridha and Odman, 1985).

The second technique, which is the mechanical pulse wave propagation method, uses velocity, attenuation and frequency to assess the mechanical behaviour of soft tissues. This is because the mechanical properties of skin are linked to its water content and as a consequence, the propagation velocity, attenuation and frequency in the gelatine gels are influenced by its water content. The technique was used to determine the mechanical behaviour of the same specific concentrations of the gelatine gels mentioned above, normal tissues from several anatomical regions and oedematous tissue from different patients. The propagation velocity for 80%, 84%, 88%, 92% and 96% gelatine gel concentrations were 3.05 ± 0.10 ms^{-1}, 2.02 ± 0.38 ms^{-1}, 1.13 ± 0.21 ms^{-1}, 0.77 ± 0.08 ms^{-1} and 0.33 ± 0.03 ms^{-1} respectively. The results showed that an increase of water content in the gelatine gel concentrations resulted in a decrease of the propagation velocity. For the tests carried out on 10 healthy subjects, the velocity varied from 1.72–8.18 ms^{-1}; for pitting oedema, it ranged from 1.19–3.18 ms^{-1} and for non-pitting oedema, it was between 13.27–14.70 ms^{-1}. Based on their findings, velocities for pitting oedema compared to the velocities of 80%, 84% and 88% gelatine gel concentrations. Overall, the propagation velocity of mechanical pulse waves was found to be lower in pitting oedema than for normal tissues and higher in non-pitting oedema (Mridha et al., 1992). Finally, their study demonstrated that subcutaneous pitting oedema

could be characterised by measuring the velocity of the mechanical pulse wave propagation. It should be noted however that the mechanical pulse wave propagation method only applies to subcutaneous pitting oedema, where techniques based on the displacement of fluid due to external compression are not pertinent (Mridha et al., 1992).

By altering the water content of these gels and subsequently varying its mechanical properties, the opportunity to determine experimentally the influence of subcutaneous tissue on microneedle performance could be investigated.

2.4.3 The muscle mimic

Pailler-Mattei et al. showed that the mechanical properties of the subcutaneous layers and the muscles influence the mechanical properties of skin. Their work involved indentations to assess the impact of the subcutaneous layers and muscles. The outcome was a reduced elastic modulus of the muscle, which was between 32 kPa and 96 kPa. Tsaturyan et al. also showed that the elasticity modulus for the papillary muscle of a rat decreased with increased quantity of sodium chloride and increased with reduced quantity of sodium chloride (Tsaturyan et al., 1984). Based on these findings, it is important to take into consideration the contributions from the subcutaneous layers and muscles to the elastic modulus of skin.

Generally, ballistic gelatin can be used to simulate the behaviour of a projectile on human tissue (Thali et al., 2002). Kwon and Subhash (2010) showed that the initial elastic modulus for ballistic gelatin was 10.9 kPa. They also reported that when loading rate increased, the compressive strength increased from 3 kPa at a strain rate of 0.0013 s^{-1} to 6 MPa at a strain rate of 3200 s^{-1} (Kwon and Subhash, 2010). A material similar to ballistic gelatine, Perma-Gel® is also a suitable substitute for muscle. Although Perma-Gel® is not ballistic gelatine, its advantages are that it can be used at room temperature unlike ballistic gelatine that has to be used at 4°C or lower. In addition, it has many of the same characteristics as 10% ballistic

gelatine (Moy et al., 2011) and is used for ballistic testing of ammunition (Ryckman et al., 2012). Therefore, Perma-Gel® is an ideal candidate as a muscle mimic (Caron-Laramee and Brouillette, 2014).

2.4.4 Summary of experimental models of skin and its sub-layers

The summary of the elastic moduli of skin and its sub-layers are presented in Table 6. The wide variation of values for skin and each sub-layer is typical for biological material. The data presented was used to develop the representative *in vitro* skin model, with elastic modulus properties in the range of 39.64–65.86 kPa for skin, 14.0–58.8 kPa for subcutaneous tissue mimic and 32–96 kPa for muscle mimic for the microneedle penetration studies carried out in this thesis.

Table 6 The elastic modulus of skin and its sub-layers obtained from the literature, * denotes reduced elastic modulus and ** denotes pressure values.

Material	Region	Elastic Modulus (kPa)	References
Skin	Neonatal porcine abdomen	$2.50 \pm 2.10 \times 10^3$	(Zak et al., 2011)
	Neonatal porcine back	$7.17 \pm 2.84 \times 10^3$	
	Human back	$83.3 \pm 34.9 \times 10^3$	(Ni Annaidh et al., 2012)
	Human forearm	39.64 ± 10.19 65.86 ± 13.37	(Groves, 2011)
	Human abdomen	0.6×10^3	(Geerligs et al., 2011)
Subcutaneous tissue	Human forearm	14.0 ± 5.0 58.8 ± 1.7	(Zheng et al., 1999)
	Pitting oedema	0–0.8**	(Guyton et al., 1971)
	Pitting oedema with fluid injected	2.0–2.67**	
	Non-pitting oedema	1.6–2.0**	
Muscle	Human forearm	32–96*	(Pailler-Mattei et al., 2008)
	Ballistic gelatine	10.9	(Kwon and Subhash, 2010)

2.4.5 Limitations of the experimental model

The work in this thesis focused on a skin model that comprised a full thickness skin sample, a subcutaneous mimic of varying water content concentration and a muscle mimic. There are many limitations with developing an *in vitro model* of skin that can adequately mimic the *in vivo* behaviour of oedematous skin. For example, the way in which the subcutaneous tissue changes with disease (Section 1.3.3) was beyond the scope of this thesis.

Furthermore, the natural tension of skin (as discussed in Section 2.3) was not considered in this experimental model due to the number of variables that were already under consideration for the experimental analysis. A postulation would be that due to the varied mechanical properties of the different water content gelatine gels, the skin tension would vary due to the contributions from the different gelatine gels.

2.5 Microneedle Arrays

This section introduces the various types of microneedles and its manufacturing process. An overview of how microneedles are applied to skin is mentioned as well as a review of its role in delivering drugs and extracting fluid from the body.

2.5.1 Microneedle designs

Microneedle arrays are a promising minimally invasive means of delivering drugs into the body via skin or extracting ISF from skin, for example for glucose measurement (Mukerjee et al., 2003). They are sub-millimetre projections capable of penetrating the stratum corneum and are typically made from a range of different materials including silicon (Henry et al., 1998), polysilicon (Zahn et al., 2000), polymers (Park et al., 2005), metal (Martanto et al., 2004) and sugars (Lee et al., 2011).

Most types of microneedles are typically fabricated as an array of up to hundreds of needles over a base substrate. Solid arrays, solid arrays coated with therapeutic compound,

biodegradable arrays of microneedles and hollow microneedles are the four main categories of microneedles, as shown in Fig. 9. Solid arrays can be used to pierce skin, discarded and the drug applied to the perforated area (Arora et al., 2008). For the coated microneedles with therapeutic compound, the drug is released upon successful penetration of skin. Biodegradable microneedle arrays are made from biodegradable or water soluble polymers that dissolve readily in skin. Hollow arrays, which use the same concept as the hypodermic needle can be used to access the fluid bed in the epidermis (Kim et al., 2012).

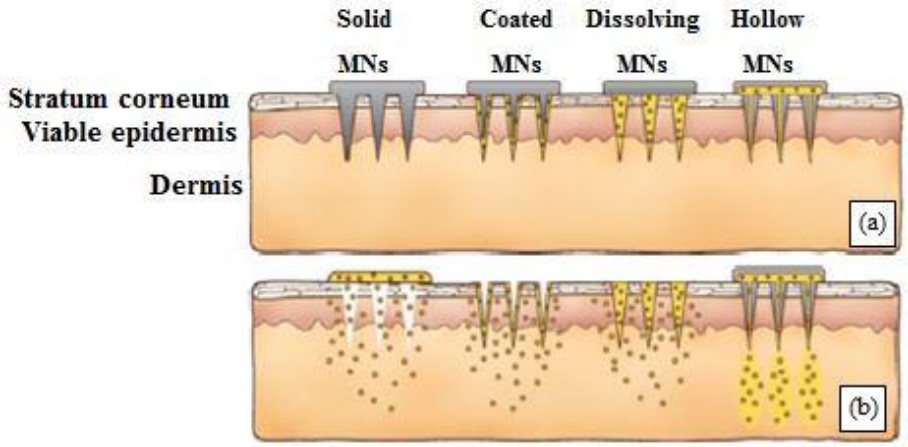

Figure 9 The four main types of microneedle design: (a) solid array inserted into skin; solid array coated with therapeutic compound; dissolving microneedles; hollow microneedles (b) drug is applied after perforation created by solid array; therapeutic compound is released with insertion; biodegradable microneedles are absorbed by skin along with therapeutic compound; therapeutic compound is released via the hollow area in the microneedle. (Figure adapted from (Kim et al., 2012)).

Microneedles are designed to bypass the stratum corneum in order to transport therapeutic compound into the epidermal layer. Microneedle drug delivery is not associated with pain or bleeding compared to conventional hypodermic needles because there are no nerve endings or vasculature within the epidermis (Arora et al., 2008). Moreover, the microchannels in skin created by the microneedles perforating the stratum corneum offers a user-friendly means of drug delivery (Prausnitz, 2001).

The design of the microneedle can increase skin permeability for drug delivery, with particular attention given to parameters such as tip radius, base radius, interspacing, number

of needles per array and penetration depth (Olatunji et al., 2009), as well as the mechanical behaviour of skin during its interaction with microneedles.

2.5.2 Microneedle fabrication methods and materials

Microneedle arrays have been manufactured using a variety of materials including silicon (Henry et al., 1998), polysilicon (Zahn et al., 2000), polymers (Park et al., 2005) and electrodeposited metals (Davis et al., 2005). Although there are advantages to using different materials to fabricate microneedles, each material has its own limitations which affect microneedle performance and effectiveness. Brittle materials such as silicon and glass can affect the structural integrity of the microneedle whereas polymers possess low elastic moduli and hardness. Electrodeposited metals such as nickel are known skin irritants (Garner, 2004). Hence, the use of biocompatible bulk titanium substrates eradicates fracture-induced failure common in more brittle elements while retaining adequate mechanical rigidity. Therefore, biocompatible bulk titanium is an ideal material for use in drug delivery applications (Parker et al., 2007). Moreover, polymer microneedles are easily fabricated and cost effective (Barrett et al., 2015) and are also an ideal material for the manufacture of microneedles.

Based on the attributes of polymers, microneedles manufactured from polymers were used for the work carried out in this thesis.

Table 7 provides a summary of the fabrication process and materials of the four main types of microneedle designs.

Table 7 Examples of previous published work on microneedles manufacturing processes.

Microneedle Type	Manufacturing Methods	Materials	Delivery Studies in Mammals Skin	
			In vivo	*Ex vivo*
Solid Arrays	**Reactive ion etching** (Henry et al., 1998) **Electrical discharge machining** (McAllister, 2003) **Photochemical etching** (Martanto et al., 2004)	**Silicon** (Henry et al., 1998) **Stainless steel** (Martanto et al., 2004) **Polymers** (Donnelly et al., 2011)	**Insulin vaccine** (Martanto et al., 2004)	**Fluorescence and dyes** (Henry et al., 1998; McAllister, 2003)
Coated Solid Arrays	**Electrospinning** (Sawicka et al., 2007)			
Biodegradable Arrays	**Micromoulding** (Donnelly et al., 2011)	**Sugars** (Lee et al., 2011) **Biodegradable polymer**s (Park et al., 2005)	**Hydrophilic molecules** (Lee et al., 2011)	
Hollow Arrays	**Micromoulding** (Davis et al., 2005) **Reactive ion etching** (Mukerjee et al., 2004)	**Polymers** (Davis et al., 2005) **Silicon** (Mukerjee et al., 2004)	**Insulin** (Davis et al., 2005)	

Microneedles with long microneedle projections (1500 μm) can cause pain comparable to that of a hypodermic needle in patients (Gupta et al., 2011). This indicated that for the design of the microneedle, the length of the microneedle projection was the most important aspect in the measurement of pain (Gill et al., 2008).

In this project three different geometries of polymeric microneedles were utilised of which one was for a pilot study (polyetheretherketone/PEEK) and the other two (polymethylmethacrylate/PMMA) were primarily used to determine penetration intensity and effectiveness. These microneedles were chosen because they have previously been used in medical application studies carried out by Renephra. During the pilot study, the PEEK microneedles caused damage to the tissue and it was hard to reproduce perforations, therefore PMMA microneedles were used for the bulk of the work in this thesis.

2.5.3 Application of microneedles in fluid extraction

A study by Mukerjee et al. describes the use of an array of hollow silicon microneedles for effective transdermal extraction of minute samples of human ISF (Mukerjee et al., 2003). Further work by Wang et al. provided the first demonstration of ISF extraction from skin's dermis following microneedles insertion in hairless rats and human subjects *in vivo*. The ISF glucose concentration measured with a conventional electrochemical glucose monitor was commensurate with glucose levels in blood (Wang et al., 2005). Later, studies by Khanna et al. used microneedles for ISF sampling, by accessing the fluid in the dermal layer (Khanna et al., 2008).

There are several mechanisms through which fluid can be extracted using microneedles, which are capillary action, osmosis and negative pressure therapy. These fluid removal mechanisms are governed by some equations (Samant and Prausnitz, 2016). The relationship between flux (Q), diffusion (D_e), surface area (A), concentration difference (ΔC) and the thickness of the barrier to diffusion (L) is described in Equation 1 for capillary action using Fick's Law.

$$Q = D_e \cdot \frac{\Delta C}{L} \cdot A \qquad \text{Equation 1}$$

The influence of the osmotic permeability coefficient (P_w) for permeation under osmotic gradient is shown in Equation 2.

$$Q = P_w \,.\, A \,.\, \Delta C \qquad \text{Equation 2}$$

Using Darcy's Law, the relationship between permeability (K), the viscosity (μ) and change in pressure (ΔP) for negative pressure therapy is given by Equation 3.

$$Q = \frac{K}{\mu} \,.\, \frac{\Delta P}{L} \,.\, A \qquad \text{Equation 3}$$

Using these equations, Samant and Prausnitz stated that the predicted flow rate using capillary action is 0.09 nL/min/MN, it is 1 nL/min/MN for osmosis and for negative pressure therapy is 12.6 nL/min/MN. The negative pressure therapy is potentially an ideal option for ISF extraction as it could yield more than 12 times the amount of fluid compared to the other mechanisms (Samant and Prausnitz, 2016). Therefore, the potential predicted flow rate for a PMMA array of 1316 microneedles is 118.44 nL/min for capillary action, 1316 nL/min for osmosis and 16581.6 nL/min for negative pressure therapy. For a PMMA array of > 6000 microneedles is 540 nL/min for capillary action, 6000 nL/min for osmosis and 75600 nL/min for negative pressure therapy.

The main motivation of this project is to obtain a greater understanding of microneedle interaction with skin to facilitate better fluid removal.

2.6 The Mechanics of Microneedle Perforation of Skin

The penetration of soft tissue by sharp implements is of widespread importance, particularly for technological applications such as the perforation of human skin by microneedles for administering drugs or fluid extraction. To date, *in vitro* tests using microneedles have been performed on various skin models. The challenge of mimicking the mechanical properties of skin with consideration given to contributions from skin's individual layers coupled with its

interaction with microneedles remains. This section considers the mechanics behind microneedles interaction with skin.

2.6.1 Insertion force as determined numerically

Kong et al. reported the outcome of numerical simulations of a single microneedle insertion into a multi-layered human skin. The outcome of their study demonstrated the feasibility of predicting the deformation and failure of skin. In addition, the insertion force of a microneedle during the insertion process was determined as ≈0.35 N and the point of insertion into skin was identified as a sudden decrease in force on the force–displacement curve. This result was in agreement with experimental studies by Bischoff et al. and Davis et al. (Bischoff et al., 2000; Davis et al., 2004). Furthermore, the numerical results showed that the stiffness, failure stress, thickness of the stratum corneum, needle tip area and the needle wall angle are primary control parameters for insertion of the tapered microneedles used in their study into the multi-layered human skin (Kong et al., 2011). For hollow microneedles with a large tip diameter however, a large wall thickness resulted in a high insertion force and for hollow microneedles with a small tip diameter, the wall thickness had almost no effect on the insertion force (Kong et al., 2011). This indicated the influence of microneedle geometry on insertion force. It appeared that contributions from parameters such as dermal thickness and the hypodermis was almost negligible (Kong et al., 2011). This observation was not consistent with work by other researchers. According to Zahouani et al. contributions from the dermal layer should not be ignored (Zahouani et al., 2009). More recently, Li et al. in their study further added that full thickness skin was paramount to understanding microneedle application to skin (Li et al., 2015).

Moreover, Groves et al. developed a numerical multi-layered skin model i.e. epidermis, dermis and hypodermis using the Ogden material model to describe the hyperelastic properties of each layer of human skin. Further, it was successfully used for a single

microneedle application to skin and the results showed that it could predict skin deformation at a micron scale (Groves et al., 2012). A combination of work by Kong et al. and Groves et al. could lead to promising outcomes in the development of specific microneedle geometries for various skin types, as the numerical analysis has demonstrated the importance of microneedle geometry for successful microneedle perforation of skin.

A detailed coverage of the numerical modelling of microneedle studies is beyond the scope of this thesis.

2.6.2 Microneedle insertion force and insertion velocity

Davis et al. demonstrated using several microneedle geometries that insertion force varied linearly with the effective area of contact between the needle tip and skin. The measured insertion forces were between 0.1–3 N for manual application (Davis et al., 2004). Verbaan et al. conducted a study, which demonstrated that with an electrical applicator, microneedle penetration could be improved with a higher insertion velocity. Their setup provided the ability to deliver low density microneedle arrays into dermatomed human skin at 1 or 3 ms^{-1} (Verbaan et al., 2008). Donnelly et al. noted that an adequate insertion force and insertion velocity was required to overcome the inherent elasticity present in the stratum corneum for successful microneedle application. It was reported that a large insertion force applied at low speed barely penetrated the stratum corneum, however, a smaller force at a higher speed perforated it (Donnelly et al., 2010). Further studies by Donnelly et al., in which a compression force was used for microneedle application, showed that 600 μm and 900 μm needle projections perforated neonatal porcine skin at a low application force of > 0.03 N/microneedle. In addition, Olatunji et al. conducted similar tests using a compression force at low insertion velocities of 1 mms^{-1} to determine the influence of microneedle interspacing

on insertion force and found that insertion force was dependent upon microneedle interspacing and the number of microneedles.

More recently, van der Maaden et al. demonstrated that the stratum corneum layer could be overcome in a reproducible manner using an impact-insertion applicator at a fixed insertion velocity of 3 ms^{-1} and insertion forces ranging from 3.43–22.1 N. Their study showed that when microneedles were manually inserted onto *ex vivo* human skin, perforations were visible following staining indicating approximately 81% microneedle penetration. However, after the stratum corneum was stripped, only 46% microneedle penetration was visible. Furthermore, it was also demonstrated that the manual application device resulted in low penetration efficiencies. In contrast, with a microneedle impact-insertion applicator efficient and reproducible penetration of high-density microneedles into skin was found. Fig. 10 shows both microneedle applicators and their perforations on skin.

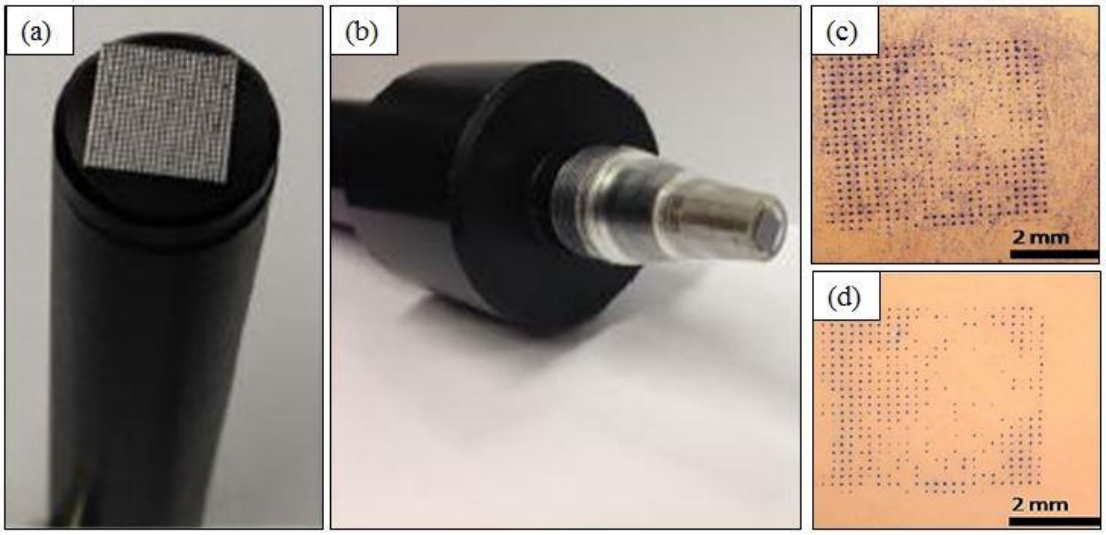

Figure 10 Microneedle application using (a) silicon microneedle array mounted on a manual insertion device, (b) an impact-insertion applicator, (c) perforations created using the impact-insertion applicator on the stratum corneum and (d) after stratum corneum removal showing that the perforations travelled beyond this layer (Reproduced from (van der Maaden et al., 2014)).

2.6.3 Microneedle applicators

Microneedles puncture skin by overcoming the inherent elasticity of the stratum corneum to create temporary microchannels for fluid to travel through (Kochhar et al., 2013b). However,

for effective and reproducible performance of these microneedles in drug delivery applications or fluid extraction, irrespective of design constraints such as, material, height and needle density, it is imperative that they successfully penetrate skin (Davis et al., 2004). The irregular surface topography of skin remains a significant challenge for reproducible microneedle penetration. It is for this reason that an appropriate device is required to ensure that microneedle penetration of skin occurs in a repeatable and predictable manner (Bouwstra et al., 2009).

Various designs of the microneedle delivery apparatus have been developed in the literature such as a Dermaroller® (Badran et al., 2009), syringe applicators (Haq et al., 2009), actuator driven applicator (Bouwstra et al., 2009), electrically driven applicator (Verbaan et al., 2008) and an impact applicator (van der Maaden et al., 2014) to determine a suitable way of breaching skin's barrier. In some instances manual application of the microneedle was introduced to skin (Verbaan et al., 2007; Verbaan et al., 2008), however, this approach did not always yield reproducible penetration. Fig. 11 shows several examples of microneedle applicators. There have been several review papers on microneedle applicators and therefore detailed coverage of it is beyond the scope of this project.

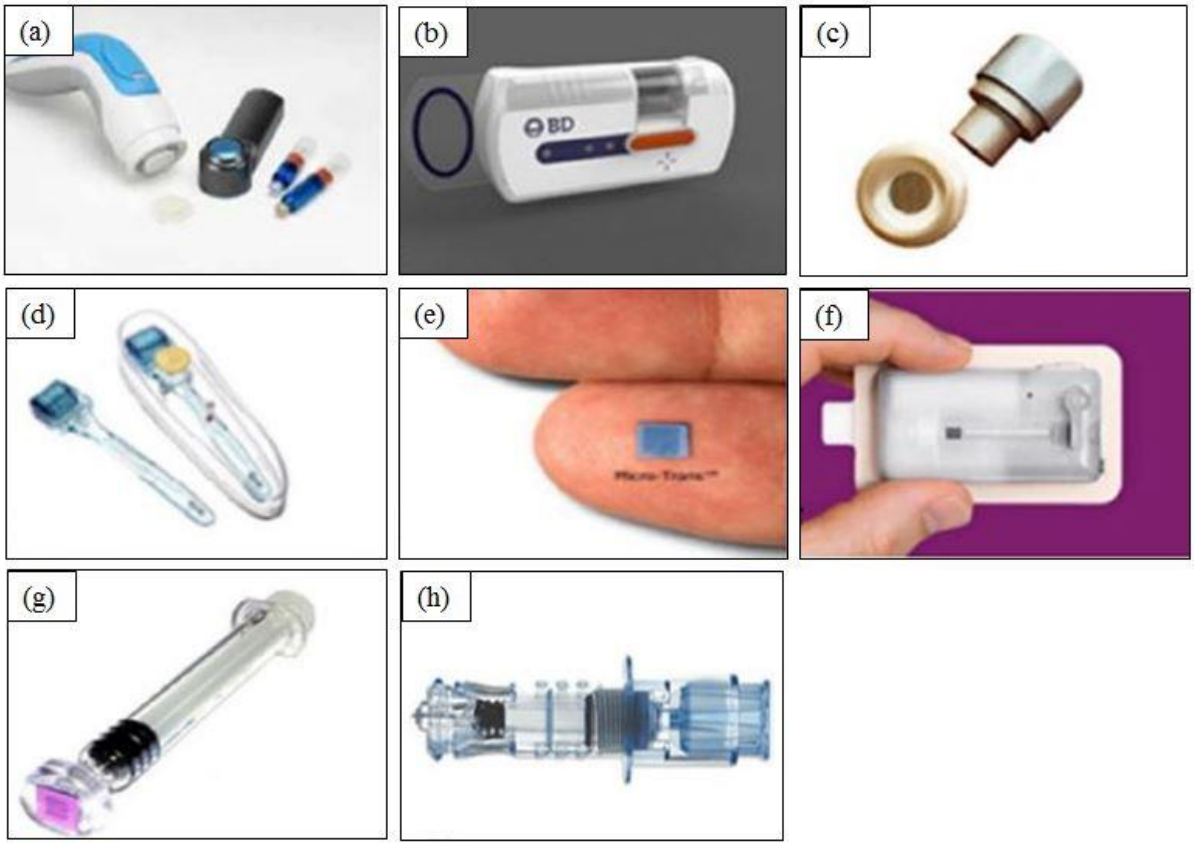

Figure 11 Microneedle applicators (a) Microstructured Transdermal System (MTS), (b) microinfusor, (c) Macroflux®, (d) Microneedle Therapy System (MTS Roller™), (e) Microtrans™, (f) h-patch™ , (g) micronjet and (h) Intanza® (Reproduced from (Indermun et al., 2014)).

2.6.4 Microneedle geometry

Design considerations of the microneedle in terms of its length, pitch, density, radius and shape are important because it affects its interaction with skin and how readily the drug is permeated (Olatunji et al., 2009; Olatunji et al., 2013). These parameters also contribute to the force at which the microneedle is fractured. The sharpness of the microneedle tip is another significant geometrical feature as it has a direct effect on the insertion force into skin (Davis et al., 2004; Park et al., 2005). Another microneedle design feature that is subject to various definitions is the aspect ratio, which has been described as the base over tip diameter (Huang and Fu, 2007). It has also been defined as the ratio of the microneedle length to the tip diameter and as the length over width of the microneedles (Davis et al., 2005). Al Qallaf et al. have said that the aspect ratio relates to the ratio of the pitch between two microneedles

to the microneedle radius. The aspect ratio is an important design feature that should not exceed 2.0 to avoid overlapping between microneedles. Furthermore, if the value < 2.0, the needles are placed too close to each other (Al-Qallaf and Das, 2008). Microneedle geometries can differ from 50–250 μm in base width, 150–1500 μm in length and 1–25 μm in tip diameter (Arora et al., 2008).

Fig. 12 shows the dye stained images from the study by Xiang et al., whereby it was revealed that if the spacing between two adjacent microneedles was larger than 400 μm, more than 95% of the microneedles successfully perforated the tissue. If however, there was smaller spacing between the microneedles, there was reduced penetration. Previous work indicated that increasing the number of needles on an array can lead to an increase in the rate of transdermal drug delivery (Yan et al., 2010). Later on, Section 2.7.1 explains dye staining techniques in more detail.

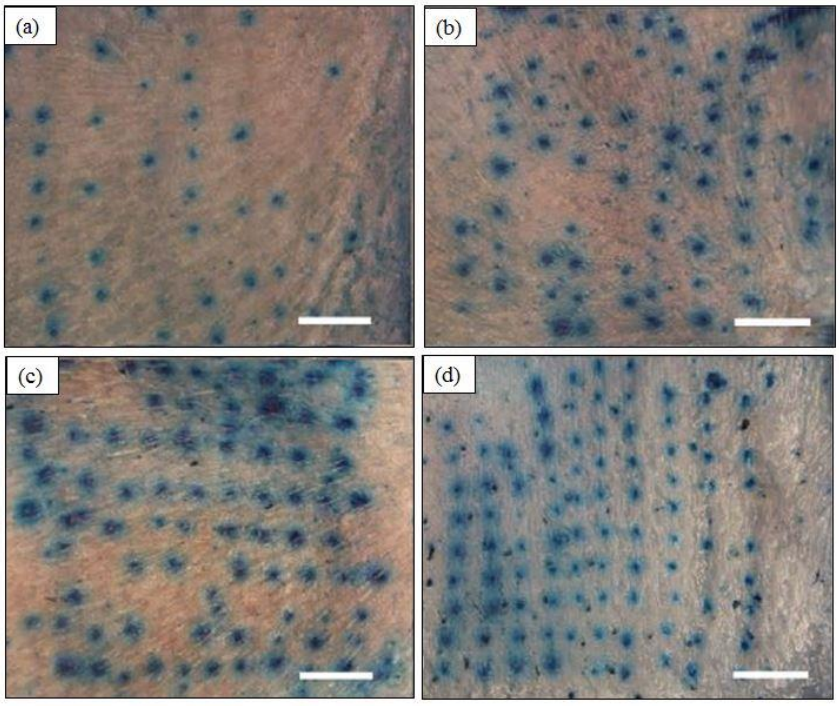

Figure 12 Dye staining shows the effect of microneedle interspacing perforation quality on rat skin (a) 250 μm (b) 300 μm (c) 350 μm and (d) 400 μm. Scale bar represents 500 μm (Reproduced from (Xiang et al., 2015)).

2.6.5 Microneedle studies on *in vitro* skin models

Over the years various types of *in vitro* skin models have been used to demonstrate the interaction between skin and microneedles. The work carried out by Park et al. placed a heat stripped epidermis from a human cadaver on ten layers of tissue paper to provide a 'tissue-like' mechanical support before a 5 × 20 array of bevelled-tip microneedles was pierced into it at a force of 4 N. Their study demonstrated the improved skin permeability with increased numbers of microneedles on the array (Park et al., 2005). In the work by Verbaan et al., dermatomed human skin was placed on a Styrofoam support to protect the microneedles from damage. The skin was pierced using a manual applicator at approximately 50 N pressure (Verbaan et al., 2007). The height of the microneedle projections was varied for insertion into skin, with 900 μm, 700 μm and 550 μm perforating the tissue. The 300 μm microneedle did not cause any perforations in the tissue. The intensity of the Trypan blue dye adhering to the microchannels created in the skin was greater for the longer microneedles than for the shorter microneedles (Verbaan et al., 2007). Later on, Section 2.7.1 discusses dye staining techniques like Trypan blue in more detail.

Badran et al. also used human skin from the abdominal region in their skin model. The subcutaneous fat was completely removed; the surface of the skin cleaned with PBS solution and then allowed to dry under ambient air conditions for 20 mins. The skin was then wrapped in foil and stored at −26°C until use. The skin was placed on filter paper soaked in PBS solution supported by cork plates. Their study showed that penetration and permeation of hydrophilic model drugs were enhanced after skin perforation with the Dermaroller® (microneedle applicator). The Dermaroller® with the longest microneedle length (500 μm) was the most promising for drug delivery into skin and the Dermaroller® with the shortest microneedle length (150 μm) led to a pronounced deposition of the model drugs in the stratum corneum (Badran et al., 2009).

Yan et al. also considered the effects of microneedle length and density on microneedle perforation quality. The difference with the above mentioned studies was that the human epidermal membrane was placed on a soft sponge pad as an underlying substrate. Their study showed that the longer microneedle length (650 μm) resulted in a pronounced deposition of the model drug across skin compared to the shorter microneedle length (≤ 300 μm). In addition, the increase of the microneedle length beyond 650 μm did not produce a significant increase in drug delivery and that the less dense microneedle arrays were more effective in boosting drug delivery (Yan et al., 2010).

Studies by Donnelly et al. and Olatunji et al. used dental wax as their underlying substrates for neonatal porcine skin. The tissue was preserved at −20°C until use. The skin model was perforated at low compression forces of approximately 0.03 N/microneedle.

An 8 × 8 microneedle array was inserted into excised pig skin cadaver. The hair was removed using an electric hair clipper and then hair removal cream. The skin samples were cleaned and stored at −80°C until use. The subcutaneous fat was removed using a scalpel and the skin fixed fully stretched on a thin 7–8 mm thick layer of modelling clay to act as the tissue-like mechanical support. The microneedles were manually inserted by applying thumb pressure for approximately 1 min. The tissue was stained with Trypan blue dye for 5 mins to highlight perforations in the stratum corneum. Haematoxylin and Eosin (H&E) staining were used to visualise the perforation detail and showed that skin layers had been breached. This therefore suggested that the encapsulated drug could be delivered efficiently. In addition, it also demonstrated that thumb pressure provided adequate force to penetrate skin (Kochhar et al., 2013a; Kochhar et al., 2013b).

As microneedle length affects its performance in skin, the microneedles used in this thesis were in a range of 352–650 μm long. Additionally, the spacing was kept between 360–1000

μm and it was also important that the microneedles were medical grade allowing for their use for *in vivo* studies.

The ideal preservation technique for the excised skin is to snap freeze the tissue sample in super-cooled isopentane and then store at –80°C. Snap freezing reduces the chance of water present in the sample forming ice crystals during the freezing process, and better maintains the integrity of the sample (Graham et al., 2011). The tissue preservation approach in some of the studies could have influenced the outcome of the microneedle perforating the skin model. Furthermore, in the studies where only the epidermal layer was placed on the substrate, the mechanical contributions from the dermal layer were ignored and this could have affected the outcome of the tests. This is because the dermal layer provides significant mechanical strength to skin (Zahouani et al., 2009). In addition, the mechanical contribution from the various substrates was not taken into consideration in these skin models, as these substrates would behave in a mechanically different way to the actual underlying substrates of skin such as tissue fluid and muscle. This therefore would make it challenging to predict microneedles response to skin in a consistent manner.

This project aims to develop a more representative *in vitro* skin model overcoming the limitations of these earlier studies.

2.7 Assessment of Microneedle Perforation of Skin

Staining is one of the methods used in determining successful perforation of skin following microneedle application. Staining of tissues involves getting the dye to the site of attachment through diffusion and holding the dye to its substrate through propulsion (Dapson, 2005). This section aims to review some of the available methodologies that are appropriate for this study.

2.7.1 Dye staining

The more commonly used dyes for staining microneedle perforated skin samples are Trypan blue and methylene blue dyes. 0.4% Trypan blue solution is normally used as a cell stain to examine cell viability using the dye exclusion test. This test can be carried out whenever cell viability is required to be established in a prompt and thorough manner. Moreover, the dye exclusion test is based upon the principle that viable cells do not absorb impermeable dyes such as Trypan blue, but instead dead cells are permeable and absorb the dye (Strober, 2001). Fig. 13 shows images of microneedle perforations stained with Trypan blue.

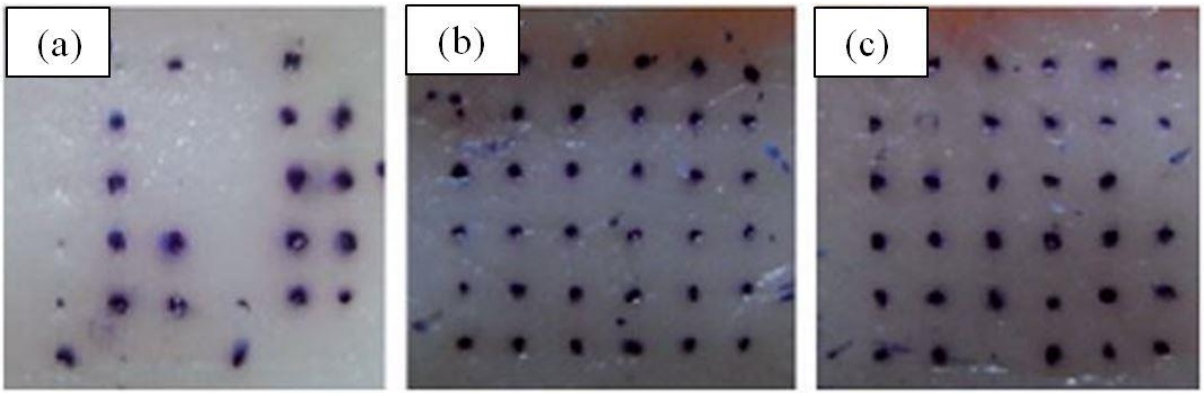

Figure 13 Dissolving microneedle arrays perforation of 6–8 weeks old female mice skin under various loads and stained with Trypan blue. (a) 1 N, (b) 2 N and (c) 4 N (Reproduced from (Qiu et al., 2015)).

Methylene blue is used as a histological stain in biological experiments. At room temperature, it appears as a dark green powder that dissolves moderately in water to form a deep blue solution. The perforated tissue is soaked in methylene blue solution for a given duration in order to detect if any microchannels have been created. The staining is as a result of the methylene blue dye attaching itself to the proteins that exist within the tissue (Jones et al., 2008). Fig. 14 presents images of methylene blue staining.

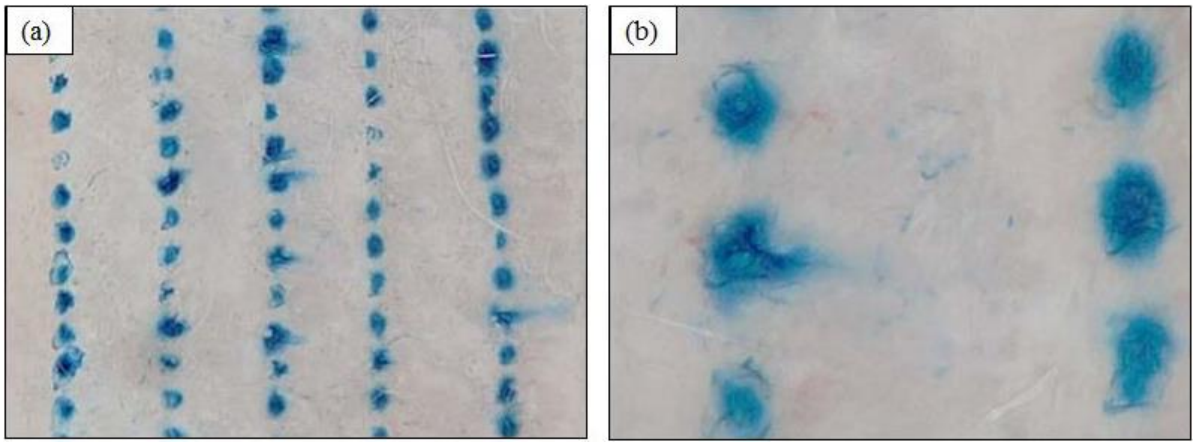

Figure 14 Solid maltose microneedle perforation of hairless rat skin and stained with methylene blue. (a) Array of microneedles perforations and (b) magnified view of the perforations (Reproduced from (Kolli and Banga, 2008)).

Both Trypan blue and methylene blue provide the same level of information when used for the assessment of microneedle perforation. The limitation with both dye techniques is that it is impossible to determine how deeply the microneedles have travelled through the layers.

2.7.2 Histological staining

The Haematoxylin and Eosin stain (H&E) is the most widely used stain in histological laboratories. It has the ability to demonstrate a wide range of normal, abnormal cell and tissue components. It is a relatively simple stain useful for conducting microscopic examination of tissue that has been paraffin embedded or cryosectioned (Larson et al., 2011). It can be performed manually or by automation and typically the manual technique is usually carried out for economic reasons and sample volume (Fischer et al., 2008). Haematoxylin exhibits a deep blue-purple colour and stains nucleic acids by a complex, incompletely understood reaction. Eosin is pink and stains proteins non-specifically. For example, in a typical tissue the nuclei are stained blue, compared to the cytoplasm and extracellular matrix that are stained in varying degrees of pink. Thus, this dye combination is capable of emphasising the fine structures of cells and tissues (Chan, 2014). Careful adherence to H&E staining protocol allows for the detection of many tissue subtleties that are necessary for accurate analysis (Cardiff et al., 2014).

Histology evaluation using H&E staining can also be used to define the layers of skin such as the stratum corneum, epidermis, dermis and hypodermis. An advantage to H&E staining is that the depth of microchannels created by microneedles within skin's layers can be readily assessed (Li et al., 2015). Fig. 15 shows examples of H&E sections of skin.

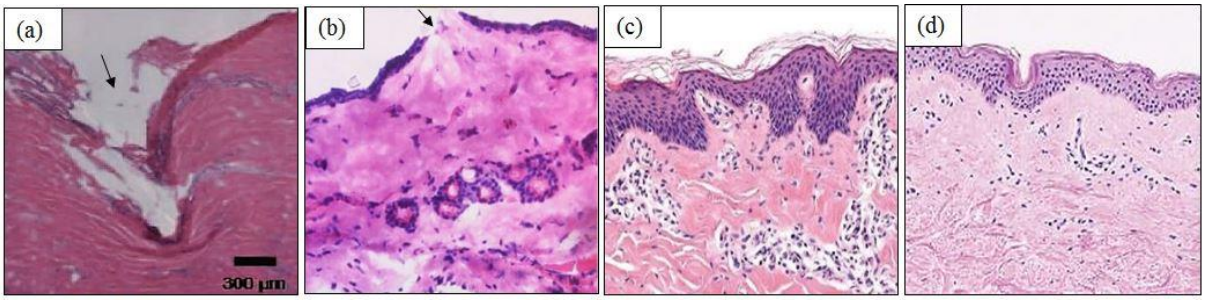

Figure 15 Images of H&E sections of previous studies (a) black arrow indicates microneedle perforation in rat skin (Reproduced from (Kochhar et al., 2013a)) (b) black arrow indicates microneedle perforation in rat skin (Reproduced from (Li et al., 2015)) (c) cross-section of porcine skin (Reproduced from (Dabboue et al., 2015)) and (d) cross-section of human skin (Reproduced from (Dabboue et al., 2015)).

The disadvantages to this method is that only a small portion of the tissue can be sectioned, which means that useful information is lost with the tissue that is discarded. It involves time-consuming fixing, sectioning and staining steps. By comparing histological results with non-invasive imaging technique, Coulman et al. reported that histological measurements lead to overestimation of measurements (Birchall et al., 2005; Coulman et al., 2010). Furthermore, there are slight inaccuracies with the measurements of the microchannels created in skin following microneedle application due to skin retraction caused by the removal of the microneedles before staining (Donnelly et al., 2010; Loizidou et al., 2016). Despite these limitations, using histology for the light microscopic assessment of skin biopsies is still regarded as the benchmark in dermatology (Holme et al., 2014; Newton et al., 2015).

2.7.3 3D image analysis

The emergence of Optical Coherence Tomography (OCT) and micro X-ray Computed Tomography (XMT) as imaging tools for soft tissue could provide the opportunity to image a

whole sample of microneedle treated tissue, without going down the laborious route of H&E staining.

Fercher et al. first suggested the use of OCT for medical diagnostic applications in order to visualise transparent tissues of the eye (Fercher et al., 1988). OCT can produce high resolution cross-sectional imaging of biological tissues *in vivo* and in real time (Huang et al., 1991; Liu et al., 2013). The major advantage of OCT is that it is capable of penetrating depths of 2 mm within skin and it can provide cross-sectional imaging of the epidermis and upper dermis *in vivo* (Fercher, 2010).

XMT is another powerful method for non-destructive imaging of soft tissue that involves a high resolution imaging technique, which has gained wide use within the scientific community (Schambach et al., 2010). Traditionally, XMT has been predominantly used for the imaging of bone structures (Buie et al., 2007). The challenge with XMT of soft tissue is as a result of its low inherent X-ray contrast (Pauwels et al., 2013; Walton et al., 2015). The use of contrast agents on soft tissue can overcome this limitation. However, there is still limited knowledge about contrast agents or staining protocol for XMT compared to light and electron microscopy imaging (Pauwels et al., 2013). Recently, Loizoudou et al. used XMT scanning in their work for the 3D visualisation of microneedle skin penetration (Loizidou et al., 2016).

2.8 Summary

This chapter has reviewed literature relevant to the anatomy of skin, mechanical properties of skin, microneedles and its application as a device to infuse or extract fluid in skin, as well as techniques for determining successful microneedle perforation of skin. Microneedles are a suitable tool for enabling the administration of therapeutic compounds to the ideal site provided by skin. To accomplish reproducible microneedle interaction with skin, an

understanding of the mechanical characterisation of skin is necessary. This literature review gave an overview of *in vitro* and *in vivo* techniques for the mechanical testing of skin, which indicated that test methodology, skin site, test condition and indenter type significantly influenced the outcome of the elastic modulus.

The mechanical contributions from the skin's sub-layers such as the dermis can influence microneedle performance. The role of the subcutaneous fluid and muscle to the overall mechanical behaviour of skin is also important and could determine microneedles interaction with skin.

The review has also highlighted the need to establish a mechanism for reproducible microneedle perforation of skin, with particular attention given to the design of the microneedle applicator. The different types of microneedle applicators varied from a manual applicator using thumb pressure to a spring-driven applicator to an electric-driven applicator or an impact applicator. Evidently, for successful and reproducible microneedle perforation of skin, an external delivery device for microneedle application is necessary. Furthermore, an adequate insertion force and insertion velocity is necessary for successful microneedle application to skin.

The skin models used in several of the studies lacked representative underlying substrates for the skin. In some instances, only the epidermal layer and underlying substrates were considered, thus ignoring significant mechanical contributions from the dermal layer. Sample preservation also varied for each study, as the tissue was not snap frozen in super-cooled isopentane before it was stored at temperatures of −20°C, −26°C and −80°C following excision. This may have introduced some level of compromise to the integrity of the tissue and therefore, may have potentially influenced the outcome of the experimental analysis.

A number of approaches were used for assessing successful microneedle perforation of skin, with dye staining being the most common in establishing disruption to the stratum corneum. One study stripped the stratum corneum following microneedle application to determine if the perforations had travelled beyond the layer. In addition, histological staining techniques were also used to determine the penetration depth through the layers of skin. Moreover, emerging technologies within biomedical research such as OCT and XMT could also be utilised in providing this detail.

Based on the literature review, this study will develop a representative *in vitro* model of skin that is within the range of elastic moduli in the literature, then using indentation techniques to determine the biomechanical properties of each layer in the skin model and developing a microneedle applicator that involves the use of force and velocity. The outcome of microneedle application to skin would be determined using imaging techniques such as methylene blue and histology staining.

Chapter 3

3. Material and Methods

3.1 Introduction

The details of the experimental work of microneedle perforation of skin are discussed in this section. Based on the review of previous studies, it is clear that microneedle geometry, applicator insertion force or velocity and skin model play a major role in achieving successful interaction between microneedles and skin. This chapter provides a detailed description of the skin model, microneedles, microneedle applicators, experimental methods and image analysis techniques used not only to achieve the primary aims and objectives established in Section 1.3 but to also address the topics summarised in Section 2.8.

3.2 The *In Vitro* Skin Model

In this thesis, a representative *in vitro* skin model was developed for microneedle application and is explained in detail in this subsection.

3.2.1 Neonatal porcine skin

Five fresh suckling pigs (7–10 weeks old) were obtained from a local abattoir. Skin samples from the back and abdomen were dissected within 3–4 hours and immediately snap-frozen by placing in super-cooled isopentane and were subsequently stored at –80°C until required. Prior to testing, the skin tissue was de-thawed for 30 mins. Commercial hair removal cream for normal skin (Veet, Reckitt Benckiser Group, Berkshire, UK) was applied to the skin surface for 5 mins to remove any hair. The samples were kept hydrated in PBS solution.

As stated in Section 1.3.3. Renehpra's device could potentially be used on various sites in the human body. It is for this reason that the work in this thesis focused on two anatomical

regions of neonatal porcine skins i.e. the abdominal tissue and back tissue due to their differences in thickness and stiffness. Skin properties such as thickness various considerably across different regions of the human body (Lee and Hwang, 2002); hence these two types of porcine skin provide a useful method of determining how the device may work in different parts of the human body. The physiological properties of neonatal porcine skin are similar to human skin (Lo Presti et al., 2012) and the stiffness is within the range of values for the stiffness of human tissue (Groves, 2011).

3.2.2 Gelatine gels as a representation of subcutaneous tissue fluid

Gelatine gel is formed because of the structural and chemical degradation of collagen (Lee and Mooney, 2001). Gelatine powder is a translucent, colourless, brittle solid substance and the type used in this study was derived from collagen obtained from porcine extract (Sigma-Aldrich 48723-500G-F, Fluka).

3.2.2.1 Determination of gelatine gels concentration

The primary application of the TFR technology is to use microneedles to gain access to the epidermis in the skin in order to extract fluid from patients with fluid overload or oedema. For the effective application of microneedles to skin, consideration must be given to how fluid overload in the *in vitro* skin model is represented. As mentioned in the literature review, gelatine gels present an ideal approach for mimicking oedema in the *in vitro* skin model. There are two forms of oedema, subcutaneous pitting oedema and subcutaneous non-pitting oedema as previously described in Section 1.1. There lies a significant challenge in quantitatively or semi-quantitatively depicting subcutaneous non-pitting oedema and it was for this reason that this project focused solely on establishing gelatine gel mimics for various severities of subcutaneous pitting oedema following the relevant literature studies.

Mridha et al. conducted two different mechanical tests, which were the mechanical impedance test and the mechanical pulse wave propagation test on various concentrations of gelatine gels and this has been previously covered in more detail in Section 2.4.2. The gelatine gel concentrations of 80%, 84%, 88%, 92% & 96% water content by weight represented the different severities of subcutaneous pitting oedema. By conducting these mechanical tests, they were able to determine the mechanical behaviour of subcutaneous pitting oedema. For mechanical impedance tests, high water content gelatine gels and subcutaneous pitting oedema tissues had lower mechanical impedance compared to subcutaneous non-pitting oedema, which exhibited higher mechanical impedance (Mridha and Odman, 1985). Conversely, for the mechanical pulse wave propagation tests, the propagation velocity of mechanical pulse waves was found to be lower in subcutaneous pitting oedema than for normal tissues and higher in subcutaneous non-pitting oedema (Mridha et al., 1992).

For normal, 'healthy' skin, the gelatine gel concentration was 67% water content by weight. This was based on a study by Caspers et al. where an *in vivo* Raman microspectroscopy technique was used to non-invasively determine the water content in healthy skin below the stratum corneum to be around 67%, with the value varying slightly depending on anatomical region (Caspers et al., 2000).

Based on these studies, four gelatine gel concentrations were used in this thesis and are presented in Table 8. The mild-severe oedema characterisation is based on the Mridha et al. studies (Mridha and Odman, 1985; Mridha et al., 1992). The lowest water content gel has the highest stiffness, whilst the highest water content gel has the lowest stiffness.

Table 8 Composition of gelatine powder and water.

Gelatine powder (g)	Water (mL)	Gelatine gel (water content by weight)	Subcutaneous mimic
20	58	67%	Normal
10	45	80%	Mild subcutaneous pitting oedema
5	37	88%	Moderate subcutaneous pitting oedema
5	120	96%	Severe subcutaneous pitting oedema

3.2.2.2 Preparation technique of gelatine gels

Several factors such as gel preparation, curing duration, cooling and measurement temperatures can influence the mechanical properties of gelatine gels (Markidou et al., 2005). Therefore, each gel concentration was prepared in a consistent manner that involved using an electronic stirrer to mix a mass of gelatine powder along with the requisite volume of distilled boiling water until all gel powder had dissolved. Several homogeneous mixtures were made for the four gelatine gel concentrations (see Table 8). The gel solution was left to cool for 1 hour, before it was cured at 5°C for 4–5 hours.

All tests were carried out within 2 hours using the same batch of samples.

3.2.3 Perma-Gel® as muscle mimic

As previously discussed in Section 2.4.3, Perma-Gel® (Perma-Gel, Inc., Albany, OR, USA) is an ideal muscle mimic. Perma-Gel® which is similar to ballistic gelatine, is used as muscle mimic (Caron-Laramee and Brouillette, 2014). Furthermore, synthetic thermoplastic materials such as Perma-Gel® are stable at room temperature and can be stored for long periods of time (Moy et al., 2011).

Perma-Gel® was obtained as a test block form (445 mm × 292 mm × 127 mm) from a third party distributor (MidwayUSA, Columbia, USA). The Perma-Gel® was cut in small specimens to fit the mechanical clamps.

3.2.4 Classification of the various *in vitro* skin models

A diagram of the representative *in vitro* skin model comprising the three layers is shown in Fig. 16.

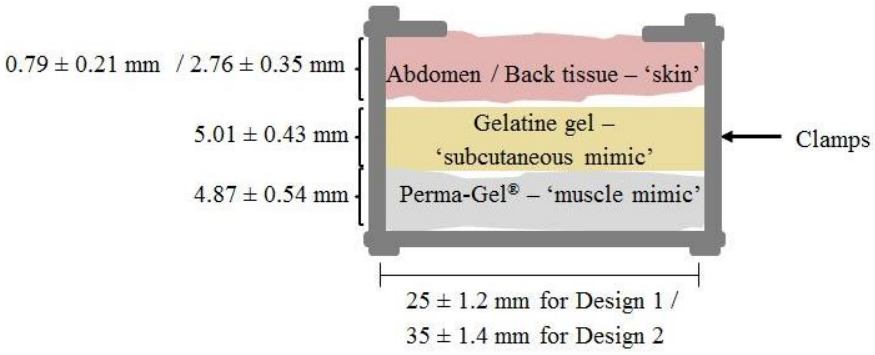

Figure 16 Diagram of the representative *in vitro* skin model showing the skin as the top layer, with gelatine gel as a second layer and Perma-Gel® as the third layer.

The skin model was secured in mechanical clamps and the mechanical clamps are shown in Fig. 17.

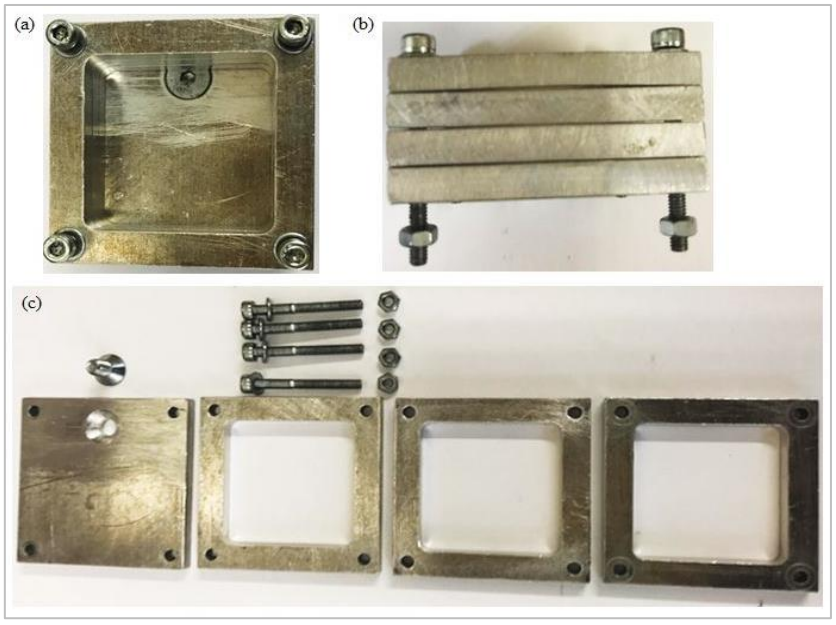

Figure 17 The mechanical clamp (a) top view of the assembled clamp (b) side view of the assembled clamp and (c) individual components of the clamp.

The *in vitro* skin models have been categorised according to anatomical site, gelatine gel concentration and Perma-Gel® and are presented in Table 9. The classification of skin model names i.e. Model 1A, Model 2A will be used for the remainder of the work carried out in later chapters of this thesis.

Table 9 The categories of two anatomical sites of neonatal porcine skin at various gelatine gel concentrations and Perma-Gel®. A = Abdominal skin and B = Back skin.

Types of Skin Model	Classification
Abdominal skin with 67% gel concentration and Perma-Gel®	Model 1A
Abdominal skin with 80% gel concentration and Perma-Gel®	Model 2A
Abdominal skin with 88% gel concentration and Perma-Gel®	Model 3A
Abdominal skin with 96% gel concentration and Perma-Gel®	Model 4A
Back skin with 67% gel concentration and Perma-Gel®	Model 1B
Back skin with 80% gel concentration and Perma-Gel®	Model 2B
Back skin with 88% gel concentration and Perma-Gel®	Model 3B
Back skin with 96% gel concentration and Perma-Gel®	Model 4B

3.2.5 Micromechanical characterisation of the layers of the skin model

A general overview of the indentation technique is mentioned along with the theory. In addition, the experimental approach is also detailed in this section.

3.2.5.1 Dynamic indentation principles

Indentation or depth-sensing instrumentation is a technique for determining localised mechanical properties of materials. With indentation, a prescribed load is applied to an indenter in contact with a specimen. As the load is applied, the depth of penetration is measured. The area of contact at full load is determined by the depth of the impression and indenter geometry (Oliver and Pharr, 1992). A schematic of a typical load-displacement

curve is shown in Fig. 18. It also involves small scale mechanical testing, which presents several advantages in the characterisation of biological materials. One of which is the small volume of material required for testing, thereby minimal sample preparation is required. Furthermore, with instrumented indentation it is possible to map out the spatial differences of properties in the sample and is a key requirement for characterising biological material (Hay, 2011). Typically, quasi-static indentation is used for testing biological tissues (Ebenstein and Pruitt, 2006). However, there are a number of challenges including difficulties in accurately detecting sample surface (Akhtar et al., 2015).

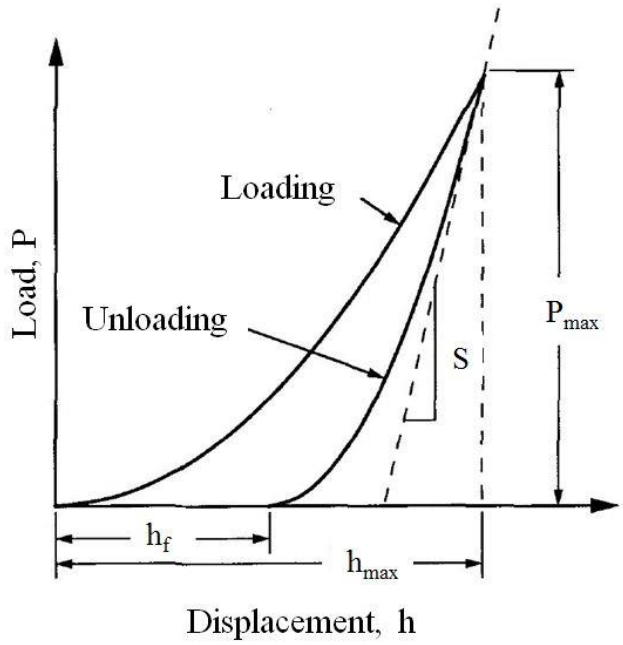

Figure 18 A schematic representation of a typical load versus indenter displacement curve. P_{max} and h_{max} are the load and displacement at highest load respectively and a is the radius of the contact circle. h_f is the final depth of the contact impression after unloading and S is the initial unloading stiffness. (Figure reproduced from (Oliver and Pharr, 1992)).

In this thesis, dynamic indentation has been utilised with a 100 μm flat punch tip, therefore resulting in micron resolution. Dynamic instrumented indentation provides a simple way to accurately measure the mechanical properties of soft biological material like skin and gelatine gels (Hay and Cherneva, 2013). Furthermore, indentation is used a lot for skin and has advantages over tensile testing. In addition, tips of this geometry (100 μm flat punch tip) are

typically used to improve surface detection with compliant materials, hence, micro-sized tips for indentation. For the characterisation of time-dependent behaviour, dynamic indentation has its advantages over quasi-static indentation because it significantly reduces the testing time through the measurement of properties over a range of frequencies rather than extended time (Odegard et al., 2005).

3.2.5.2 Theory

With the Keysight Technologies DCM-II head, as shown in Fig. 19, it is possible to perform dynamic (oscillatory) indentation and determine the complex shear modulus (G^*), which exhibits real and imaginary components and gives the shear storage modulus (G'), which depicts the energy stored and viscous or the shear loss modulus (G''), which depicts the energy dissipated as heat. Therefore, the relationship between the elastic and viscous properties of the material is shown in Equation 4:

$$G^* = G' + i\,G'' \qquad \text{Equation 4}$$

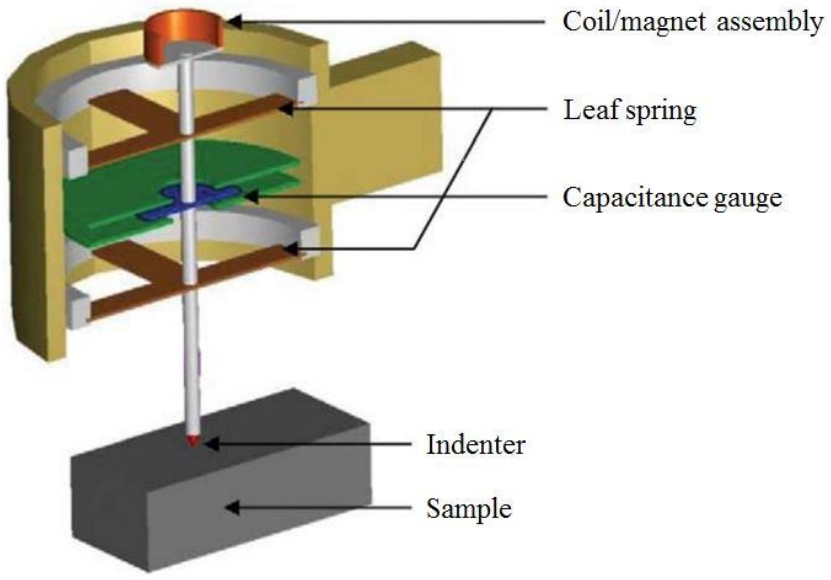

Figure 19 A schematic of the DCM-II head. (Figure reproduced from (Hay, 2012)).

The theory is covered in greater detail in Hay (2011) and Hay and Cherneva (2013). In brief, by indenting samples with a flat-ended cylindrical punch, the relationship between the shear

modulus (G'), Poisson's ratio (ν) , elastic contact stiffness (S) and punch diameter (D) can be determined using the analysis developed by Sneddon, (1965) as shown in Equation 5:

$$G' = \frac{S(1-\nu)}{2D} \qquad \text{Equation 5}$$

The influence of contact damping, $C\omega$ on the viscous properties, G'' is given by the following equation:

$$G'' = \frac{C\omega(1-\nu)}{2D} \qquad \text{Equation 6}$$

The contact stiffness, S, must be obtained by subtracting the instrument stiffness, K_i from the total measured stiffness, K_s and is given by the following equation:

$$S = K_s - K_i \qquad \text{Equation 7}$$

Likewise, the contact damping, $C\omega$ must be obtained by subtracting the instrument damping, $Ci\omega$ from the total measured damping, $Cs\omega$ and is given by the following equation:

$$C\omega = Cs\omega - Ci\omega \qquad \text{Equation 8}$$

By oscillating the indenter electromagnetically, the stiffness and damping are obtained. To begin with, the same conditions (e.g. same position, frequency and oscillation amplitude) that are used to measure the stiffness and damping of the head only are subsequently used for testing. The indenter head is moved down towards the sample until contact is made. During this period, a pre-compression is applied so that the indenter maintains total contact with the sample surface. The indenter is then vibrated at a fixed frequency and oscillation amplitude. Therefore, at the initial oscillation cycle, the indenter head is calibrated *in situ*. The stiffness and damping inputs from the head can then be deducted from the measured signal in order to

find the contact only response. Afterwards, the second oscillation cycle acquires the material properties (Akhtar et al., 2015).

3.2.5.3 Experimental setup

All indentation experiments were carried out on gelatine gels, Perma-Gel® and fresh full thickness skin samples. The tissue was hydrated in PBS solution. Indentation tests were conducted using a Keysight indenter G200 (Keysight Technologies, Chandler, AZ, USA) instrument with an ultra-low load dynamic contact module indentation head (DCM-II actuator). The indentations were performed at ambient temperature (24.3–27.2ºC), using a 100 μm flat punch indenter tip (Synton-MDP Ltd, Nidau, Switzerland). A custom sample holder was designed in to which the gelatine gel samples were placed. The well in the sample holder was 1 cm^2 and 4 mm deep.

For the experiments conducted in this thesis, a pre-compression of 5 μm for the gelatine gels and Perma-Gel® were selected, whilst 8 μm was used for the skin samples. The indenter was fully in contact with the sample surface. The indenter was then vibrated at a frequency of 110 Hz (the resonant frequency of the indenter) and with an oscillation amplitude of 500 nm. To obtain the response of the contact only, the stiffness and damping contributions from the indenter are subtracted from the measured signal. This means that the second oscillation sequence acquires the material properties. 10 different sites were tested on each sample, with 100 μm spacing between each indent on the sample. The tip of the indenter head was cleaned by indenting a piece of double-sided Scotch tape positioned on an adjacent sample puck before repositioning on a new area on the sample following each indent.

A Poisson's ratio, ν, of 0.5 was chosen because skin is regarded as fully incompressible (Bhushan et al., 2010) and this value was used to calculate the elastic modulus, E, which was subsequently, determined using the formula in Equation 9.

$$G' = \frac{E}{2(1+\nu)}$$ Equation 9

G', G'' and the loss factor, tan (δ) given in Equation 10 were calculated for each indentation.

$$\tan(\delta) = \frac{G'}{G''}$$ Equation 10

The surface detection relies on a phase shift of the displacement measurement, as presented in Fig. 20. As a standard for accurate surface detection, the method reported by Akhtar et al. was used. With this method, the phase shift is monitored over several data points in order to eliminate random spikes which were found to occur in some instances over short time intervals such as 2 data points and thus resulting in an erroneous surface detection. Once the surface detection condition had been met over a predefined number of data points, the initial contact was determined from the first point in that sequence.

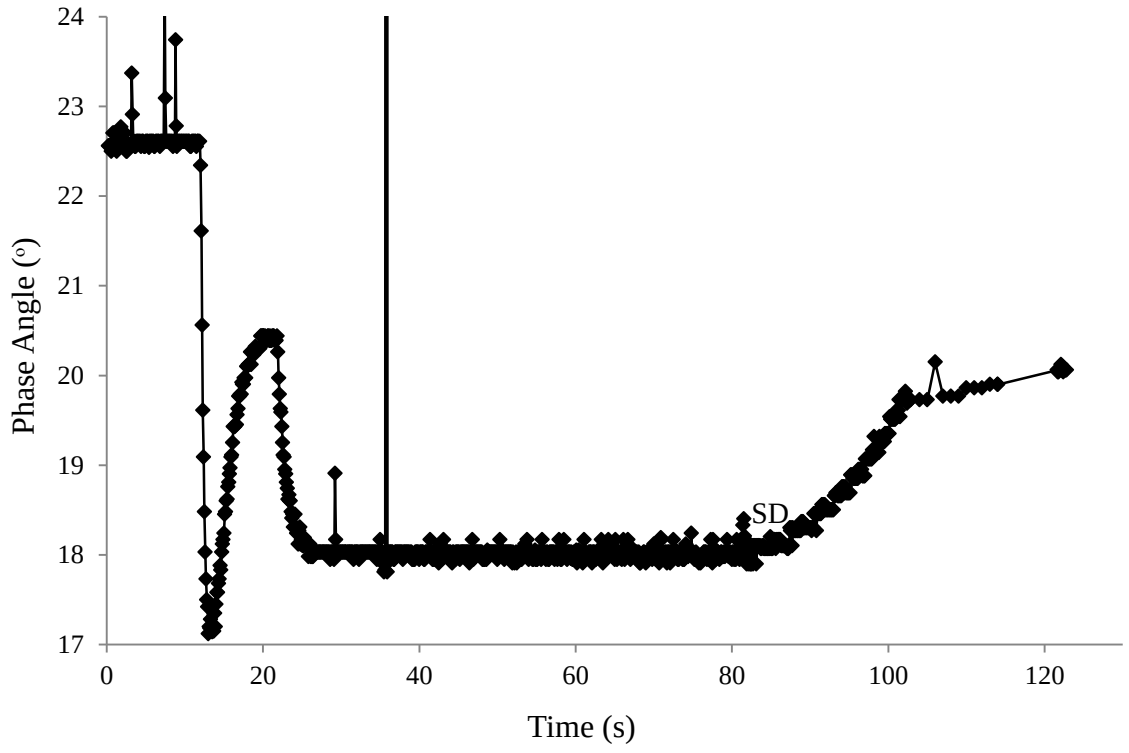

Figure 20 Profile of phase angle as a function of time that is used for accurate surface detection of 67% gelatine gel. Point SD is the surface detection, which starts with a gradient increase in the phase angle.

3.3 The Microneedle Arrays

This section provides details about the types of microneedles used in this thesis, the material they were made from, their manufacturing process and design. These specific medical grade microneedles were sourced because of their intended use on human subjects.

3.3.1 Polyetheretherketone microneedle arrays

Custom manufactured polyetheretherketone (PEEK) microneedle arrays (Laser Micromachining Ltd, St Asaph, UK) were used for the early experimental analysis. These were hollow microneedles as shown in Fig. 21 and were manufactured using laser etching or laser finishing following injection moulding to a height, width and 1 mm interspacing between the microneedles.

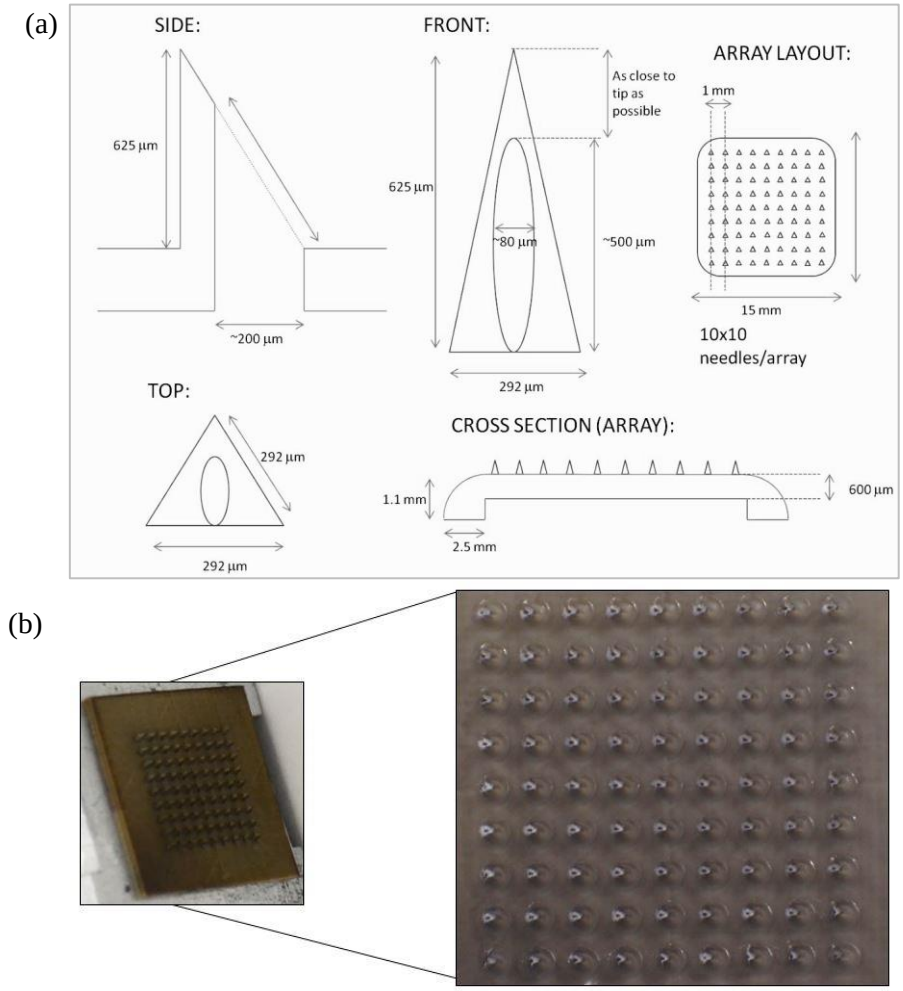

Figure 21 Medical grade PEEK microneedles, where (a) drawing including dimensions and (b) image of the array.

The PEEK microneedles were 9 × 9 arrays consisting of 81 individual needles on 15 mm × 15 mm base and 0.65 μm in height. These medical grade microneedles were provided by Renephra Ltd.

3.3.2 Polymethylmethacrylate microneedle arrays

Dense polymethylmethacrylate (PMMA) microneedle arrays (10x technology, IL, USA) were used for all subsequent experiments reported in this thesis. Microneedles embossing mould and embossing machine was used to manufacture the microneedle array to a specific height, width and regular interspacing between the microneedles. Fig. 22 shows the PMMA microneedles, which is marginally larger than a £1 coin.

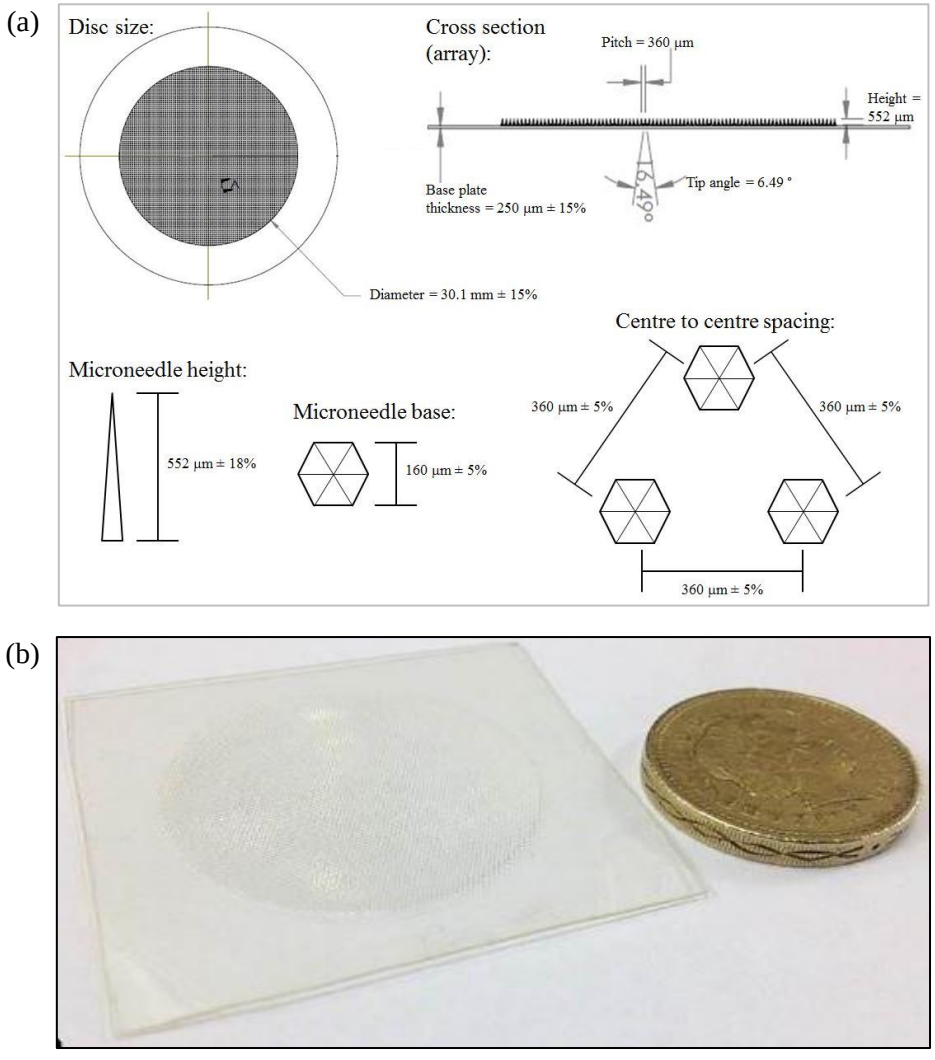

Figure 22 Medical grade Design 2 PMMA microneedle array, where (a) drawing including dimensions and (b) as compared to a £1 coin (Renephra, 2015).

The full specifications for the PMMA microneedles are presented in Table 10. These microneedles are medical grade and have been used in *in vivo* patient tests since 2014 by Renephra Ltd.

Table 10 PMMA microneedles specification.

Type	Height (μm)	Disc size diameter (mm)	Needles per unit area (mm^2)	Base (μm)	Centre-to-centre spacing (μm)	No. of needles per array
Design 1	356	15.8	6.7	177	386	1316
Design 2	552	30.1	7.7	160	360	>6000

3.3.3 Scanning Electron Microscopy of microneedle arrays

Consideration was given to microneedle integrity to determine the number of times it could be used on tissue. Scanning Electron Microscopy (SEM) images of microneedles were recorded using a Hitachi S-4800 FE-SEM at 3 kV with 1.5 kV deceleration (Tokyo, Japan). The PEEK or PMMA samples were fixed onto the aluminium stubs with carbon tabs. The samples were gold coated using a sputter-coater (EMITECH K550X) prior to imaging.

Impact tests with microneedles on tissue were carried out once and SEM images were taken. Further impact tests were repeated five times using the same microneedle and SEM images taken.

3.4 The Microneedle Applicators

This section details the two types of microneedle applicators used for microneedle applications to the skin model. All impact tests were conducted at ambient temperature, which was ideal for maintaining the stability of the gelatine gels used in the models.

3.4.1 Impact applicator system

The governing principles of a dropped weight impact-testing rig have been detailed in this section and the experimental setup described extensively in Sections 3.4.1.3. and 3.4.1.4.

3.4.1.1 Determination of the dropping heights

The dropping heights were calculated by inputting values for velocity in the simple motion equation, where *v* is velocity, *g* is acceleration due to gravity and *h* is the dropping height.

$$v = \sqrt{2\,g\,h} \qquad \text{Equation 11}$$

Table 11 shows the equivalent dropping heights for the velocities calculated from Equation 11. Each dropping height was marked along the length of the drop tower guide.

Table 11 Velocity as a function of dropping height.

Velocity (ms^{-1})	1	2	3	4	5
Dropping height (m)	0.05	0.20	0.46	0.82	1.27

3.4.1.2 Theory

Impact acceleration occurs whenever there is an abrupt change in velocity, such as an instantaneous deceleration in a car crash or the sudden halt of a falling lift down a shaft. As a consequence, impact forces are usually in milliseconds and human tolerance to them is determined by the mechanical strength of body tissues (Glaister, 1975). Therefore, the perforation potential of microneedles in skin during a given impact is related to the amount of work done or energy absorbed by the tissue.

During impact, some compression of the tissue occurs and there may also be a rebound of the drop mass as residual energy is dissipated, however, for simplicity purposes, rebound is ignored in this theory. Furthermore, there is an elastic potential energy (Equation 12), which

is the stored energy the drop mass (m) possesses due to its position in a stressed elastic system. Conversely, because the drop mass is released from a known height it also has potential energy, which is the energy stored up in the drop mass as a result of its position in a gravitational field (Equation 13).

$$Elastic\ Potential\ Energy = \frac{1}{2}\ k\ x^2 \qquad \text{Equation 12}$$

$$Potential\ energy = m\ g\ h \qquad \text{Equation 13}$$

The spring potential energy is obtained from Equations 12 and 13, and is given by Equation 14, where x is the compression distance and k is the spring constant.

$$m\ g\ h = \frac{1}{2}\ k\ x^2 \qquad \text{Equation 14}$$

By rearranging Equation 14, the compression distance (x) is given by Equation 15

$$x = \sqrt{\frac{2\ m\ g\ h}{k}} \qquad \text{Equation 15}$$

Fig. 23 illustrates the relationship between the elastic potential energy and the potential energy due to gravitational fields using a simple spring.

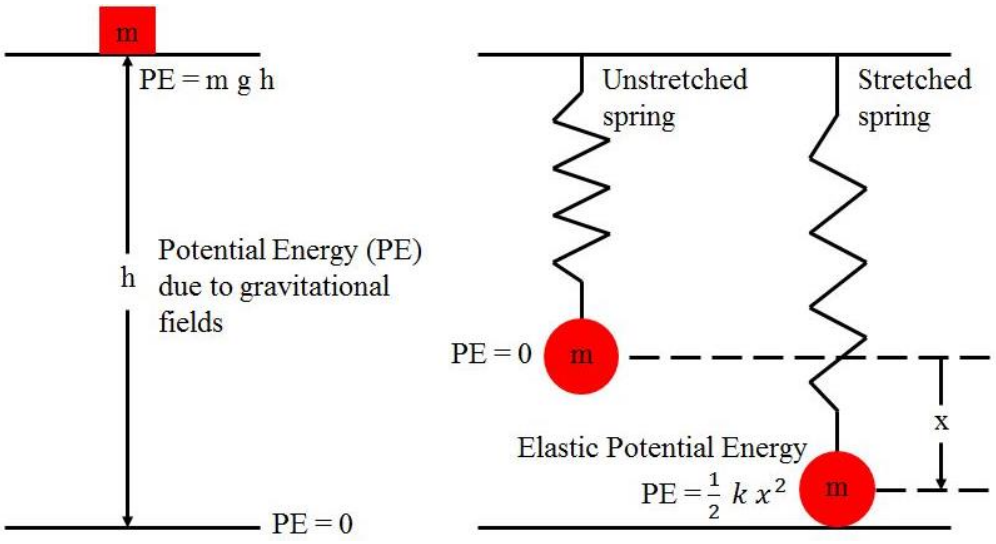

Figure 23 Schematic of the potential energy due to gravity and the energy stored up in a spring energy indicating the compression distance (x).

Using Hooke's Law in Equation 16 to establish a relationship between force (*F*) and compression distance (*x*).

$$F = k\,x \qquad \text{Equation 16}$$

Substituting the compression distance (*x*) in Equation 15 into Equation 16 gives the expression

$$F = k\,x = \sqrt{2\,m\,g\,h\,k} \qquad \text{Equation 17}$$

The velocity for microneedle perforation of skin can be derived from the conservation of energy principle because the potential energy is converted into kinetic energy.

$$Kinetic\ energy = \frac{1}{2}\,m\,v^2 \qquad \text{Equation 18}$$

Equating the kinetic energy and the potential energy gives the expression in Equation 19

$$\frac{1}{2}\,m\,v^2 = m\,g\,h \qquad \text{Equation 19}$$

Making the velocity (*v*) the subject of the formula gives

$$v = \sqrt{2\,g\,h} \qquad \text{Equation 20}$$

The force can be obtained by substituting Equation 20 into Equation 17

$$F = v\sqrt{m\,k} \qquad \text{Equation 21}$$

Based on the interpretation of Equations 12–21, the following conclusions were drawn:

- A low mass object will produce a lower magnitude of force compared to a large mass object.
- An increase in the force will result in an increase in velocity.

- Increasing the dropping heights will result in an increase in velocity. There is contribution from the acceleration due to gravity as the drop mass is released from rest.
- The mass of the object influences the impact energy; a small mass will release less energy, whilst a large mass will expend more energy.

3.4.1.3 First generation impact applicator

The early dropped weight impact testing rig comprised a drop tower of height 1.86 m, with a drop tower guide of height 1.78 m, a piezoelectric accelerometer of 10.96 mV/g sensitivity (Unit Type A/126/S, Serial No. 035, Birchall Instruments) connected to a power supply, which was connected to a digital oscilloscope (Part No. 54641A, Agilent Technologies) along with the proprietary Agilent IntuiLink software (Version 3.1). The accelerometer was fastened to one end of the 36 g drop mass and the microneedle array fixed to the free end of the drop mass using superglue. The experimental setup is shown in Fig. 24.

The early impact tests were conducted on only skin and gelatine gels. Five repeats of the impact tests were performed on eight different skin models i.e. back skin with four gelatine gel concentrations and abdominal skin with four gelatine gel concentrations. The acceleration is captured on the oscilloscope as voltage–time plots, which is then converted to an acceleration–time plot using the accelerometer sensitivity before it is eventually converted to a velocity–time plot.

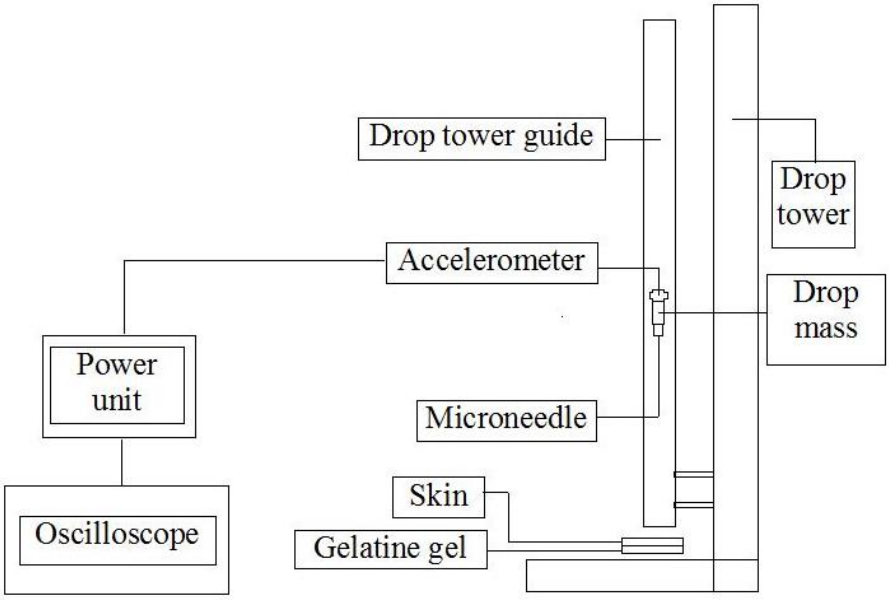

Figure 24 Schematic diagram of the early dropped weight impact-testing rig.

3.4.1.4 Improved impact applicator

The improved impact test setup included the addition of a force transducer, power units and a beam detector to the early impact applicator system.

The setup used a piezoelectric accelerometer with 10.71 mV/g sensitivity (Model 3225F-1, Dytran Instruments, Inc., CA, USA) and a piezoelectric force transducer with 22.4 mV/N sensitivity (Model 1022V, Dytran Instruments, Inc., CA, USA). Both the accelerometer and the force transducer were connected to their respective amplifiers (Model 4105C, Dytran Instruments, Inc., CA, USA), which had a frequency response of 0.1–100 000 Hz gain ×1 used for velocities 1–2 ms^{-1} and 0.1–50 000 Hz gain ×10 used for velocities 3–5 ms^{-1}. This was then connected to a digital oscilloscope (54641A, Keysight Technologies, Berkshire, UK) and utilised with Keysight IntuiLink software (Version 3.1). The sampling rate was 20 kHz. The accelerometer was connected to the top of the custom-made drop mass, whilst the force transducer was fastened to its bottom end. Two 630–650 nm wavelength (red) with a power output <1mW laser diode modules (PL-Series, Hero Electronics, Dunstable, UK) were attached to two drill holes on the lower part of the drop tower guide so that a break in signal, caused when the drop mass is released, was captured by a beam detector, thus activating the

external trigger on the oscilloscope. Subsequently, the force and acceleration outputs were captured on the oscilloscope. The experimental setup is shown in Fig. 25.

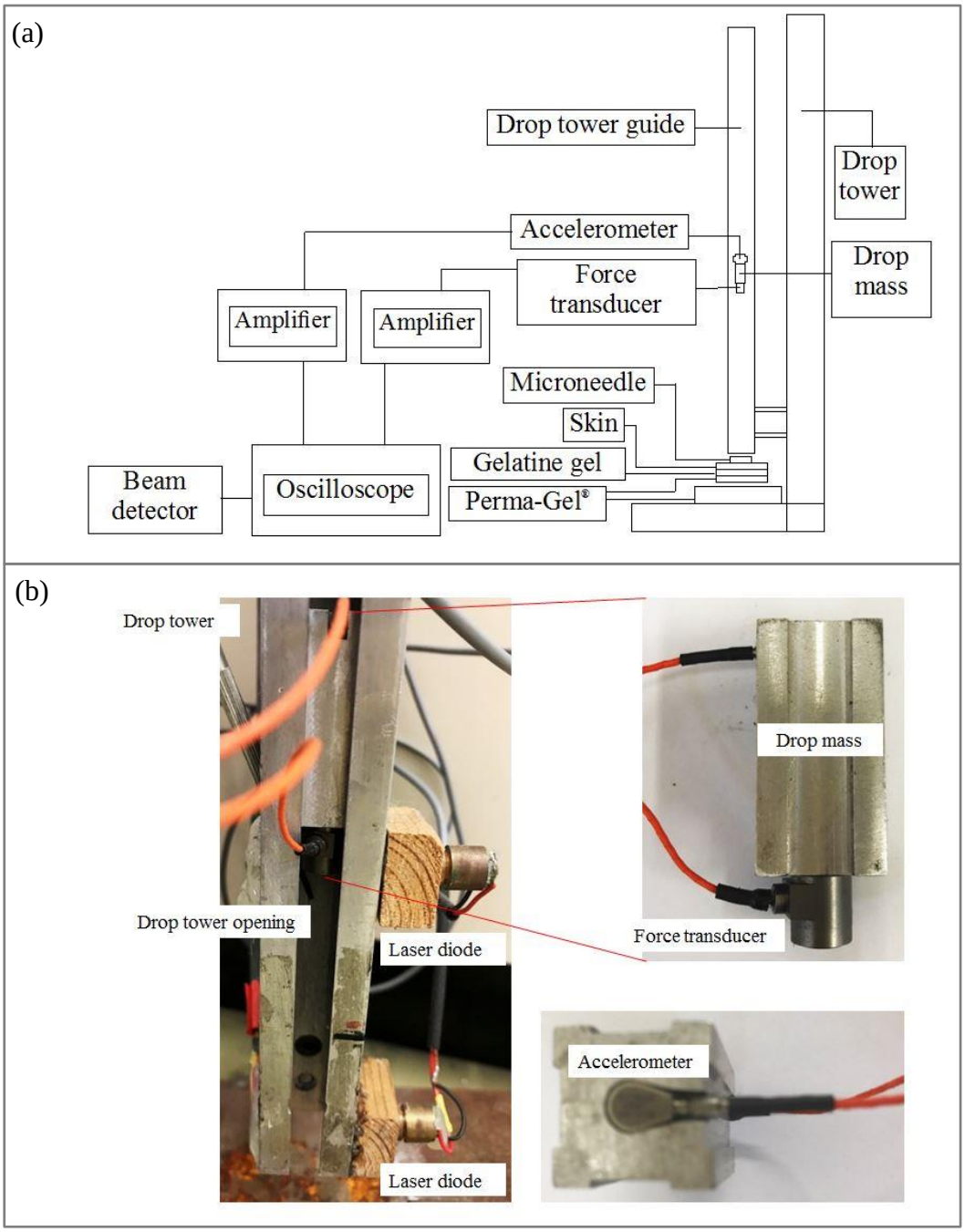

Figure 25 The improved impact applicator, where (a) is the schematic diagram and (b) includes complimentary pictures of the setup.

The relevant dropping heights in Table 11 were marked along the length of the drop tower guide. The opening in the drop tower guide as shown in Fig. 25b allowed for the movement

of the cables fastened to the accelerometer and force transducer. The drop mass along with the accelerometer and force transducer were positioned at the appropriate dropping height and held in place with the aid of a flat-head screwdriver via the opening along the length of the drop tower guide. The screwdriver was removed, thus releasing the drop mass along with the accelerometer and force transducer to impact the microneedles placed on the skin model at the bottom of the drop tower guide.

For this research work, five repeats of impact tests using the improved impact applicator were conducted on individual samples of skin for Models 1A–4B i.e. five repeats of individual samples of skin Model 1A or five repeats of individual samples of skin Model 2A etc. (see Table 9 in Section 3.2.4 for skin model classification). The acceleration and the force are captured on the oscilloscope as voltage–time plots, which are then converted to acceleration–time plots and force–time plots using the sensitivities of the accelerometer and force transducer respectively. The acceleration–time plot is then converted to a velocity–time plot.

3.4.1.5 Calibration of the impact applicator

The results of tests utilising a loadcell or a force transducer is dependent on the accuracy of the loadcell and how it is used. A simple and accurate measure of loadcell evaluation is to compare the output of the loadcell against a reference mass. For the calibration tests, a mass of 5 kg was mounted onto the loadcell and the results captured on the PC as a force–time graph. Then, the second law of motion was used to work out the mass registered by the loadcell, which was equivalent to the mass of the known weight.

A vibration calibrator (Bruel & Kjaer, Type 4294, Serial No. 1683419) was used to check the accuracy of the accelerometer. The vibration calibrator produces an acceleration of 10 ms^{-2} equivalent to an acceleration level of 140 dB re 1×10^{-6} ms^{-2}, at a frequency of 159 Hz (1 radian). The accelerometer was fixed to the vibrating surface of the calibrator using beeswax.

The calibration signal was then used to check the measurement chain from the accelerometer to the display in order to confirm that it was at the correct calibration level.

3.4.2 Clinical applicator system

For their *in vivo* patient tests, Renephra used a clinical applicator for microneedle perforated skin. The clinical applicator was also used for some of the *in vitro* work presented in this thesis. The perforation tests using the clinical applicator was conducted at ambient temperature, which was ideal for maintaining the stability of the gelatine gels used in the skin models. The clinical applicator setup is detailed in this section.

3.4.2.1 Clinical applicator mechanism

A schematic of the clinical applicator, which is based on a spring and hammer-driven mechanism, is shown in Fig. 26.

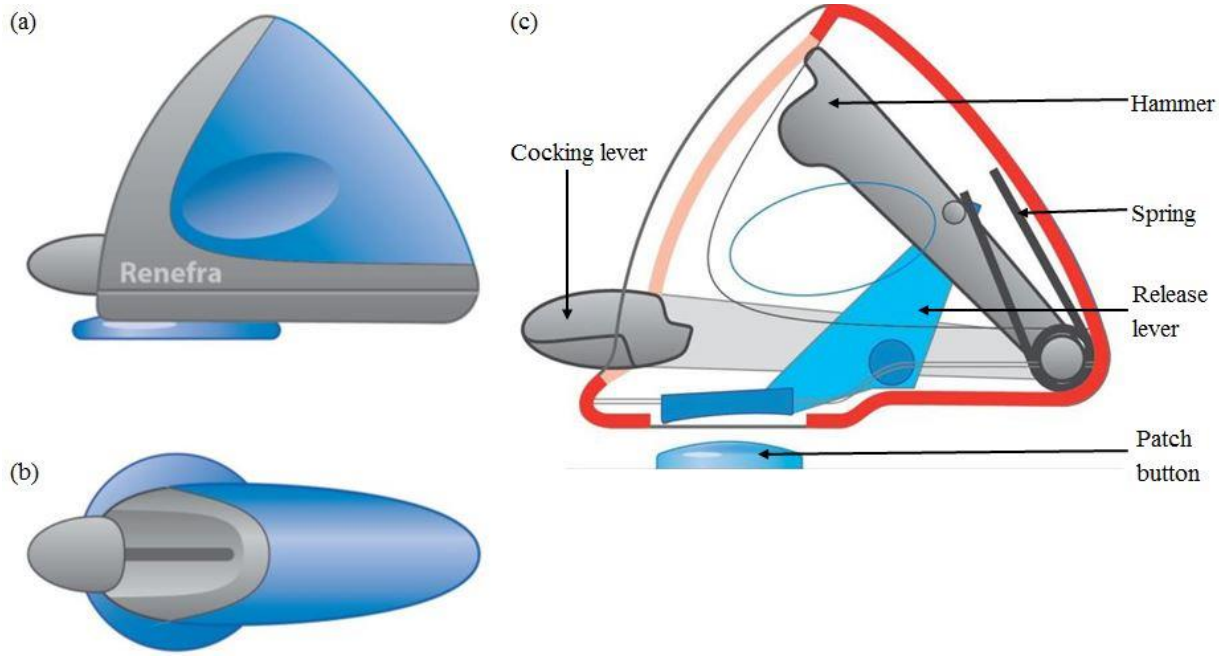

Figure 26 Diagram of Renephra's clinical applicator. (a) Side view of the applicator. (b) top view of the applicator and (c) the internal components of the applicator. (Courtesy Renephra Ltd).

In order to use the clinical applicator, the patch button shown in Fig. 25c was placed onto the microneedles resting on the skin model. Prior to use, the applicator was first cocked into

position by lifting the lever. The cocked lever returned on the spring and was ready for use. The applicator was then pressed onto the patch button and this triggered the hammer, which was launched to impact the patch button, thereby making contact with the microneedles on the skin model lying beneath the patch button.

3.4.2.2 Determination of the clinical applicator force

Although the clinical applicator has been used for *in vivo* patient tests by Renephra, the device does not measure the insertion force. Hence, in order to determine the force produced by the clinical applicator, the clamped skin model was fastened onto a 20 kg loadcell (CZL635 micro loadcell, Active Robots, Somerset, UK). The loadcell was connected to a data acquisition tool (i100 instruNet network device, GW Instruments, Inc., Massachusetts, USA). The instruNet was used to process the loadcell data output and was also connected to a PC setup so as to obtain the graphical output. During testing, the microneedle array was placed onto the skin model with the patch button placed directly onto the microneedle array. The clinical applicator was cocked into position and then pressed onto the patch button until the trigger was released. The force produced by the applicator was detected by the loadcell and the data captured on the instruNet/PC setup. The diagram of the clinical applicator system is shown in Fig. 27.

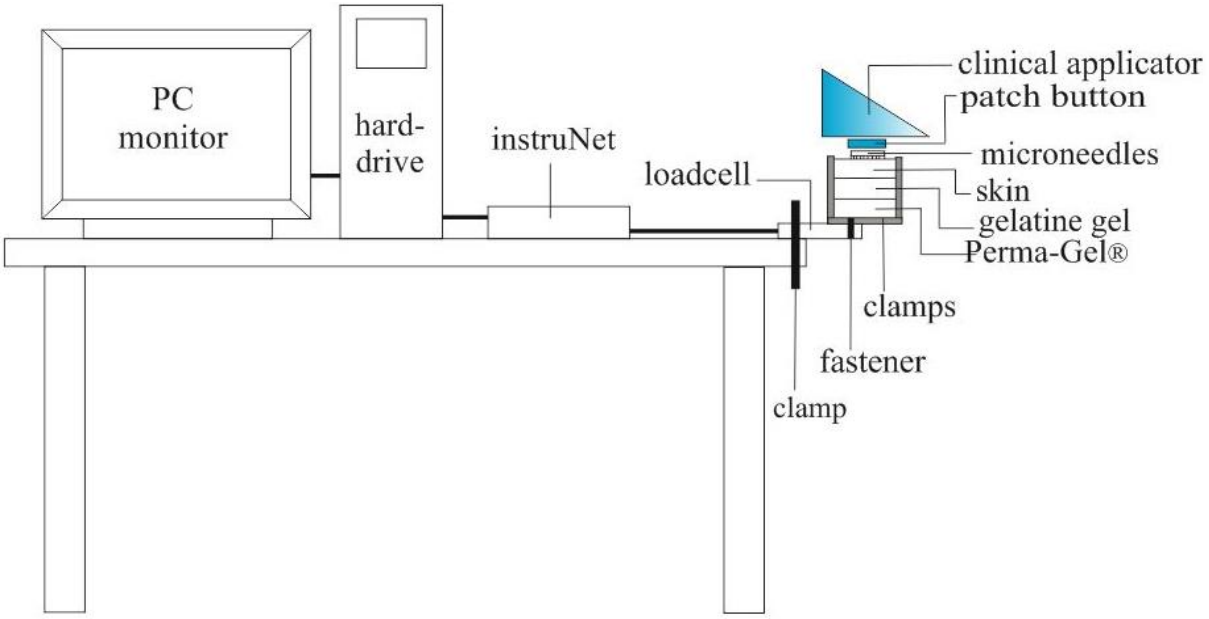

Figure 27 Schematic diagram of the clinical applicator setup.

However, it was found following initial tests that the clinical applicator failed to trigger and launch the hammer onto the patch button on the skin model shown in Fig. 19. Therefore, the patch button had to be placed onto an elevated profile of the skin model. The elevated profile of the skin model was achieved by using double the amount of Perma-Gel®, as shown in Fig. 28. The elevated profile of the skin did not influence the outcome of the interaction between the microneedles and skin as determined from the methylene blue and H&E stained images.

Four repeats of clinical applicator tests were conducted on individual samples of skin for Models 1A–4B i.e. four repeats on individual samples of skin Model 1A or four repeats on individual samples of skin Model 2A etc.

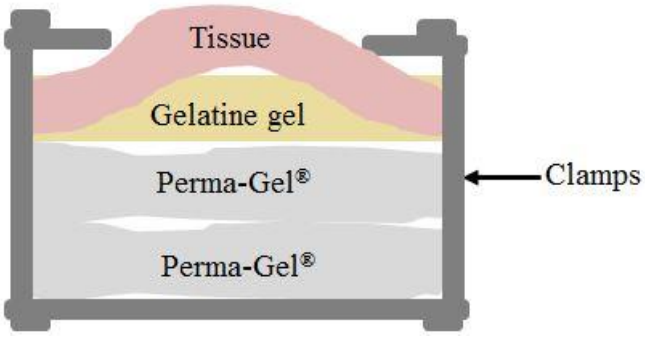

Figure 28 Diagram of the elevated profile of the skin model.

3.5 Imaging Techniques for Assessing Microneedle Perforation of Skin

Various imaging techniques were used to assess the depth and extent of the deformation resulting from microneedle perforation of skin. This section details the specific imaging techniques.

3.5.1 Visual examination and penetration efficiency calculation of microneedle perforated skin

Methylene blue staining is used to detect microneedle perforations of skin. The staining of tissues occurs because the methylene blue dye binds itself to the proteins that are found in tissue (Jones et al., 2008). The image of methylene blue staining indicates successful breach of the stratum corneum and the creation of microchannels on skin. Typically, the hydrophobic nature of the stratum corneum cannot absorb the hydrophilic low molecular weight of the methylene blue solution, however, once the stratum corneum has been disrupted by microneedle assault, the methylene blue diffuses through the skin (Li et al., 2009).

For all experiments, a 2% weight to volume solution was prepared for methylene blue dye. The microneedle treated tissue was soaked in methylene blue solution for 30 mins for the purpose of detecting microchannels created following penetration tests. The tissue was removed from the methylene blue solution and the tissue surface wiped down with ethanol so that any microchannels were detected. Methylene blue stained skin samples were imaged with Nikon digital camera D5100 (Surrey, UK), as shown in Fig. 29.

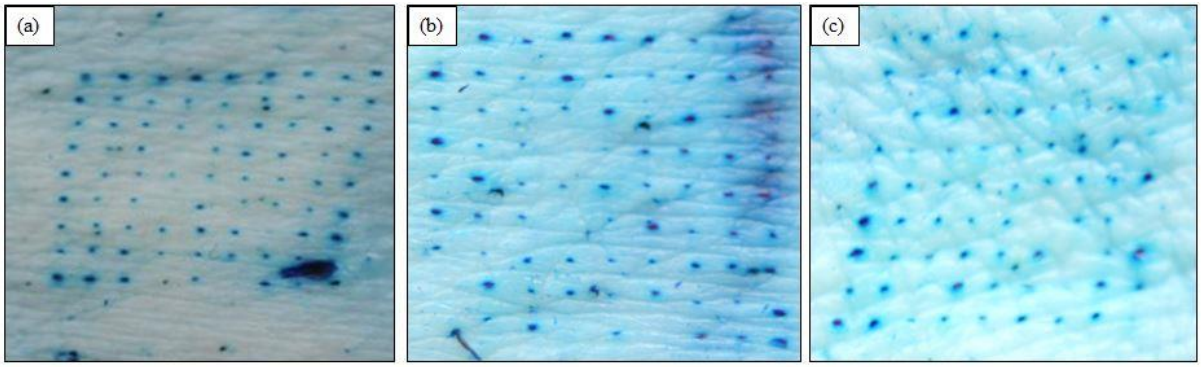

Figure 29 Methylene blue stained images of 9 × 9 PEEK microneedle array on abdominal skin model at 67% gelatine gel concentration, where (a) 5 ms^{-1}, (b) 4 ms^{-1} and (c) 3 ms^{-1}.

In order to determine the Penetration Efficiency (PE) from the methylene blue stained images, a method similar to that of van der Maaden et al. was used (van der Maaden et al., 2014). PE can be defined as the percentage of the number of blue spots from the methylene blue staining of microchannels created by a microneedle array on the stratum corneum, divided by the total number of microneedles on the array.

The size of the microneedle array for Design 1 microneedles was 15.8 mm in diameter and the density of the microneedles was 1316. Therefore, PE is given by the formula in Equation 22.

$$PE = \frac{number\ of\ blue\ spots}{1316} \times 100\% \qquad \text{Equation 22}$$

where 1316 represents the total number of microneedles on a 15.8 mm diameter microneedle disc.

In contrast, the size of the microneedle array for Design 2 microneedles was 30.1 mm in diameter and the density of microneedles > 6000, therefore, it proved challenging to quantify PE following methylene blue staining for the entire disc. As a consequence, for quantitative analysis, a central region of 5 × 5 mm was cropped for each image and used for determining the PE. The revised formula for calculating PE is given in Equation 23.

$$P\,E = \frac{number\ of\ blue\ spots}{193} \times 100\% \qquad \text{Equation 23}$$

where 193 represents the expected number of microneedles for a 25 mm^2 area of the sample given that there are 7.7 microneedles per unit mm^2 as presented in Table 10.

3.5.2 Histology examination of the microneedle perforated skin

After impact testing, the tissue was prepared for cryosectioning by freezing in Optimal Cutting Temperature resin (Sakura Fintek Europe B.V, Alphen aan den Rijn, The Netherlands) and then snap frozen in super-cooled isopentane (Graham et al., 2011). The perforated skin was snap frozen immediately following removal of the microneedles to minimise skin retraction as well as maintain the sample's integrity. The tissue was then sectioned to fit in a cryomold.

For this project, a standard process used in dermatology for skin histology was used based on an established protocol (Watson, 2013). Histology evaluation using H&E staining was used to define the layers of skin and for the purpose of this study was useful in assessing the depth of the microchannels created and the extent of the deformation within skin. The perforated tissue was sectioned using a Leica CM1850 cryostat (Milton Keynes, UK). The thickness of the cryosections was optimised via trial and error, therefore, it was determined that a thickness of 12 μm was appropriate. The sectioned tissue was stained with H&E using a standard protocol, which is summarised here: the sectioned tissue was fixed in 4% paraformaldehyde for 10 mins, rehydrated in distilled water for 2 mins, immersed in haematoxylin for 3 mins before running tap water over it for 5 mins. The glass slide was placed in 1% hydrochloric acid (HCl)/70% industrial methylated spirit (IMS) acid/alcohol for 10 seconds before running tap water over it for a further 5 mins. The glass slide was then immersed in eosin for 1 minute, rinsed in distilled water for 1 min, rinsed in 70% IMS for 1 min and then rinsed in 95% IMS for another minute. The sectioned tissue was rehydrated at

100% IMS for 4 mins, then cleared in Histo-Clear (National Diagnostics, Atlanta, GA, USA) and mounted in Depex mounting medium (Electron Microscopy Sciences, Washington, PA, USA).

The stained tissue was imaged with a Nikon Eclipse Ci microscope (Surrey, UK). Fig. 30a shows the H&E staining of a section of skin that has not undergone hair removal treatment. The image shows an intact stratum corneum as well as epidermis and dermis. The image in Fig. 30b is of a section of skin that has been pre-treated with hair removal agent. The image also shows an intact stratum corneum as well as epidermis and dermis and therefore demonstrates that the tissue has borne no adverse effects from the application of the chemical.

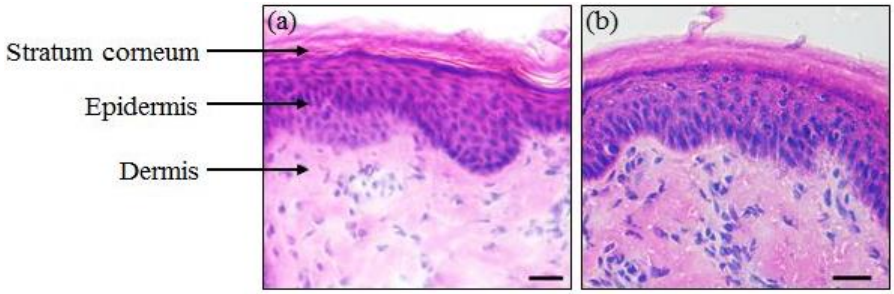

Figure 30 Inspection technique of the perforated tissue using H&E staining, where (a) is the untreated sectioned tissue showing the three histological layers of skin and (b) is the sectioned tissue already treated with the hair removal agent. Scale bar represents 100 μm.

Throughout this thesis, the following colour coded arrows on the H&E stained images shown in Fig. 31 have been used to denote the disruptions through the stratum corneum, epidermis and dermis.

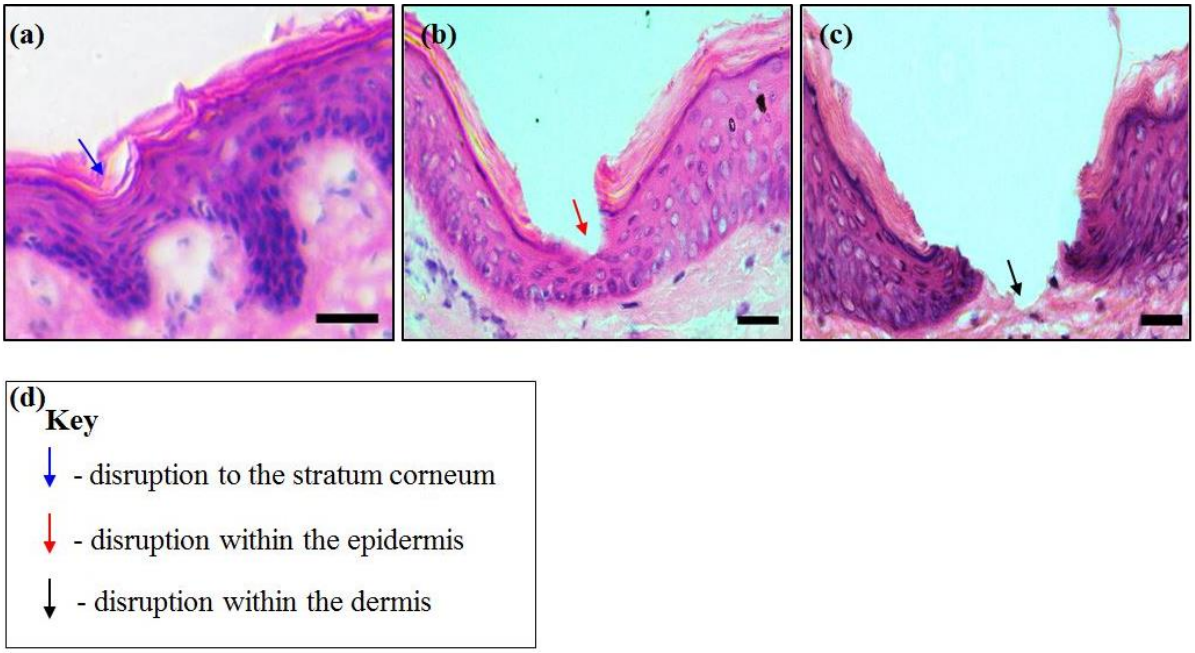

Figure 31 Labelling of the H&E stained images, where (a) blue arrow indicates disruption to the stratum corneum, (b) red arrow indicates that the breach is contained within the epidermis, (c) black arrow indicates that breach has extended into the dermis and (d) key describing the colour coded arrows. Scale bar represents 100 μm.

The improvements on the conventional methods of measurement from histological images are to utilise a custom image analysis routine for determining breach area.

3.5.3 Quantitative image analysis using Image SXM software

A custom routine was written in Image SXM (Heilbronner and Barrett, 2014) for semi-automated analysis of the histology images to determine the breach area within the skin following microneedle application. The optical microscopy images were found to vary in contrast, brightness and colour balance and hence a histogram of pixel values was used to determine the optimum threshold in order to highlight the pixels above the epidermal layer. For images in which the epidermal layer had not been breached, it was found that combining the red and blue colour channels of the images produced the most reliable discrimination of the edge of the epidermal layer. For images in which the epidermal layer was breached, it was found that the green channel gave the most reliable discrimination. Automatic detection of a breach was not possible with the routine; hence the most appropriate mode was selected for

each image. Only those images in which the epidermal layer was clearly discriminated from the rest of the image could be analysed to determine the breach area. For these images, the extent of the microneedle puncture was marked by clicking on the two points (Fig. 32a) that delineate the puncture at the upper surface of the epidermal layer (Fig. 32b). The area of the puncture was measured and logged (Fig. 32c). Subsequently, the next image was loaded and displayed ready for user input.

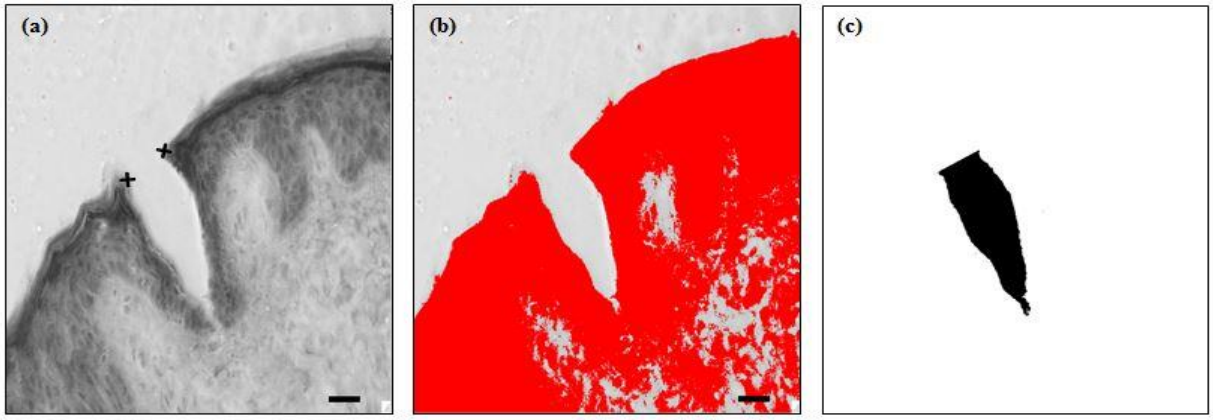

Figure 32 Quantitative image analysis results using ImageSXM of back skin model. (a) Grayscale of histology image. (b) Red pixel saturation of the histology image. (c) Quantification of the breach area. Scale bar represents 100 μm.

Over 500 images were analysed for the quantification of the breach areas, as more than 30 images of impact tests with the Design 2 microneedles on eight skin models i.e. Models 1A–4B selected at random were assessed. Additionally, more than 30 images of Design 1 microneedles penetration of Model 3B selected at random were analysed.

3.5.3.1 Assessment of microneedle perforation depth

ImageJ (Version 1.48, National Institutes of Health) (Abramoff et al., 2004) was used to assess the perforation depth of the histology image as shown in Figs 33a and 33b. Similarly, approximately 30 images of impact tests with Design 2 microneedles on eight skin models i.e. Models 1A–4B and Design 1 microneedles on Model 3B selected at random were assessed. The user-defined line was drawn from the stratum corneum to the maximum point of penetration in the skin, which was either located within the epidermis or the dermis.

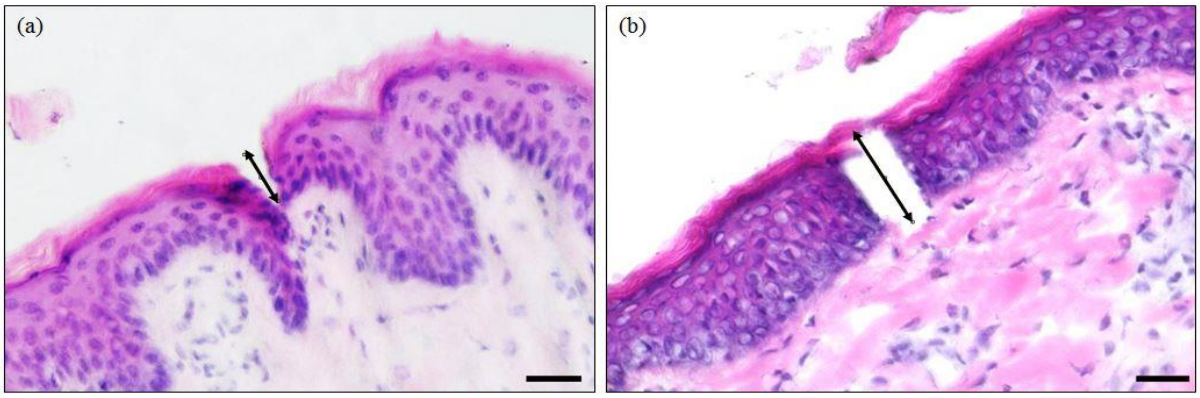

Figure 33 Image analysis results of the perforation depth of Model 3B using ImageJ for impact tests with (a) Design 2 microneedles and (b) Design 1 microneedles. Scale bar represents 100 μm.

3.5.3.2 Breach area classification

To better analyse the outcome of the image analysis, the breach areas were placed into three groups comprising 0 < breach area < 10 000 μm^2, which indicates that the perforation has travelled through the stratum corneum and just interfaces with the epidermis; 10 000 < breach area < 20 000 μm^2, which indicates that there is a significant level of deformation within the epidermis and 20 000 < breach area < 50 000 μm^2, which indicates that the perforation has gone beyond the epidermis into the dermis. Examples of the three groups have been illustrated in Fig. 34. The breach area was measured in the way specified in order to determine the extent of the perforation and if the perforation varied due to contributions from gelatine gels with its different stiffness.

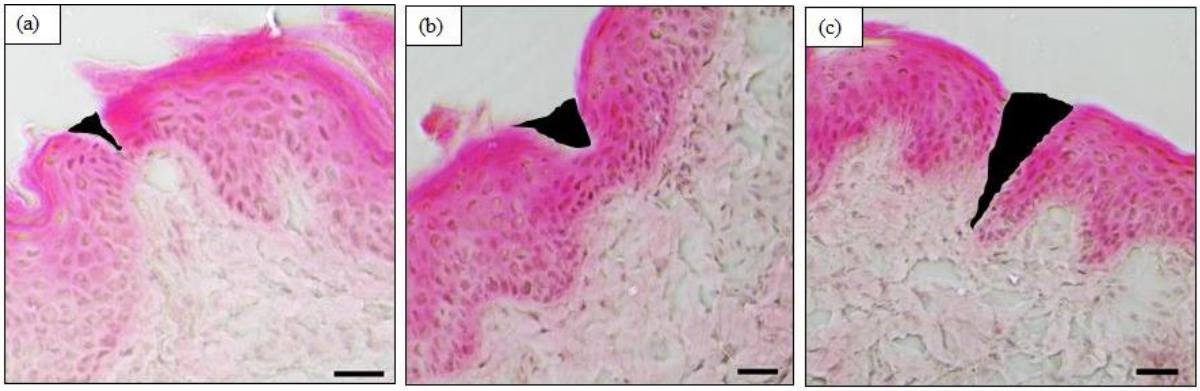

Figure 34 The H&E images illustrate breach area groupings. The area shaded in black represents the breach area size, where (a) 0 < breach area < 10 000 μm^2 small deformation within the epidermis (b) 10 000 < breach area < 20 000 μm^2 large deformation within the epidermis and (c) 20 000 < breach area < 50 000 μm^2 deformation within the dermis. Scale bar represents 100 μm.

As stated in the literature review regarding the histology process being time consuming, labour intensive and resulting in slight inaccuracies of the measurements of the microchannels due to skin retraction caused by the removal of the microneedles before staining (Donnelly et al., 2010; Loizidou et al., 2016), using 3D imaging techniques could lead to improved accuracies of measuring the deformations in microneedle treated skin. Furthermore, the microneedles could be imaged with the skin *in situ*.

3.6 Statistical Analysis

Statistical analysis for the determination of differences in the measured properties between and within groups was accomplished using a single factor analysis of variance (ANOVA) utilising Microsoft Excel Data Analysis ToolPak.

All data were presented as a mean value with its standard deviation indicated (Mean ± SD). For all the tests in this thesis, the following notations for probability were used:

$p > 0.05$ – not significant (ns)

$p \leq 0.05$ – statistically significant (*)

$p \leq 0.01$ – statistically significant (**)

$p \leq 0.001$ – statistically significant (***)

$p \leq 0.0001$ – statistically significant (****)

3.7 Summary

The chapter has detailed the experimental approach for determining the biomechanical interaction between skin and microneedles. This was based on the outcome of the literature review, which described neonatal porcine skin as an ideal substitute for human skin and for its close biomechanical properties to human skin. It also demonstrated the significance of a representative underlying substrate in the skin model. Moreover, it highlighted the importance of tissue preservation in maintaining the integrity of the sample, as this could

influence the outcome of the experimental analysis. For microneedle application studies of skin, the challenge to effective microneedle penetration is to bypass the inherent elasticity of the stratum corneum. Previous studies indicated that insertion velocity and insertion force influence perforation of the stratum corneum with microneedles. Furthermore, the introduction of microneedles in skin to any depth requires the assistance of external pressure using a microneedle delivery apparatus.

Chapter 4

4. Results

4.1 Introduction

In this chapter, the results from all the experimental work will be presented. In Section 4.2, the results obtained from the dynamic nanoindentation tests to determine the mechanical properties of each of the different layers that make up the *in vitro* skin model are presented. In Section 4.3, the results obtained from the preliminary studies of microneedles on skin using the impact applicator during the early stage of its development are detailed. In Section 4.4, data obtained using the fully developed impact applicator on the *in vitro* skin models are presented. Results from studies using clinical applicator on *in vitro* skin models are presented in Section 4.5. The section concludes with a comparison between the performance of the impact and clinical applicators (Section 4.6).

4.2 Micromechanical Characterisation of Skin's Sub-layers

The outcome of indentation tests on abdominal skin, back skin, 67%, 80%, 88% gelatine gels and Perma-Gel® are presented in this section.

4.2.1 Indentation tests on abdominal and back skin samples

Fig. 35 shows the storage modulus, loss modulus and loss factor for abdominal and back skin samples following 38 successful indentations. It was found that for the abdominal skin samples, the loss modulus (G'') dominates over the storage modulus (G'). In contrast, for back skin, the storage modulus dominates over the loss modulus (Fig. 35b). Back skin exhibited a much higher elastic modulus component compared to abdominal skin. For the viscous component, back skin was higher than abdominal skin. Abdominal skin was found to

have a higher damping capacity, as determined from the loss factor in Fig. 35c. The storage and loss factor results were statistically significant, whilst there was no statistically significant difference between the samples for the loss modulus.

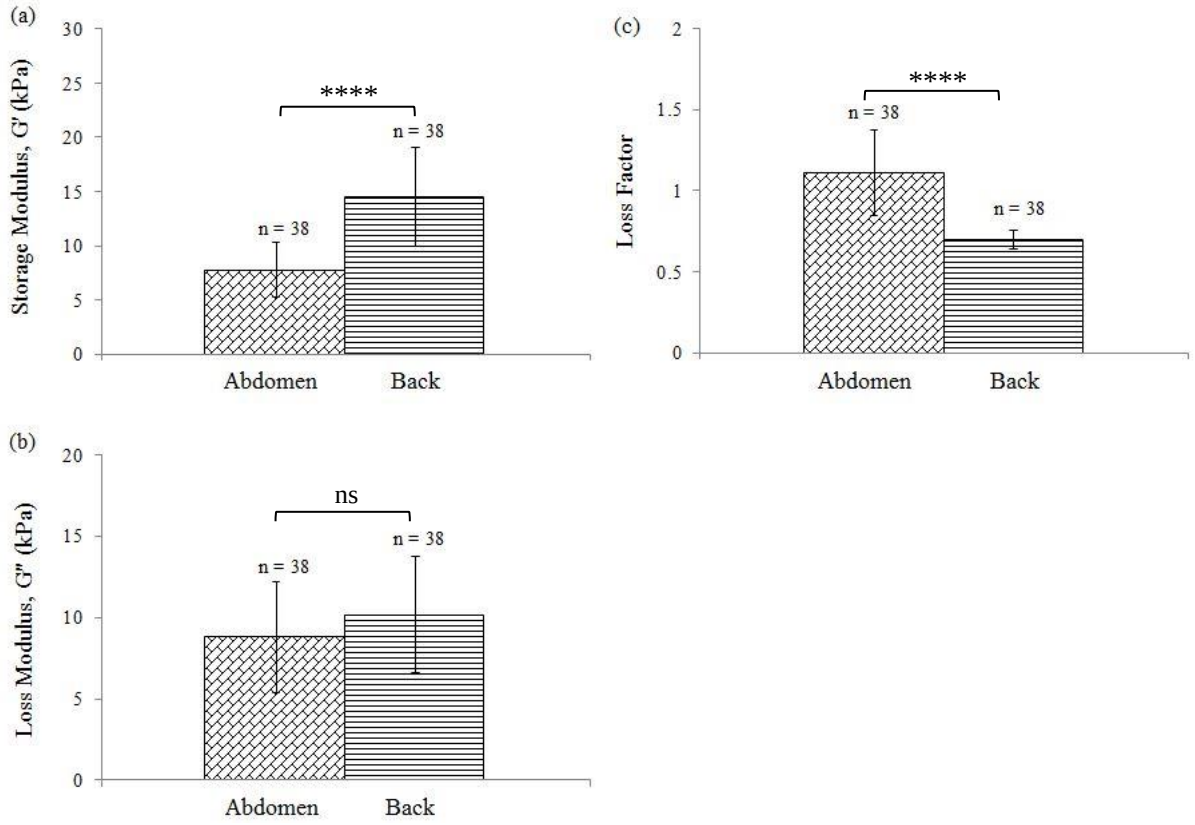

Figure 35 Micromechanical properties of neonatal porcine abdominal and back skin, with the number of indentations (n) listed above each bar chart. (a) Storage modulus, *G´* (b) loss modulus, *G˝* and (c) loss factor. Error bars depict SD.

As shown in Fig. 36, the back skin samples (45.89 ± 9.61 kPa), produced a higher elastic modulus compared to the abdominal skin samples (24.49 ± 5.47 kPa). The variation between groups for abdominal and back skin groups was found to be statistically significant.

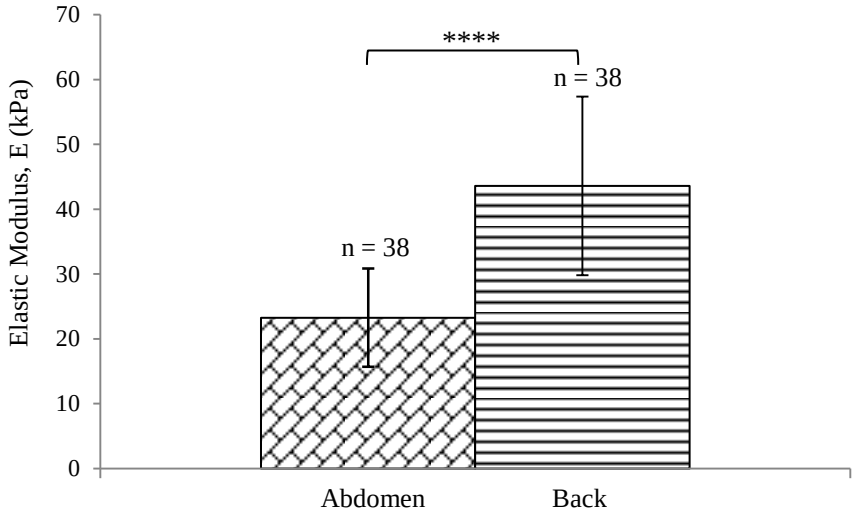

Figure 36 Elastic modulus of neonatal porcine abdominal and back skin following micromechanical tests, with the number of indentations (n) listed above each bar chart. Error bars depict SD.

4.2.2 Indentation tests on gelatine gel samples

Fig. 37 presents the mechanical properties for each of the gelatine gels following 40 successful indentations. The storage modulus (G') dominates over the loss modulus (G'') for each of the gelatine gels (Figs 37a & 37b). The gelatine gel with the lowest water content (67%) had the highest elastic component, whilst the gelatine gel with the highest water content (88%) had the lowest elastic component. Similarly, the gelatine gel with the lowest water content (67%) had the highest viscous component, whilst the gelatine gel with the highest water content (88%) had the lowest viscous component. The gelatine gel at 88% concentration was found to have the highest damping capacity, as determined from the loss factor in Fig. 37c. Unfortunately, it was challenging conducting tests on 96% gelatine gel concentration because of the high water content in the gel. The gel was too compliant to test with the indenter and thus produced spurious results. Hence, no data for this gel concentration were obtained. The storage modulus, loss modulus and loss factor between groups for the gelatine gels was statistically significant.

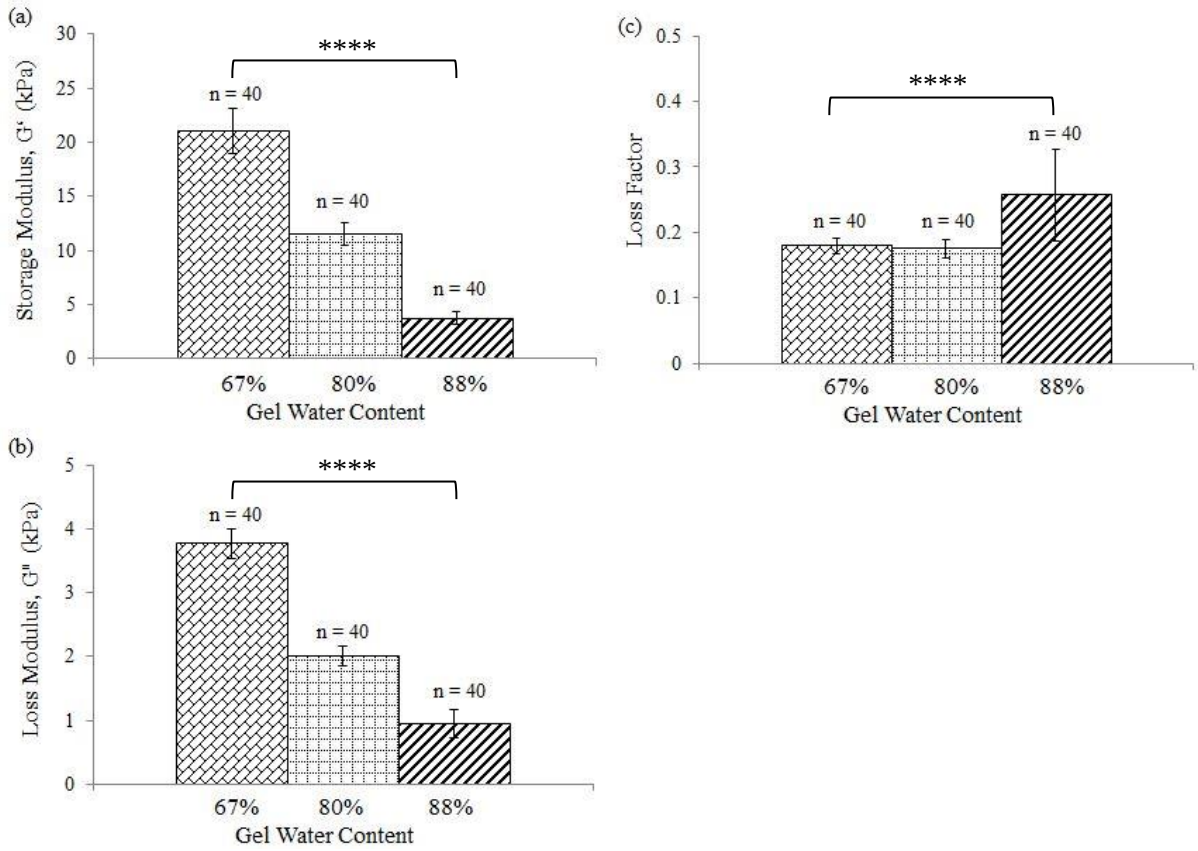

Figure 37 Micromechanical properties of gelatine gels for 67%, 80% and 88% water content, with the number of indentations (n) listed above each bar chart. (a) Storage modulus, *G´* (b) loss modulus, *G˝* and (c) loss factor. Error bars depict SD.

Fig. 38 shows the elastic modulus for the gelatine gels. The comparison between repetitions showed close agreement for each of the samples of the different gelatine gels. Predictably, the gelatine gel with the highest water content (88%) had the lowest elastic modulus. The variation between groups for gelatine gels was found to be statistically significant.

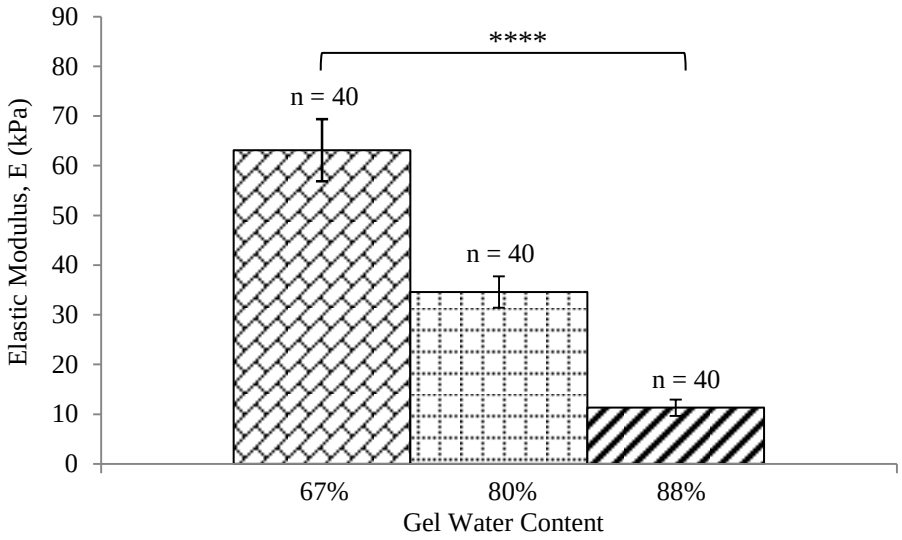

Figure 38 Elastic modulus of the different gelatine gels following micromechanical tests, with the number of indentations (n) listed above each bar chart. Error bars depict SD.

Fig. 39 presents an image of the residual impression in the gelatine gel following indentation.

These appear to be more pronounced in the gelatine gel with 67% water content.

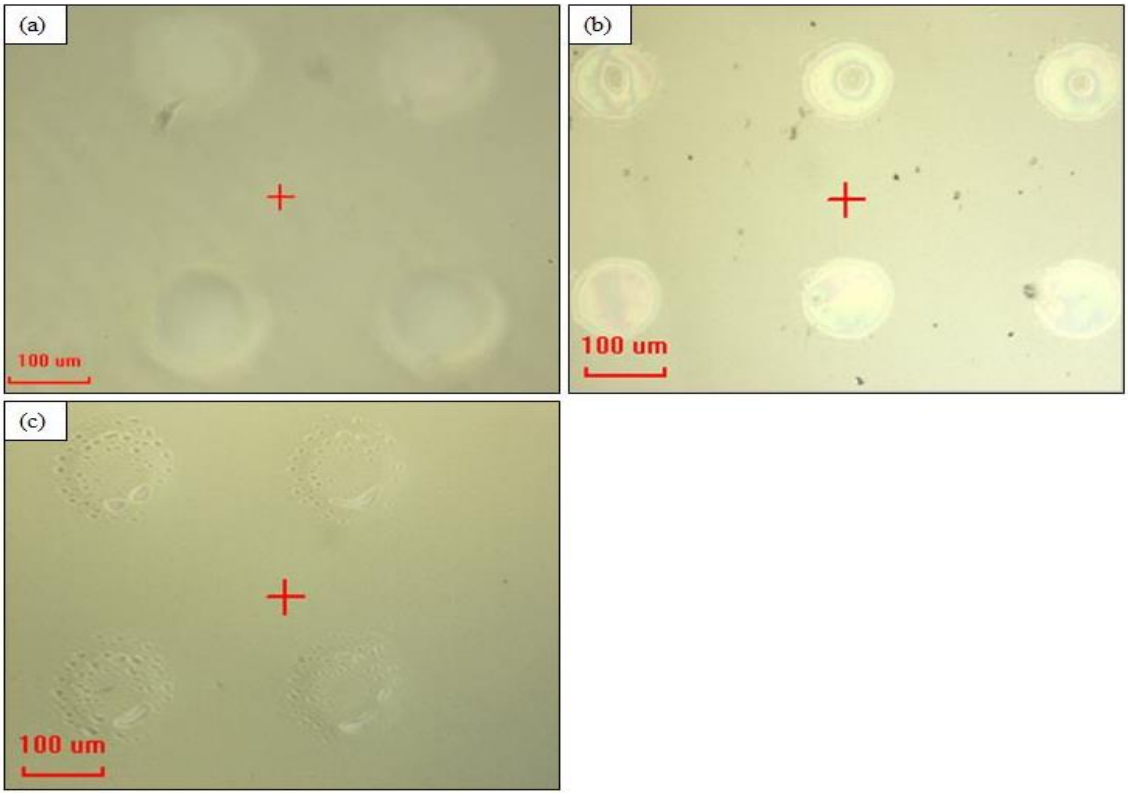

Figure 39 Optical images showing the residual impression left visible in the gelatine gels following indentation with water content of (a) 67%, (b) 80% and (c) 88%.

4.2.3 Indentation tests on Perma-Gel® samples

Fig. 40 presents the mechanical properties determined for Perma-Gel®. Similar to the gelatine gels, the storage modulus (*G´*) dominates over the loss modulus (*G˝*). Perma-Gel® exhibited a higher elastic component compared to its viscous component. The damping capacity was determined from the loss factor in Fig. 40c.

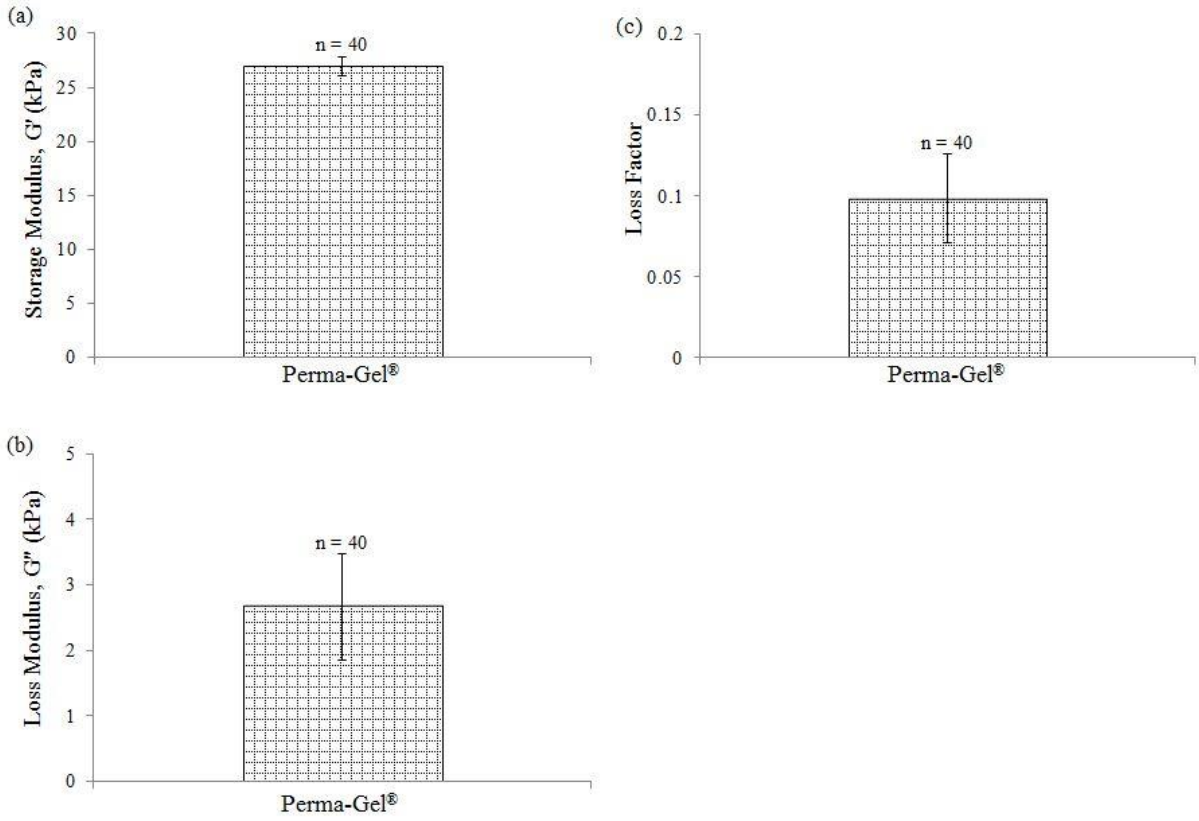

Figure 40 Micromechanical properties of Perma-Gel®, with the number of indentations (n) listed above each bar chart. (a) Storage modulus, *G´*, (b) loss modulus, *G˝* and (c) loss factor. Error bars depict SD.

The data obtained from a typical indentation experiment on Perma-Gel® are shown in Fig. 41. The comparison between repetitions showed close agreement for each of the samples used in the indentation tests.

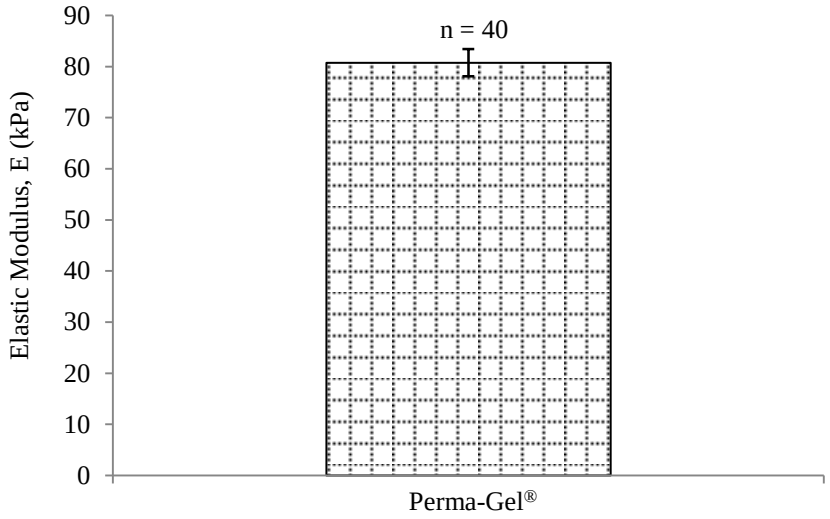

Figure 41 Elastic modulus of Perma-Gel® following micromechanical tests, with the number of indentations (n) listed above the bar chart. Error bar depicts SD.

Fig. 42 shows an optical image of a sample of Perma-Gel® following indentation tests and unlike the gelatine gels no residual impression was observed under the optical microscope.

Figure 42 Optical image of Perma-Gel® following indentation test.

4.2.4 Summary of the micromechanical properties of the sub-layers of the skin model

The summary of the average micromechanical properties of four individual samples of abdominal skin, back skin, three different gelatine gels of varying water content and Perma-Gel® is presented in Table 12. Of all the sub-layers in the skin model, it was found that

Perma-Gel® had the highest elastic component, whilst the 88% gelatine gel had the lowest elastic component. Back skin had the highest viscous component, whilst 88% gelatine gel had the lowest viscous component. Abdominal skin exhibited the highest damping capacity, whilst Perma-Gel® had the lowest damping capacity.

Table 12 Micromechanical properties of the different layers of the skin model (Mean ± SD).

Material	Storage Modulus (kPa)	Loss Modulus (kPa)	Loss Factor	Elastic Modulus (kPa)
Abdominal skin	8.16 ± 1.82	9.96 ± 3.88	1.11 ± 0.26	24.49 ± 5.47
Back skin	15.3 ± 3.20	10.71 ± 2.74	0.70 ± 0.06	45.89 ± 9.61
67% (w/v) gel	21.04 ± 2.08	3.77 ± 0.24	0.18 ± 0.01	63.11 ± 6.23
80% (w/v) gel	11.52 ± 1.05	2.01 ± 0.16	0.17 ± 0.01	34.56 ± 3.16
88% (w/v) gel	3.77 ± 0.55	0.94 ± 0.23	0.26 ± 0.07	11.30 ± 1.64
Perma-Gel®	26.91 ± 0.89	2.66 ± 0.81	0.10 ± 0.02	80.73 ± 2.67

An increase in water content in the gelatine gels resulted in a subsequent reduction in the magnitude of the respective elastic modulus, which is depicted in a linear relationship shown in Fig. 43. G' and G'' both decreased with increasing water content. The damping factor also decreased with increasing water content. Interestingly, the normal tissue fluid mimic (67%) had higher mechanical properties compared to either abdominal or back skin.

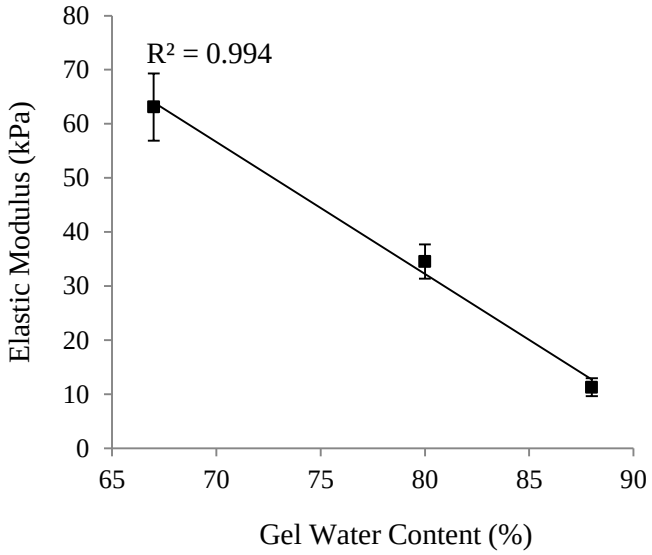

Figure 43 Linear relationship between elastic modulus and gel water content following micromechanical tests. Error bars depict SD.

4.3 Development of the Impact Applicator

This section details the preliminary tests using the impact applicator. Initially tests were performed to determine the relationship between force and velocity and afterwards further tests were conducted using microneedles.

4.3.1 Preliminary tests using the impact applicator

Prior to conducting impact tests on the full skin model, impact tests were performed on Perma-Gel® only and on microneedles resting on Perma-Gel® in order to establish the relationship between force and velocity in relation to how a material or combination of materials responds to impact load and the velocity at which the load is introduced to it.

Several impact tests were carried out on Perma-Gel® block at five different velocities calculated from dropping heights (see Table 11) using three different aluminium drop masses weighing 36 g, 17 g and 7 g. The trends for the three different drop masses are shown in Fig. 44. A linear relationship between velocity and force for each of the three drop masses was observed, as the velocity increased, the force increased.

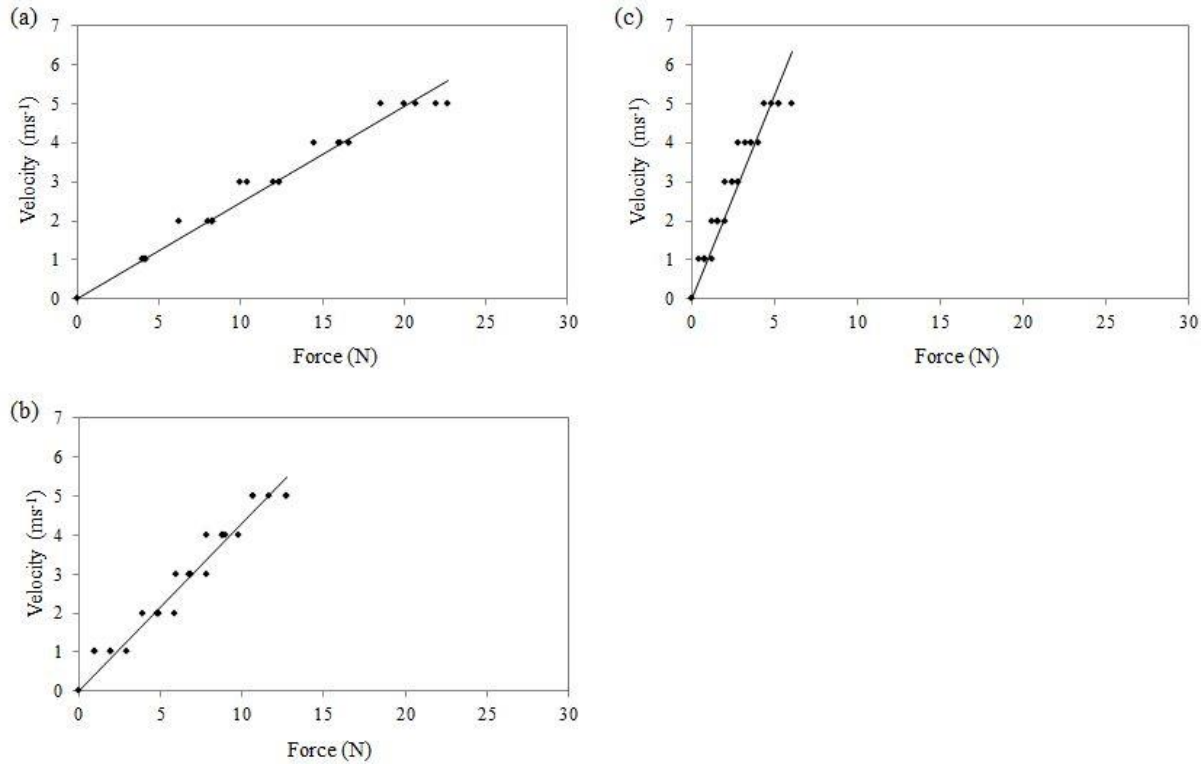

Figure 44 Linear plots of velocity as a function of force for impact tests of Perma-Gel® using various drop masses, (a) 36 g (b) 17 g and (c) 7g.

Additional testing was conducted by placing Design 1 microneedles on Perma-Gel®. Fig. 45 shows the relationship between velocity and force. The linear relationship shows that as velocity increases, the force also increases. Furthermore, more than twice the force was observed for impact tests of microneedles on Perma-Gel® as compared to on Perma-Gel® only.

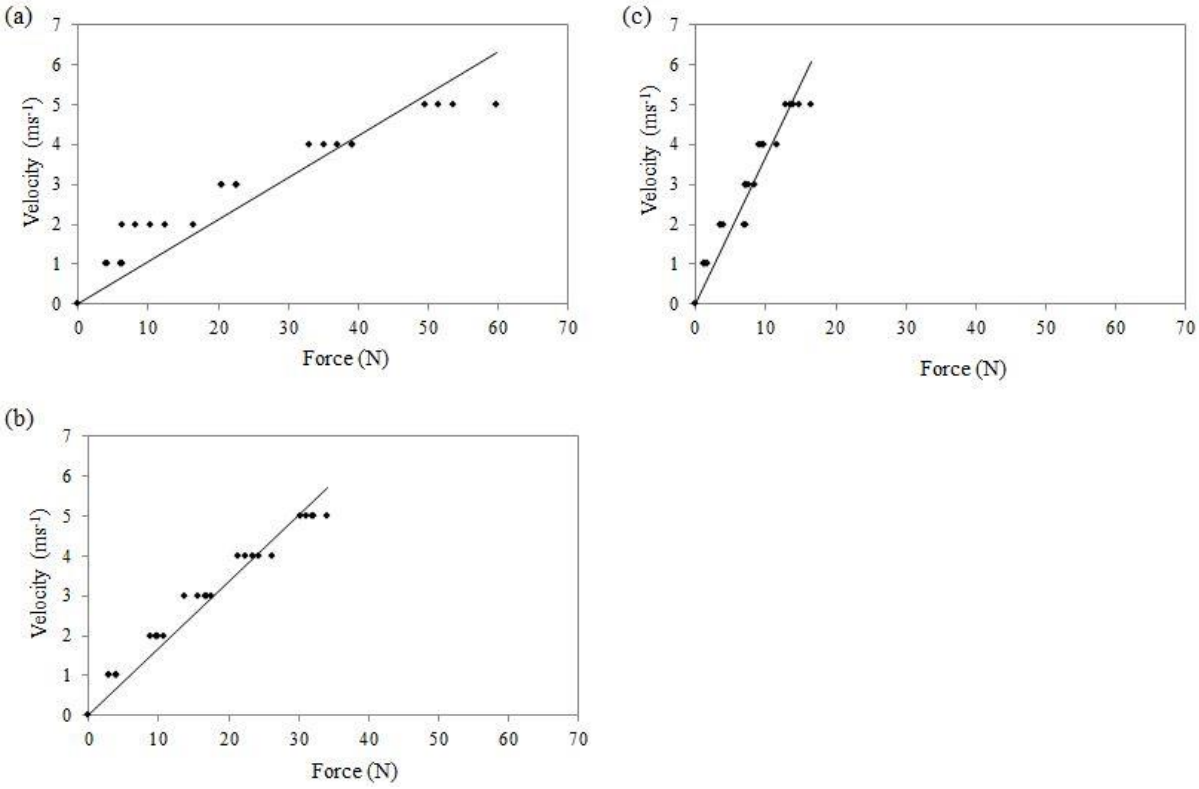

Figure 45 Linear plots of velocity as a function of force for impact tests with Design 1 microneedles on clamped Perma-Gel® using various drop masses weighing, (a) 36 g (b) 17 g and (c) 7g.

4.3.2 Skin penetration tests using PEEK microneedles

A pilot study of impact tests using the impact applicator on full thickness skin on different gelatine gels was carried out using PEEK microneedles, which have been used for *in vivo* studies on patients and the results are detailed in this section. Visual examination of the microneedles was performed in order to determine how often the microneedles could be used for impact tests on the skin models.

4.3.2.1 SEM imaging of PEEK microneedles following multiple applications

SEM imaging of PEEK microneedles were taken before and after they were applied to the skin and the images are presented in Fig. 46. The images show the profile of the needle tips. The figure also shows that the uneven profile of the microneedles was consistent for both images, indicating no change of shape to the tip and surrounding areas. The microneedles remained intact after impact tests on tissue and therefore were suitable for repeated use.

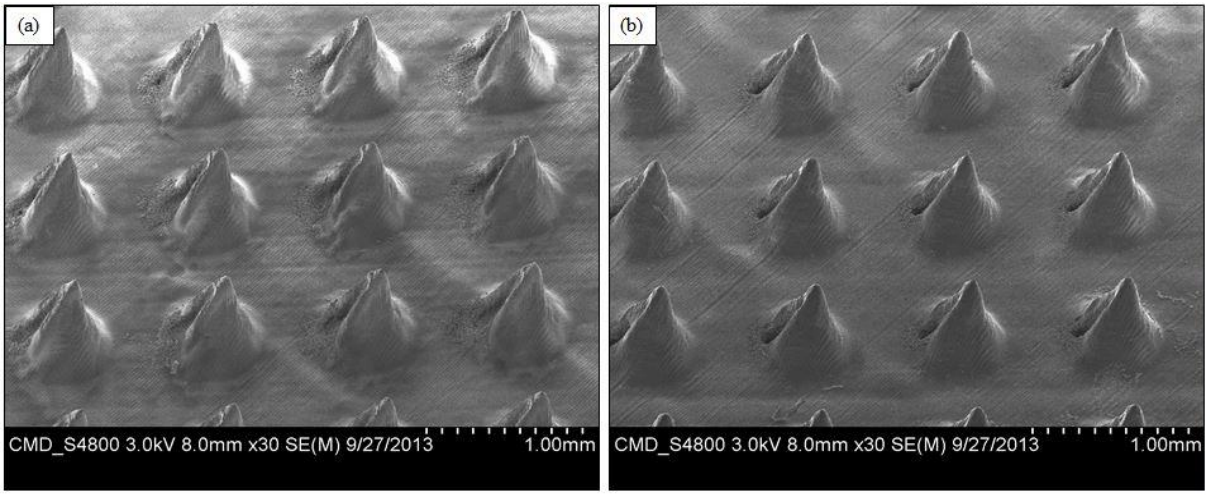

Figure 46 Comparison of SEM images for PEEK microneedles before and after impact tests. (a) before test and (b) after five applications.

4.3.2.2 The effects of differences in skin properties

The structural difference between the two skin regions examined is that abdominal tissue is thinner (0.79 ± 0.21 mm) as compared to tissue from the back region (2.73 ± 0.35 mm). Fig. 47 presents the methylene blue stains of microchannels created in abdominal and back skin models at various gelatine gel concentrations. There appears to be greater damage to back skin as compared to abdominal skin.

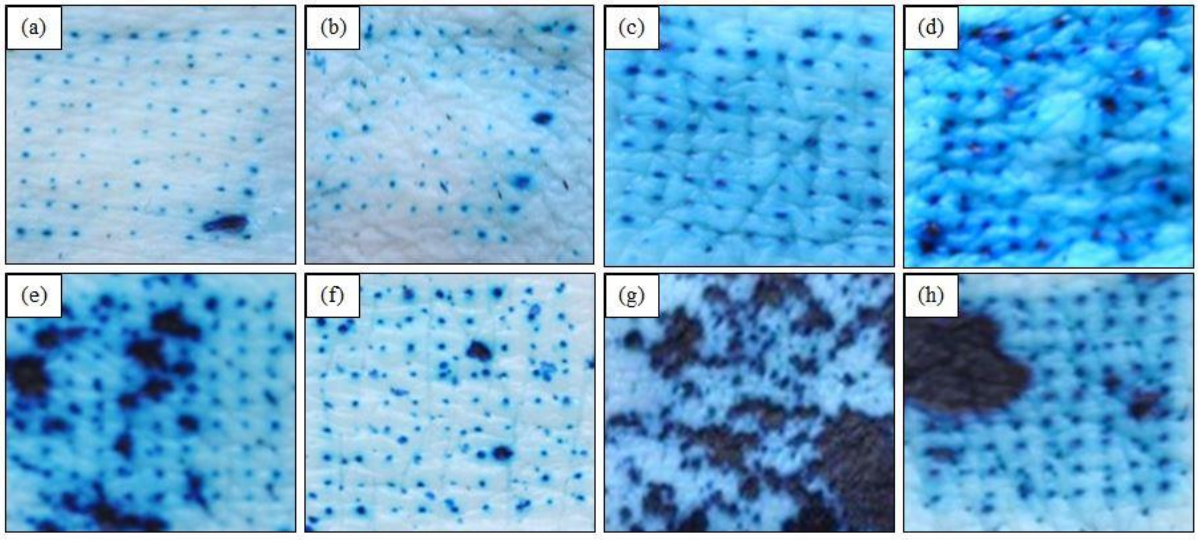

Figure 47 Methylene blue stained images of microchannels created by PEEK microneedles at a velocity of 5 ms^{-1} on abdominal skin model, where (a) 67%, (b) 80%, (c) 88%, (d) 96% gel water content and back skin model, where (e) 67%, (f) 80%, (g) 88%, (h) 96% gel water content.

4.3.2.3 Contributions from the subcutaneous mimic

Fig. 48 shows that the intensity of the methylene blue stain appears to increase with increasing water content in the gelatine gels. Fig. 48e also shows a significant reduction in the number of perforations on the stratum corneum, where there was an absence of a bed of gelatine gel to act as underlying substrate.

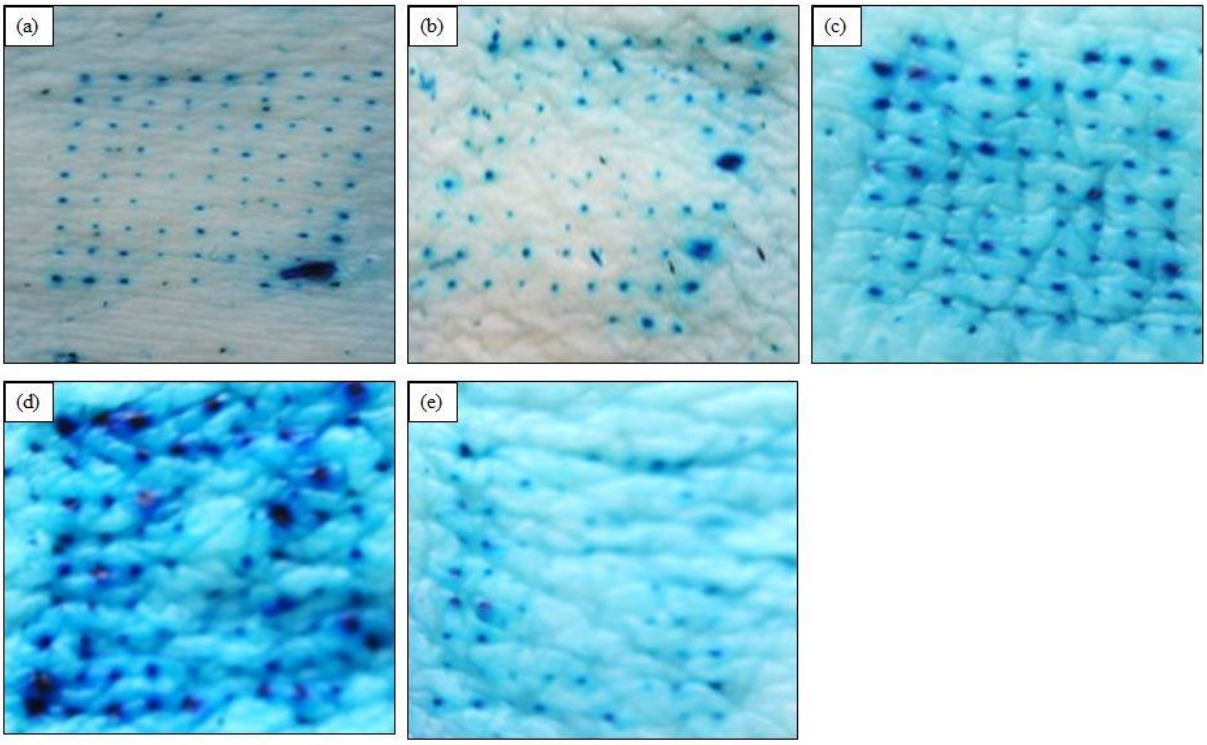

Figure 48 Methylene blue stained images of the microchannels created by PEEK microneedles on abdominal skin model comprising different amounts of water content in its gelatine gels at a velocity of 5 ms^{-1}, where (a) 67%, (b) 80%, (c) 88%, (d) 96% and (e) no gelatine gel as an underlying substrate.

Again, it was noted that for back skin, the quality of penetration appeared to improve with increasing water content in the gelatine gels (see Fig. 49). At 88% gelatine gel concentration however, no penetration was observed due to tissue damage, as shown in Fig. 49c. It was unclear, if the tissue damage was due to the impact of the microneedles or caused by existing bruising on the skin.

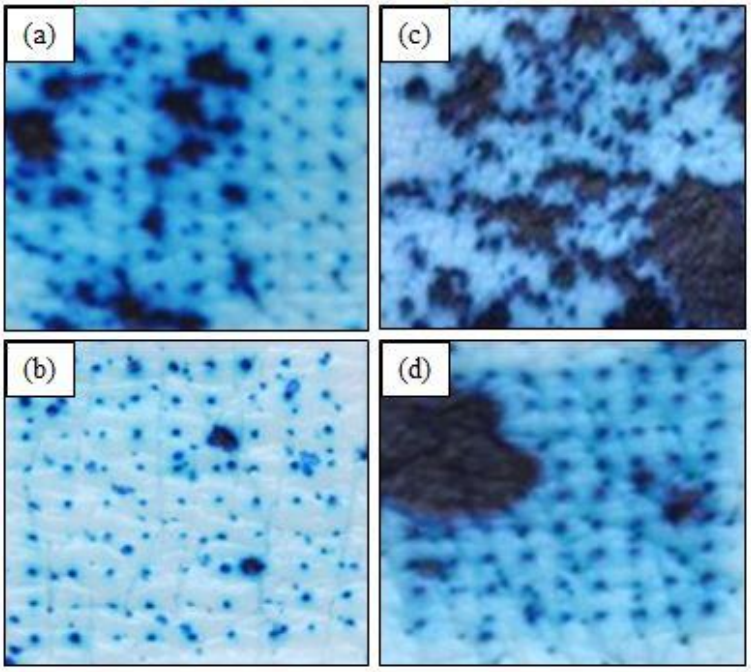

Figure 49 Methylene blue stained images of the microchannels created by PEEK microneedles on back skin model comprising different amounts of water content in its gelatine gels at a velocity of 5 ms^{-1}, where (a) 67%, (b) 80%, (c) 88% and (d) 96%.

Representative histology images of back skin model at 88% gelatine gel water content are shown in Fig. 50. Most of the perforations are contained within the epidermis, with the disruption extending into the dermis for two of the images. Although, successful breach of the epidermis occurred with PEEK microneedles for back skin model, it was challenging to consistently reproduce these perforations.

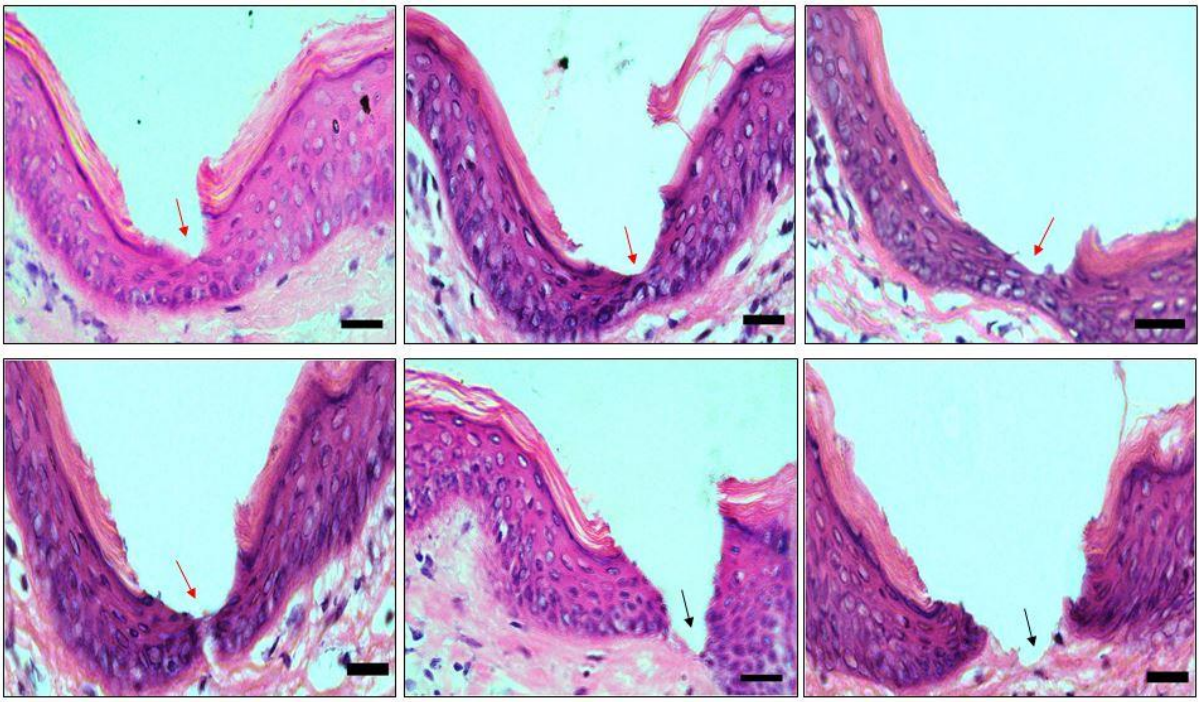

Figure 50 H&E images of back skin model with 88% water content in its gelatine gel at a velocity of 5 ms^{-1}. Red arrows indicate that the breach is contained within the epidermis and the black arrows indicate that the breach has extended into the dermis. Scale bar represents 100 μm.

4.3.2.4 Impact velocity

No penetration was achieved on the back skin model with 67% water content gelatine gel at velocities of 1–3 ms^{-1} following methylene blue staining. At velocities of 4–5 ms^{-1}, however there was perforation. For the abdominal skin model containing 67% water content in its gelatine gel, penetration was achieved at velocities of between 3–5 ms^{-1}. It was noted that even when the microneedle remained in tissue for two minutes following impact, it had no bearing on the quality of penetration.

4.3.3 Summary of the development of the impact applicator

Microneedle application on skin was achieved using an early development impact applicator. The parameters for penetration were a drop mass of 36 g, 3–5 ms^{-1} velocity on abdominal skin models and 4–5 ms^{-1} velocity on back skin models. The challenges with reproducible back skin perforations using PEEK microneedles meant that a different design of polymer microneedles were utilised for the work with the improved impact applicator.

4.4 Impact Applicator Studies

Reproducibly perforating the stratum corneum, epidermis and dermis was challenging with PEEK microneedles and therefore they were not used for further tests in this thesis to evaluate microneedles interaction with skin. The results however did provide velocity and force parameters, which were used as a basis for subsequent tests involving skin Models 1A–4B (see Table 9 in Section 3.2.4 for skin model classification) and PMMA microneedles (see Table 10 in Section 3.3.2 for PMMA microneedles details). Both designs of PMMA microneedles were medical grade.

Design 1 and 2 microneedles have been used for *in vivo* tests with patients (Renephra, 2015) and were the microneedles used for the bulk of the work carried out in this thesis. Moreover, Renephra conducted *in vivo* studies using these PMMA microneedles and the results from this thesis would complement and enhance their work, as the *in vitro* tests could be performed indiscriminately on neonatal porcine skin. Visual examination using SEM imaging was carried out on Design 2 microneedles in order to determine the frequency of use during testing. These tests were only conducted on Design 2 microneedles and not on Design 1 microneedles since the former arrays were used more extensively in testing. Furthermore, Design 2 microneedles were also used by Renephra for most of the clinical studies.

4.4.1 Visual examination of Design 2 microneedles using SEM imaging

SEM images of the Design 2 microneedles are shown in Fig. 51. With these microneedles it was found that with a single impact test on tissue, the needle tips had deformed (Fig. 51b). When five tests were carried out using the same microneedle array on five different skin models, the tips had broken off in some rows of needles as shown in Fig. 51c. To standardise testing as far as possible, Design 1 and 2 microneedles were only used once.

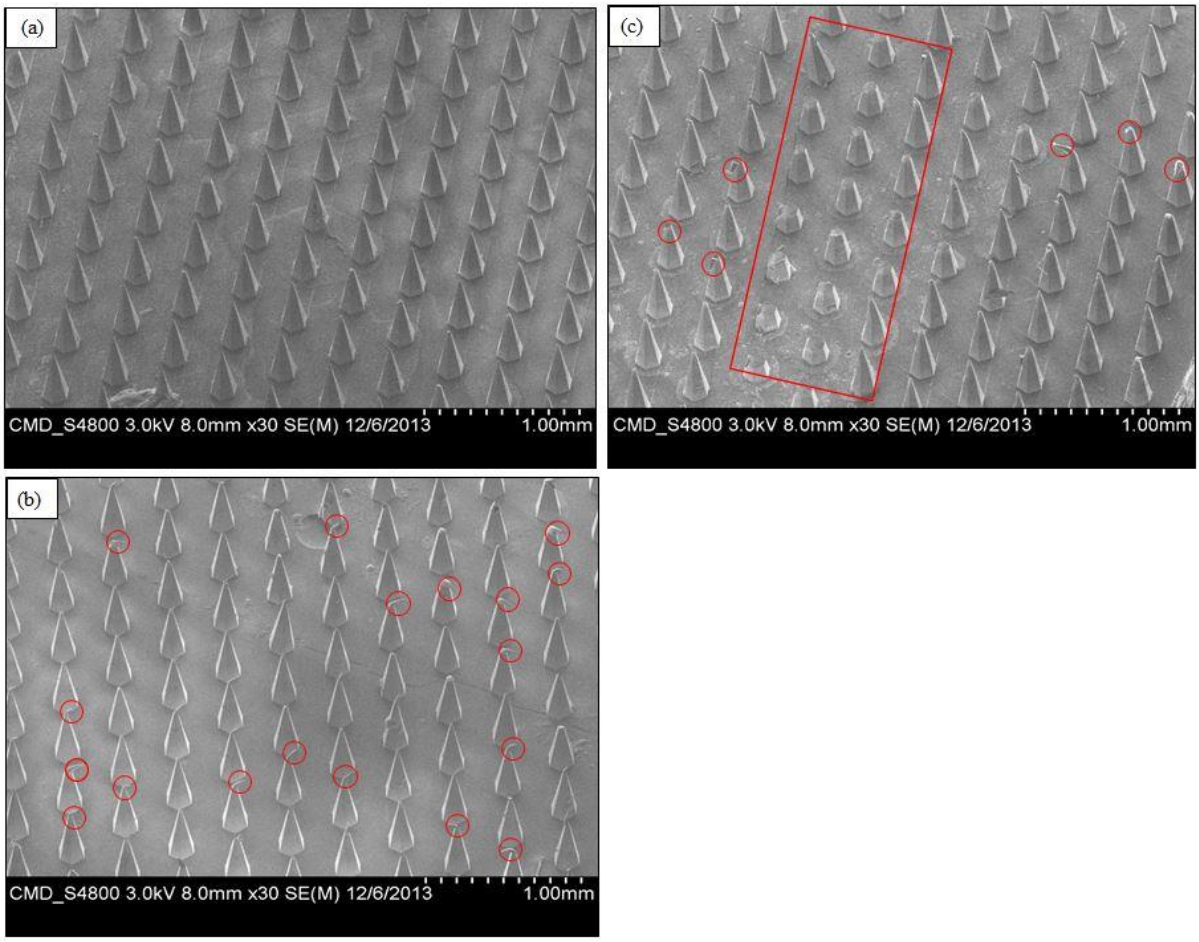

Figure 51 Comparison of SEM images for Design 2 PMMA microneedles before and after impact tests. (a) before test, (b) after single application and (c) after five applications.

4.4.2 Penetration efficiency

The images in Fig. 52 and 53 illustrate the effects of varying the water content in gelatine gels in the abdominal and back skin models respectively. It would appear that majority of the microneedles on the array created microchannels in each skin model. In addition, Fig. 52a–d appears to show that the intensity of methylene blue dye reduced with increasing water content in the gelatine gels.

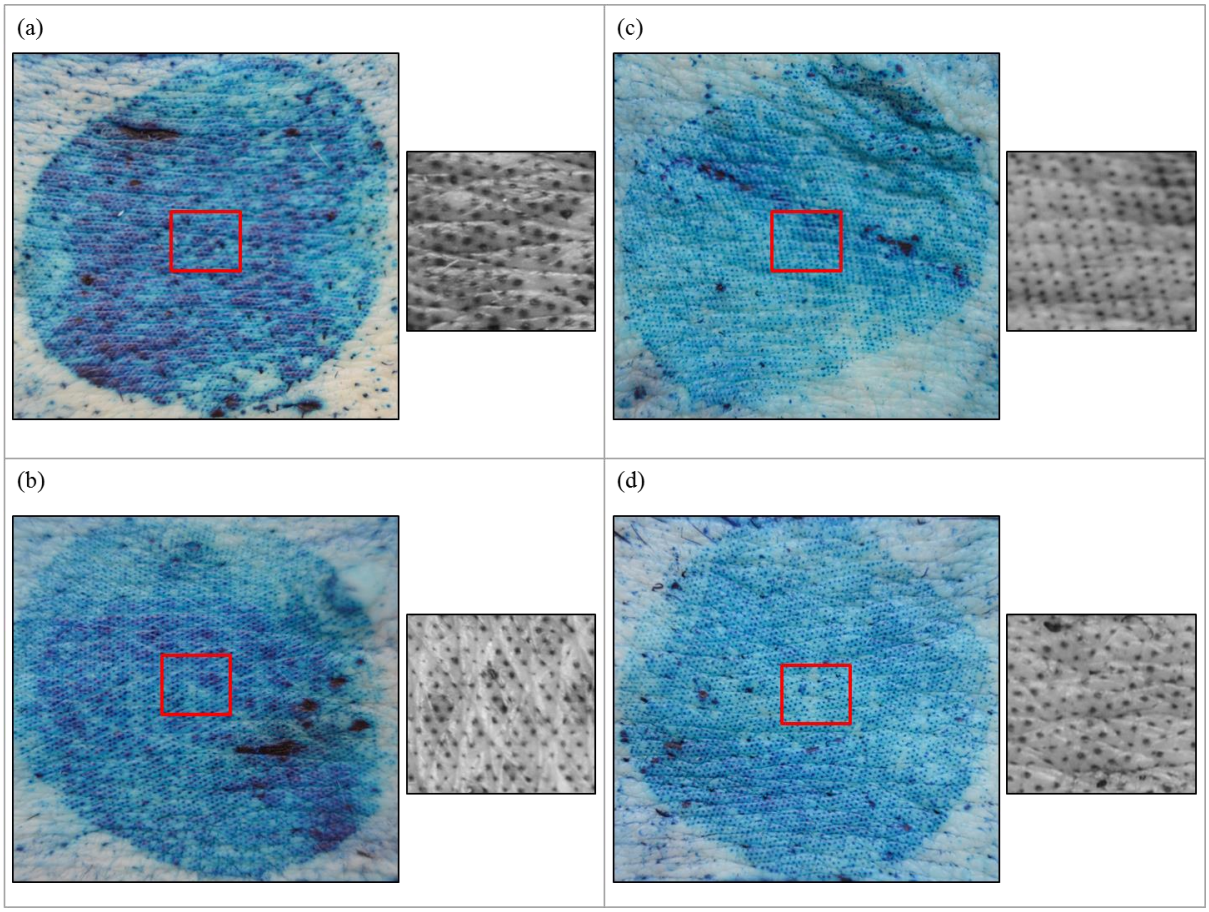

Figure 52 Inspection technique of impact applicator tests on Models 1A–4A for penetration efficiency with methylene blue staining where the whole disc provides visual confirmation of penetration and the cropped image, which is the selection highlighted in red is 5 × 5 mm in size and was used for calculating penetration efficiency for (a) 67%, (b) 80%, (c) 88% and (d) 96% of water content in the gelatine gels. The diameter of the microneedle disc is 30.1 mm.

Fig. 53a–d also appears to show that majority of the microneedles on the disc caused perforations on the stratum corneum. Although by comparing Figs 52 and 53, it is observed that there appears to be more perforations on abdominal skin models (Models 1A–4A) as

compared to back skin models (Models 1B–4B). It should also be noted that there is a physiological difference between abdominal and back skin, as full thickness abdominal tissue (≈ 0.79 mm) is thinner as compared to full thickness back tissue (≈ 2.43 mm). For human abdominal skin, the thickness varies from 1.71 ± 0.27 mm in children to 2.15 ± 0.42 mm in adults (Lo Presti et al., 2012), which is similar to the thickness of neonatal porcine back skin.

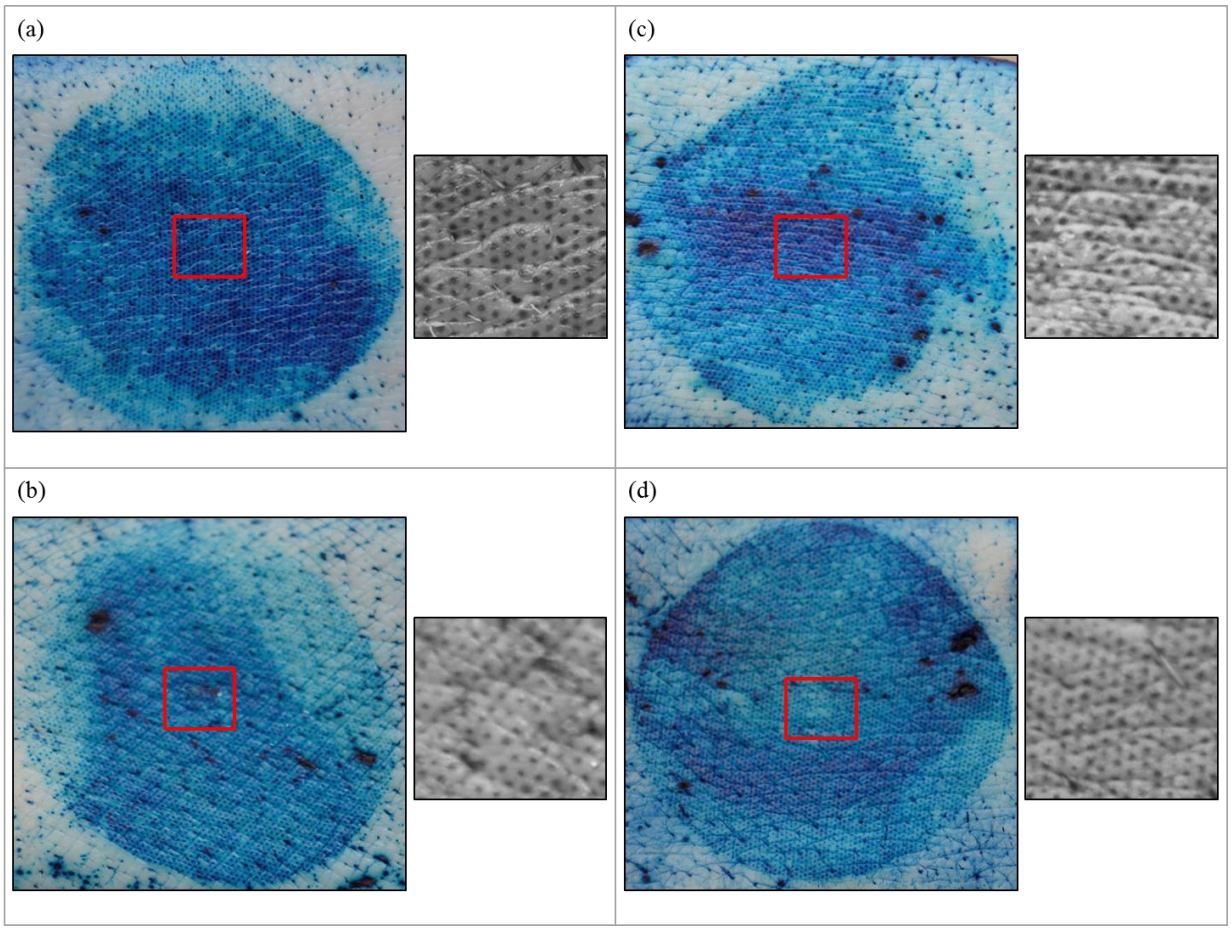

Figure 53 Inspection technique of impact applicator tests on Models 1B–4B for penetration efficiency with methylene blue staining where the whole disc provides visual confirmation of penetration and the cropped image, which is the selection highlighted in red is 5 × 5 mm in size and was used for calculating penetration efficiency for (a) 67%, (b) 80%, (c) 88% and (d) 96% of water content in the gelatine gels. The diameter of the microneedle disc is 30.1 mm.

Again, visual quantification of the entire methylene blue stained image was challenging using imaging software, which was due to the densely populated number of individual microneedles on Design 2 (> 6000 on array). The cropped area of 5 × 5 mm were selected from the centre of the images (Figs 52 & 53) and assessed to determine penetration efficiency

for abdominal and back skin models. The results of the penetration efficiency are presented in Fig. 54. As expected, 100 % penetration efficiency was not achieved (van der Maaden et al., 2014). There was no significant difference between abdominal and back skin samples.

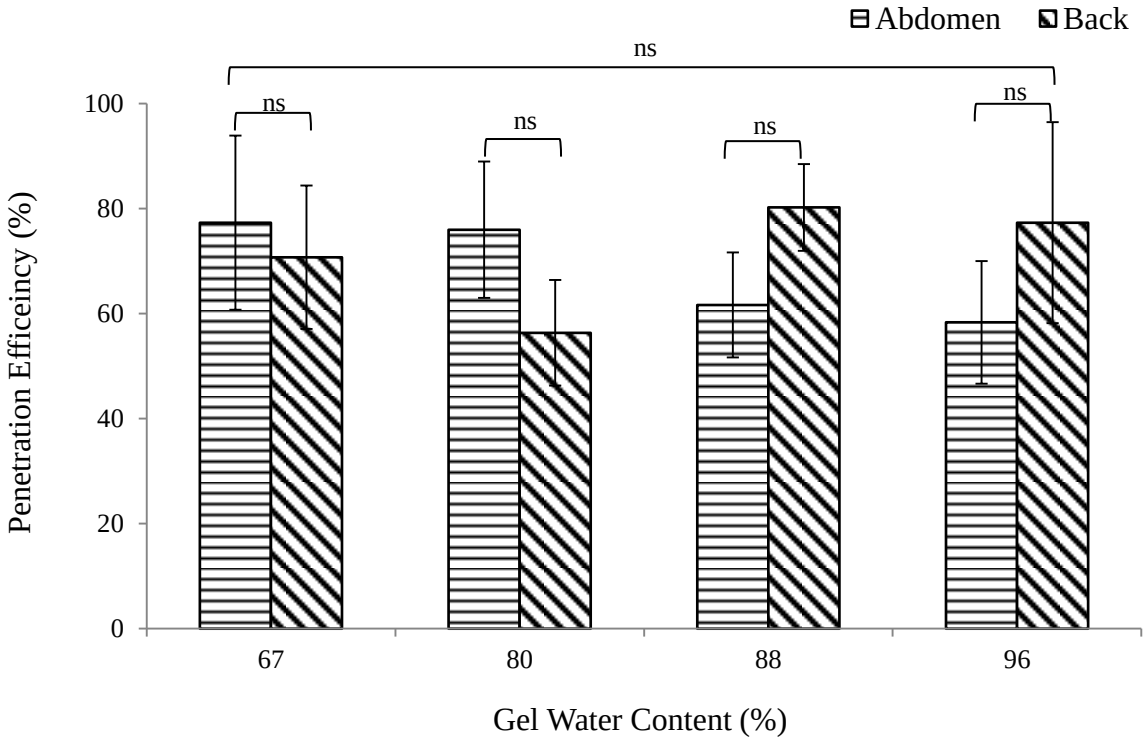

Figure 54 Penetration efficiency determined from the methylene blue images for impact applicator tests on 3 samples each of Models 1A–4B. Error bars depict SD.

4.4.3 The effects of differences in skin properties

Although the methylene blue staining provided quick visual confirmation that the majority of the microneedles had successfully penetrated the stratum corneum, the H&E images provided additional details in terms of the deformation extent. In addition, the H&E images also showed that not all perforations observed actually propagated through the stratum corneum to the epidermis or dermis. The H&E images in Fig. 55a–b show that both the abdominal and back tissue respond in a similar way to microneedle application with the deformation extending into the epidermis. However, the deformation in Models 1A & 2A was observed deep in the layers, whilst the deformation within Models 1B & 2B was predominantly contained within the epidermis. Fig. 55c shows the comparison between Models 3A and 3B, which is 88% water content in the gelatine gels. At this gelatine gel concentration, there appears to be a more significant deformation through the layers for Model 3A as compared to Model 3B. The comparison between Models 4A & 4B, which is depicted in Fig. 55d shows that the abdominal and back tissue exhibited a similar response to microneedle application as significant deformations were observed through the skin, extending into the dermis.

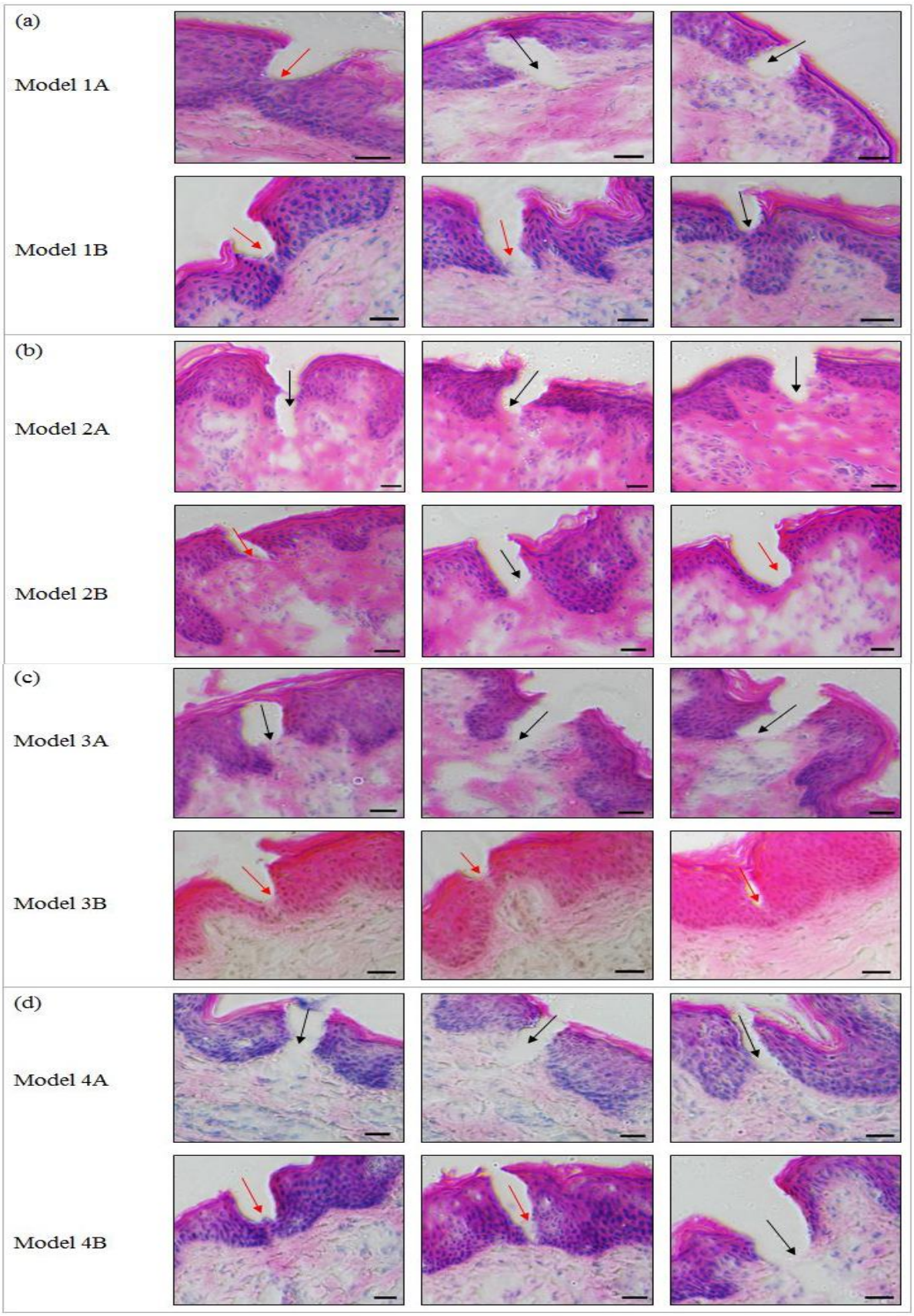

Figure 55 Comparison of perforation depths (H&E staining) using the impact applicator for abdominal and back skin models with respect to altering the water content in gelatine gels. Red arrows indicate that the breach is contained within the epidermis and the black arrows indicate that the breach has extended into the dermis. Scale bar represents 100 μm and the diameter of Design 2 microneedle disc is 30.1 mm.

4.4.4 The role of the subcutaneous mimic property on microneedle performance

The depth of penetration for each of the skin models is shown in Fig. 56. For Models 1A–4A (Fig. 56a), the depth of penetration increased with gel water content (from Models 1A to 3A) but was lowest for Model 4A at its highest gel water content. For the back skin models, the depth of penetration was lower at each gel concentration relative to the abdominal skin models except for Model 4B. The values for Model 3B with 88% gel water content were lower following the trends observed with qualitative assessment of the H&E images mentioned in Section 4.4.3 and insertion force data in Section 4.4.6.

Generally, the perforation depth for abdominal skin models was marginally greater than back skin models as shown in Fig. 56, with Model 4A the exception. For the mean breach areas in Fig. 57 however, there was no evident trend between abdominal and back skin models.

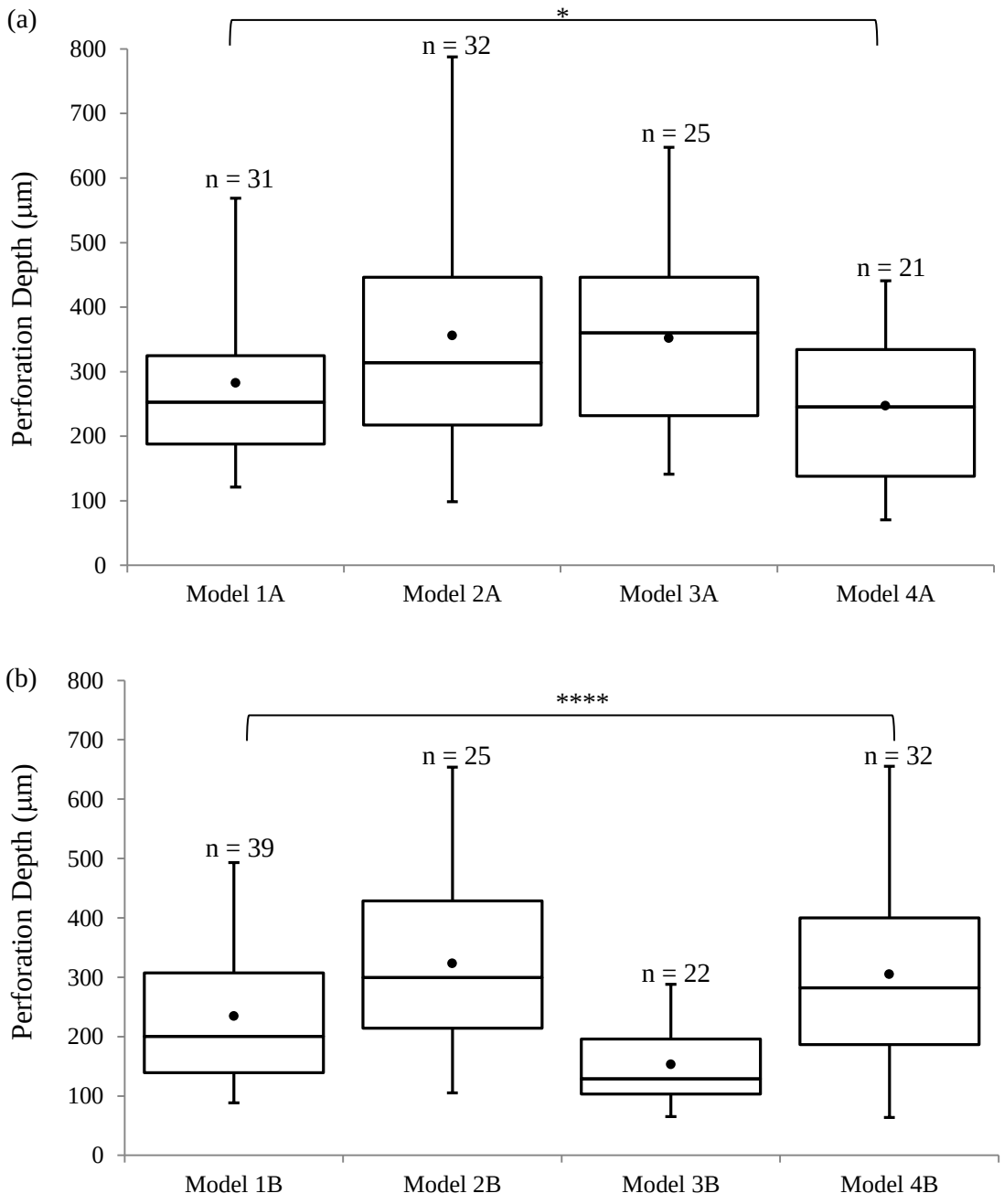

Figure 56 Perforation depth data for impact applicator tests using 36 g drop mass at a velocity of 3 ms^{-1}, where (a) abdominal skin models and (b) back skin models, with the number of images (n) in each group listed above each box and whisker plot.

The overall trends in the breach area for Models 1A–4B are shown in Fig. 57 and are similar to those for penetration depth (shown in Fig. 56). In Fig. 57a, the mean breach area for Models 1A–4A increased with gel water content but reduced for Model 4A at its highest gel water content. In Fig. 57b, the mean breach area for Models 1B–4B, the depth of penetration was slightly higher at each gel concentration relative to the abdominal skin models except for

Model 4B. The values for Model 3B with 88% gel water content were much lower following the trends observed with the insertion force data. There appears to be a relationship between perforation depth and breach area as indicated, with the mean trends being similar for perforation depth (Fig. 56) and breach area (Fig. 57).

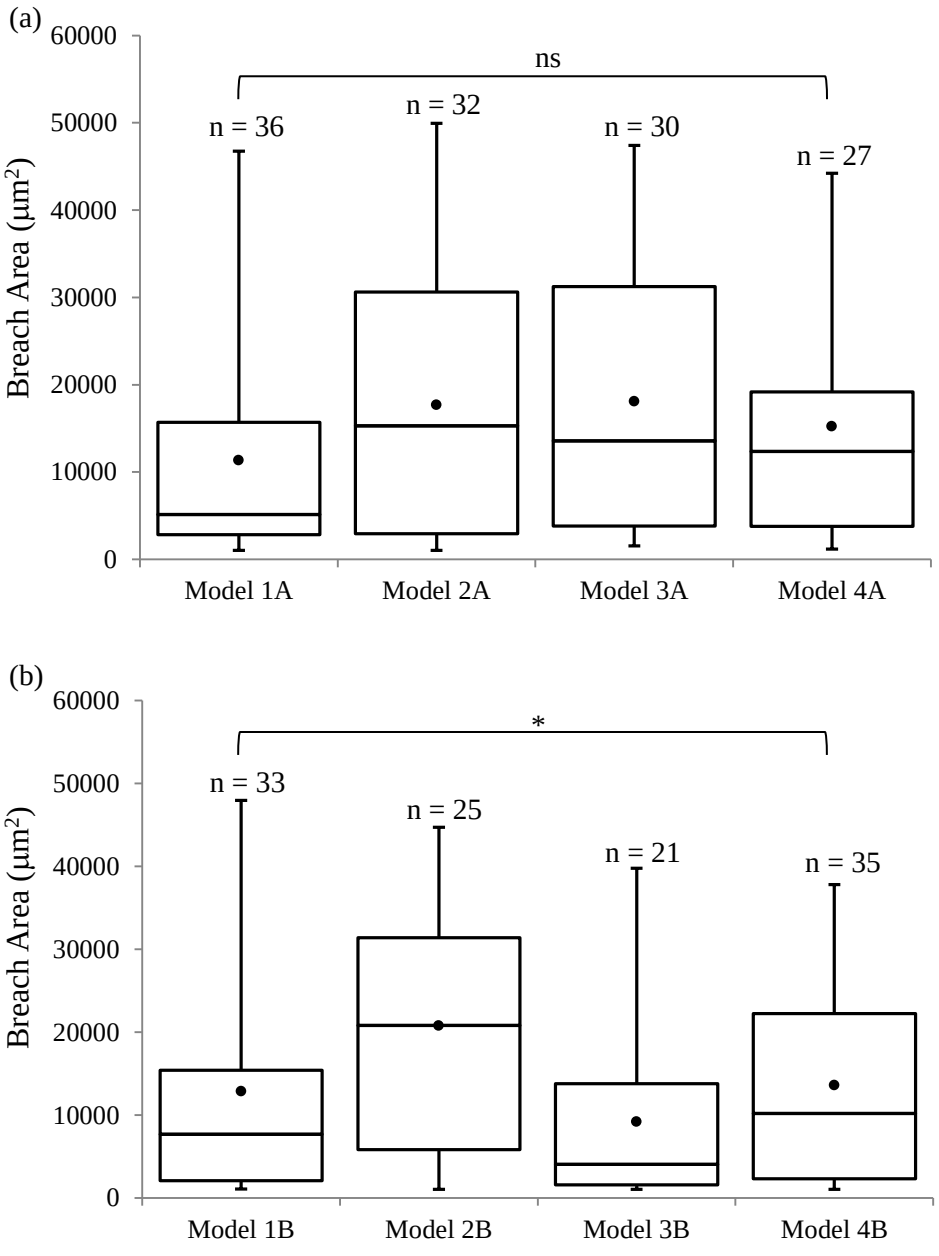

Figure 57 Breach area data for impact applicator tests using 36 g drop mass at a velocity of 3 ms^{-1}, where (a) abdominal skin models and (b) back skin models, with the number of images (n) in each group listed above each box and whisker plot.

For the abdominal skin models, over 60% of the measured perforations were 0 < breach area < 10 000 μm^2 for Model 1A, which is the model with the lowest water content gel (Fig. 58a). There was over 70% for Model 3B in this category, which had a higher water content gel (Fig. 58b). The frequency of the breach area reduced at > 10 000 μm^2 for all skin models, Therefore, the majority of microneedles interaction with skin occurs at the stratum corneum–epidermal interface (as defined in Section 3.5.3.2). A contrast between abdominal skin model compared to back skin model was that perforations occurred in each breach area category, whilst there was no breach areas observed in some categories for back skin model. Generally, as epidermal breach occurs at 10 000 < breach area < 20 000 μm^2 (as previously described in Section 3.5.3.2), therefore, it can be said that both anatomical regions appear to be ideal sites for microneedle application for fluid extraction on neonatal porcine skin, whilst the breach areas in excess of 10 000 μm^2 could indicate penetration effectiveness.

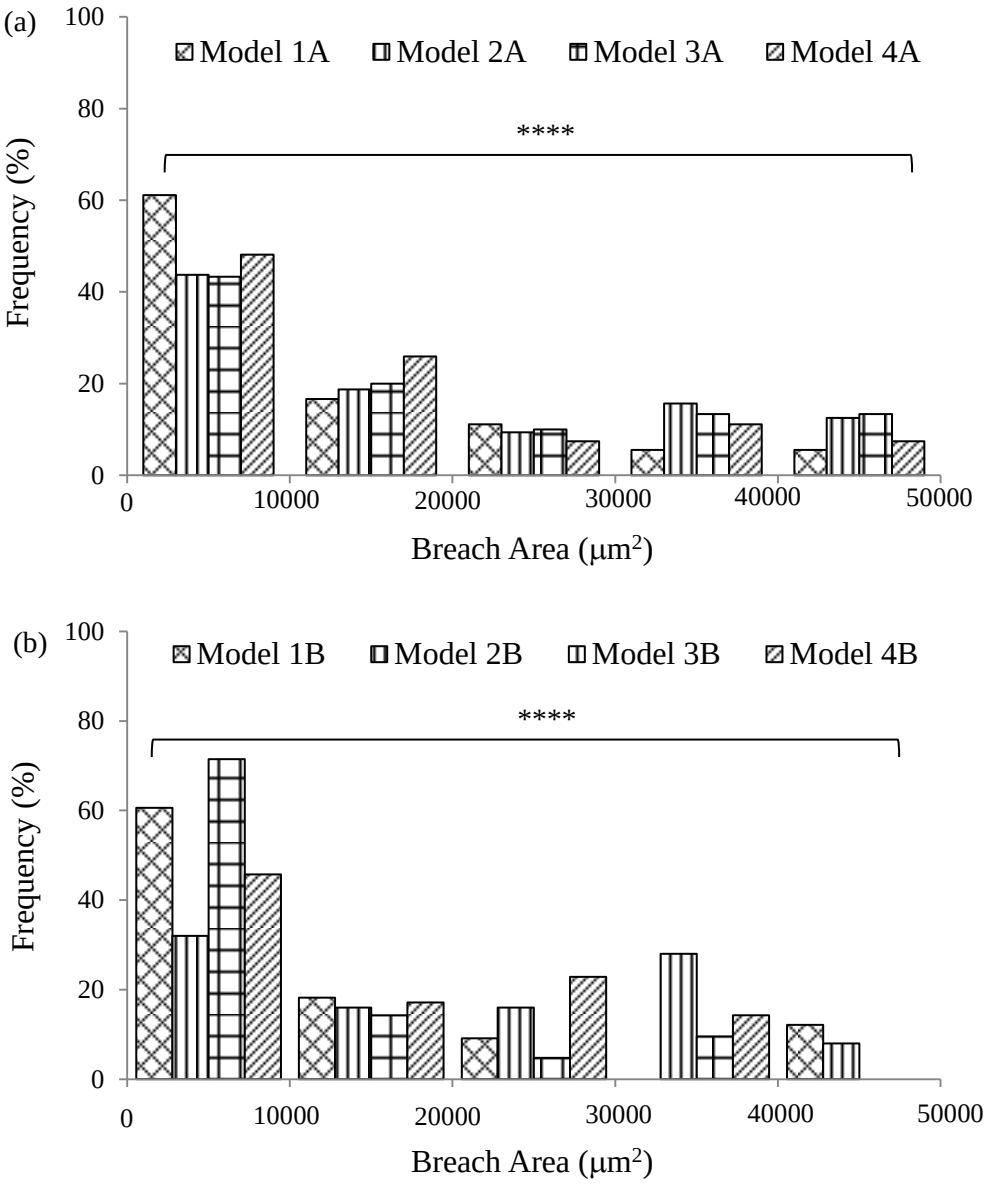

Figure 58 Frequency distribution of the breach area for impact applicator tests on (a) abdominal skin models and (b) back skin models.

4.4.5 Impact applicator force and velocity

As mentioned in the literature, the introduction of microneedles in biological tissue to any depth requires the assistance of external pressure to penetrate skin. This required assistance can be achieved using a microneedle delivery apparatus. Work by Bouwstra et al. suggests that the optimal method for microneedle application requires velocities in excess of 2 ms^{-1} (Bouwstra et al., 2009). Firstly, the challenge to effective microneedle penetration is to bypass the inherent elasticity of the stratum corneum (Bal et al., 2008). Secondly, the appropriate insertion velocity and insertion force to achieve penetration of the stratum corneum with microneedles is necessary (Donnelly et al., 2011).

Typical force and velocity plots obtained with Design 2 microneedles are shown in Fig. 59. Due to the high velocity from the impact test setup, it was difficult to precisely determine the exact moment that the microneedles penetrated through the skin. However, due to the characteristics of the plots shown in Fig. 59a and 59b, the insertion force and insertion velocity could be inferred.

The insertion force, which was 37.1 N and the insertion velocity, which was 2.5 ms^{-1} were obtained from the force–time see Fig. 59a. The maximum force reached was 107 N. Accounting for some elastic recovery of skin and to ensure that the microneedles were fully embedded in the skin (Lara et al., 2012), the microneedles were left in the skin for approximately 2 mins prior to removal for subsequent imaging, so as to minimise skin retraction following removal of microneedles (Donnelly et al., 2010; Loizidou et al., 2016).

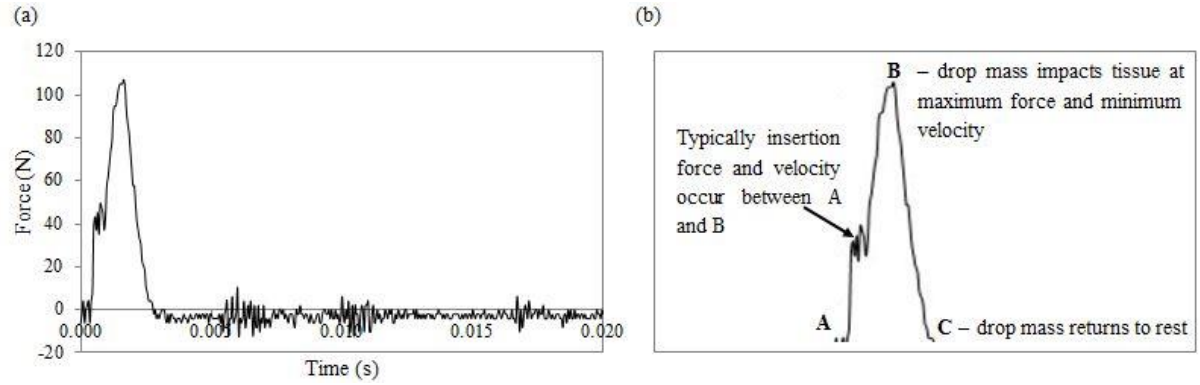

Figure 59 Impact tests of Design 2 microneedles on Model 2B, where (a) force–time plot and (b) the description of points along the force–time curve. The impact occurred at 0.9 ms, where the velocity was approximately 2.5 ms^{-1}, the force was 37.1 N and the maximum force reached was 107 N. The data suggest that the initial insertion occurred at 0.9 ms. Hence, at this point the velocity was approximately 2.5 ms^{-1}, the force was 37.1 N and the maximum velocity and force reached were 3 ms^{-1} and 107 N respectively. In the absence of any microneedles, a smooth force-time plot up to the maximum load would be expected for a drop mass impacting on a tissue sample (Burgin and Aspden, 2007).

The insertion force which was inferred from the force-time plots (Fig. 59a) did not vary with gel water content for the skin models, but was approximately 10 N higher for most of the back skin models as compared to the abdominal skin models (Fig. 60a). Fig. 60b shows the variation of the maximum force across the different abdominal skin models and as can be seen decreased progressively with increasing water content of the subcutaneous mimic. This was found to be related to the elastic modulus of these gels (Fig. 60c). For back skin models, the maximum force was relatively constant for most of the gel water content except for Model 3B, which contained 88% gel water content (Model 1B/67% - 102 N, Model 2B/80% - 100 N, Model 3B/88% - 46 N, Model 4B/96% - 102 N). Furthermore, histological examinations of perforation depths and breach area also showed a small depth and area for Model 3B as compared to Models 1B, 2B and 4B, which indicate that the size of the force is commensurate with the size of the deformation. For Models 1A and 1B, which contained 67% gel water content, there was no difference in the maximum force with the two different types of skin i.e. the thicker and stiffer back skin did not require a larger insertion force. The difference in the force values for the two different anatomical skin models was more pronounced at higher water contents in the subcutaneous mimic.

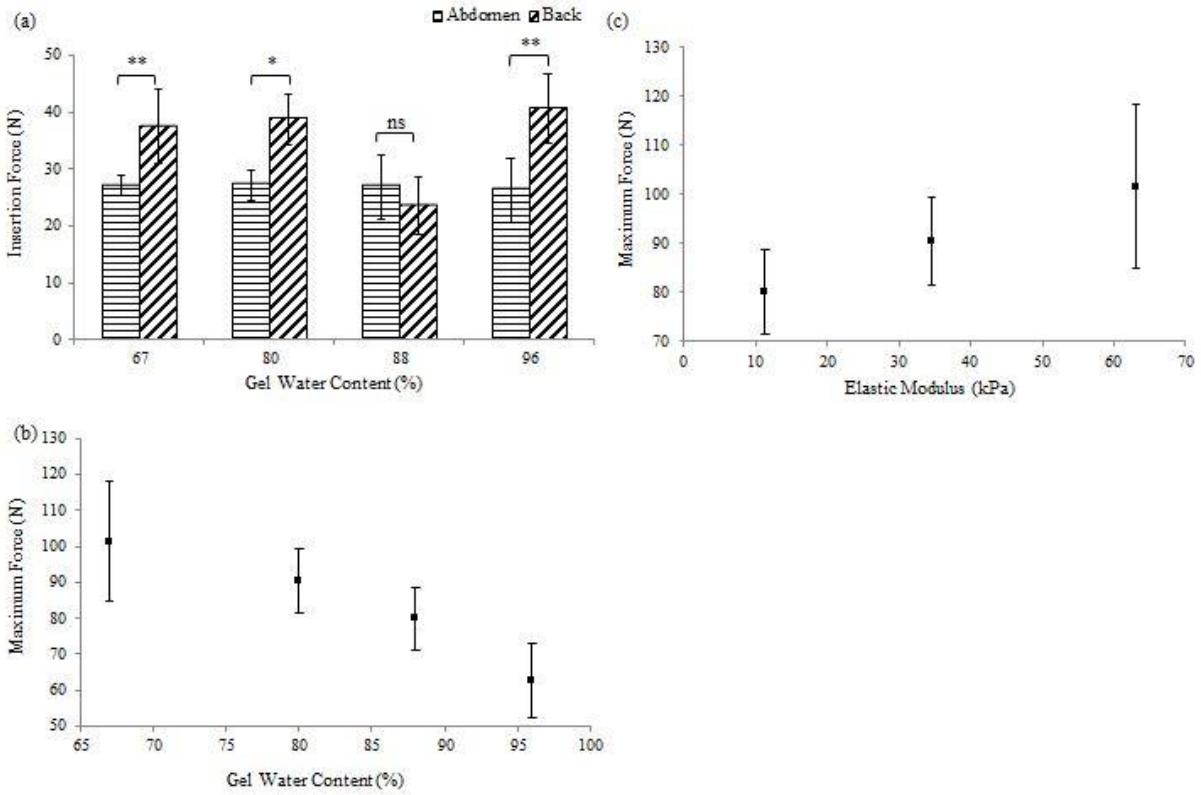

Figure 60 Force data for impact applicator tests, where n = 5 for each skin model (a) insertion force data for abdominal and back skin models, (b) variation of the maximum force as a function of gel water content in abdominal skin Models 1A–4A and (c) maximum force for Models 1A–4A vs elastic modulus of the gelatine gels. Error bars depict SD.

4.4.6 The effects of microneedle geometry on skin penetration

Neonatal porcine back skin bears similar thickness to human skin (Lo Presti et al., 2012) as compared to abdominal skin. Further, neonatal porcine back skin has similar mechanical properties to human skin (Groves, 2011) and was chosen for tests involving the two designs of PMMA microneedles. A high water content gel was selected for all the tests comparing the two microneedle designs on back skin. This was because of the relevance to oedema to this project (Section 1.2). Hence, the 88% gelatine gel was selected as the 96% gelatine gel was too compliant. Thus, skin Model 3B was used for these tests. This section compares impact applicator tests for Design 1 (1316 microneedles on the array/356 μm length) with Design 2 (> 6000 microneedles on the array/552 μm length) microneedles using this model.

4.4.6.1 Microneedle penetration on skin Model 3B

This section details the results of impact tests using Design 1 and Design 2 microneedles on skin Model 3B.

4.4.6.1.1 Comparison between visual examination and perforation depth

Representative methylene blue and histology images of impact applicator tests on Model 3B using Design 1 and 2 microneedles are presented in Fig. 61. As shown in Figs 61a–b, the methylene blue staining confirmed the successful perforation of the stratum corneum, whilst the histology showed the depth of perforation through the layers. In Fig. 61a, image analysis using ImageJ showed that 80% of Design 2 microneedles perforated the stratum corneum of Model 3B compared to 55% of Design 1 microneedles in Fig. 61b. The H&E images show comparable levels of deformation within the layers.

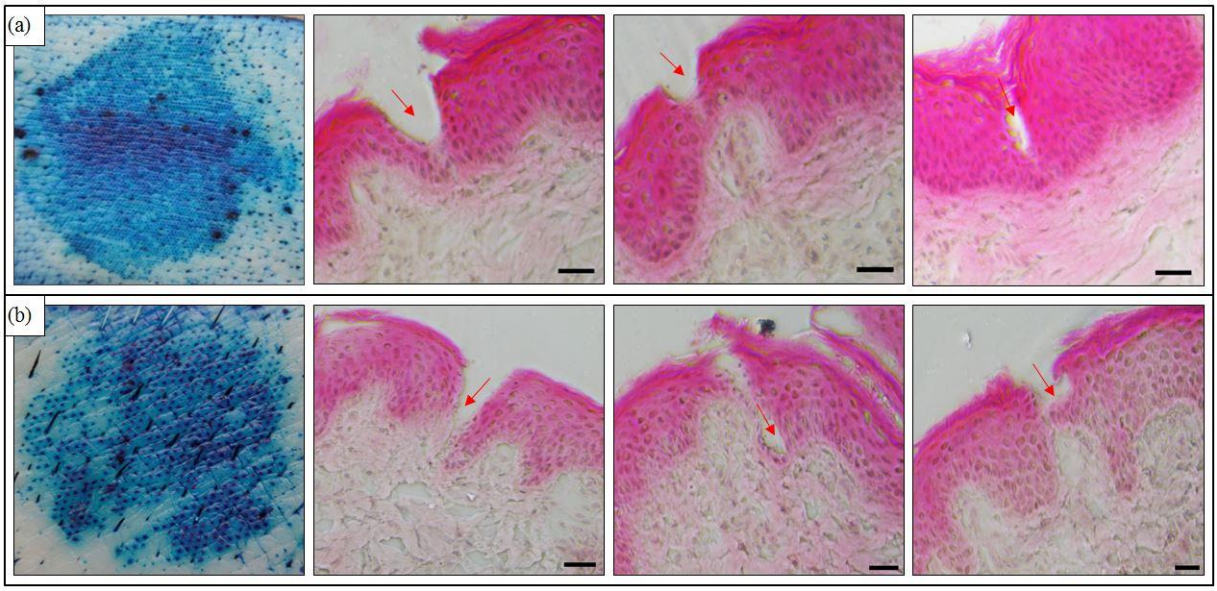

Figure 61 Design 1 and 2 microneedles comparison on perforation quality (methylene blue staining) and perforation depth (H&E staining) for impact applicator tests on Model 3B. (a) Design 2 (b) Design 1. The diameter of Design 2 microneedle disc is 30.1 mm. The diameter of Design 1 microneedle disc is 15.8 mm. Red arrows indicate that the breach is contained within the epidermis. Scale bar represents 100 μm.

The depth of penetration in Model 3B for Design 1 and 2 microneedles is shown in Fig. 62. The greatest perforation depth was 351 μm for Design 1 microneedles as compared to 288 μm for Design 2 microneedles. In addition, the mean penetration depth is greater for Design 1 microneedles as compared to Design 2 microneedles.

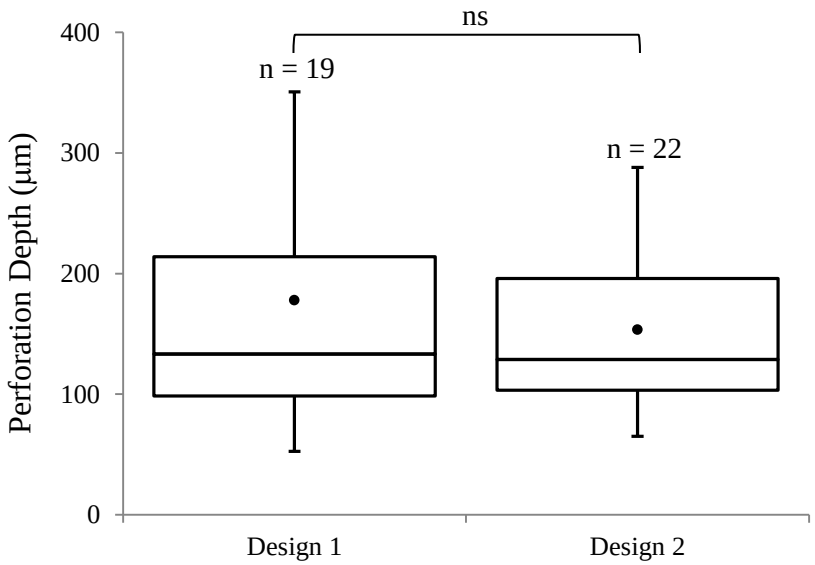

Figure 62 Perforation depth data for impact applicator tests comparing results of Design 1 and 2 microneedles on Model 3B, with the number of images (n) in each group listed above each box and whisker plot.

4.4.6.1.2 Histological examination of breach area

The results of the breach area on model 3B for Design 1 and 2 microneedles are shown in Fig. 63. The percentage frequency of perforations shows that the highest number of perforations occurred between 0 < breach area < 10 000 μm^2 range and the lowest number of perforations occurred between 40 000 < breach area < 50 000 μm^2 range. The frequency chart shows that there is a decline in the frequency of perforations at increased breach area. The chart also highlighted a higher proportion of breach area (10 000 μm^2) for Design 2 microneedles as compared to Design 1 microneedles.

The general trend for the frequency distribution of deformation within Model 3B, showed that Design 2 microneedles produced the greatest deformation area at 0 < breach area < 10 000 μm^2, however, at categories > 10 000 μm^2, Design 1 microneedles created greater breach areas.

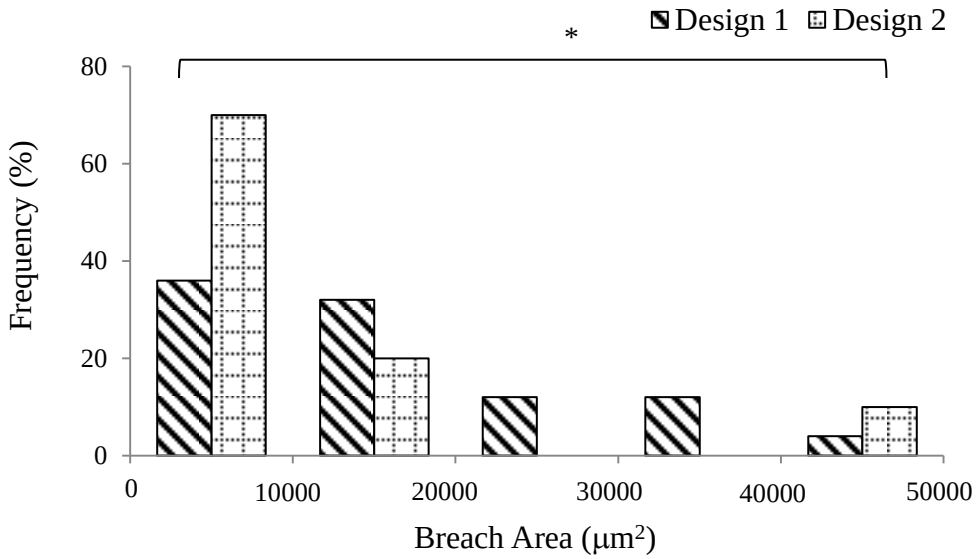

Figure 63 Frequency distribution for impact tests at 3 ms^{-1} using a 36 g drop mass on Design 1 and 2 microneedles on Model 3B.

4.4.6.2 Impact force and velocity for skin Model 3B

This section presents the force and velocity outcome of Design 1 microneedles on skin Model 3B. Later in the section, the force and velocity outputs are compared to the results of Design 2 microneedles.

4.4.6.2.1 Variation of the velocity and force

Penetration of the stratum corneum was assessed qualitatively from the methylene blue images shown in Fig. 64. Following visual examination, a greater concentration of methylene blue dye was observed on Model 3B after the application of Design 1 microneedles using 36 g and 17 g drop masses at velocities of 5 and 4 ms^{-1}. At 3 ms^{-1}, a significant proportion of the microneedles penetrated the stratum corneum with the 36 g drop mass shown in Fig. 64a. However, at the same velocity penetration appeared lower with the 17 g drop mass shown in Fig. 64b. At 2 ms^{-1}, the intensity of methylene blue staining was further reduced with the 36 g drop mass shown in Fig. 64a but minimal staining was observed at this velocity with the 17 g drop mass shown in Fig. 64b. These images demonstrated that the microneedle arrays successfully perforated Model 3B at velocities $\geq$ 3 ms^{-1} with the highest drop mass used in this study, which could be useful details in the development of Renephra's applicator. The quality of penetration in terms of perforations on the stratum corneum and intensity of the methylene blue dye decreased with the lower drop mass weights.

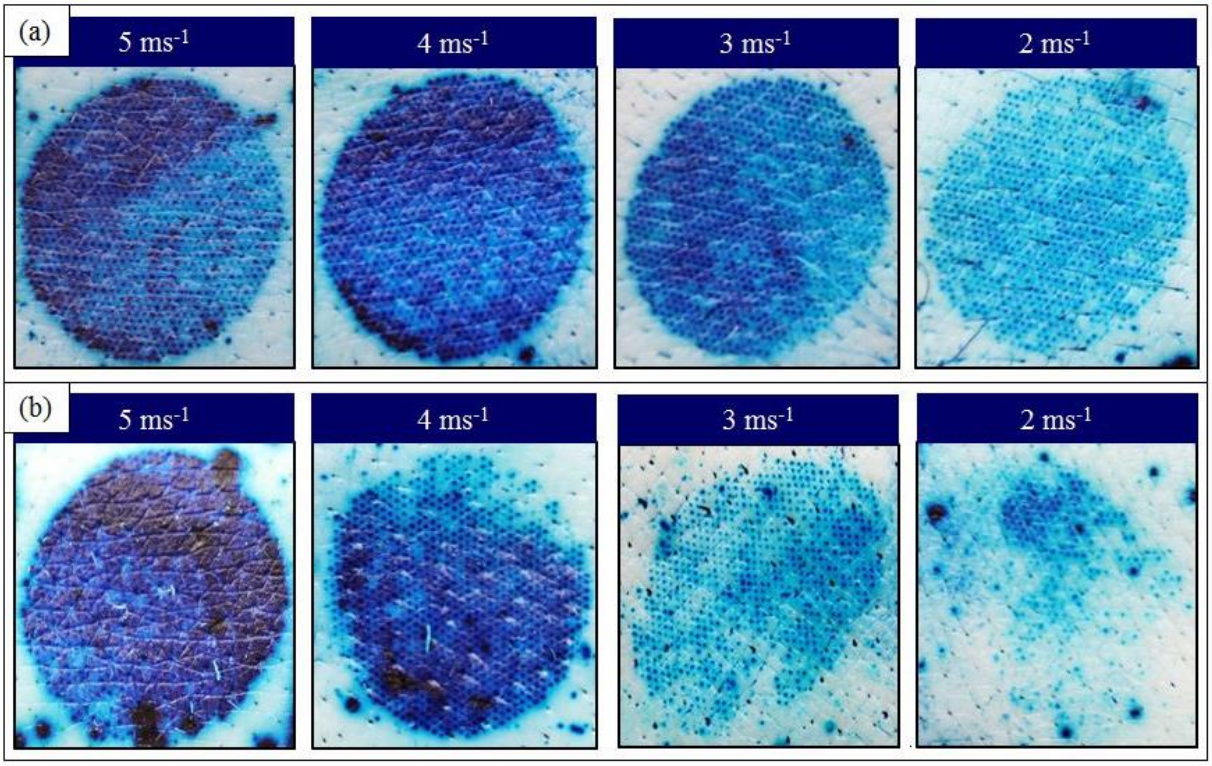

Figure 64 Example images of methylene blue stained skin model 3B following impact tests at various velocities with (a) 36 g drop mass (b) 17 g drop mass. Diameter of Design 1 microneedle disc is 15.8 mm.

Microneedles are designed to effectively penetrate the stratum corneum without causing any damage to the dermal layer (Kim et al., 2012). Hence, histological staining was used to examine the penetration profile, complementing the methylene blue assessment. In some cases, only minute breaches in the epidermal layer were found as shown in Fig. 65. Although under all the tested parameters some damage to the stratum corneum layer was consistent and repeatable, epidermal breach (illustrated in Fig. 30) was not consistent when the velocity was < 3 ms^{-1} or with drop masses 7 g and 17 g.

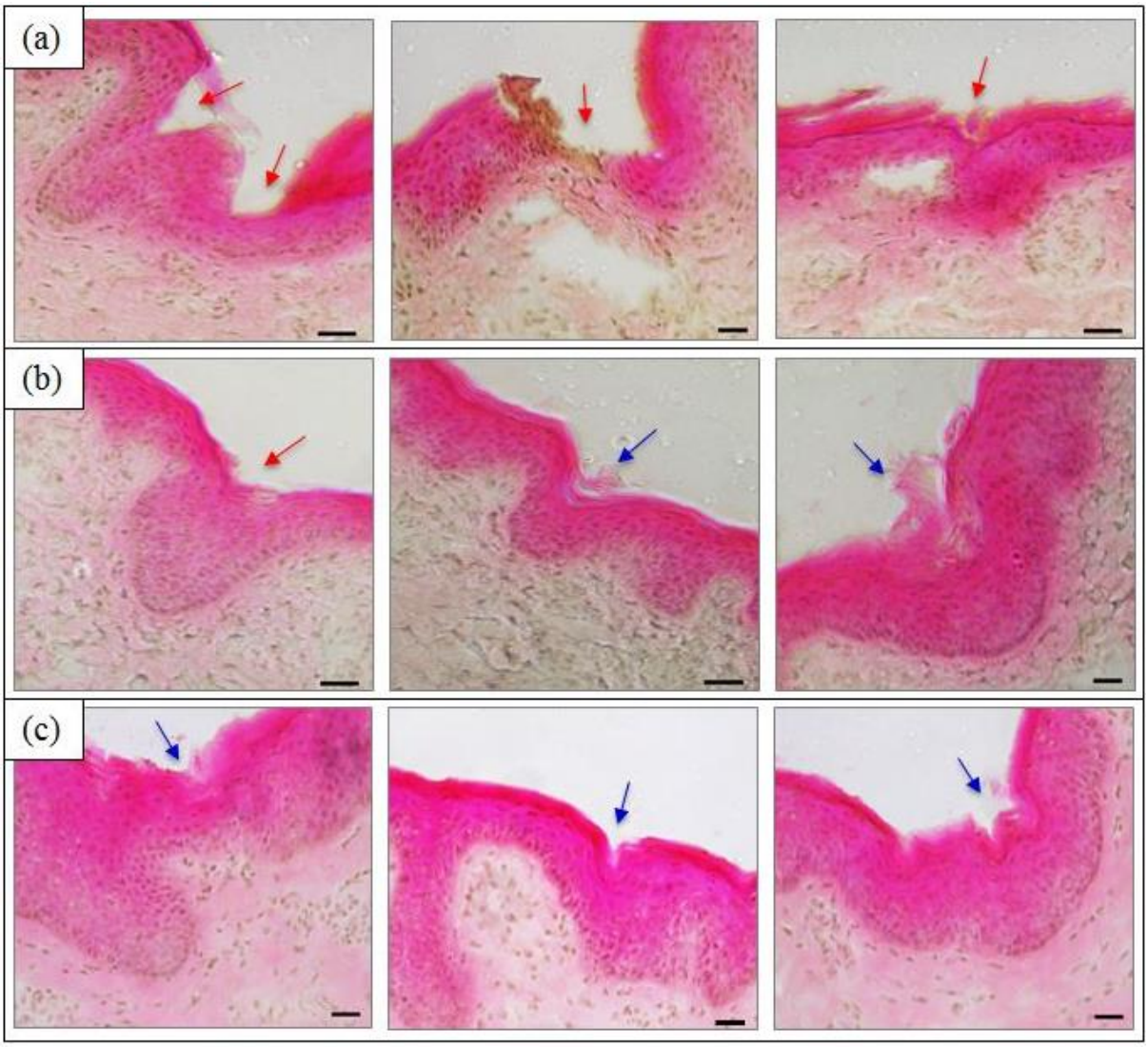

Figure 65 Histology images of skin following microneedle application at a constant velocity (2 ms^{-1}), using Design 1 microneedles under various loads (a) 36 g (b) 17 g (c) 7 g. Blue arrows indicate disruption to the stratum corneum and the red arrows indicate that the breach is within the epidermis. Scale bar represents 100 μm.

A comparison between the methylene blue and histology images are shown in Fig. 66. By comparing the methylene blue stained images in Figs 66a and 66d and the histological cross-sections in Figs 66b–c and 66e–f, a more holistic insight into the interaction between microneedles and skin was obtained. The methylene blue stains confirmed successful perforation of the stratum corneum with a sizeable quantity of microneedles at 2 ms^{-1} using the 36 g drop mass (Fig 66d). The histology images however in Figs 66e–f showed that there was minimal disruption to the stratum corneum. In contrast, there was substantial breach to the epidermal layer at 3 ms^{-1} as shown in Figs 66b–c.

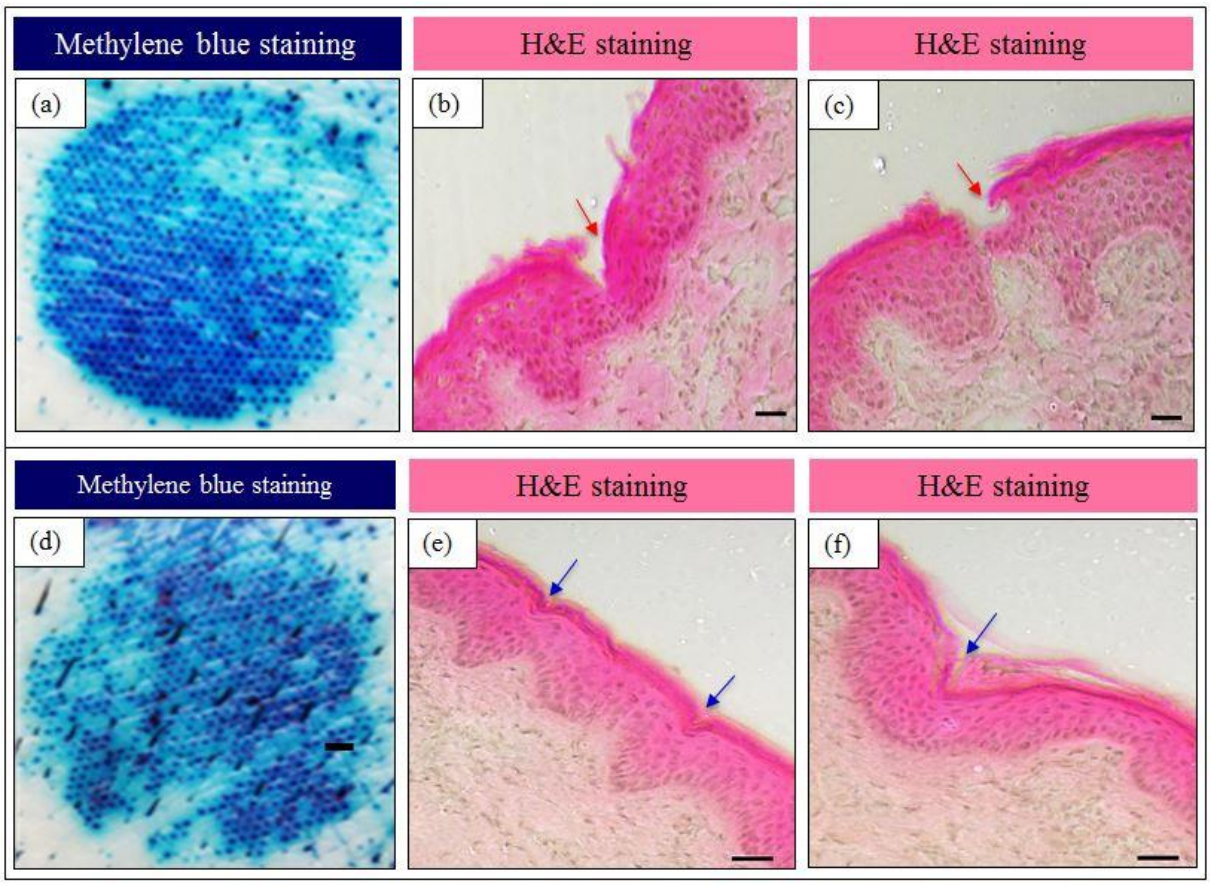

Figure 66 The influence of velocity on perforation quality (methylene blue staining) and perforation depth (H&E staining), with the impact applicator at 3 ms^{-1} (a) methylene blue stained image (b) and (c) example histology images. The influence of velocity on perforation quality (methylene blue staining) and perforation depth (H&E staining), with the impact applicator at 2 ms^{-1} (d) methylene blue stained image (e) and (f) example histology images. Blue arrows indicate disruption to the stratum corneum and the red arrows indicate that the breach is contained within the epidermis. Scale bar represents 100 μm and diameter of Design 1 microneedle disc is 15.8 mm.

4.4.6.2.2 Graphical output

Fig. 67 shows the force and velocity graphs for impact tests on Model 3B at 5 ms^{-1}, using a drop mass load of 36 g with Design 1 microneedles. The insertion force, which was 17.5 N and the insertion velocity, which was 4.96 ms^{-1} were obtained from the force–time plot shown in Fig. 67a. The maximum force reached was 84.4 N. Design 2 microneedles remained in skin for around 2 mins before removal for staining and imaging in order to account for skin's elastic recovery.

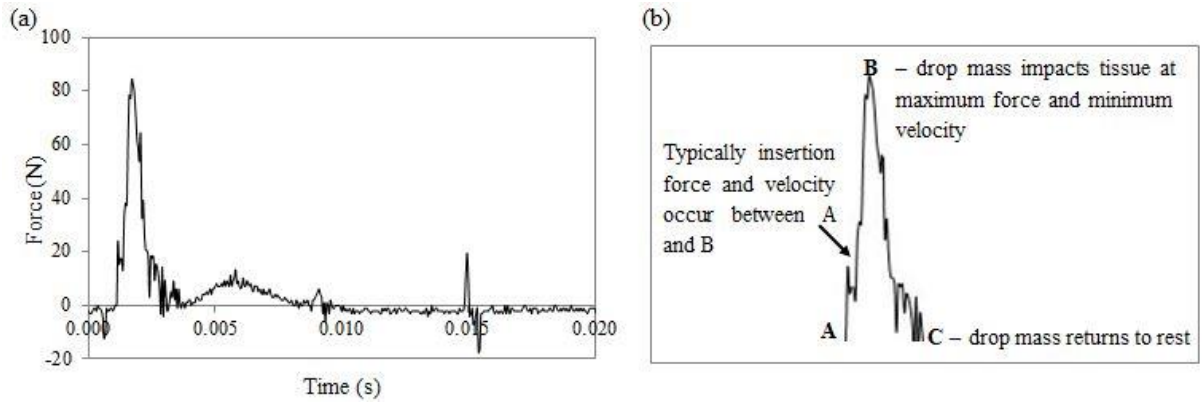

Figure 67 Impact tests of Design 1 microneedles on Model 3B, where (a) force–time plot and (b) the description of points along the force–time curve. The impact occurred at 0.13 ms, where the velocity was approximately 4.96 ms^{-1}, the force was 17.5 N and the maximum force reached was 84.4 N. The data suggest that the initial insertion occurred at 0.13 ms. Hence, at this point the velocity was approximately 4.96 ms^{-1}, the force was 17.5 N and the maximum velocity and force reached were 5 ms^{-1} and 84.4 N respectively.

The maximum force value was 90.67 ± 10.68 N (n = 5) at 5 ms^{-1} velocity, 49.83 ± 15.74 N (n = 5) at 4 ms^{-1} and 42.93 ± 11.08 N (n = 5) at 3 ms^{-1}. The insertion force values were around 27.13 ± 11.05 N at 4.96 ms^{-1} insertion velocity, 13.40 ± 3.70 N at 3.83 ms^{-1}, 9.33 ± 2.76 at 2.96 ms^{-1}. At 1–2 ms^{-1}, it was challenging to determine insertion force values and maximum force values using the impact applicator.

The insertion force for Design 1 microneedles was 9.33 ± 2.76 N (n = 5) as compared to that of Design 2, which was 23.50 ± 4.97 N (n = 5). Therefore, Design 1 microneedles required a lower insertion force for microneedle application on Model 3B as compared to Design 2 microneedles. The maximum force for Design 1 microneedles was 42.93 ± 11.08 N, whilst that of Design 2 was greater at 46.24 ± 8.57 N. The insertion velocity for Design 1 microneedles was 2.96 ms^{-1} as compared to Design 2 microneedles, which was 2.64 ms^{-1}.

4.4.7 Summary of impact applicator studies

Reproducible microneedle penetration of skin was achieved with the improved impact applicator using Design 1 and 2 microneedles. Methylene blue staining confirmed breach of the stratum corneum, however, H&E staining provided details of the extent of the breach through the layers. 100% penetration was not achieved for both skin models, with the size of

perforations larger in abdominal skin as compared to back skin. PE for abdominal skin models decreased with increasing fluid content in the subcutaneous layer. Furthermore, the insertion force was relatively constant for both skin models, however, the maximum force acting on back skin did not vary with fluid content in the subcutaneous layer except for Model 3B.

Design 1 microneedles produced larger perforation depths as compared to Design 2 microneedles, therefore highlighting the role that microneedle geometry plays in skin penetration studies. It was also noted that the size of the deformation is related to the magnitude of the force, thus a small force results in a small deformation and a high force in a large deformation. Majority of the deformation through the layers of skin occurs past the stratum corneum bordering the epidermis, with the frequency of perforations reducing at higher breach areas.

4.5 Clinical Applicator Studies

As previously mentioned clinical applicator tests were conducted so as to compare with experimental results *in vitro* using the impact applicator. Furthermore, as the clinical applicator was used for *in vivo* studies carried out by Renephra, it was necessary to understand the penetration effectiveness and efficiency using both methods of application.

Due to the fact that the position of the loadcell in the impact and clinical setup differed, impact tests using the force transducer and loadcell was conducted in order to establish whether the results from the two experimental setups (Fig. 24 and Fig. 26) were comparable. In order to achieve this, the clinical applicator's loadcell was fastened to the mechanical clamps and placed at the bottom of the drop tower guide; the setup was similar to the impact applicator setup in Fig. 24. The tests (n = 7) were conducted on only Perma-Gel® placed in the clamps. The mean force transducer force output was 24.41 ± 0.76 N. By comparison, the clinical applicator (n = 7), yielded a mean loadcell force output of 29.80 ± 6.90 N. Statistical analysis (Student's t-Test) was conducted in order to determine if there was any statistically significant difference between the force transducer (impact applicator setup) and loadcell (clinical applicator setup) force outputs. The outcome of the t-Tests produced $p = 0.063$ for the tests conducted on Perma-Gel®. Hence, there was no statistically significant difference between both data sets.

4.5.1 Penetration efficiency

Visual examination of abdominal skin models in Fig. 68 shows that successful perforation of the stratum corneum occurred. Ideally, an even spread of perforations across the circular impression created by the microneedles on the stratum corneum is expected. The skin model setup, however, resulted in a raised profile of the skin (see Fig. 27), therefore, the entire disc of Design 2 microneedles was not flush against skin before the clinical applicator was

utilised. This setup resulted in some instances, in partial perforation on the stratum corneum as shown in Figs 68b and 68d.

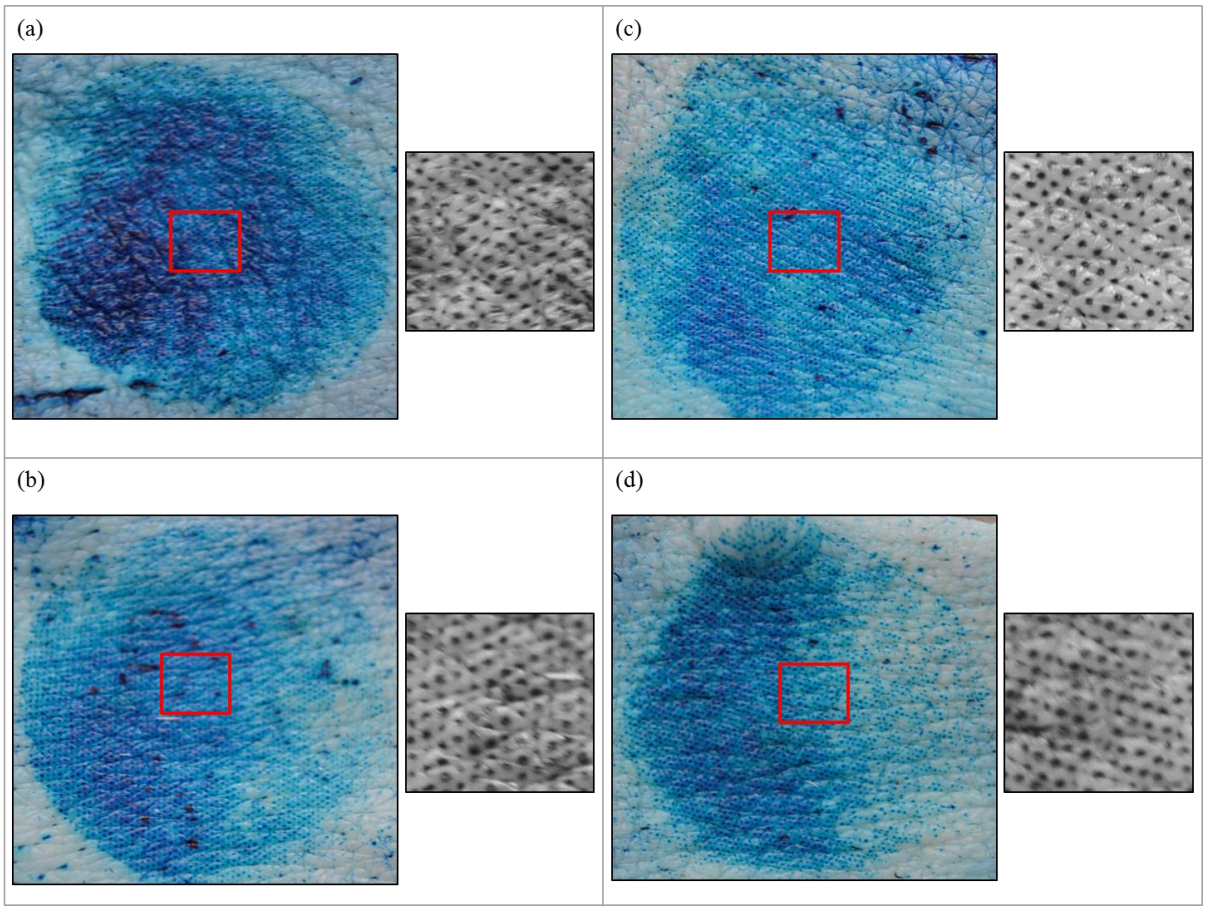

Figure 68 Inspection technique of clinical applicator tests on Models 1A–4A for penetration efficiency with methylene blue staining where the whole disc provides visual confirmation of penetration and the cropped image, which is the selection highlighted in red is 5 × 5 mm in size and was used for calculating penetration efficiency for (a) 67%, (b) 80%, (c) 88% and (d) 96% of water content in the gelatine gels. The diameter of Design 2 microneedle disc is 30.1 mm.

Fig. 69 also confirms the successful disruption to the stratum corneum. By comparing Figs 68 and 69, it was observed that the intensity of the methylene blue dye appeared to be greater in back skin models (Models 1B–4B) as compared to abdominal skin models (Models 1A–4A). As already mentioned, the variation in perforation density in different regions of the same skin as shown in Figs 69b, 69c and 69d is due to the skin setup. The central region was still cropped for PE analysis as majority of the perforations covered at least two-thirds of skin for abdominal tissue. Although this was not the case with back tissue, however for consistency and comparison purposes, the reduced number of perforations on back skin was an important

result, as it may have been due to the clinical applicator performance or a combination of the clinical applicator performance on the thicker back skin.

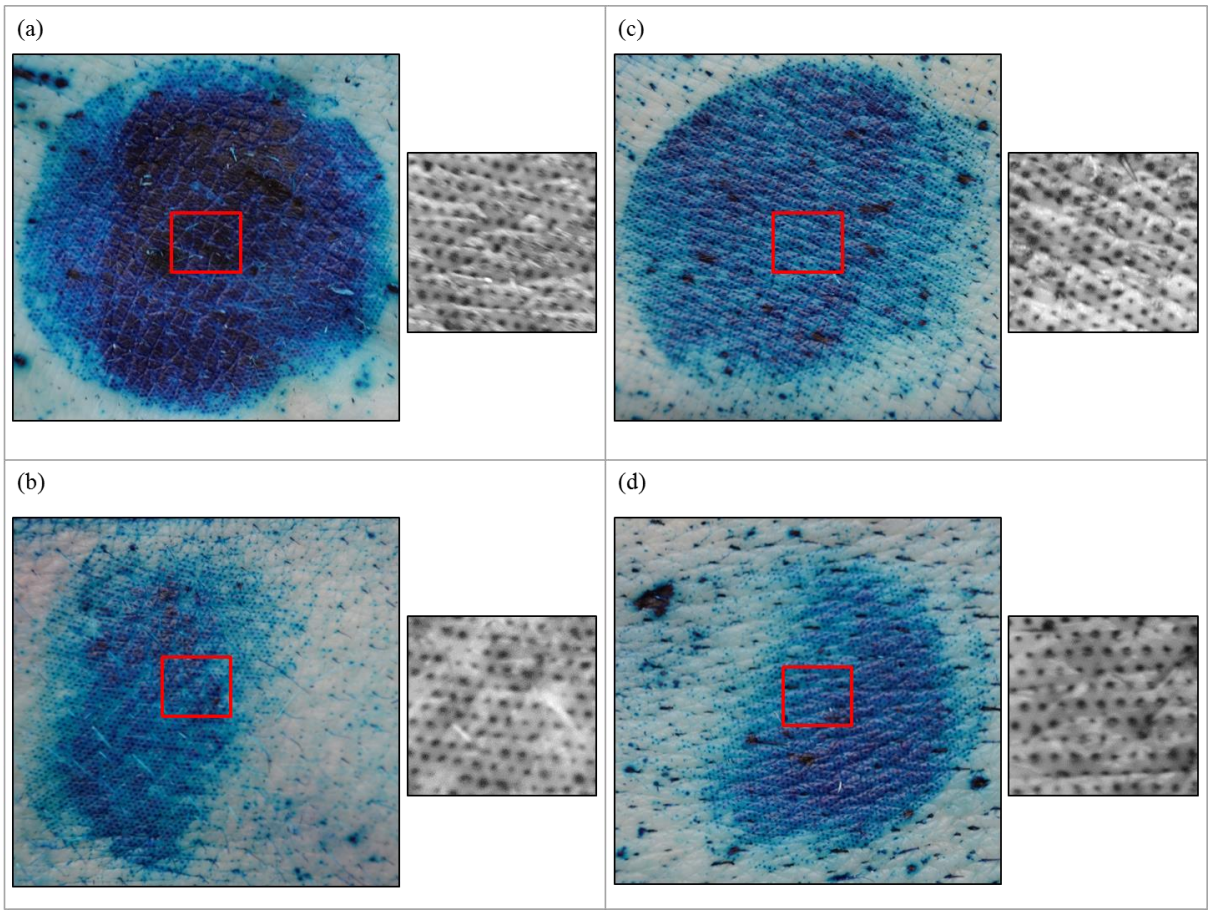

Figure 69 Inspection technique of clinical applicator tests on Models 1B–4B for penetration efficiency with methylene blue staining where the whole disc provides visual confirmation of penetration and the cropped image, which is the selection highlighted in red is 5 × 5 mm in size and was used for calculating penetration efficiency for (a) 67%, (b) 80%, (c) 88% and (d) 96% of water content in the gelatine gels. The diameter of Design 2 microneedle disc is 30.1 mm.

In order to validate the visual observations of perforation density and assess PE, a cropped central location of the perforations on abdominal and back skin models were analysed using imaging techniques. PE results are presented in Fig. 70 and show that it decreased with increasing water content for abdominal (Models 1A–4A) and back skin (Models 1B–4B). Again as expected, 100 % penetration efficiency was not achieved.

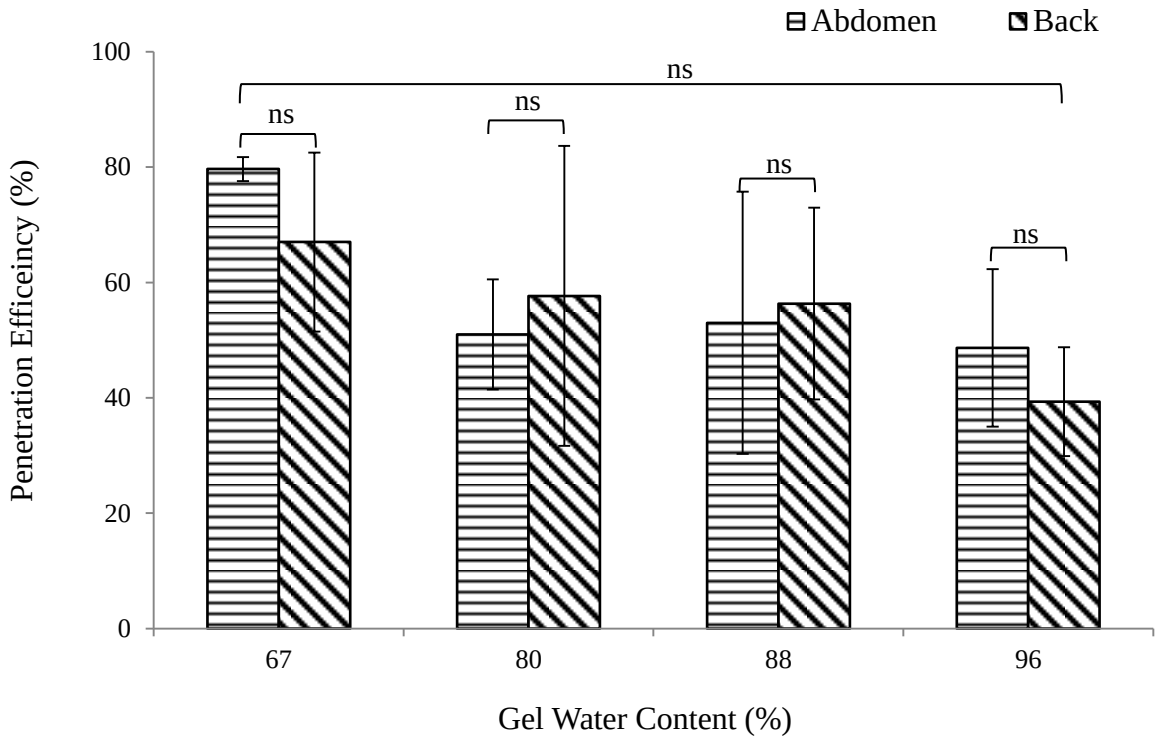

Figure 70 Penetration efficiency determined from the methylene blue images for clinical applicator tests on 3 samples each of Models 1A–4B. Error bars depict SD.

4.5.2 The effects of differences in skin properties

The H&E stained images are presented in Fig. 71. There was significant deformation within all of the abdominal skin models (Models 1A–4A), with the extent of the perforations propagating deep into the dermis. For back skin models (Models 1B–4B) however, the deformation was predominantly within the epidermis and just interfacing with the dermis. The application of Design 2 microneedles using the clinical applicator on abdominal skin models caused greater deformation as compared to back skin models.

There was no obvious relationship between PE from methylene blue images and perforation depth from H&E stained images. The H&E stained images indicated that the microneedles interacted differently through the layers of abdominal and back skin models. The perforation profile of the back skin model was narrower and barely interfaced with the dermal layer, whilst the perforation profile of the abdominal skin was wider and extended into the dermis. This contrasts the PE determined from the methylene blue stained images, which showed that PE decreased with increasing gel water content for both skin models.

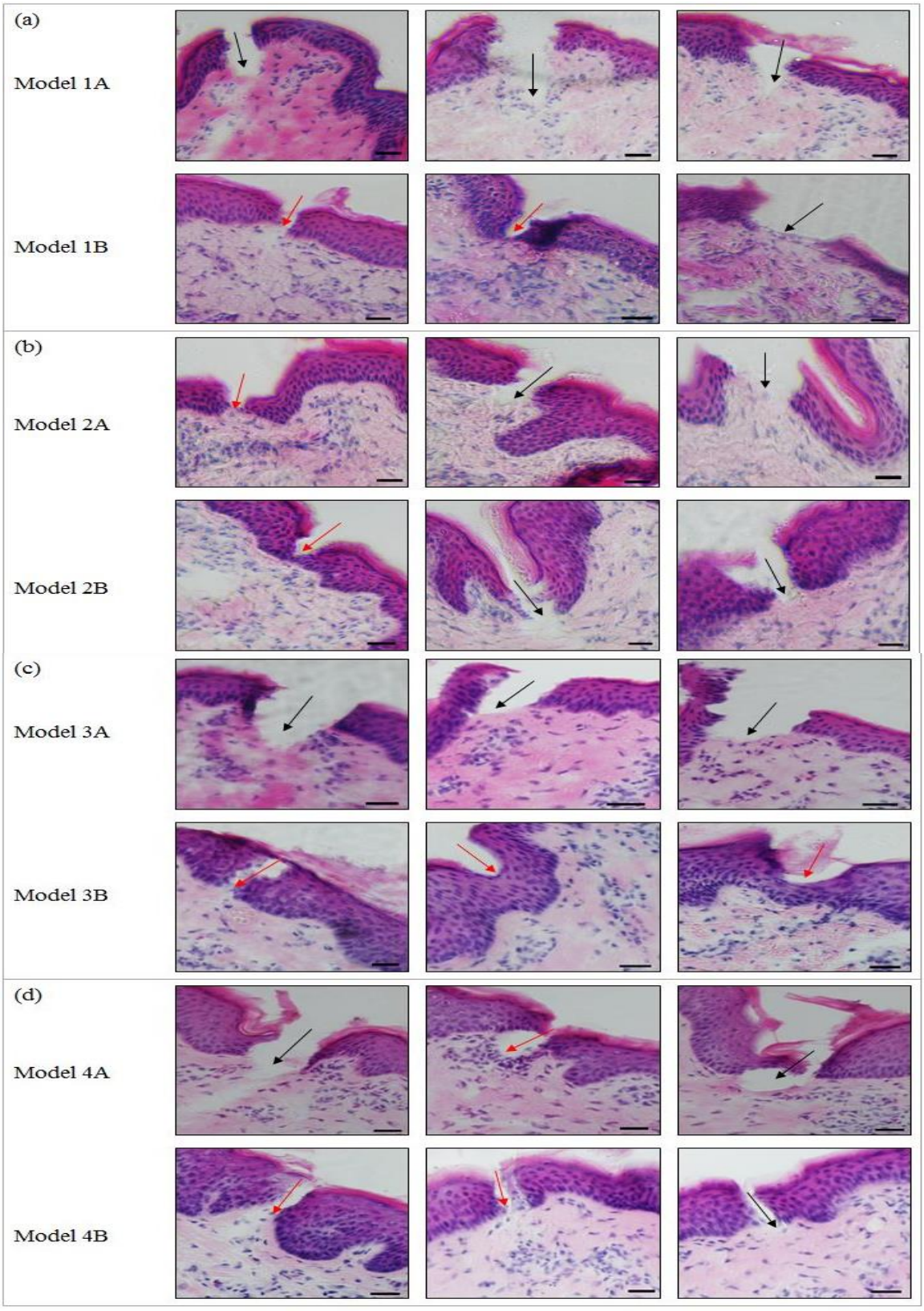

Figure 71 Comparison of perforation depths (H&E staining) using the clinical applicator for abdominal and back skin models with respect to altering the water content in gelatine gels. Red arrows indicate that the breach is contained within the epidermis and the black arrows indicate that the breach has extended into the dermis. Scale bar represents 100 μm and diameter of Design 2 microneedle disc is 30.1 mm.

4.5.3 The role of the subcutaneous mimic property on microneedle performance

The methylene blue stained images in Fig. 68 showed that by varying the gel water content in the subcutaneous mimic, the perforation density appears consistent for Models 2A–4A, the exception being Model 1A, which seemed to be more densely perforated. A similar trend was observed for back skin models (Models 1B and 4B differed). Conversely, the H&E images in Fig. 71a–d showed that with the increase in the gel water content in the subcutaneous mimic, the needles fully opened up the epidermis and the dermis in the abdominal skin model. This trend was not apparent in back skin models, as the deformation appeared narrower and in some instances extended into the dermis (Fig. 71a–c).

In terms of penetration depth for each skin model, which is shown in Fig. 72, there was no apparent trend for varying the gel water content in the subcutaneous mimic. For abdominal skin models presented in Fig. 72a, the mean penetration depth increases with increased gel water content. For the back skin models, the depth of penetration did not follow this trend and showed an increase in penetration depth from Model 1B to 2B, followed by a decline from Model 2B to 3B and then an increase from Model 3B to 4B.

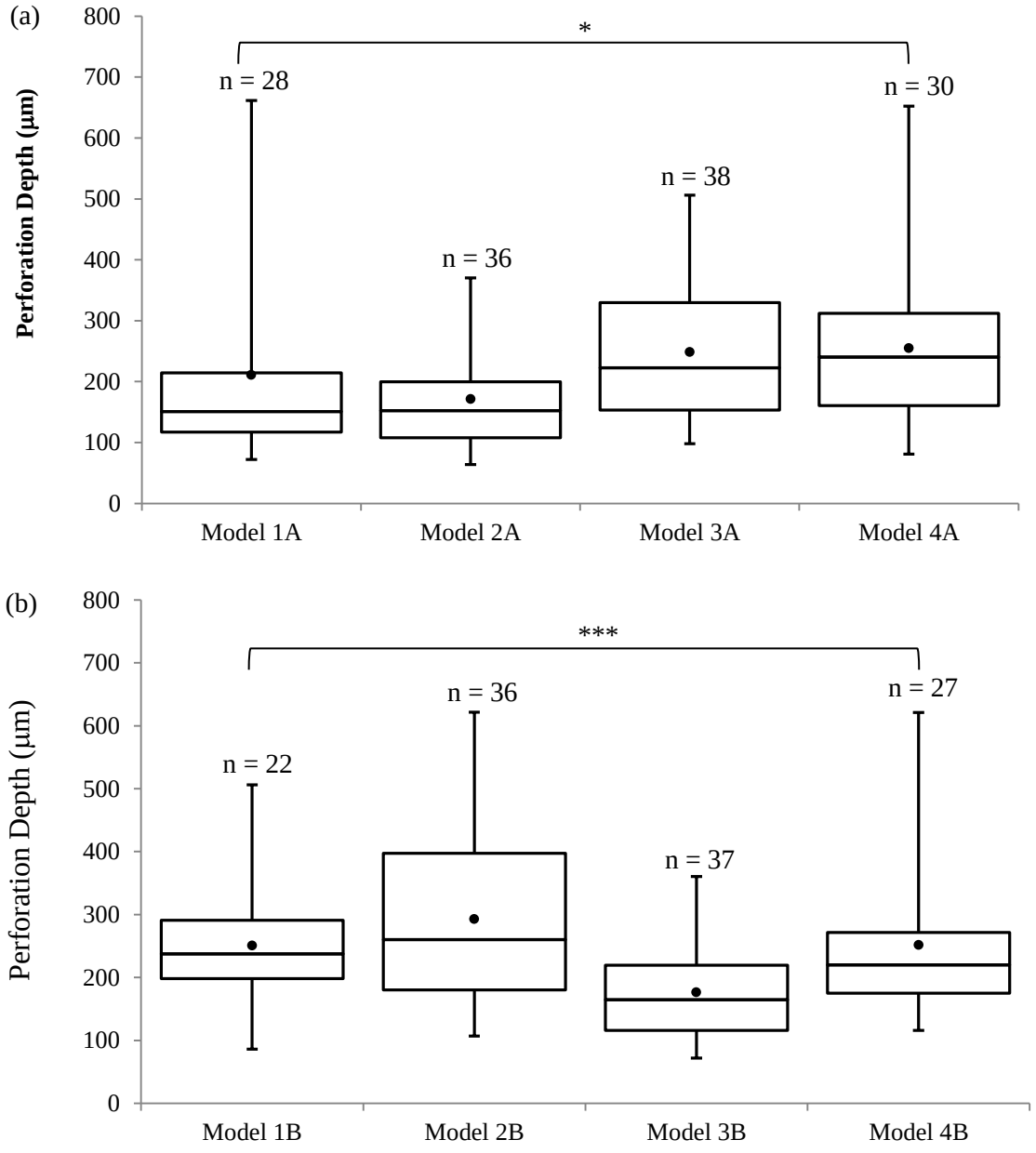

Figure 72 Perforation depth data for clinical applicator tests, where (a) abdominal skin models and (b) back skin models, with the number of images (n) in each group listed above each box and whisker plot.

For the results of the breach area shown in Fig. 73, there was no significant difference for abdominal skin models 1A–4A (Fig. 73a). As shown in 73b, the mean breach area for Models 1B–4B was lower at each gel concentration relative to the abdominal skin models. For PE comparison with the mean breach area, the trend differed for abdominal skin models but was similar to the perforation depth results for back skin models. Therefore, for back skin model,

there is a relationship between perforation depth and the size of the deformation within the layers (Figs 72b & 73b).

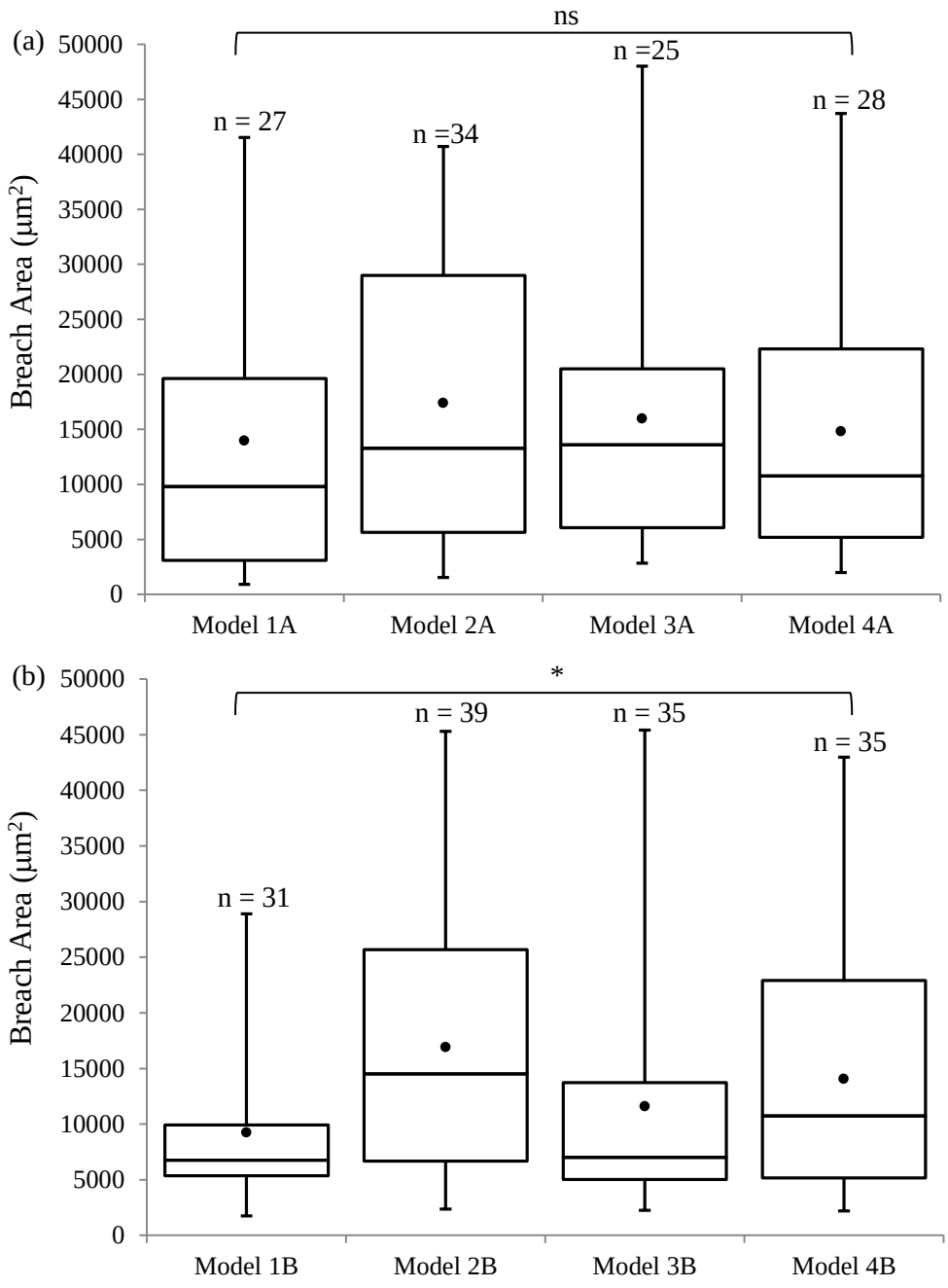

Figure 73 Breach area data for clinical applicator tests, where (a) abdominal skin models and (b) back skin models, with the number of images (n) in each group listed above each box and whisker plot.

As shown in Fig. 74, the frequency of perforations reduced as the breach area increased, which suggests that not every microneedle is deeply embedded in the skin, indicating that majority of the microneedles interaction with skin occurs at the stratum corneum layer.

There was a higher incidence of perforations in the abdominal skin models as compared to the back skin models. Model 1A (Fig. 74a) & 1B (Fig. 74b) had the highest frequencies for breach area, where the gel water content in the subcutaneous mimic is for normal skin. Again, perforations occurred in each breach area category for the abdominal skin models, whilst there was no breach area observed in some categories for the back skin model. There was no obvious correlation between perforation areas and variation of the gel water content in the subcutaneous mimic. As expected, there were very few perforations at the larger sizes.

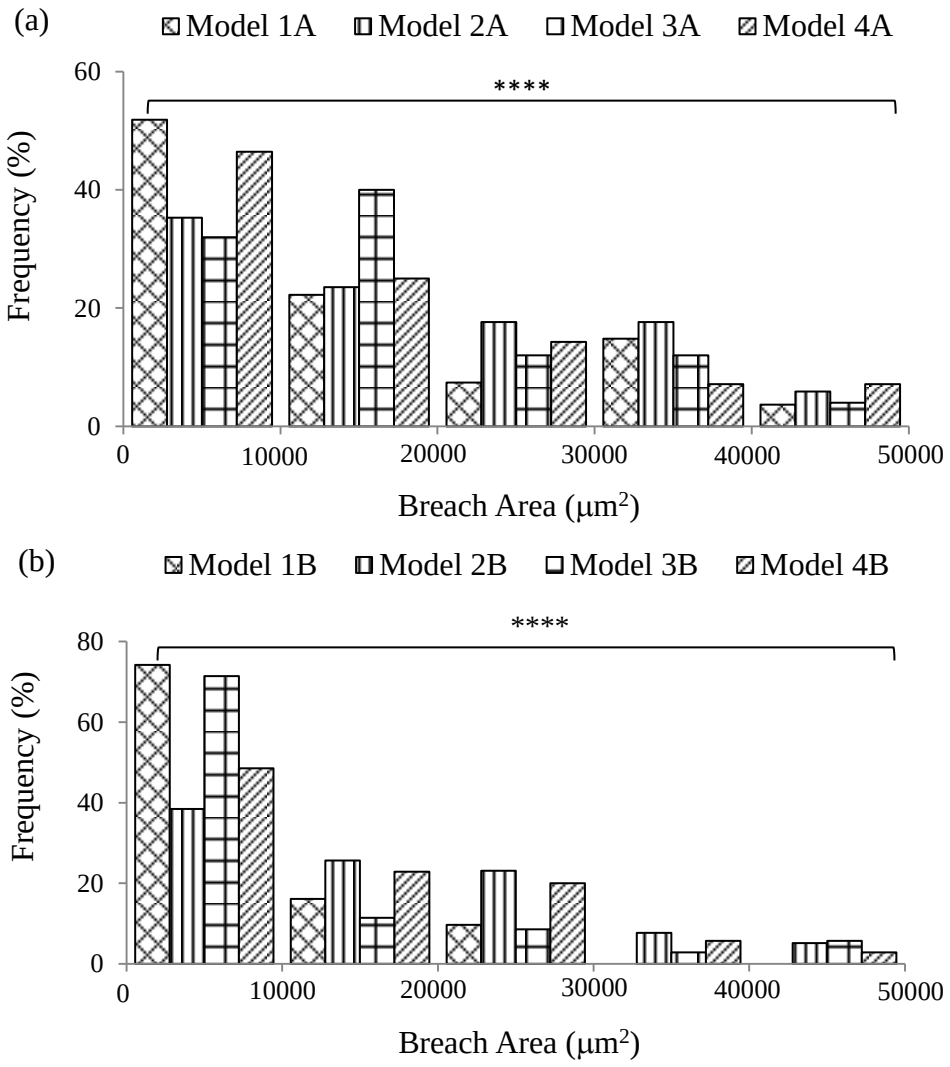

Figure 74 Frequency distribution of the breach area for clinical applicator tests on (a) abdominal skin models and (b) back skin models.

4.5.4 Clinical applicator force

The force results obtained from clinical applicator studies on skin Models 1A–4B are detailed in this section.

An example force–time plot is shown in Fig. 75a. The insertion force was 61.8 N and the maximum force achieved was 80.8 N. In order to account for elastic recovery of skin, the microneedles remained embedded in skin for approximately 2 mins before removal and the skin prepared for staining and imaging.

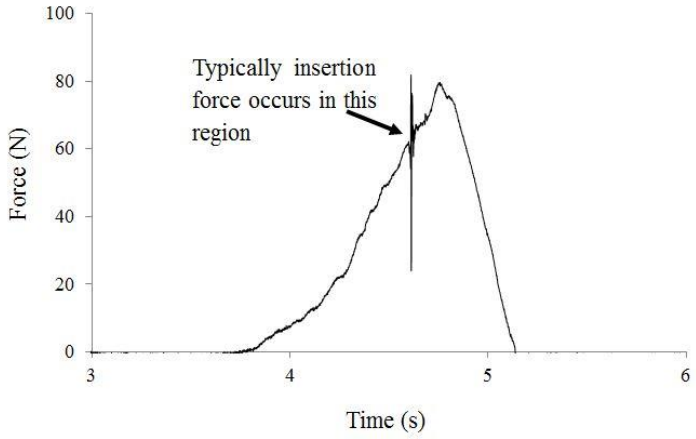

Figure 75 The force–time plot for clinical applicator tests of Design 2 microneedles on Model 1A. The impact occurred at 4.62 s, where the force was 61.8 N and the maximum force reached was 80.8 N. The data suggests that the initial insertion occurred at 4.62 s. Hence, at this point the force was 61.8 N and the maximum force reached 80.8 N.

Fig. 76a details the insertion force for the abdominal and back skin models. The trend shows that the insertion force increases at higher gel water content in the subcutaneous mimic of the skin models for all skin models. The insertion force for Models 4A and 4B are higher than for all other skin models. The insertion force was low for Model 1A as compared to the other skin models considering that this model contains the lowest gel water content in its subcutaneous mimic and therefore, has a higher elastic modulus. In addition, the insertion force is influenced by skin site, with the back skin models requiring greater insertion force as compared to the abdominal skin models, with the exception being Models 4A and 4B, where the insertion force values are in close agreement. Fig. 76b shows the variation of the

maximum force across the different abdominal skin models and as can be seen is an almost constant value with increasing water content of the subcutaneous mimic, except for Model 4A, which is greater. A similar trend was observed with back skin models. There was no relationship between gel water content and elastic modulus and a trend could not be determined, as error bars for the maximum force were high (Fig. 76c). A similar trend was also observed with back skin models.

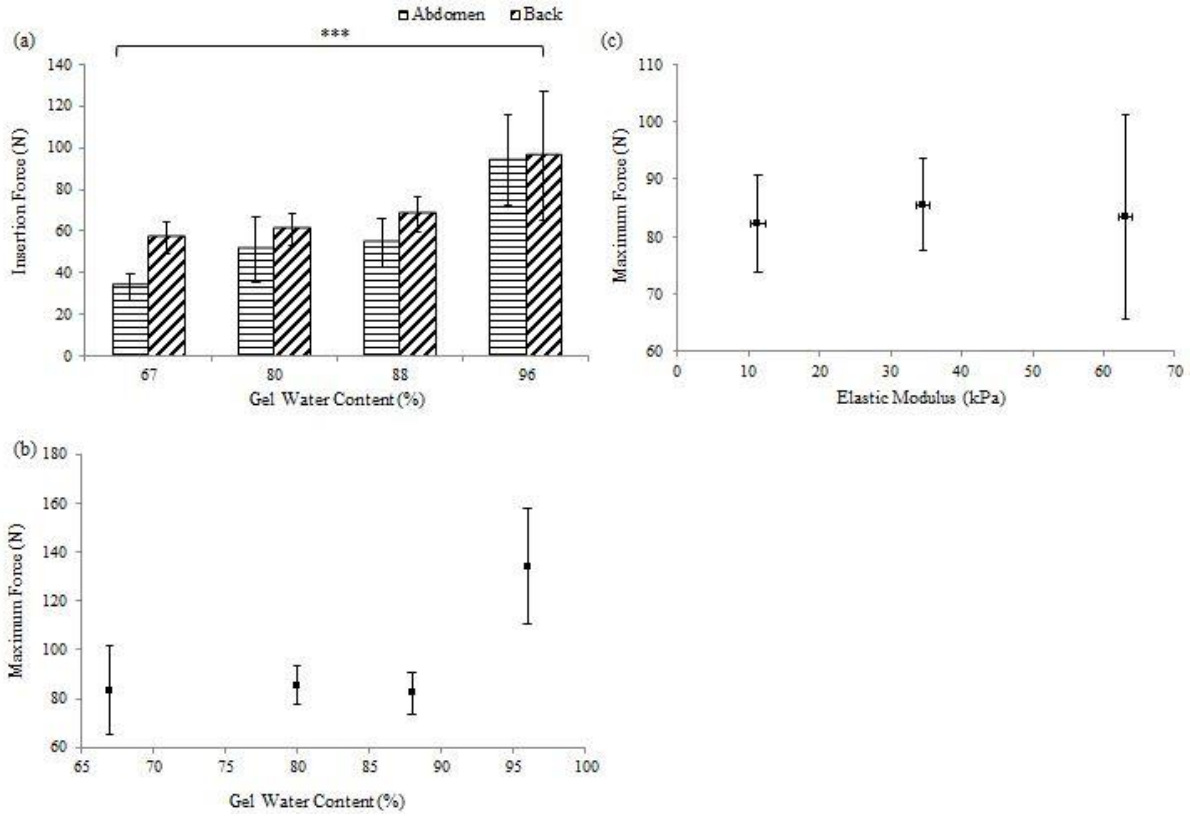

Figure 76 Force data for clinical applicator tests, where n = 4 for each skin model (a) insertion force data for the abdominal and back skin models, (b) maximum force–gel water content for Models 1A–4A and (c) maximum force for Models 1A–4A vs elastic modulus of the gelatine gels.

4.5.5 The effects of microneedle geometry on skin penetration

This section compares clinical applicator studies for Design 1 (1316 microneedles on the array/356 μm length) with Design 2 (> 6000 microneedles on the array/552 μm length) microneedles on Model 3B.

4.5.5.1 Microneedle penetration on skin Model 3B

Microneedle perforation of skin Model 3B is detailed here using Design 1 and 2 microneedles.

4.5.5.1.1 Comparison between visual examination and perforation depth

The results of clinical applicator tests using Design 1 and 2 microneedles on Model 3B are presented in Fig. 77. Methylene blue staining in Figs 77a and 77b showed the disruptions to the stratum corneum, whilst histology showed the extent of the deformation through the layers. In Fig. 77a, image analysis using ImageJ to assess PE showed that 56% of Design 2 microneedles perforated the stratum corneum of Model 3B as compared to 64% of Design 1 microneedles in Fig. 77b. The H&E images showed greater deformation within the layers for Design 1 microneedles as compared to Design 2 microneedles.

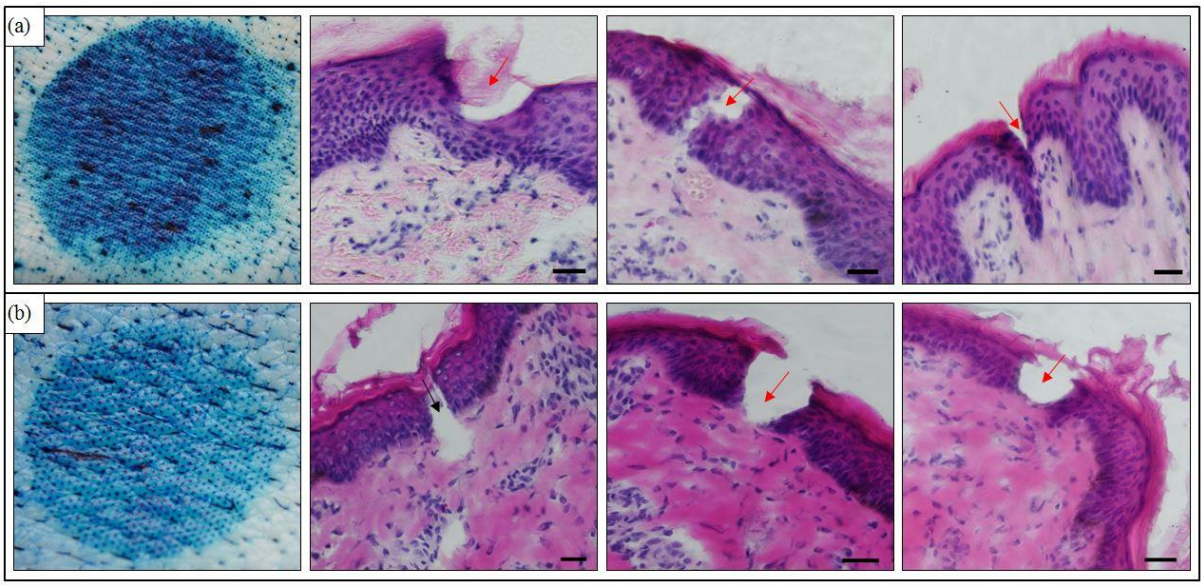

Figure 77 Clinical applicator studies for the comparison of Design 1 and 2 microneedles on perforation confirmation (methylene blue staining) and perforation depth (H&E staining), on Model 3B. (a) Design 2 and (b) Design 1. The diameter of Design 1 microneedle disc is 15.8 mm. The diameter of Design 2 microneedle disc is 30.1 mm, Red arrows indicate that the breach is contained within the epidermis and the black arrows indicate that the breach has extended into the dermis. Scale bar represents 100 μm.

The penetration depth in Model 3B for Design 1 and 2 microneedles is shown in Fig. 78. The greatest perforation depth was 360 μm for Design 2 microneedles as compared to 311 μm for Design 1 microneedles. In addition, the mean penetration depth was similar for both types of microneedles.

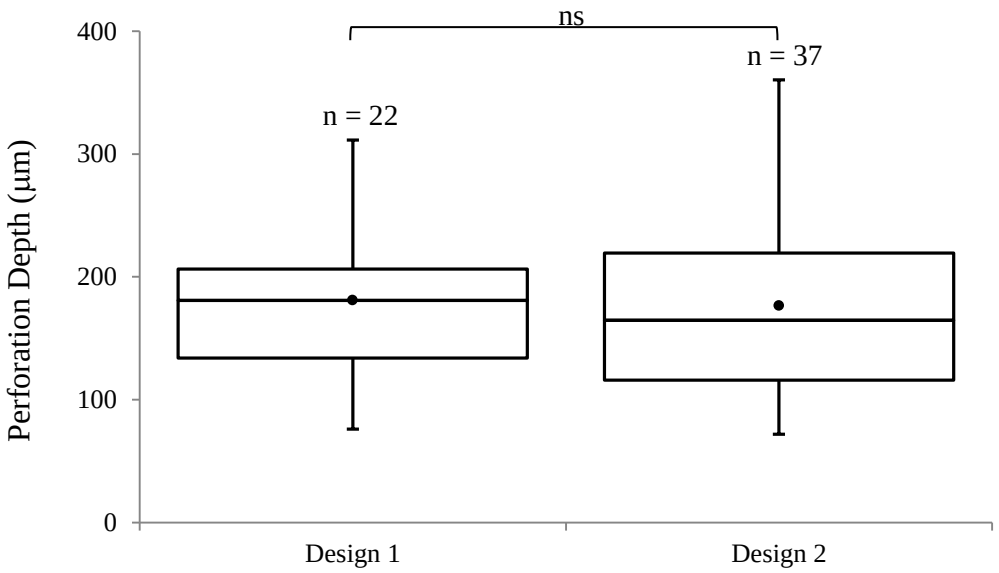

Figure 78 Perforation depth data for clinical applicator tests comparing results of Design 1 and 2 microneedles on Model 3B, with the number of images (n) in each group listed above each box and whisker plot.

4.5.5.1.2 Histological examination of breach area

The general trend for the frequency distribution of deformation within Model 3B presented in Fig. 79 showed that Design 2 microneedles produced the highest frequency of deformations at 0 < breach area < 10 000 μm^2. At categories > 10 000 μm^2 however Design 1 microneedles created greater breach areas.

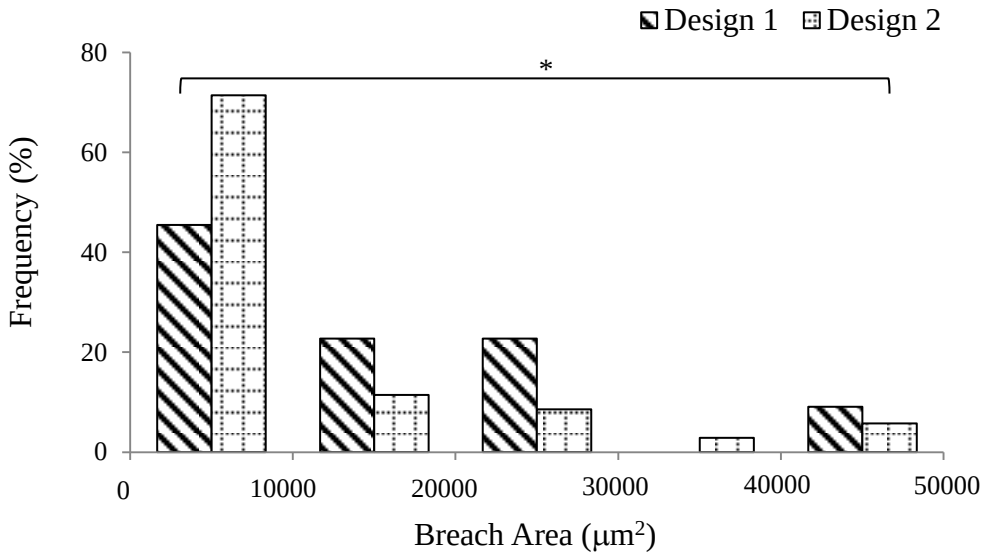

Figure 79 Frequency distribution for clinical applicator studies using Design 1 and 2 microneedles on Model 3B.

4.5.5.2 Clinical applicator force on skin Model 3B

The insertion force for Design 1 microneedles was 66.70 ± 3.11 N (n = 4) as compared to that of Design 2, which was 68.00 ± 8.77 N (n = 4). Therefore, Design 1 microneedles required a similar magnitude of insertion force for microneedle application on skin Model 3B as compared to Design 2 microneedles. The maximum force for Design 1 microneedles was 91.00 ± 2.83 N, whilst that of Design 2 was lower at 77.30 ± 15.55 N.

4.5.6 Summary of clinical applicator studies

The results of the clinical applicator studies showed that reproducible microneedle penetration of skin occurred for all the skin models using Design 1 and 2 microneedles. Visual examination of methylene blue images for the clinical applicator showed that the

intensity of the methylene blue dye appeared greater on abdominal skin models as compared to back skin models. PE for the clinical applicator was between 39–80%, indicating that not all the microneedles perforated skin.

The insertion force increased with increasing water content in the gelatine gels for both abdominal and back skin models, with the insertion force on back skin greater than the insertion force on abdominal skin. This result showed that altering the fluid content in the subcutaneous layer had an effect on the insertion force. The maximum force on the skin models was relatively constant for both abdominal and back skin models, with no particular trend observed.

In addition, the performance of the clinical applicator was affected by microneedle geometry, as it produced poorer perforation results with Design 1 microneedles as compared to Design 2 microneedles, with a higher proportion of the perforations occurring in the region of $\leq 10\ 000\ \mu m^2$ breach area.

4.6 Comparison between Impact and Clinical Applicator Studies

Impact and clinical applicators were used to insert microneedles into abdominal and back skin models. The force and velocity were obtained from the impact applicator, whilst only the force was obtained from the clinical applicator. The impact applicator was developed for *in vitro* tests on neonatal porcine skin, whilst the clinical applicator has been used for *in vivo* tests on patients by Renephra. Therefore, it was necessary to perform *in vitro* tests with the clinical applicator and compare the results to the results of the impact applicator tests. This section compares the effect of the impact and clinical applicators on the microneedle treated skin models.

4.6.1 Penetration efficiency

With respect to PE, it can be seen in Fig. 80 that the impact applicator produces a better result for Design 2 microneedle application to abdominal skin models as compared to the clinical applicator. It also appears that the clinical applicator plateaus around 50% PE for Models 2A–4A. The results also show that for the impact applicator, PE reduces with increased water content in the subcutaneous mimic.

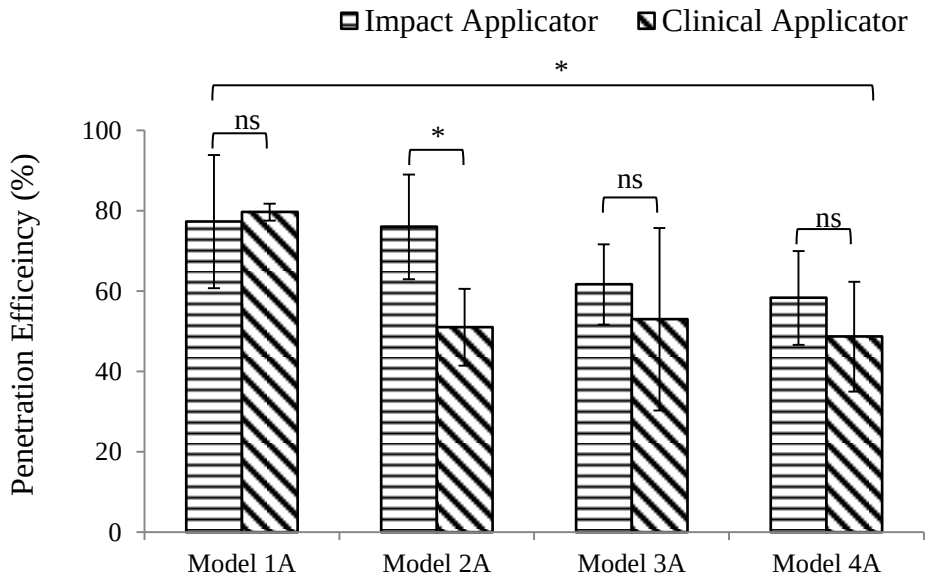

Figure 80 Penetration efficiency as determined from the methylene blue images for impact and clinical applicator tests on abdominal skin models (Model 1A–4A).

The PE data for back skin models is presented in Fig. 81 and showed that for impact applicator tests, an increase in gel water content in the subcutaneous mimic leads to higher PE values, which was not the case for abdominal skin models. In contrast, for the clinical applicator however, an increase in gel water content leads to a decline in PE.

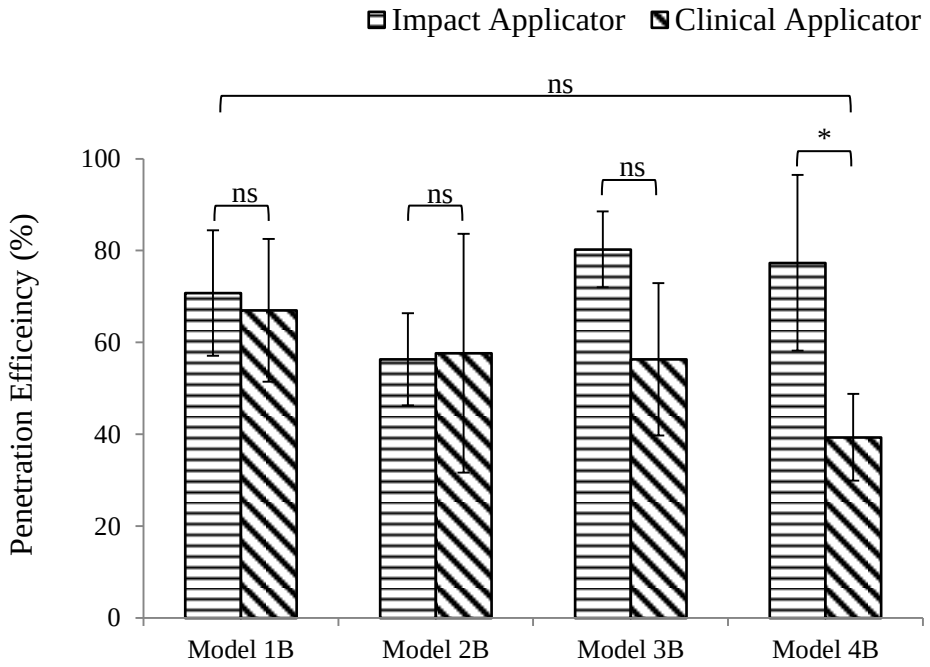

Figure 81 Penetration efficiency determined from the methylene blue images for impact and clinical applicator tests on back skin models (Model 1B–4B).

4.6.2 The effects of differences in skin properties

The images in Fig. 82 present a comparison of the methylene blue and H&E staining for impact and clinical applicator tests on abdominal skin models (Models 1A–4A). Fig. 82a appears to show a greater intensity in the methylene blue dye for the clinical applicator tests as compared to the impact applicator tests. Furthermore, the microneedle perforations travelled beyond the epidermis into the dermis. The H&E images for the impact applicator showed that most of the disruption through the layers was contained within the epidermis, with exception to the last image.

In Fig. 82b–d, the intensity of the methylene blue dye appeared to be greater for the clinical applicator as compared to the impact applicator. For the impact applicator, the H&E images showed that the deformation was contained mainly within the epidermis, barely interfacing with the dermis as the gel water content increased. The deformation within Model 4A in Fig. 82d extended more into the dermis. On the other hand, the H&E images for the clinical applicator showed that the microneedle perforations extended into the dermis.

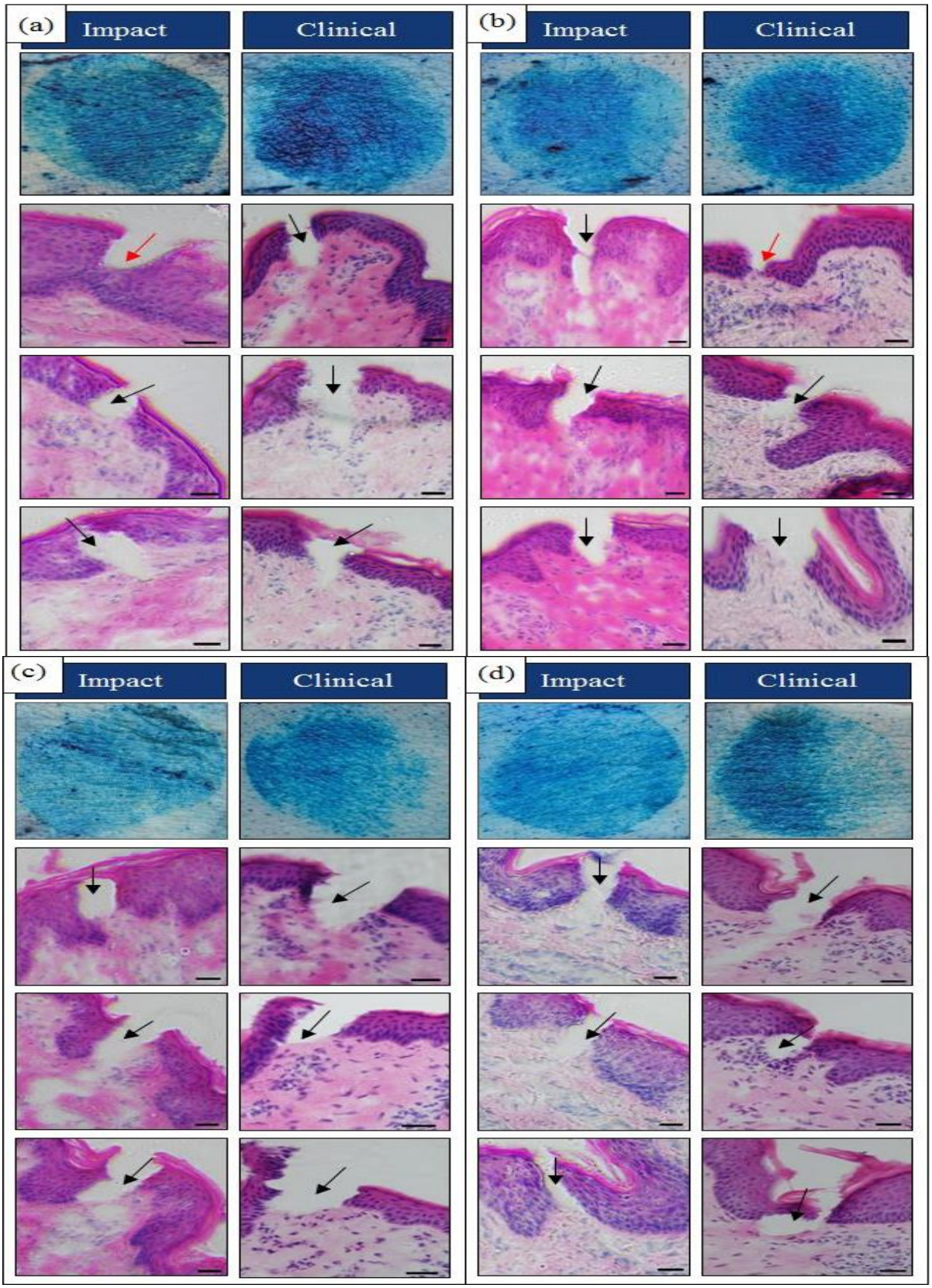

Figure 82 Impact and clinical applicators interaction with abdominal skin models by varying the gel water content to determine that perforation is achieved (methylene blue staining) and perforation depth (H&E staining) using Design 2 microneedles. (a) 67% (b) 80% (c) 88% and (d) 96% gel water content. Red arrows indicate that the breach is contained within the epidermis and the black arrows indicate that the breach has extended into the dermis. Scale bar represents 100 μm and diameter of Design 2 microneedle disc is 30.1 mm.

In Fig. 83a, the intensity of the methylene blue dye appears deeper for the clinical applicator as compared to the impact applicator. The disruptions through the layers for both applicators were predominantly contained within the epidermis, except with the second image for the impact applicator and the third image for the clinical applicator. As shown in Fig. 83b, the methylene blue stained images was comparable for both applicators and so were the deformations caused by microneedle interference through the layers in the H&E images. Fig. 83c showed that the intensity of the blue dye for the clinical applicator was greater than that of the impact applicator. In Fig. 83d, the methylene blue stained images showed similar dye intensity for both applicators. It was also found that for the clinical applicator, not all the microneedles on the array perforated the stratum corneum, although more than 50% perforations were seen on the stratum corneum.

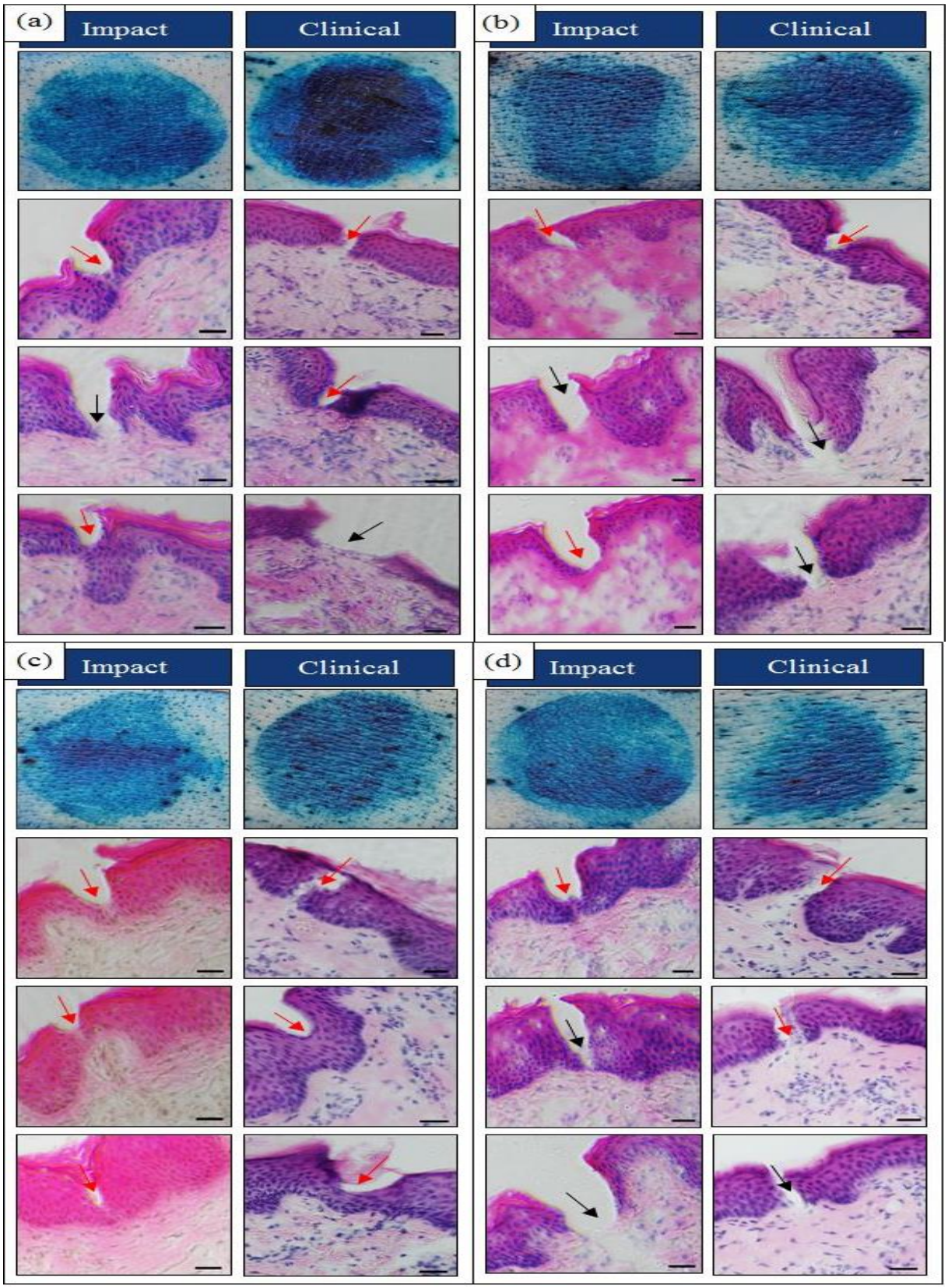

Figure 83 Impact and clinical applicators interaction with back skin models by varying the gel water content to determine that perforation is achieved (methylene blue staining) and perforation depth (H&E staining) using Design 2 microneedles. (a) 67% (b) 80% (c) 88% and (d) 96% gel water content. Red arrows indicate that the breach is contained within the epidermis and the black arrows indicate that the breach has extended into the dermis. Scale bar represents 100 μm and diameter of the microneedle disc is 30.1 mm.

4.6.3 The role of the subcutaneous mimic property on microneedle performance

The impact applicator produced the highest perforation depth in the abdominal skin model (Model 2A), as shown in Fig. 84. Conversely, the smallest perforation depth was produced by the clinical applicator on Model 2A. Generally, the impact applicator produced higher values for mean perforation depths across all abdominal skin models.

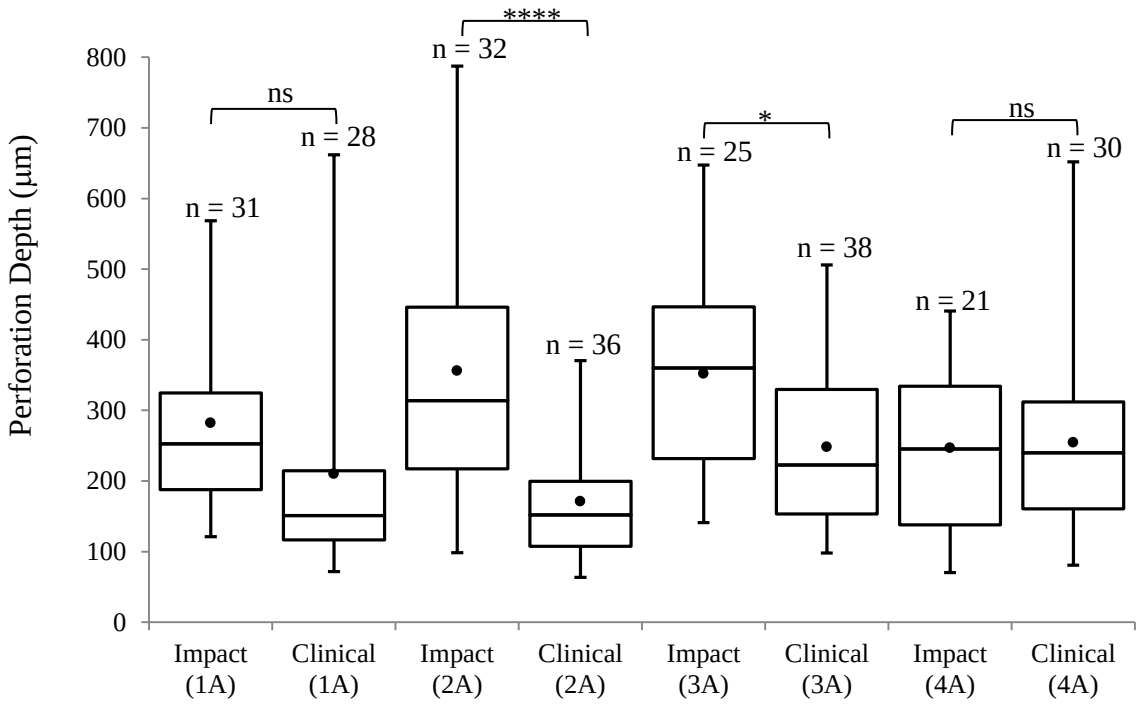

Figure 84 Perforation depth data for impact and clinical applicator tests comparison on abdominal skin models, where 1A–4A refers to Models 1A–4A, with the number of images (n) in each group listed above each box and whisker plot.

In Fig. 85, there was no significant difference between the impact and clinical applicator on back skin Models 1B–4B. Therefore, it is likely that the thicker and higher elastic modulus of the back skin model could be a contributory factor.

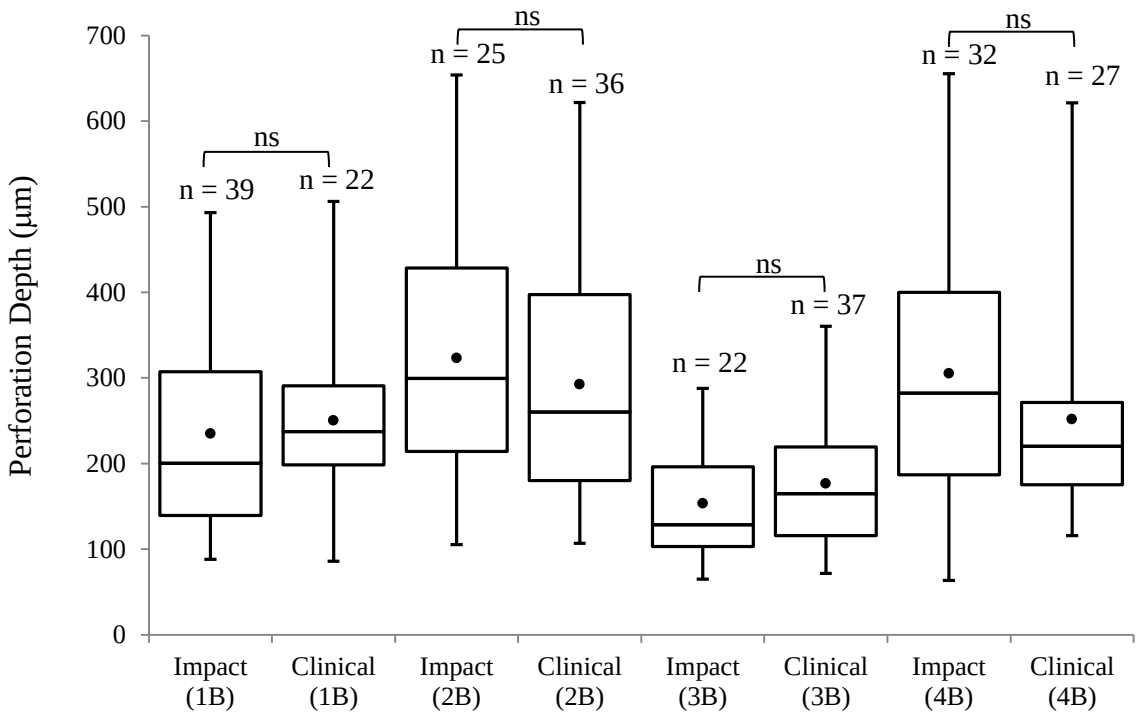

Figure 85 Perforation depth data for impact and clinical applicator tests comparison on back skin models, where 1B–4B refers to Models 1B–4B, with the number of images (n) in each group listed above each box and whisker plot.

In terms of the breach area, the overall trends seen on the skin models showed that there was no significant difference between impact and clinical applicator performance on abdominal skin models as shown in Fig. 86.

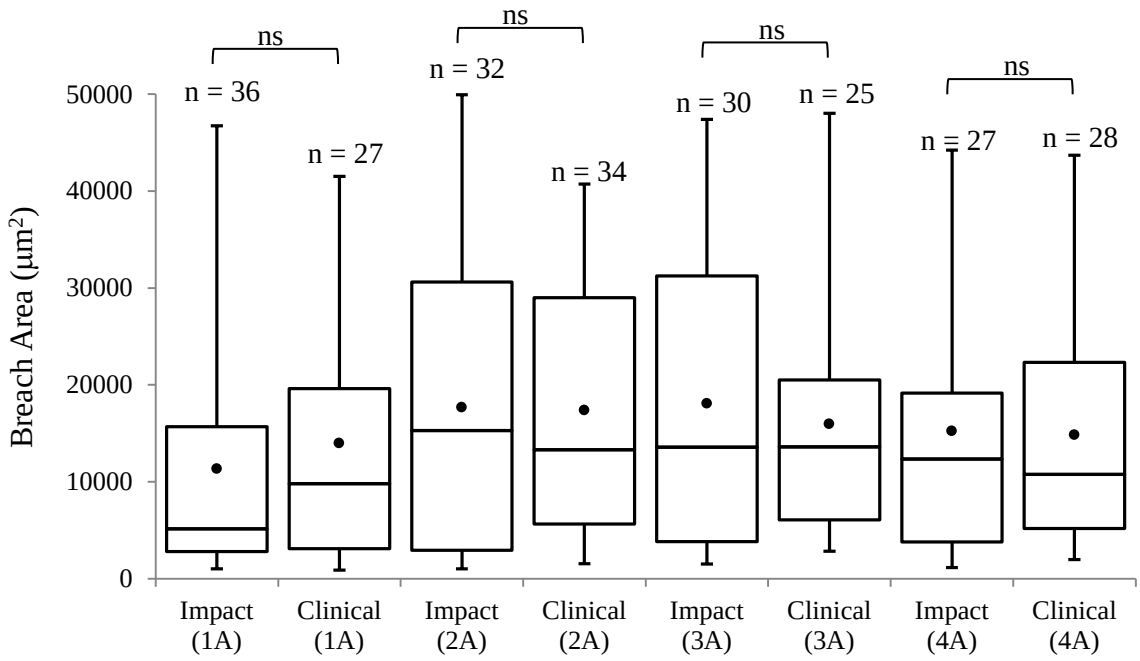

Figure 86 Breach area data comparison between impact and clinical applicator tests on abdominal skin models, with the number of images (n) in each group listed above each box and whisker plot.

There was no significant difference in breach area between the impact and clinical applicator performance on back skin models as shown in Fig. 87.

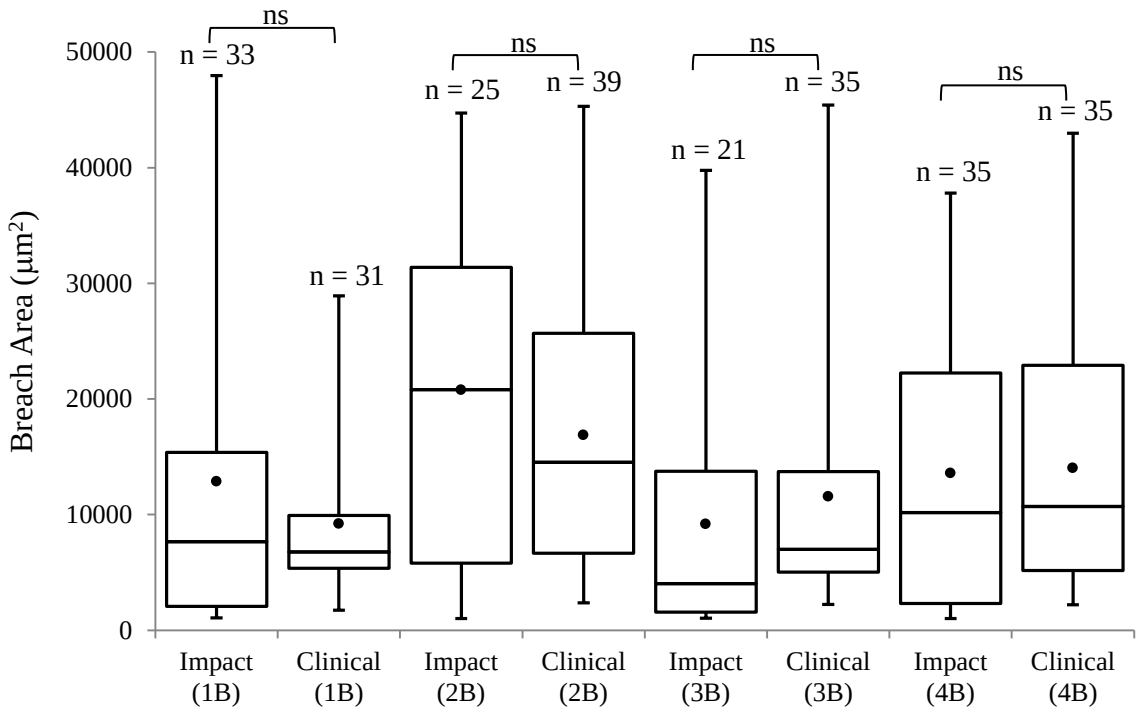

Figure 87 Breach area data comparison between impact and clinical applicator tests on back skin models, with the number of images (n) in each group listed above each box and whisker plot.

Histogram distribution of the breach area is shown in Fig. 88. The impact applicator produced greater breach area frequency as compared to the clinical applicator for the abdominal skin model. For the back skin models however, the clinical applicator performed better than the impact applicator.

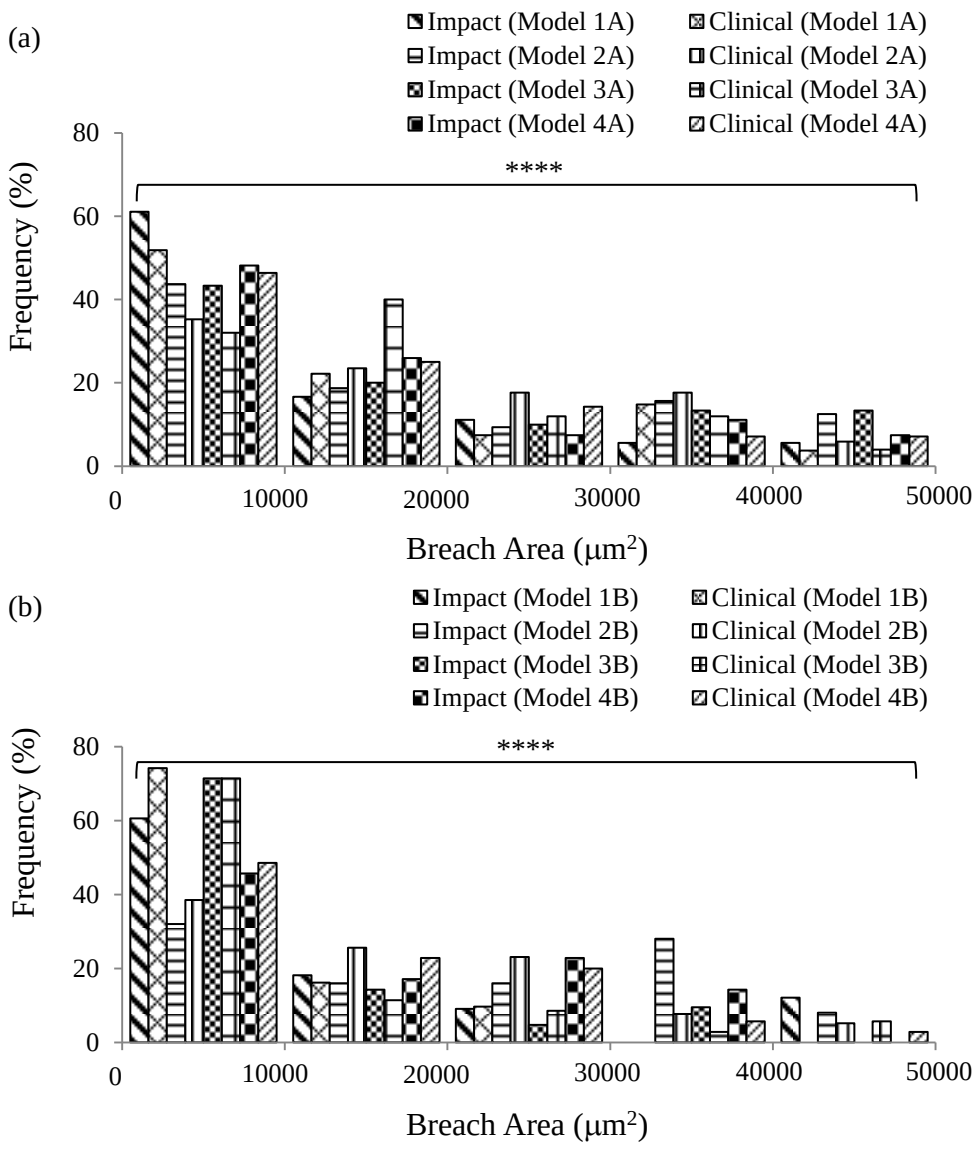

Figure 88 Frequency distribution for impact and clinical applicator studies using Design 2 microneedles on (a) abdominal skin models and (b) back skin models.

4.6.4 The effects of microneedle geometry on skin penetration

This section details the comparison between the impact and clinical applicators on Design 1 and 2 microneedles using skin Model 3B.

4.6.4.1 Comparison between visual examination and perforation depth

The images in Fig. 89 compare perforation success using methylene blue staining and perforation depth using H&E staining for Design 1 and 2 microneedles on Model 3B. For Design 1 microneedles, the clinical applicator caused more disruptions to the stratum as majority of the microneedles perforated this layer as compared to the impact applicator. The H&E images show that the deformation was contained within the epidermis for the impact applicator and that the breach size was narrower. In contrast, for the clinical applicator, the deformation extended deep into the dermal layer in some instances and slightly interfaced with the dermis (Fig. 89a).

For Design 2 microneedles, shown in Fig. 89b, the intensity of the methylene blue dye was greater for the clinical applicator treatment as compared to the impact applicator. The H&E stained images showed that the breach was contained within the epidermis for both applicators.

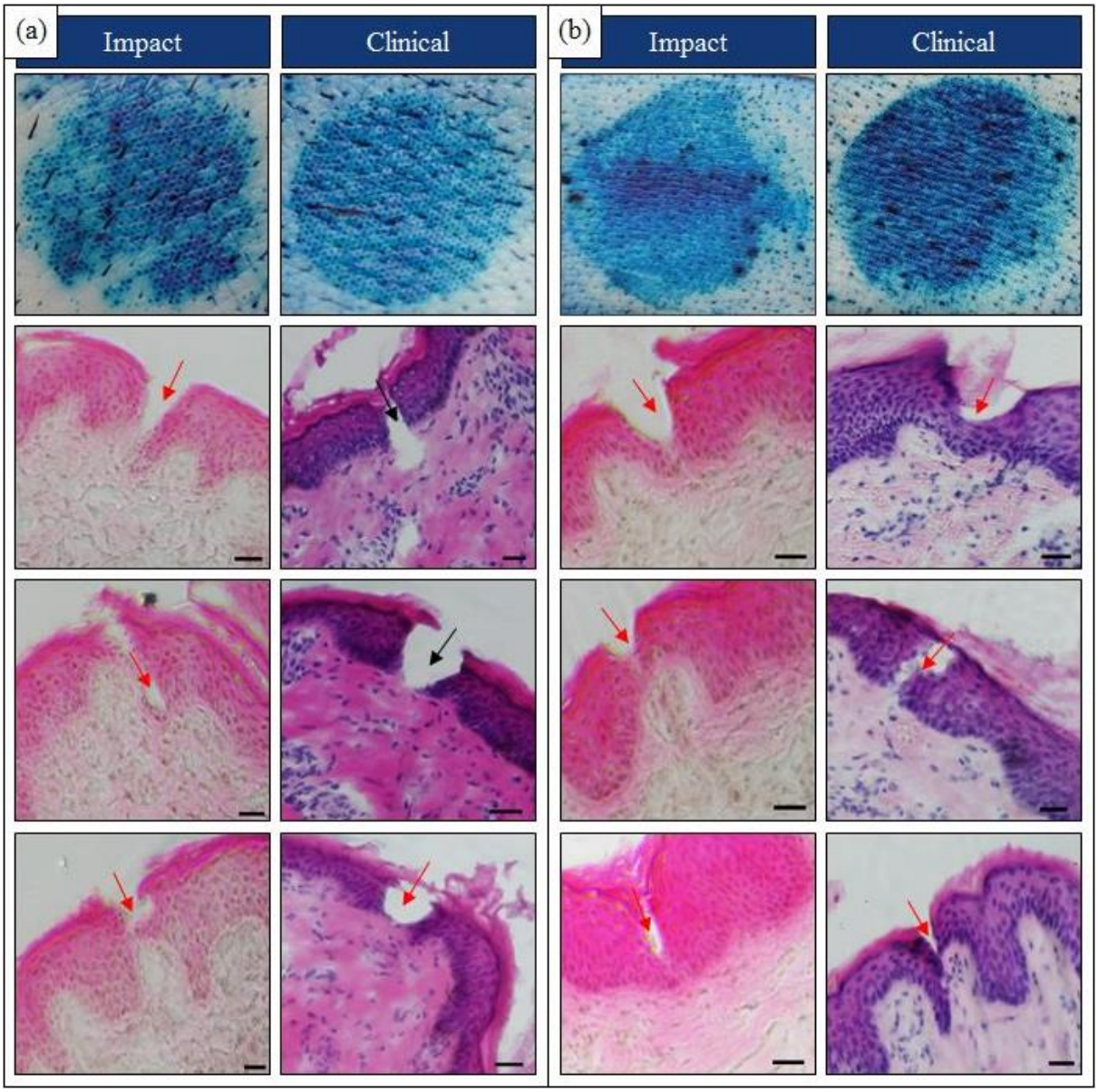

Figure 89 Impact and clinical applicator studies for the comparison of Design 1 and 2 microneedles on perforation confirmation (methylene blue staining) and perforation depth (H&E staining), on Model 3B. (a) Design 1 and (b) Design 2. The diameter of Design 1 microneedle disc is 15.8 mm. The diameter of Design 2 microneedle disc is 30.1 mm. Red arrows indicate that the breach is contained within the epidermis and the black arrows indicate that the breach has extended into the dermis. Scale bar represents 100 μm.

For the clinical applicator, the image analysis using ImageJ showed that 64% of Design 1 microneedles perforated the stratum corneum of Model 3B as compared to the impact applicator treatment, yielding 55% perforations. Furthermore, for the impact applicator, 80% of Design 2 microneedles perforated the stratum corneum as compared to 56% perforation by the clinical applicator treatment.

The perforation depth due to impact and clinical applicator treatment is shown in Fig. 90. The trend shows that the mean perforation depth is relatively close in value for the impact and clinical applicators. The impact applicator appears to produce a consistent performance in skin irrespective of microneedle geometry as compared to the clinical applicator which appeared to be more affected by microneedle geometry. This is because with similar magnitude of force, the clinical applicator produced a smaller perforation depth for Design 1 microneedles as compared to Design 2 microneedles. In contrast, the impact applicator produced a higher perforation depth at a relatively low force for Design 1 microneedles as compared to Design 2 microneedles. The impact applicator insertion force was also lower than the clinical applicator insertion force, which indicates that at a higher insertion force comparable to the clinical applicator insertion force, greater perforation depths could be achieved, since it has already been demonstrated that the magnitude of force is commensurate with the size of the deformation.

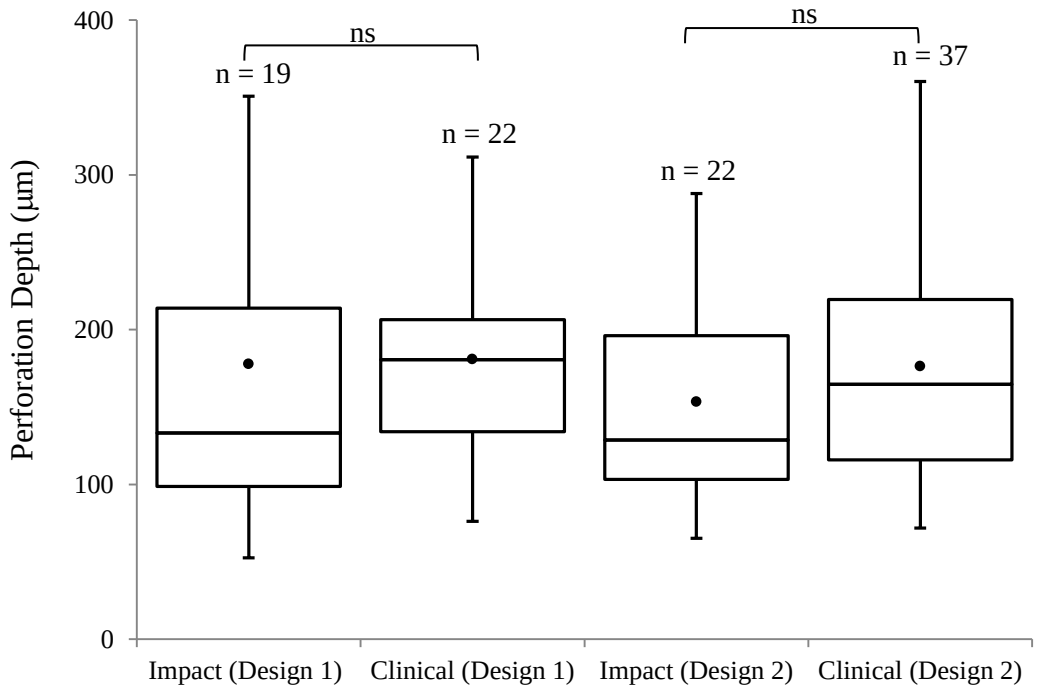

Figure 90 Perforation depth data for impact and clinical applicator tests comparing results of Design 1 and 2 microneedles on Model 3B, with the number of images (n) in each group listed above each box and whisker plot.

4.6.4.2 Histological examination of breach area

For Design 2 microneedles, the clinical applicator produced a greater breach area as compared to the impact applicator at ≤ 10 000 μm^2 as shown in Fig. 91. As expected, there were less perforation areas for larger breach area categories.

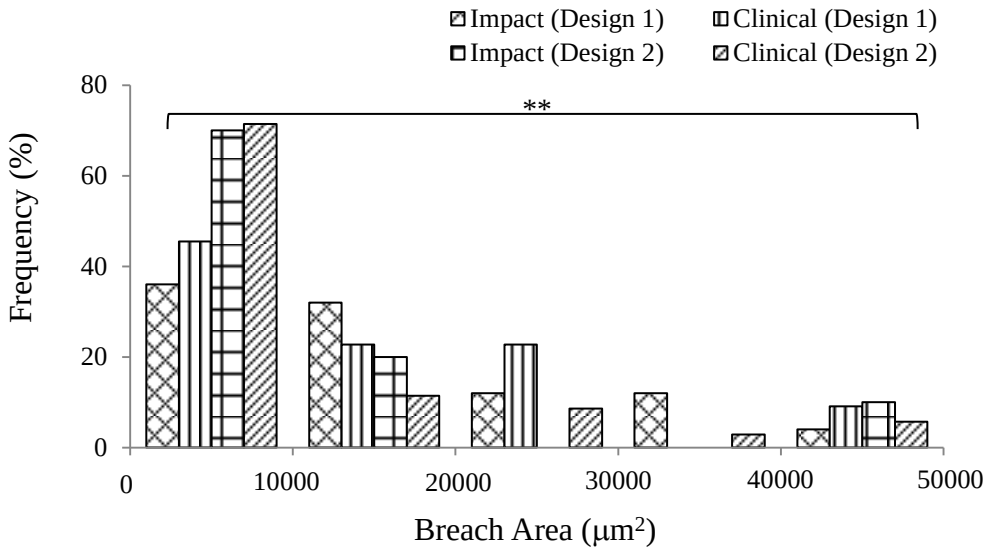

Figure 91 Frequency distribution for impact and clinical applicator studies using Design 2 microneedles.

4.6.5 Impact and clinical applicator force

For the impact applicator, the insertion force for Design 1 microneedles was 9.33 ± 2.76 N (n = 5) as compared to that of the clinical applicator, which was 66.70 ± 3.11 N (n = 4). For Design 2 microneedles, the insertion force was 23.50 ± 4.97 N for the impact applicator and 68.00 ± 8.77 N for the clinical applicator. The maximum force for Design 1 microneedles was 46.24 ± 8.57 N for the impact applicator and it was 91.00 ± 2.83 N for the clinical applicator. For Design 2 microneedles, the maximum force was 42.93 ± 11.08 N for the impact applicator as compared to 77.30 ± 15.55 N for the clinical applicator.

The insertion force comparison between the impact and clinical applicators for tests on all the skin models provide an interesting insight into the influence of skin's properties with respect to microneedle application. Fig. 92a shows a constant insertion force value for skin Models 1A–4A for the impact applicator and an increase in insertion force values for the clinical applicator with increased water content in the subcutaneous mimic. A similar trend was also observed for back skin model in Fig. 92b, except that Model 3B exhibited the lowest insertion force produced by the impact applicator.

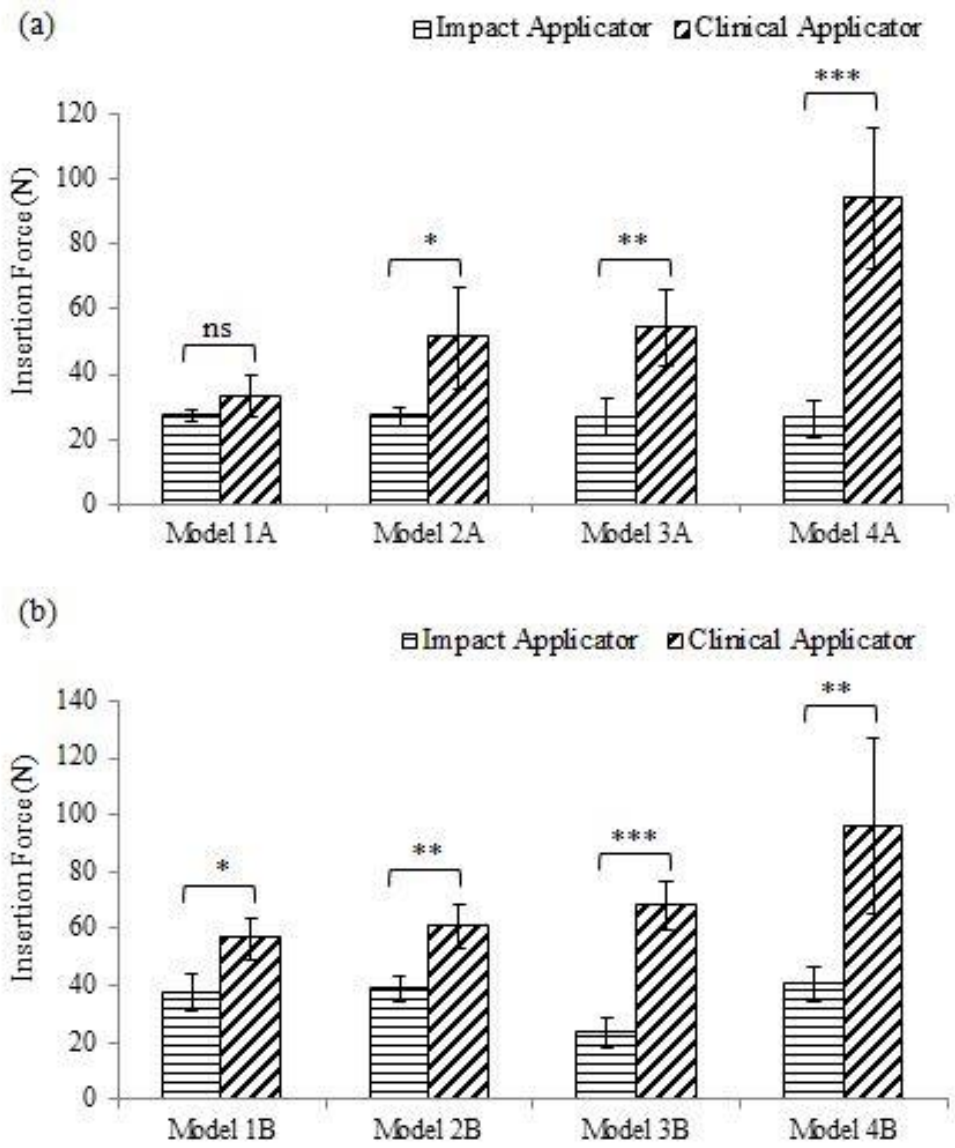

Figure 92 Force data comparison between the impact and clinical applicator tests on (a) abdominal skin models and (b) back skin models.

4.6.6 Summary of the comparison between impact and clinical applicator studies

Impact and clinical applicator studies of microneedle penetration of skin were reproducible as detailed in previous sections. 100% penetration was not achieved on all skin models for the clinical applicator and this was also observed with the impact applicator studies as well as mentioned in the literature. Furthermore, PE reduced with increasing fluid content in the subcutaneous layer for the clinical applicator as compared to the impact applicator.

For both applicators, the mean breach area for all skin models increased with an increase fluid content of the subcutaneous layer.

Microneedle geometry also highlighted how each applicator influenced skin penetration with the impact applicator demonstrating that the magnitude of force played a major role in the size of the deformation through the layers. Whilst the clinical applicator showed that with a similar magnitude of force on both Design 1 and 2 microneedles, Design 2 microneedles produced higher perforation depths in skin.

Finally, in terms of insertion force, for the impact applicator, abdominal and back skin was relatively constant. However, for the clinical applicator the insertion force increased with increasing fluid content in its subcutaneous layer.

Chapter 5

5. Discussion

5.1 Introduction

The results presented in Chapter 4 demonstrate that the micromechanical properties of the skin model with respect to anatomical region and altering the fluid content in the subcutaneous layer influence the effectiveness of microneedle perforation of skin. In the body, subcutaneous adipose tissue contributes to skin deformation during loading and load transfer from skin to deeper layers (Geerligs et al., 2010b). To date, the role of subcutaneous tissue on microneedle performance has largely been ignored due to incomplete *in vitro* skin models. Therefore, the work carried out in this thesis using a representative skin model shows the importance of the role of the subcutaneous layer for determining microneedle performance. Furthermore, although skin thickness is related to elastic modulus because the thinner abdominal skin produces a lower elastic modulus as compared to the thicker back skin with a higher elastic modulus, nonetheless, contributions from the subcutaneous layer, particularly the compliant 96% gel water content yielded comparable maximum force values for both abdominal and back skin models using the clinical applicator. This result however was not observed with the impact applicator. Additionally, microneedle geometry and microneedle applicator also contributed to microneedle performance in skin. The study found that microneedle penetration of skin was reproducible and repeatable, however the extent of the deformation through the layers varied according to microneedle geometry and microneedle applicator. Further, the mechanical properties of the various layers was quantified and related to microneedle performance. Insertion force, insertion velocity and maximum force values were obtained for the impact and clinical applicators as these

influenced effective microneedle penetration of skin. The findings from these studies are now discussed in further detail and as it relates to previous findings reported in the literature.

5.2 Micromechanical Characterisation of Skin's Sub-layers

The mechanical behaviour of skin varies due to various factors including age (Daly and Odland, 1979; Leveque et al., 1980), pathology such as scleroderma, polyfibromatosis (Pierard and Lapiere, 1977), species (e.g. human, porcine or murine) and anatomical site. Data reported in the literature also varies depending on test conditions (e.g. *in vivo* or *in vitro*) and test type e.g. indentation (Pailler-Mattei et al., 2007b), suction (Diridollou et al., 2000) or tension (Manschot and Brakkee, 1986).

The micromechanical tests using the nanoindentation setup allowed for the characterisation of the different layers of the skin model and thereby comparison with values reported in the literature for skin's subcutaneous and muscle tissue. The difference in elastic modulus for abdominal skin compared to back skin was consistent with published data (Zak et al., 2011). The storage modulus (elastic properties) was greater than the loss modulus (viscous properties) for both abdominal and back skin. This result was consistent with the work carried out utilising nanoindentation testing on murine skin (Kendall et al., 2007). The importance of a full thickness skin sample in the skin model was reinforced by Zahouani et al. who showed that the dermis made a significant contribution to skin because of its load bearing capabilities (Zahouani et al., 2009). Furthermore, it is easier to penetrate the human epidermis without the dermal layer (Li et al., 2015), which would not be an ideal way to demonstrate successful microneedle interaction with skin. For the work carried out in this thesis, unlike in some studies, a full thickness skin sample comprising the stratum corneum, epidermis and dermis as well as subcutaneous layers represented by gelatine gels and Perma-Gel® as muscle mimic were used. The mechanical tests on three concentrations of gelatine

gels (67%, 80% and 88%) showed that the elastic modulus decreased with increased fluid content in the gelatine gels matching trends reported by Mridha and Odman (1985) and Mridha et al. The storage modulus was significantly greater than the loss modulus for the gelatine gels. In the literature, for subcutaneous tissue, G' of 7.5 kPa for porcine tissue was reported (Geerligs et al., 2008). For the work in this thesis, G' ranged from 3.8–21 kPa, which was also comparable with the literature given the much higher frequency that was utilised during testing i.e. 110 Hz for this study as compared to approximately 1.6 Hz in the rheology study by Geerligs et al. The tests on Perma-Gel® yielded a mean G' of 29.9 ± 0.9 kPa, which matched values reported in the literature for the shear modulus of muscle (Pailler-Mattei et al., 2008).

As already reported, skin site, test method and test condition influence the outcome of skin's mechanical characterisation. The study by Zahouani et al. also demonstrated the similarity in stiffness between dermal equivalents and volar forearm (Pailler-Mattéi and Zahouani, 2006; Pailler-Mattei et al., 2008; Zahouani et al., 2009), which suggests that during *in vivo* tests, the mechanical contribution from the dermis is prominent. *Ex vivo* tests on the stratum corneum layer only, yielded a low elastic modulus (Pailler-Mattei et al., 2007b). This single layer of tissue is not ideal for microneedle penetration studies as the key mechanical strength provided by the dermis is absent. Uniaxial tensile tests confirmed that back tissue was stiffer and has a higher elastic modulus than abdominal tissue (Zak et al., 2011), which was also demonstrated in this study. The values of the elastic modulus in the Zak et al. study using tensile testing techniques were between 100–200 times greater than results obtained from the dynamic nanoindentation tests carried out in this thesis. The disparity in mechanical property data reported for various biomechanical studies in the literature highlights complexities due to different tissue types and testing methodologies.

Another noteworthy observation was that the range of elastic modulus obtained lay within the range of mechanical properties of previous studies listed in Table 3 (Section 2.3.1.2) and Table 4 (Section 2.3.2), with particular reference to the values from Groves (2011) and Zahouani et al. *in vivo* studies. Therefore, the micromechanical properties of skin in this study were comparable to the results of the *in vivo* studies.

As previously mentioned in the literature review in Chapter 2 (Section 2.3.1.2, Table 2), Crichton et al. demonstrated the effects of varying the indentation probe diameter and its influence on the elastic modulus of murine ear skin. They found that the elastic modulus increased with the smaller probe diameters and decreased with the larger probe diameters (Crichton et al., 2013). Kendall et al. previously found a similar trend in a nanoindentation study of murine skin using two different probe diameters (Kendall et al., 2007). Crichton et al. also stated that the mechanical behaviour of mice skin was comparable to human skin and cited indentation tests carried out by Geerligs et al. on frozen human tissue (Geerligs et al., 2011). Geerligs et al. used an *ex vivo* abdominal human tissue and reported that the elastic modulus of the stratum corneum (2.6 ± 0.6 MPa) was greater than the epidermis (1.1 ± 0.2 MPa). They also showed that a reduction in the stiffness of the viable epidermis causes an increase in indentation depth.

Another study by Kocchar et al., which focused on microneedle tests on soft tissue, also used rat skin and argued that for microneedle penetration studies, rat skin behaved similar to human skin (Kochhar et al., 2013b). Groves et al. demonstrated in their study involving *ex vivo* murine and human skin that under low loads, the extension in human skin was significantly greater as compared to murine skin and careful consideration should be taken when using murine skin as a biomechanically representative model of human skin (Groves et al., 2013). Ding et al. also found mouse skin to be thinner but more flexible than human skin (Ding et al., 2009).

Furthermore, Li et al. in their study of microneedle interaction with skin showed that the epidermal thickness of rat skin (≈ 15 μm) was very different to human skin (≈ 100–200 μm), which made it easier to strain rat skin following microneedle application (Li et al., 2015). They also found that it was easier to deeply penetrate rat skin due to its thinner epidermis. Therefore, rat skin may not be a suitable soft tissue model for microneedle application studies. Moreover, the work in this thesis using neonatal porcine skin has shown that the thickness of abdominal skin (≈ 0.79 mm) and back skin (≈ 2.43 mm) does contribute to microneedle performance, therefore, microneedle perforation of abdominal skin occurred more readily and is an ideal site for microneedle application. The micromechanical tests highlighted the difference in elastic modulus for the back skin (45.89 ± 9.61 kPa), which was almost twice that of abdominal skin (24.49 ± 5.47 kPa). The depth of penetration was typically lower in the back skin at lower gel water content i.e. Models 1B and 2B relative to the abdominal skin (Fig. 56 Section 4.4.4). In addition, the elastic component (G') and viscous component (G'') was also lower for abdominal skin compared to back skin. Furthermore, neonatal porcine skin exhibits close biomechanical properties to human skin (Shergold et al., 2006; Cilurzo et al., 2007) as well as similar histological, physiological and immunological properties (Avon and Wood, 2005). Therefore, if access to human tissue is challenging, then neonatal porcine skin can be used as a suitable substitute.

The variation of the elastic modulus in soft tissue demonstrated in several studies also highlighted the extremely variable nature of biological material in general.

5.3 Impact Applicator Studies

A number of different methods have been employed in the literature to apply microneedles to skin. Dermaroller® (Badran et al., 2009), syringe applicators (Haq et al., 2009), actuator driven applicator (Bouwstra et al., 2009) and an electrically driven applicator (Verbaan et al., 2008) have all been used for microneedle application to skin. The more commonly used microneedle applicators are the spring-driven applicators; however, some studies have shown that the impact applicator setup is a more suitable option for microneedle application in soft tissue as compared to manual application (Burgin and Aspden, 2007). Furthermore, van der Maaden et al. used an impact applicator for reproducible perforation of skin (van der Maaden et al., 2014).

In this thesis, impact applicator studies support the assertion in the literature that reproducible microneedle perforation of both abdominal and back skin models are achievable at velocities in excess of 2 ms^{-1}. As a consequence, attempts have been made to relate the force, velocity, mechanical properties of the skin model layers, microneedle geometry to microneedle penetration results. Therefore, the findings of impact applicator tests on all skin models are discussed in this section.

5.3.1 Visual examination of microneedles using SEM imaging

SEM images showed that PEEK microneedles remained intact after five applications during impact tests on skin, whilst the tips of Design 2 PMMA microneedles deformed after single application and completely fractured following five applications. The elastic modulus for PEEK is 4.1 GPa (Victrex, 2014) and 1.7 GPa for PMMA (Ianches, 2015), which suggests that PEEK microneedles were more robust in its design because of its higher elastic modulus and due to its construction had design integrity. Furthermore, in the polymer family, PEEK

also has the highest fracture toughness, a value of 2.73–4.30 MPa$\sqrt{}$m (Granta, 2003), which also explains why it exhibits superior design integrity.

Design 2 PMMA microneedle tips were sharper than PEEK microneedle tips. Therefore, these design intricacies could explain why PEEK microneedles produced poor perforation results as compared to Design 1 and Design 2 PMMA microneedles. The tip sharpness of the PMMA microneedles as compared to the PEEK microneedles may have influenced the integrity of the needles during multiple uses i.e. a small diameter tip is more likely to deform after a single insertion than a blunter, larger diameter tip. In addition, Renephra's clinical trials by Ebah (2012) using PEEK microneedles also reported that the design of the microneedles may have hindered its performance in skin *in vivo*.

5.3.2 Penetration efficiency

Visual examination using methylene blue staining and histological examination using H&E images showed that with Design 1 and 2 PMMA microneedles, 100% penetration was not observed. These results were consistent with findings from other researchers who had less densely populated arrays i.e. 16–576 microneedles on the array (van der Maaden et al., 2014; van der Maaden et al., 2015) as compared to Design 1 microneedles (1316 microneedles on the array) and Design 2 microneedles (> 6000 microneedles on the array) used in this study. Furthermore, the PE determined from methylene blue staining varied from 43–93% for the regions analysed. For this reason, the expected frequency of microneedle breaches i.e. with clearly visible breaches every 360 µm were not seen during the analysis of H&E images. In addition, this may also be attributable to the substantial irregular surface topography of skin (see Figs 95 and 96 in the Appendix). Moreover, there may be unavoidable issues due to the tissue sectioning process (see Fig. 97 in the Appendix).

PE as determined in other studies has largely relied on methylene blue or Trypan blue staining to assess penetration efficiency (Park et al., 2005; Verbaan et al., 2008; Haq et al., 2009; Kochhar et al., 2013b; Olatunji et al., 2013; van der Maaden et al., 2014; Qiu et al., 2015; van der Maaden et al., 2015), however as shown in Fig. 66, a combination of methylene blue staining with histology is required to fully assess the extent of microneedle penetration of skin. In the study by van der Maaden et al., the stratum corneum was stripped from the skin in order to effectively determine that the perforations had propagated through to the epidermis (van der Maaden et al., 2014). As already established the methylene blue staining only confirms disruption to the stratum corneum layer and not perforation depth, which is why it should not be considered as a technique for measuring successful epidermal penetration. Microneedle penetration success should be defined as the complete breach of the stratum corneum that extends to the epidermal layers. This is because in this study, there have been instances where some microneedles on the array have only caused dents in the stratum corneum, thus creating a temporary pocket that carries the methylene blue solution. This would be observed as successful methylene blue staining through visual examination, however, there is no breach in skin. van der Maaden et al. also noted a similar occurrence in their study, as some of the dye solution was stored in dents in the stratum corneum. A further observation was that not every microneedle on the array seemed to fully penetrate through to the epidermis; however, the majority of the microneedles did deform the stratum corneum layer, as shown in Figs 66d–f. This phenomenon was also observed in other methylene blue or Trypan blue stained image studies, where every single microneedle on the arrays did not perforate the stratum corneum (Haq et al., 2009; Qiu et al., 2015; Xiang et al., 2015). Moreover, emerging technologies within biomedical research such as OCT and XMT could also be utilised in providing this detail.

5.3.3 The effects of differences in skin properties

There are currently only a few studies which have explored how microneedles performance is influenced by the physiological and mechanical properties of skin. In this thesis, it was observed that microneedle perforation occurred more readily in the thinner abdominal skin as compared to the thicker back skin. This occurrence was similar to the study by Al-Qallaf and Das (2008), who demonstrated that increasing drug permeability in skin with microneedles varied due to differences in epidermal thickness between Caucasian and Korean groups. The thicker epidermis found in the Korean group exhibited lower skin permeability as compared to the thinner epidermis in the Caucasian group, which had higher skin permeability (Al-Qallaf and Das, 2008). As already noted that neonatal porcine back skin bears similar thickness (Lo Presti et al., 2012) and has a comparable mechanical property to human skin (Groves, 2011), therefore, the outcome of studies on neonatal back skin provides details of how microneedles could interact in human skin. In addition to skin thickness, Verbaan et al. postulated that age and skin region due to the variation in the elasticity of skin makes microneedle perforation of skin less reproducible (Verbaan et al., 2008). Furthermore, Olatunji et al. showed computationally that the insertion force for microneedles was significantly higher for aged human skin as compared to younger skin (Olatunji et al., 2013).

As fluid overload and oedema are conditions common to elderly patients suffering from heart or kidney failure (McMurray and Stewart, 2000), it is therefore important to address the likely effects of microneedle application to ageing skin. Although no study was carried out on ageing skin in this thesis, contributions from insertion force and insertion velocity could play a role in the postulations by Verbaan et al. and Olatunji et al. regarding the reproducibility of microneedle perforations in ageing skin. According to Kelchen et al. for their *in vivo* comparison study between elderly and young subjects, manual application of microneedle created microchannels in skin for both subjects. The difference noted was the time taken for

microchannel closure, which was longer in elderly subjects as compared to young subjects (Kelchen et al., 2016). Furthermore, ageing skin is thinner due to epidermal thinning (Kelchen et al., 2016) as compared to younger skin; hence, the structural differences between ageing and young skin could influence microneedle performance. This thesis demonstrated that structural differences between abdominal and back skin resulted in different outcomes, with more deformation occurring in abdominal skin as compared to back skin. Likewise, the thicker back skin required a higher insertion force as compared to the thinner abdominal skin. The difference between the insertion force of abdominal and back skin indicates that microneedle penetration of skin is influenced by the difference in thickness at different anatomical sites.

Another factor for microneedle performance in different skin regions could be due to variation in skin topography. Skin has a natural undulation, which varies in size and depth (see Figs 94 and 95 in the Appendix). This could explain why some of the microneedles perforated deeper into skin in some regions as compared to other regions. The histology images also illustrated 2D profiles of skin's topography, with some cross-sections having flatter ridges as compared to other cross-sections having more pronounced ridges.

There are certain disadvantages associated with the analysis of histology images. This is because only a small portion of the tissue can be sectioned during histology, which means that useful information is lost with the tissue that is discarded. Furthermore, it involves time-consuming fixing, sectioning and staining steps. Coulman et al. demonstrated that histological measurements of microneedle penetration led to an overestimation (Birchall et al., 2005; Coulman et al., 2010). This error is also compounded by the introduction of slight inaccuracies due to skin retraction caused by the removal of the microneedles before staining (Donnelly et al., 2010; Loizidou et al., 2016). Despite these limitations, using histology for the light microscopic assessment of skin biopsies is still regarded as the benchmark in

dermatology (Holme et al., 2014; Newton et al., 2015). In order to improve on conventional methods of measurement from histological images, a custom image analysis routine was used for all measurements of breach area from histology images.

5.3.4 The role of the subcutaneous mimic property on microneedle performance

As mentioned previously in Section 2.6.5, several microneedle *in vitro* studies have used skin models with underlying substrates that do not provide a true representation of the mechanical characteristics of skin's underlying layers (Park et al., 2005; Verbaan et al., 2007; Badran et al., 2009; Yan et al., 2010; Donnelly et al., 2011; Kochhar et al., 2013a; Kochhar et al., 2013b; Olatunji et al., 2013). Hence, the additional novelty of the approach outlined in this thesis was that microneedle tests were performed on a more representative *in vitro* skin model that incorporated a subcutaneous tissue layer and muscle mimic that were comparable in mechanical behaviour to skin's underlying layers. Early on, the role of gelatine gels as an underlying substrate for skin in the study involving PEEK microneedles showed that penetration was marginal when skin was not placed on a gelatine gel bed. Typically, the human anatomy contains organs, muscles, fat and is supported by a skeleton, which gives skin support. Understandably, the lack of a gelatine gel bed reinforces the requirement for the *in vitro* tissue to have a representative layer that can mimic the subcutaneous layers of skin.

For methylene blue staining utilising Design 2 microneedles with back skin models, it was observed that penetration quality improved with increasing water content in the gelatine gels. As noted by Mridha et al. gelatine gels with high water content have low mechanical impedance and this phenomenon could explain the improved penetration of skin with high water content gelatine gels following microneedle application. Although skin tension with respect to oedema was not measured during experimental investigation, contributions from the subcutaneous layer cannot be ignored as, the influence of the lowest stiffness gelatine gels

was prominent for skin Models 4A and 4B, where the deformation in abdominal and back skin were significant in terms of their large breach sizes. Typically, the stiffer back tissue contained most of the deformation within the epidermis for Models 1B, 2B and 3B. It was also noted that the thinner abdominal tissue produced deeper breach sizes that extended into the dermis with increased fluid content in the gelatine gels.

Overall, it was found that for abdominal skin model, increased fluid content in the gelatine gels resulted in larger deformations in terms of breach area. Therefore, manipulating the water content in the gelatine gels compromised the integrity of the skin model. Additionally, it was found that the mechanical performance of abdominal skin model was influenced by the mechanical contribution from the gelatine gel layer, as an increase in water content affected its interaction with microneedles. Moreover, as abdominal tissue is thinner and has a lower elastic modulus, it offers all the right components to make it easy for microneedles to bypass its skin barrier and cause deformation. This could mean that microneedles could cause greater deformation in patients with oedematous tissues or epidermal thinning associated with ageing (Kelchen et al., 2016). The histograms presented in Section 4.4.4 showed that there were more perforations for a breach size of 10 000–20 000 μm^2 in the abdominal skin relative to the back skin. This could also be related to the thickness of the abdominal skin, which means that it has a reduced ability to resist the disruptive influence of microneedle assault as compared to back skin.

5.3.5 Impact applicator force and velocity

The impact applicator used for the work carried out in this thesis allowed for both force and velocity to be varied. This was in contrast to other studies which have tended to use a fixed force (van der Maaden et al., 2014) or only considered the application velocity (Verbaan et al., 2008; Ding et al., 2009).

At higher drop mass loads and higher velocities, as shown in Figs 64a–b, the intensity of the methylene blue dye increased for Design 1 microneedle penetration on the stratum corneum of skin Model 3B. Verbaan et al. used intensity of Trypan blue dye as an assessment of perforation effectiveness in their study. In addition, they also quantified their Trypan blue intensity tests by conducting separate transepidermal water loss (TEWL) studies on samples of microneedle perforated tissues without dye staining. TEWL is a standardised way of measuring the changes in skin barrier properties (Treffel et al., 1994; Rosado et al., 2005) and can be used as an additional indicator of stratum corneum disruption (Haq et al., 2009). Their TEWL results were consistent with the results obtained from their visual observation studies using Trypan blue (Verbaan et al., 2007). The methylene blue staining results also highlighted the influence of force and velocity on the quality and consistency of incorporation of the high-density Design 1 microneedles into Model 3B. Furthermore, the quality of perforation through skin improved at a higher velocity of 3 ms^{-1} as compared to 2 ms^{-1}. This observation was in line with the study by Donnelly et al., which concluded that perforation of skin could occur at high velocities and low loads (Donnelly et al., 2010). Furthermore, van der Maaden et al. achieved perforation of skin at 3 ms^{-1} and at a force in the range of 3.43–22.1 N (van der Maaden et al., 2014). The insertion force, which is indicated in Figs 59 and 67, is likely to be the point at which the force exerted on the microneedles causes piercing of the skin, as described by Olatunji et al. (Olatunji et al., 2013). Therefore, the optimal parameters of insertion velocity and insertion force for reproducible and predictable penetration of skin Model 3B using Design 1 microneedles were 2.96 ms^{-1} and 9.33 ± 2.76 N respectively.

There was some correlation between insertion force and the extent of the deformation in skin, as the size of the insertion force used for microneedle application was commensurate with the size of the deformation. This was particularly evident in skin Model 3B, whereby a low

insertion force resulted in a small breach size as compared to the breach size observed in Models 1B, 2B and 4B (Fig. 55c). The insertion force using Design 2 microneedles on Model 3B was 23.50 ± 4.97 N, which was lower than the insertion forces of 37.52–40.72 N on Models 1B, 2B and 4B (Fig. 67a). These skin models produced higher breach areas as compared to Model 3B (Fig. 55). This also suggests that the size of the insertion force is important for ideal microneedle interaction within skin. Furthermore, Donnelly et al., used a spring-driven applicator of varying forces (4.4–16.4 N/array) to demonstrate that increasing the insertion force led to a significant enhancement in the depth of microneedle penetration into skin (Donnelly et al., 2010).

In comparison to back skin models, a lower insertion force and insertion velocity was required for microneedle penetration of abdominal skin models. It has already been established that the elastic modulus as well as the elastic and viscous effects for back skin is higher than for abdominal skin, therefore, it is for this reason that the stiffer back skin requires a higher insertion force as compared to the less stiff abdominal skin. The insertion force values were not overly influenced by the subcutaneous mimic properties in any of the abdominal skin models because as the fluid content increased in the gelatine gels, the insertion force remained relatively constant. The maximum force however increased with increasing water content in the gelatine gels, which indicates the prominent role played by the subcutaneous mimic in microneedle interaction with skin. This would indicate that at greater force values, the integrity of the gelatine gels becomes compromised and disintegrates, unable to withstand the force. It was noted that the maximum force measured by the force transducer decreased by approximately 37% from Model 1A containing 67% gel water content to Model 4A containing 96% gel water content. Although PE decreased marginally with gel water content, the average depth size and breach area increased with gel water content. Also noteworthy, was the reduction in these parameters with Model 4A containing

96% gel water content. It appears that the high compliance of the subcutaneous mimic in this model seems to result in poorer microneedle interaction with skin, the histogram data however (Fig. 58a) shows that the distribution of small (< 10,000 μm) and large breach areas (> 20,000 μm) is comparable to Models 2A and 3A containing 80% and 88% gel water content respectively.

The maximum force did not decrease for back skin models as in the case of abdominal skin models with increasing compliance of the subcutaneous mimic. Again, this can be related to the relative stiffness and thickness of back skin. The overall trends for average depth size and breach area matched those found in abdominal skin. The key difference between abdominal and back skin was the average data reported for Model 3B containing 88% gel water content. The histogram data for back skin models (Fig. 58b), however, also demonstrates that the overall trends are relatively consistent in terms of microneedle performance as compared to gel water content. The inherent issues with histological assessment of microneedle perforation of skin cannot be ignored as contributory factors for some of the disparities.

5.3.6 The effects of microneedle geometry on skin penetration

The stratum corneum is the stiffest layer in skin and the least extendable under applied load (De Rigal and Leveque, 1985; Hendriks, 2001). It is also the first surface that comes into contact with microneedles. Thus, the stratum corneum remains a barrier against the application of microneedles (Prausnitz, 2001). PEEK and PMMA microneedles successfully bypassed the stratum corneum, with the deformation extending into the epidermis. The reproducible perforation of skin was an issue with PEEK microneedles and may have been due to its method of manufacture, laser machining, as its original design was for sharper tips. For the PMMA microneedles however, reproducible and repeatable perforation of skin occurred for both abdominal and back skin models due to consistency of tip sharpness attributable to its microfabrication process.

For the work in this thesis, the microneedle tip diameters were of similar construction and its size was ≈ 10 μm for Design 1 and 2 PMMA microneedles. The variation in needle length was 356 μm for Design 1 microneedles and 552 μm for Design 2 microneedles. In terms of needle density, it was 1316 for Design 1 microneedles and > 6000 for Design 2. The difference in interspacing was 386 μm for Design 1 microneedles and 360 μm for Design 2 microneedles.

Design 1 microneedles penetrated through the stratum corneum to the epidermal layer and in some instances caused deformation to the dermal layer. The objective of microneedle penetration studies is to achieve epidermal breach, since this layer contains few nerve endings or blood vessels. It was noted by Henry (1998) that even though microneedles are long enough to penetrate the dermis, they are however short and narrow enough to avoid stimulating dermal nerves (Henry et al., 1998). Although the histological images in Fig. 61 did not show any significant difference between Design 1 and 2 microneedles interaction with skin, the insertion force for Design 2 microneedles was more than twice the magnitude required for Design 1 microneedles. Therefore, this increase in insertion force for the more densely populated, longer length Design 2 microneedles (> 6000) as compared to the less densely populated, shorter length Design 1 microneedles (1316) demonstrates that microneedle geometry plays a role in the force outputs for microneedle interaction with skin. Liu et al. also showed that insertion force varies with microneedle geometry (Liu et al., 2016). Furthermore, Loizidou et al. demonstrated that design elements such as microneedle length, interspacing, base diameter that affect microneedle geometry are critical parameters that influence skin penetration (Loizidou et al., 2016). The differences in interspacing between individual microneedles for Design 1 microneedles (386 μm) and Design 2 microneedles (360 μm) as well as differences in needle density for Design 2 microneedles (>

6000), which is approximately four times that of Design 1 microneedles (1316) were factors in determining how both microneedles behaved in skin.

For Model 3B, Design 2 microneedles produced a greater number of perforations ≤ 10 000 μm^2 however, Design 1 microneedles produced perforations in skin at all measurement ranges, whilst there were some ranges where no perforations were recorded for Design 2 microneedles. This observation suggests that despite the lower insertion force of the Design 1 microneedles as compared to Design 2 microneedles, Design 1 microneedles were completely embedded in skin at its highest perforation depth of 351 μm (Fig. 62). However, the insertion force per microneedle highlights that almost two times the insertion force per microneedle is acting on Design 1 microneedles (0.007 N/microneedle) as compared to Design 2 microneedles (0.004 N/microneedle). This was further corroborated by other studies in which microneedle perforation depth improves with insertion force (Donnelly et al., 2010) and insertion velocity (Crichton et al., 2010).

Another design difference between Design 1 and 2 microneedles is the height, where Design 1 microneedles were 356 μm in height as compared to Design 2 microneedles height of 552 μm. As already mentioned in Section 5.3.2, following microneedle interaction with skin, the skin is initially indented before perforation of the stratum corneum occurs. Consequently, several studies have reported that microneedle perforation depth varies widely from 10–80% of the length of the microneedle (Coulman et al., 2010; Donnelly et al., 2010; Kalluri et al., 2011). This could perhaps explain the observation in this study why Design 2 microneedles did not penetrate as deeply into skin.

Verbaan et al. demonstrated using the same design of microneedles, which were a 4 × 4 array of lengths 300 μm, 550 μm, 700 μm and 900 μm that TEWL increased with the increasing length of the microneedle. The 900 μm microneedle produced the best TEWL results. The

only variable with their microneedles was its length, as needle density and interspacing were the same. This made it possible in determining that increased microneedle length resulted in increased perforation of skin (Verbaan et al., 2007). On the other hand, Yan et al. conducted several tests on a wide number of microneedle lengths with various needle densities. In their study, they found that the longer microneedle length (650 μm) with needle density of 400 or 900 resulted in increased skin perforation as compared to the shorter microneedle length (≤ 300 μm) with needle density of 11 900 (Yan et al., 2010). Moreover, Romgens et al. further stated that the length of the microneedle also influenced the perforation depth, in contrast to the interspacing between individual microneedles on an array and that microneedles with a tip diameter of < 15 μm insert microneedles to a desired perforation depth (Romgens et al., 2014). In this thesis, PMMA microneedle tip diameters were of similar construction, however, there were variations in needle length, needle density and interspacing. These differences further influenced microneedles performance in Model 3B, with Design 1 microneedles producing larger perforation depths and breach areas as compared to Design 2 microneedles.

Due to the significant differences in microneedle length, needle density and interspacing between Design 1 and Design 2 microneedles, it is difficult to separate out the effects of each of these variables. However, as stated in this section, length and the number of needles on the array appears to have the greatest effect on microneedle performance. It was beyond the scope of the thesis to investigate each of these effects separately. Testing was only conducted on those arrays being utilised by Renephra for clinical trials.

Overall, for the desired application it would seem that Design 1 microneedle is most suitable because it produced more consistent deformations within skin following successfully bypassing the stratum corneum layer and PE ≥ 30%.

5.4 Clinical Applicator Studies

Clinical applicator induced microneedle tests were conducted on abdominal and back skin models using Design 1 and 2 microneedles. Therefore, the findings of the clinical applicator tests are discussed in this section.

5.4.1 Penetration efficiency

In order for the hammer mechanism to be launched when the clinical applicator was used, the microneedles were placed flush on the raised profile of skin, which ensured that the hammer mechanism of the clinical applicator depressed the microneedles into skin. The PE determined from methylene blue staining varied from 39–80% for the regions analysed. Although the raised profile of skin may have contributed to the reduced number of perforations observed, however, as already noted from previous studies that not every microneedle on the array will perforate skin, this reduced frequency means that breaches were not observed for every 360 µm of interspacing on the array during assessment of the H&E images. Moreover, a further reason why not every microneedle perforated skin may be due to the irregular surface topography of skin.

5.4.2 The effects of differences in skin properties

The deformation created within the abdominal skin model was wider and extended into the dermis as compared to the back skin model, where the deformation was narrow and on occasion also stretched into the dermis. This may be attributed to physiological differences between abdominal tissue and back tissue, as abdominal tissue is thinner than back tissue.

In addition to physiological differences between abdominal and back skin, the difference in their mechanical characteristics could also explain the ease with which microneedle insertion instigated by the clinical applicator caused significant deformation in abdominal tissue as compared to back tissue. Furthermore, back tissue has a higher elastic modulus as compared

to abdominal tissue (Zak et al., 2011). Similarly, in this thesis, the elastic modulus of back skin was higher than abdominal skin as reported in Section 5.2. Moreover, in the literature, it was mentioned that the difference in skin thickness was found to affect its viscoelastic characteristics (Nguyen and Banga, 2015), as a full thickness skin sample was found to be more elastic and more resistant to microneedle insertion force (Nguyen and Banga, 2015).

The mechanism of the clinical applicator required manual pressure to be applied on the microneedles in addition to the clinical applicator force. Therefore, this added manual pressure may have also contributed to the extent of the deformation within the thinner abdominal tissue as compared to the thicker back tissue. There was also a difference in insertion force for abdominal and back skin models, with a higher insertion force required for back skin and a lower insertion force required for abdominal skin. This suggests that insertion force varies according to skin site, even though a similar magnitude of maximum force was applied on both skin models.

5.4.3 The role of the subcutaneous mimic property on microneedle performance

The mean penetration depth increased with increasing water content in the subcutaneous mimic, which were similar to the results of the impact applicator studies. The breach area increased with increasing water content in gelatine gels for abdominal skin, however, at the most compliant gel water content (96%), it reduced. This trend was not observed for back skin model and therefore, a plausible explanation for this outcome would be that back skin is stiffer and thicker.

The median values of breach areas for the abdominal skin model was around 10 000 μm^2 as compared to the back skin model, which was circa 5000 μm^2 for Models 1B and 3B. There appeared to be no obvious trend for the effects of the influence of the subcutaneous mimic. It

was noted however, that in terms of the length of the microneedle embedded in skin that at least 50–60% of the microneedle length breached skin's layers, which was in accordance with trends observed (Coulman et al., 2010; Donnelly et al., 2010; Kalluri et al., 2011), irrespective of fluid content in the subcutaneous layer

5.4.4 Clinical applicator force

There was an increase in insertion force with increased gel water content for abdominal and back skin models. This trend was also observed for the maximum force on both skin models. Although, there were no successful micromechanical tests conducted on the 96% gelatine gel because of its extremely high water content, logically, it can be assumed that it would have exhibited the lowest elastic modulus of the gelatine gels. Likewise, it can also be stated that at the lower water content gelatine gel such as 67%, its higher elastic modulus would require a higher insertion force. As reported by Cheung et al. a high elastic component (G') indicates that the skin will be more resistant to microneedle insertion (Cheung et al., 2014). It was found that the insertion force was lowest on Model 1A, containing the lowest water content gelatine gel and could be due to the elastic modulus of skin being lower than that of the 67% gelatine gel. Furthermore, as skin is the first surface that experiences the effects of the clinical applicator force could explain why a low insertion force was required for the microneedle to perforate skin for Model 1A. Therefore, the contributions from varying the water content in the gelatine gels is more pronounced in terms of how the clinical applicator insertion force is applied on the microneedle. Therefore for Model 4A, the highest insertion force recorded may have been as a result of the compliant nature of the 96% gelatine gel which led to the clinical applicator probably interfacing with the Perma-Gel®. A similar trend was also observed for back skin models.

In the study by Donnelly et al., it was reported that microneedle penetration could occur at a relatively low insertion force of 4.4 N/array (0.49 N/microneedle) using a spring-driven

applicator. The clinical applicator used in this study is also spring-driven; however, the addition of a hammer in its design means that it performs differently to a solely spring-driven applicator. The clinical applicator produced an insertion force of ≈68 N/array (0.011 N/microneedles) for Design 2 microneedles on skin Model 3B. Furthermore, other microneedle applicator types that are not spring-driven yielded low insertion forces (Olatunji et al., 2013; van der Maaden et al., 2014; Qiu et al., 2015). For example, in the study by Olatunji et al. their applicator device produced an insertion force of 0.03 N/microneedle, which is in the same order of magnitude as the clinical applicator insertion force. Although Donnelly et al. reported a low insertion force, their insertion force per microneedle was considerably greater than the insertion force utilised in this study.

5.4.5 The effects of microneedle geometry on skin penetration

Visual assessment of methylene blue images showed comparable microneedle performance on the stratum corneum for Design 1 and 2 microneedles. The analysis of H&E images indicated that Design 1 microneedles were completely embedded in Model 3B at a perforation depth of 311 μm considering the microneedle length is 356 μm (Fig. 78). Hence the deformations were more significant as compared to those caused by Design 2 microneedles, which had a perforation depth of 360 μm, approximately 65% of its length travelled within skin. This may have been as a result of the number of microneedles on the array for Design 2 microneedles as compared to less densely populated Design 1 microneedles.

The insertion force applied on Design 1 and 2 microneedles were of similar magnitude, which meant that the same amount of force was acting on the less densely populated Design 1 microneedles (0.051 N/microneedles) as compared to the more densely populated Design 2 microneedles (0.011 N/microneedles). As already stated in Section 5.3.5, several studies have

been conducted in the literature with respect to microneedle length and its influence on perforation depth. Furthermore, according to Kochhar et al., a decrease in the number of microneedles on an array and increased spacing, produced an incremental force per needle and a higher percentage of microneedle penetration (Kochhar et al., 2013b), which was consistent with the findings in this section on the variation of microneedle length. The general conclusion from the literature is that variables such as needle density, interspacing and needle length contribute significantly to perforation depth. Therefore, for the work in this study, it was observed that the size of the deformations caused in skin was not commensurate with the size of the insertion force imposed upon the microneedles by the clinical applicator as compared to the impact applicator.

For the clinical trials, an understanding of the role of microneedle length is important for *in vivo* work. Nguyen and Banga showed that as the microneedle length increased, drug delivery increased and was as a result of microneedle treatment duration and equilibration time (Nguyen and Banga, 2015). Although this implies that the microneedles travelled deeper into skin, however, consideration must be given to the duration that the microneedles were left in skin as this could explain the improved drug delivery in their study. This is because the duration of the microneedles in skin results in more time for the drug to have diffused into skin and not necessarily improved microneedle penetration of skin. Gupta et al. demonstrated that extremely long microneedle projections (1500 μm) can cause pain comparable to that of a hypodermic needle in patients (Gupta et al., 2011). This observation was also consistent with previous literature that indicated that for the design of the microneedle, the length of the microneedle projection was the most important aspect in the measurement of pain (Gill et al., 2008). Furthermore, clinical trials using the clinical applicator on Design 2 microneedles produced minimal pain and bleeding in patients (Renephra, 2015).

In terms of breach areas, Design 2 microneedles produced a higher number of perforations in the breach area category where the stratum corneum was fully bypassed and the deformation extended into the epidermis. At breach areas greater than this, Design 1 microneedles performed considerably better than Design 2 microneedles. Therefore, as there is a higher insertion force per microneedle acting on Design 1 microneedles as compared to Design 2 microneedles would explain the greater deformation produced by Design 1 microneedles as compared to Design 2 microneedles. This result demonstrates that the clinical applicator is affected by microneedle geometry and therefore, the clinical applicator should be used on Design 2 microneedles.

5.5 Comparison between Impact and Clinical Applicator Studies

Two types of microneedle applicators were used to insert microneedles into the abdominal and back skin models for the work in this thesis. The microneedle applicators employed different mechanisms for operation; the impact applicator depended on impact acceleration to drive the microneedles into skin, whilst the clinical applicator design was based on a spring and hammer mechanism. Therefore, it was important to assess microneedles interaction with the skin models by comparing the results from both applicators. The impact applicator setup allowed for measurements of insertion force and insertion velocity, whilst only measurements of insertion force were obtained from the clinical applicator setup. A comparison of impact and clinical applicator tests are discussed in this section.

5.5.1 Penetration efficiency

PE can be defined as the percentage of the number of blue spots from the methylene blue staining of microchannels created by a microneedle array on the stratum corneum, divided by the total number of microneedles on the array. It was found that 100% penetration was not observed using both applicators and these results were consistent with findings from other researchers using different designs of applicators (Kolli and Banga, 2008; van der Maaden et al., 2014; Xiang et al., 2015). PE varied from 43–93% for the regions analysed using the impact applicator to 39–80% for the regions analysed using the clinical applicator, thus, these ranges are similar. The results in study were better as the arrays used were more densely populated. Likewise, for both applicators it was not possible to observe microneedle perforations every 360 µm during the analysis of H&E images.

Furthermore, for the impact applicator, PE reduced for abdominal skin models and increased for back skin models with increasing water content in the subcutaneous mimic. Conversely, for the clinical applicator, PE reduced for both skin models with increasing water content in

the subcutaneous mimic. It would appear that with the clinical applicator, compliance of the subcutaneous layer had a profound effect on PE even in the stiffer and thicker back skin. Therefore, PE did not reduce drastically with compliance in back skin with the impact applicator as it did with the clinical applicator. These differences in the outcome of applicator performance may have been due to the physical act of pressing the applicator onto the microneedles on skin in order to use the clinical applicator. This approach introduces some variability associated with the initial manual pressure applied on the microneedles. For the impact applicator however, as the drop mass is released, there is no added intervention to facilitate microneedle application to skin.

5.5.2 The effects of differences in skin properties

With the impact applicator, the size of the deformation increased with increased water content for abdominal skin. However, with the clinical applicator the size was considerably larger and was contained in the dermis for all abdominal skin models. For the back skin model, the deformations were predominantly contained within the epidermis for both applicators. This highlights the role that the physiological differences between abdominal tissue and back tissue play in applicator induced microneedle interaction with skin, as larger deformations were found within the thinner abdominal tissue as compared to back tissue. Therefore, for the work carried out in this thesis, it was the abdominal skin models that underwent larger deformations in comparison to the back skin models irrespective of applicator type.

5.5.3 The effect of the subcutaneous mimic property on microneedle performance

The average perforation depth in abdominal skin models was higher for the impact applicator as compared to the clinical applicator. This suggests that the impact applicator performs comparatively better than the clinical applicator on abdominal skin models. For the breach

areas, the impact applicator had a higher percentage in the category where the stratum corneum is disrupted and extends to the epidermis in the abdominal skin model (Fig. 88a), whilst the clinical applicator had a higher percentage of breaches in the category where the epidermis is fully opened up.

There was no obvious trend for perforation depth for back skin models and this indicated that there was a higher degree of variability associated with back skin models. The clinical applicator had higher percentages of breaches for $\leq 10\ 000\ \mu m^2$ as compared to the impact applicator (Fig. 88b) for the back skin models. This also implies that the clinical applicator is able to overcome the elastic modulus of the stiffer back tissue as compared to the impact applicator. Although, it must be noted that the clinical applicator produced a higher number of smaller perforations in back skin as compared to the impact applicator's lower frequency of larger perforations in back skin. Ideally, larger perforations are preferred, as there are higher chances that the perforations have extended beyond the stratum corneum into the epidermis, where the fluid bed can be accessed for fluid extraction.

The analysis of H&E images showed that with the impact applicator larger deformations were made as determined by the breach area with increasing fluid content in the abdominal skin models. It was therefore established that manipulating the water content in the gelatine gels compromised the integrity of the abdominal skin model. In contrast, the size of the breach area in the back skin model reduced with increased fluid content in the gelatine gels and may be due to a combination of the magnitude of the insertion force per microneedle as well as its higher elastic modulus. For the clinical applicator however, smaller breach areas were seen in the abdominal skin model across all gelatine gel concentrations for deformations contained within the epidermis as compared to back skin model. For deformations that extended into the dermis however, larger breach areas were seen in the abdominal skin model

as compared to back skin model. These observations have highlighted the influence of applicator input in perforation quality, where it appears that the size of the breach area produced by the impact applicator is influenced by the mechanical strength of the skin model, which was not the case with the clinical applicator. The contrast in applicator performance may be due to application technique, for instance, the impact applicator's drop mass is released from a height to make contact with the microneedles and skin model. In the case of the clinical applicator, the patch button is placed onto the microneedles and skin model, with an initial manual pressure applied onto the patch button before the trigger is released and therefore could be a likely explanation for the difference in perforation quality between both applicators. Furthermore, the results of clinical applicator studies showed large SD values (Fig. 81), which imply the high degree of variability linked to use of the clinical applicator as compared to the impact applicator.

5.5.4 Impact and clinical applicator force

For the impact applicator, an insertion force of ≈0.005 N/microneedle was required to perforate Models 1A–4A. In contrast, for the clinical applicator, an insertion force of 0.006–0.016 N/microneedle was required for Models 1A–4A. Conversely, for the back skin models, a slightly higher insertion force (0.004–0.007 N/microneedle) was required for microneedle application using the impact applicator. For the clinical applicator, an insertion force of 0.009–0.016 N/microneedle was required. It was observed that the clinical applicator's performance was hugely influenced by fluid content in the gelatine gels, as it produced its highest insertion force on Models 4A (94. 03 N) and Model 4B (96.05 N). Therefore, it was postulated that due to the compliant nature of the 96% gelatine gel concentration, it is plausible that the clinical applicator interfaced with the Perma-Gel® layer in the skin model. Notably, the Perma-Gel® also had the highest elastic modulus in the skin model, as shown in Table 12.

The ability to vary the insertion force and insertion velocity for the impact applicator is a significant advantage over the clinical applicator, where the insertion force cannot be varied. Furthermore, only a relatively low insertion force and a low insertion velocity as compared to the clinical applicator's comparatively higher insertion force was required to successfully penetrate skin irrespective of the level of fluid content in the underlying subcutaneous layer. Albeit, this limitation with the design of the clinical applicator has demonstrated how the application of an insertion force on biological tissue such as skin is absorbed, since it appears that the underlying subcutaneous layer of the gelatine gel at its highest fluid content was unable to withstand the clinical applicator's insertion force. Generally, the clinical applicator's insertion force was higher than the impact applicator's insertion force and was in the order of 2–7 times the force produced by the impact applicator. In this thesis, both devices produced reproducible microneedle penetration of both skin models. Therefore, the impact applicator at a relatively lower insertion force yielded similar if not better results when compared to the outcome of tests involving the clinical applicator.

The other parameter that contributed to the impact applicator performance was the influence of insertion velocity. Most microneedle studies have relied on only insertion force (Park et al., 2005; Donnelly et al., 2010; Kochhar et al., 2013b; Olatunji et al., 2013) or only insertion velocity (Verbaan et al., 2008; van der Maaden et al., 2014) to assess successful microneedle perforation of skin. The novelty of the work carried out in this thesis was the ability to vary insertion force and insertion velocity using the impact applicator setup.

Furthermore, the relatively low insertion force and low insertion velocity using the impact applicator system provides an alternative applicator design for Renephra to achieve reproducible perforation of skin.

5.5.5 The effect of microneedle geometry

For the impact and clinical applicator, reproducible penetration occurred in abdominal and back skin models at all gelatine concentrations with Design 2 microneedles. The clinical applicator produced better perforation results with Design 2 microneedles as compared to Design 1 microneedles. This could be due to an inherent design feature of the clinical applicator, as it has already been demonstrated through the work carried out in this thesis that the clinical applicator produced a higher frequency of smaller perforations in skin with Design 2 microneedles. This outcome indicates that for the clinical applicator, the length of the microneedles is important for effective skin penetration. Hence, as the results have shown, the length of the shorter Design 1 microneedles is not adequate for effective skin penetration using the clinical applicator.

Although the magnitude of force produced by the clinical applicator was similar for both Design 1 and 2 microneedles, variables such as needle density differed. This difference meant that a greater insertion force per microneedle was acting on Design 1 microneedles (0.051 N/microneedle) as compared to Design 2 microneedles (0.011 N/microneedle). Despite the lower force applied to Design 2 microneedles, it still produced better penetration results when compared to the penetration results of Design 1 microneedles. Therefore, the result reinforces the fact that clinical applicator performance is influenced by microneedle geometry.

Contrastingly, the impact applicator system was not influenced by microneedle geometry, which means that both Design 1 and 2 microneedles can be successfully applied to skin. Furthermore, comparing the insertion force per microneedle applied to Design 1 microneedles by both applicators showed an insertion force of 0.007 N/microneedle for the impact applicator as compared to the clinical applicator's insertion force of 0.051 N/microneedle. The value of the clinical applicator's insertion force was more than 7 times that of the impact applicator. Despite this difference in insertion force per microneedle, the

impact applicator still had a higher perforation depth as compared to the clinical applicator. The better perforation depth produced by the impact applicator could also be due to contributions from insertion velocity.

Moreover, the highest perforation depth for Design 1 microneedles (Fig. 90) showed that the impact applicator caused 98% of the microneedle length to disrupt skin's layers as compared to the deformation caused by the clinical applicator which only involved 56% of the microneedle length. In addition, for Design 2 microneedles, the insertion force per microneedle for impact applicator was 0.004 N/microneedle as compared to 0.011 N/microneedle for the clinical applicator. Again, the value of the clinical applicator insertion force per microneedle was more than twice that of the impact applicator. Furthermore, the highest perforation depth for Design 2 microneedles (Fig. 90) showed that at this comparatively lower insertion force, the impact applicator caused 52% of the microneedle length to disrupt skin's layers. For the clinical applicator however, with more than twice the insertion force as compared to the impact applicator only caused deformation in tissue utilising 65% of the Design 2 microneedle length. Therefore, the insertion force and the geometry of the microneedles (i.e. needle density, interspacing and needle length) influence how microneedles interact with skin for the clinical applicator.

Generally, a higher number of deformations caused by the clinical applicator were found in the first category at a measurement range of $\leq$ 10 000 μm^2, where the stratum corneum is disrupted and the deformation extends into the epidermis. And the more significant deformations caused by the impact applicator were located within the epidermis at a measurement range of 10 000–20 000 μm^2. This observation was consistent with the result of the perforation depth, which showed that for the highest perforation depth, some of Design 1

microneedles were fully embedded in skin for the impact applicator as compared to more than half the length of Design 2 microneedles embedded in skin for the clinical applicator.

Although, it was not possible to test whether or not the nerves were stimulated due to microneedle application for either *in vitro* applicator studies, the literature has already established that microneedle projections of 1500 μm or more will stimulate the nerves in skin and thus cause pain as they reach into the dermis (Gill et al., 2008; Gupta et al., 2011), therefore, Design 1 and Design 2 microneedles of length 356 μm and 552 μm respectively were not within the threshold to cause pain. Furthermore, *in vivo* studies using Design 2 microneedles inserted into skin with the comparatively higher insertion force of the clinical applicator demonstrated that patients experienced minimal pain (Renephra, 2015).

5.6 Summary

Several factors need to be considered for successful microneedle application to skin. Parameters such as microneedle geometry, microneedle applicator, insertion force and insertion velocity, influence of anatomical site and altering the fluid content in the subcutaneous layer of skin were investigated so as to determine effective microneedle penetration of skin.

The work in this thesis demonstrated that reproducible microneedle penetration was achieved utilising the impact and clinical applicators. Based on the outcome of individual studies of the impact and clinical applicator performance, the results showed that the impact applicator produced better penetration results as compared to the clinical applicator, as it produced better PE and caused more deformation in skin at a lower insertion force. In addition, a disadvantage of the clinical applicator was that its performance was dependent on microneedle design. The clinical applicator produced better results for Design 2 microneedles as compared to Design 1 microneedles. For the impact applicator however, its performance was not microneedle geometry dependent.

The insertion force was considerably higher for the clinical applicator as compared to the impact applicator. Despite the fact that more than twice the insertion force was produced by the clinical applicator on Design 2 microneedles as compared to the impact applicator, the magnitude of the insertion force was not commensurate with the size of the deformation created by the clinical applicator. In the case of the impact applicator, the magnitude of the force was commensurate with the size of the resulting deformation in skin.

The viscoelastic properties of skin contributed to microneedle performance, as thinner regions of skin such as abdominal tissue were less resistant to microneedle intervention.

Furthermore, the results of impact applicator studies showed that the insertion force applied to abdominal tissue was lower as compared to the force applied to back tissue.

The influence of the subcutaneous mimic was observed in the abdominal skin models following impact applicator tests, as the maximum force declined with increasing fluid content. Furthermore, a relationship between maximum force and the elastic modulus of the gelatine gels of the subcutaneous mimic was also established, because an increase in the elastic modulus of the gelatine gels resulted in an increase in maximum force. Hence, for microneedle application studies, contributions from the subcutaneous layer of skin should not be ignored as it affects parameters such as force, which influence microneedle behaviour in skin.

For effective microneedle application to skin, the impact applicator is a more suitable device because it operates at a relatively low insertion force and insertion velocity as compared to the clinical applicator. It also produced larger deformations within skin, which is important for the success of microneedle technology like the TFR, as fluid can be more readily extracted from the larger fissure. Furthermore, the ability to control the force and velocity means that the parameters of the impact applicator can be tailored to suit specific patient requirements.

Chapter 6

6. Conclusions and Further Work

6.1 Summary

Fluid overload or oedema is associated with heart and kidney failure and remains a global challenge. Based on work by Renephra, a novel medical device, the TFR utilising microneedle technology is under development for the relief of fluid overload. TFR could lead to a reduction in the amount of fluid overload or oedema and improved patient prognosis. As such, there was a need to understand the mechanical behaviour of skin and how it influences the performance of microneedle devices. In order to investigate this, microneedle tests on skin were necessary, however, most *in vitro* and *ex vivo* experimentation studies used to evaluate microneedle performance do not consider the biomechanical properties of skin or that of its subcutaneous layers. Therefore, a representative *in vitro* skin model was developed for microneedle application studies. Typically, microneedles are not designed to travel beyond the epidermis to the dermis where nerve endings may be stimulated or blood vessels damaged. Hence, minimal or no pain or bleeding occurs to the patient following microneedle application. Despite significant advances in the field of microneedles, the complexity of the mechanical behaviour of skin coupled with the inherent elasticity of the stratum corneum still pose a challenge for microneedle application.

The primary aim of the work carried out in this thesis was to investigate microneedle performance in a representative *in vitro* skin model by establishing the optimal parameters for reproducible penetration of skin. Furthermore, by altering the fluid content in the subcutaneous layer of the skin model, an understanding of the interaction between the biomechanics of the skin layer and microneedles was revealed. Additional parameters such as

microneedle geometry, applicator type further established the intricacies associated with producing repeatable perforation of skin.

6.2 Conclusions

The aims and objectives of this study were achieved using a range of techniques, namely; impact applicator tests, clinical applicator tests, micromechanical tests using dynamic nanoindentation, methylene blue staining, H&E image analysis and Image SXM custom image analysis software. Consequently, the results of the experimental phase of the study using the aforementioned techniques and material acquired within the literature led to the following conclusions:

6.2.1 Experimental analysis of the mechanical properties of skin

Micromechanical tests were conducted on skin samples from the abdominal and back regions of neonatal pigs; on three concentrations of the gelatine gels, as the fourth gelatine gel concentration was too compliant and on Perma-Gel®. Perma-Gel® produced the highest elastic modulus, which showed that it made a significant contribution to the other layers in the skin model. Of the gelatine gels, the gel with the lowest water content produced the highest elastic modulus. Furthermore, the elastic modulus decreased with increasing water content in the gelatine gels. This observation demonstrated that excessive fluid in the skin model compromised its mechanical integrity. The back region of skin produced a higher elastic modulus as compared to the abdominal region. The physical attributes of the back region were also different from the abdominal region and could also explain the difference in their mechanical properties. For instance, back tissue was thicker and stiffer than abdominal tissue.

Skin is an extremely complex functional system made of three stratified layers that are made up of sub-layers. The natural function of skin is to act as a chemical barrier, limiting

penetration by foreign substances and preventing loss of water and other fluids. The barrier function is located in the stratum corneum. In order to breach the stratum corneum for microneedle application, numerous *in vitro* tests using microneedles were carried out on a variation of abdominal and back skin models. The literature review highlighted that unrepresentative or even inappropriate experimental skin models had been used previously in other studies. The main drawback with the skin models used in the literature was that the material used as underlying substrates were not representative of biological material and would therefore exhibit a different mechanical behaviour as compared to a biological material like tissue fluid or muscle found in skin's underlying layers. Therefore, the representative *in vitro* skin model used in this thesis comprised neonatal porcine skin, gelatine gels at various concentrations to mimic the subcutaneous layer and Perma-Gel® to mimic muscle behaviour and to also provide adequate support. Furthermore, for a reasonable evaluation of microneedle interaction with skin, it was important to establish this type of representative skin model.

6.2.2 Development of the impact applicator system

The second objective was to develop an impact applicator system. The literature covered numerous designs for a microneedle delivery device such as an electrically driven applicator, an actuator driven applicator, a Dermaroller® and syringe applicators etc. For reproducible microneedle application to skin, an external force was required. After careful consideration of these various designs, it was imperative to develop an impact applicator that was suitable for purpose. The literature recommended a velocity in excess of 2 ms^{-1} as a reasonable microneedle insertion velocity. Therefore, a dropped weight impact-testing rig was developed that could produce velocities in excess of 1 ms^{-1}. Furthermore, the force could be measured from the drop mass using a force transducer.

The optimal parameters for reproducible microneedle penetration of skin utilising the

impact applicator setup were established in this study for Design 1 microneedles on skin Model 3B and it was 3 ms^{-1} velocity with a 36 g drop mass. These parameters were used for the rest of the study involving Design 2 microneedles on abdominal and back skin models at all gelatine gel concentrations.

The results of the impact applicator setup demonstrated that the mechanical behaviour of skin influences microneedle performance. The microneedle geometry also influenced penetration, as the less densely populated Design 1 microneedles caused significant deformation within skin's layers as compared to the more densely populated Design 2 microneedles.

6.2.3 The clinical applicator system

The third objective was to carry out a study using the clinical applicator and to compare the results with the impact applicator system. The study revealed that both applicators produced reproducible microneedle penetration. The impact applicator performed better than the clinical applicator because it had better PE, caused more deformation in skin at a relatively lower insertion force as compared to the clinical applicator. Moreover, the performance of the impact applicator was not affected by microneedle geometry, which was not the case with the clinical applicator as it produced poorer perforation results with Design 1 microneedles as compared to Design 2 microneedles. The clinical applicator insertion force was about twice that of the impact applicator insertion force for Design 2 microneedles and more than seven times that of the impact applicator insertion force for Design 1 microneedles.

Ideally, microneedle application should be contained within the epidermis in order to avoid stimulation of nerve endings and blood vessels that may cause pain and bleeding *in vivo*. Therefore, the comparison study identified the impact applicator as the preferred method of microneedle application because penetration could be achieved at a relatively low insertion force, with the deformations contained within the epidermis.

Although, the research in this thesis did not involve ISF extraction, the microneedle penetration studies *in vitro* were important in determining the effects of Design 2 microneedles perforations across the layers through histology staining and image analysis to complement the *in vivo* work carried out by Renephra Ltd. Their recent studies show that ISF was extracted following the application of Design 2 microneedles and negative pressure therapy in 56% cases as compared to the use of a hypodermic needle, which gave a 10% success rate. The ISF extracted was 800 mL over 4 hours using a 10 × 10 cm surface (Renephra, 2015). Mukerjee et al. was arguably the first to successfully demonstrate the feasibility of using hollow microneedles and capillary action to extract ISF from skin (Mukerjee et al., 2004). Furthermore, Wang et al., (2005) extracted a considerably small amount of ISF (1–10 μL) for glucose monitoring using solid microneedles and negative pressure therapy.

6.2.4 Quantitative image analysis of microneedle treated skin

The fourth objective was to conduct extensive image analysis of the perforated skin. The evaluation of the microchannels created in the skin following microneedle treatment was determined through methylene blue staining, H&E staining and quantitative image analysis. The methylene blue dye adhered to the microchannels created in the tissue, the histology images showed the depth of microneedle penetration through skin's sub-layers and image analysis provided the size of the deformation area within the H&E stained images.

Although the methylene blue stained images confirmed successful breach of the stratum corneum, it was the H&E stained images that indicated that in some instances not all the microneedles had completely bypassed the stratum corneum to fully perforate the epidermis. Furthermore, the H&E stained images also revealed those instances where the deformation caused by microneedle intervention had travelled beyond the epidermis into the dermis.

For a complete analysis of the H&E stained images, it was important to carry out image analysis of over 30 images per skin model in order to better determine the effects of the microneedle deformation through skin's layers. Interestingly, the image analysis demonstrated that the clinical applicator device is affected by microneedle geometry as demonstrated by the differences in magnitude of the deformations caused by Design 1 and 2 microneedles in Model 3B.

A pilot study of 3D imaging of microneedle treated skin was conducted using XMT to compliment the analysis of H&E images. The results of the XMT analysis showed that it was a promising technique for microneedle application to skin. Further details of XMT can be found in Section 8.1 of the Appendix.

Finally, the findings in this project such as the optimal parameters for reproducible microneedle penetration of skin, the contribution of skin's mechanical properties, the effects of a variation of the water content in the gelatine gels as a mimic for tissue fluid in the skin model, the influence of anatomical site, microneedle geometry and the magnitude of deformations caused by microneedle treatment of skin could be used to aid the development of Renephra's microneedle fluid extraction device (TFR). Based on the outcome of the study, Renephra could develop an applicator similar to the impact applicator that can measure the insertion force and insertion velocity, as it has been demonstrated that the clinical applicator produces high forces and is affected by microneedle geometry.

6.3 Further Work

The work carried out during this study provides important information related to the mechanical behaviour of skin and how it affects microneedle performance. Based on the work carried out during this study, there are still many opportunities for further advances through research and a few potential studies are mentioned in this section.

6.3.1 3D image analysis of microneedle treated skin

The emergence of micro XMT as an imaging tool for soft tissue could provide the opportunity to image a whole sample of microneedle treated tissue, without going down the laborious route of H&E staining. The limitation with H&E staining is that it affords only a small area for sectioning, with the remaining tissue containing vital information discarded. The main drawback of micro XMT imaging of soft tissue is that grayscale colour contrast is challenging to decipher. The non-destructive method of examining skin using XMT is a promising technique for determining microneedle induced breach in skin. The challenge remains that consideration needs to be given to an adequate staining protocol in order to achieve good contrast definition between skin's layers without having to undergo the arduous and time-consuming task of having to carry out a significant amount of manual segmentation of the images caused by noise in the data or poor contrast.

Further, development of the staining and image segmentation methods for soft tissue XMT may make this a powerful technique for microneedle research.

6.3.2 Optical Coherence Tomography studies of microneedle application to skin

The primary focus of this thesis was on the *in vitro* studies of microneedle performance in a representative skin model. The data obtained from the work carried out on the representative *in vitro* skin model is useful for improving the microneedle device, however, the *in vitro* skin model still has a limitation in that it cannot in its entirety fully mimic all the mechanical characteristics of the *in vivo* skin such as anisotropy, viscoelasticity, non-linearity, patient age, progression of the disease. These factors contribute to the overall behaviour of skin and its interaction with microneedles.

Therefore, an exhaustive *in vivo* investigation into microneedles interaction with skin should be conducted using techniques like OCT as shown in Fig. 93. The stratum corneum is visible in the image; however, it is challenging to determine the epidermal and dermal layers in Fig. 93b. Therefore, further work is required to ascertain whether OCT can be utilised for *in vivo* studies of microneedle perforated skin.

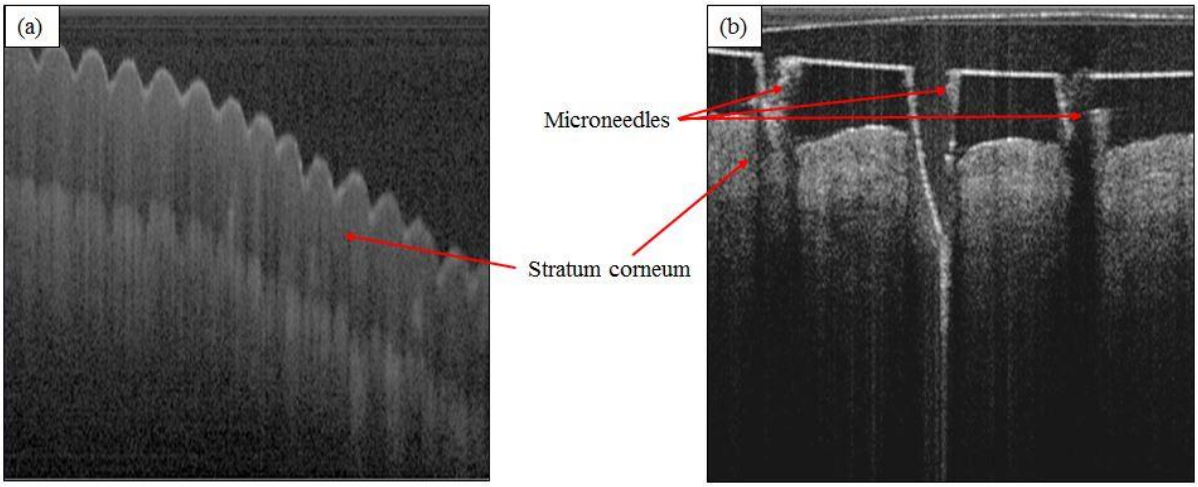

Figure 93 Optical Coherence Tomography images of skin, where (a) palmar region of skin with no microneedle perforations and (b) skin from the inner wrist with microneedles embedded. (Courtesy Renephra Ltd).

6.3.3 Impact applicator

The results produced by the impact applicator demonstrated that reproducible penetration of skin could be achieved at a relatively low force. It was further demonstrated that penetration was achieved irrespective of Design 1 or Design 2 microneedles, which is a good indication that it can perform well with some changes in microneedle design. As the applicator system was a rather large setup that was difficult to move to various locations, it would be advantageous for a smaller device to be manufactured in its place. The new device could be based on the parameters of the improved impact applicator setup, thus having the ability to vary its velocity and force. This device could then be used for further *in vitro* studies, whereby the design of microneedles are restricted to just one variable i.e. varying only the interspacing between individual microneedles or only the height of the microneedles. As a

further improvement to the subcutaneous mimic in the *in vitro* skin model, fluid could be injected into a membrane placed within the subcutaneous layer. Furthermore, the device could possibly be utilised for *in vivo* studies.

Chapter 7

7. References

Abramoff MD, Magalhaes PJ, Ram SJ. 2004. Image Processing with ImageJ. Biophotonics International 11:36-42.

Adams KF, Jr., Fonarow GC, Emerman CL, LeJemtel TH, Costanzo MR, Abraham WT, Berkowitz RL, Galvao M, Horton DP. 2005. Characteristics and Outcomes of Patients Hospitalized for Heart Failure in the United States: Rationale, Design, and Preliminary Observations from the First 100,000 Cases in the Acute Decompensated Heart Failure National Registry (ADHERE). American Heart Journal 149:209-216.

Agache PG, Monneur C, Leveque JL, de Rigal J. 1980. Mechanical Properties and Young's Modulus of Human Skin In Vivo. Archives of Dermatological Research 269:221-232.

Agar JWM. 2012. Personal Viewpoint: Hemodialysis-Water, Power and Waste Disposal: Rethinking our Environmental Responsibilities. Hemodialysis International 16:6-10.

Ahearne M, Yang Y, El Haj AJ, Then KY, Liu KK. 2005. Characterizing the Viscoelastic Properties of Thin Hydrogel-Based Constructs for Tissue Engineering Applications. Journal of the Royal Society Interface 2:455-463.

Akhtar R, Draper ER, Adams DJ, Pfaff H. 2015. Complex Shear Modulus of Hydrogels Using a Dynamic Nanoindentation Method. In: Tekalur SA, Zavattieri, Pablo, Korach, Chad S editor. 5th International Symposium on the Mechanics of Biological Systems and Materials, Volume 6 of the Proceedings of the 2015 SEM Annual Conference & Exposition on Experimental and Applied Mechanics. Costa Mesa, USA: Springer. p 141-145.

Al-Qallaf B, Das DB. 2008. Optimization of Square Microneedle Arrays for Increasing Drug Permeability in Skin. Chemical Engineering Science 63:2523-2535.

Alexander H, Cook TH. 1977. Accounting for Natural Tenson in the Mechanical Testing of Human Skin. The Journal of Investigative Dermatology 69:310-314.

Antlanger M, Hecking M, Haidinger M, Werzowa J, Kovarik JJ, Paul G, Eigner M, Bonderman D, Hörl WH, Säemann MD. 2013. Fluid Overload in Hemodialysis Patients: A Cross-Sectional Study to Determine its Association with Cardiac Biomarkers and Nutritional Status. BioMed Central Nephrology 14:1-10.

Arora A, Prausnitz MR, Mitragotri S. 2008. Micro-Scale Devices for Transdermal Drug Delivery. International Journal of Pharmaceutics 364:227-236.

Avon SL, Wood RE. 2005. Porcine Skin as an In Vivo Model for Ageing of Human Bite Marks. The Journal of Forensic Odonto-Stomatology 23:30-39.

Awad HA, Wickham MQ, Leddy HA, Gimble JM, Guilak F. 2004. Chondrogenic Differentiation of Adipose-Derived Adult Stem Cells in Agarose, Alginate and Gelatin Scaffolds. Biomaterials 25:3211-3222.

Bader DL, Bowker P. 1983. Mechanical Characteristics of Skin and Underlying Tissues In Vivo. Biomaterials 4:305-308.

Badran MM, Kuntsche J, Fahr A. 2009. Skin Penetration Enhancement by a Microneedle Device (Dermaroller) In Vitro: Dependency on Needle Size and Applied Formulation. European Journal of Pharmaceutical Sciences 36:511-523.

Barbenel JC, Evans JH. 1977. The Time-Dependent Mechanical Properties of Skin. The Journal of Investigative Dermatology 69:318-320.

Barrett C, Dawson K, O'Mahony C, O'Riordan A. 2015. Development of Low Cost Rapid Fabrication of Sharp Polymer Microneedles for In Vivo Glucose Biosensing Applications. ECS Journal of Solid State Science and Technology 4:S3053-S3058.

Bart BA. 2009. Treatment of Congestion in Congestive Heart Failure: Ultrafiltration is the Only Rational Initial Treatment of Volume Overload in Decompensated Heart Failure. Circulation: Heart Failure 2:499-504.

Bates DO, Levick JR, Mortimer PS. 1994. Quantification of Rate and Depth of Pitting in Human Edema using an Electronic Tonometer. Lymphology 27:159-172.

Berry C, Murdoch DR, McMurray JJ. 2001. Economics of Chronic Heart Failure. European Journal of Heart Failure 3:283-291.

Bhushan B, Tang W, Ge S. 2010. Nanomechanical Characterization of Skin and Skin Cream. Journal of Microscopy 240:135-144.

Birchall J, Coulman S, Pearton M, Allender C, Brain K, Anstey A, Gateley C, Wilke N, Morrissey A. 2005. Cutaneous DNA Delivery and Gene Expression in Ex Vivo Human Skin Explants via Wet-Etch Micro-Fabricated Microneedles. Journal of Drug Targeting 13:415-421.

Bischoff JE, Arruda EM, Grosh K. 2000. Finite Element Modelling of Human Skin using an Isotropic Nonlinear Elastic Constitutive Model. Journal of Biomechanics 33:645-652.

Bleyer AJ, Russell GB, Satko SG. 1999. Sudden and Cardiac Death Rates in Haemodialysis Patients. Kidney International 55:1553-1559.

Bouwstra JA, Verbaan FJ, Van den Berg DJ. 2009. Microneedle Injecting Apparatus. In. Netherlands.

Brater DC. 1998. Diuretic Therapy. The New England Journal of Medicine 339:387-395.

Brown LM, Liu KD, Matthay MA. 2009. Measurement of Extravascular Lung Water using the Single Inidcator Method in Patients: Research and Potential Clinical Value. American Journal of Physiology Lung Cellular and Molecular Physiology 297:L547-L558.

Buie HR, Campbell GM, Klinck RJ, MacNeil JA, Boyd SK. 2007. Automatic Segmentation of Cortical and Trabecular Compartments Based on a Dual Threshold Technique for In Vivo Micro-CT Bone Analysis. Bone 41:505-515.

Burgin LV, Aspden RM. 2007. A Drop Tower for Controlled Impact Testing of Biological Tissues. Medical Engineering and Physics 29:525-530.

Cardiff RD, Miller CH, Munn RJ. 2014. Manual Hematoxylin and Eosin Staining of Mouse Tissue Sections. Cold Spring Harbor Protocols 2014:655-658.

Caron-Laramee A, Brouillette M. 2014. Spherical Indentation Testing on Ballistic Gelatin and Perma-Gel. In: Proceedings of the ASME 2014 International Mechanical Engineering Congress and Exposition. Montreal, Quebec, Canada: ASME. p 1-6.

Caspers PJ, Lucassen GW, Bruining HA, Puppels GJ. 2000. Automated Depth-Scanning Confocal Raman Microspectrometer for Rapid In Vivo Determination of Water Concentration Profiles in Human Skin. Journal of Raman Spectroscopy 31:813-818.

Cavalli A, DelVecchio L, Manzoni C, Locatelli F. 2010. Haemodialysis: Yesterday, Today and Tomorrow. Minerva Urologica E Nefrologica 62:1-12.

Chan JK. 2014. The Wonderful Colors of the Hematoxylin-Eosin Stain in Diagnostic Surgical Pathology. International Journal of Surgical Pathology 22:12-32.

Chao CY, Zheng YP, Cheing GL. 2012. The Association between Skin Blood Flow and Edema on Epidermal Thickness in the Diabetic Foot. Diabetes Technology and Therapeutics 14:602-609.

Chin MP, Wrolstad D, Bakris GL, Chertow GM, de Zeeuw D, Goldsberry A, Linde PG, McCullough PA, McMurray JJ, Wittes J, Meyer CJ. 2014. Risk Factors for Heart Failure in Patients with Type 2 Diabetes Mellitus and Stage 4 Chronic Kidney Disease Treated with Bardoxolone Methyl. Journal of Cardiac Failure 20:953-958.

Cho S, Atwood JE. 2002. Peripheral Edema. The American Journal of Medicine 113:580-586.

Cilurzo F, Minghetti P, Sinico C. 2007. Newborn Pig Skin as a Model Membrane in In Vitro Drug Permeation Studies: A Technical Note. PharmSciTech 8:E1-E4.

Cook C, Cole G, Asaria P, Jabbour R, Francis DP. 2014. The Annual Global Economic Burden of Heart Failure. International Journal of Cardiology 171:368-376.

Costanzo MR, Saltzberg M, O'Sullivan J, Sobotka P. 2005. Early Ultrafiltration in Patients with Decompensated Heart Failure and Diuretic Resistance. Journal of the American College of Cardiology 46:2047-2051.

Cotter G, Metra M, Milo-Cotter O, Dittrich HC, Gheorghiade M. 2008. Fluid Overload in Acute Heart Failure - Re-Distribution and Other Mechanisms Beyond Fluid Accumulation. European Journal of Heart Failure 10:165-169.

Coulman SA, Birchall JC, Alex A, Pearton M, Hofer B, O'Mahony C, Drexler W, Považay B. 2010. In Vivo, In Situ Imaging of Microneedle Insertion into the Skin of Human Volunteers Using Optical Coherence Tomography. Pharmaceutical Research 28:66-81.

Crichton ML, Ansaldo A, Chen X, Prow TW, Fernando GJ, Kendall MA. 2010. The Effect of Strain Rate on the Precision of Penetration of Short Densely-Packed Microprojection Array Patches Coated with Vaccine. Biomaterials 31:4562-4572.

Crichton ML, Chen X, Huang H, Kendall MA. 2013. Elastic Modulus and Viscoelastic Properties of Full Thickness Skin Characterised at Micro Scales. Biomaterials 34:2087-2097.

Croft JB, Giles WH, Pollard RA, Keenan NL, Casper ML, Anda RF. 1999. Heart Failure Survival Among Older Adults in the United States. The Journal of the American Medical Association Internal Medicine 159:505-510.

Dabboue H, Builles N, Frouin É, Scott D, Ramos J, Marti-Mestres G. 2015. Assessing the Impact of Mechanical Damage on Full-Thickness Porcine and Human Skin using an In Vitro Approach. BioMed Research International 2015:1-10.

Daly CH, Odland GF. 1979. Age-Related Changes in Mechanical Properties of Human Skin. The Journal of Investigative Dermatology 73:84-87.

Dapson RW. 2005. Dye-Tissue Interactions: Mechanisms, Quantification and Bonding Parameters for Dyes used in Biological Staining. Biotechnic and Histochemistry 80:49-72.

Davis SP, Landis BJ, Adams ZH, Allen MG, Prausnitz MR. 2004. Insertion of Microneedles into Skin: Measurement and Prediction of Insertion Force and Needle Fracture Force. Journal of Biomechanics 37:1155-1163.

Davis SP, Martanto W, Allen MG, Prausnitz MR. 2005. Hollow Metal Microneedles For Insulin Delivery To Diabetic Rats. IEEE Transactions on Biomedical Engineering 52:909-915.

De Rigal J, Leveque JL. 1985. In Vivo Measurement of the Stratum Corneum Elasticity. Bioengineering and Skin 1:13-23.

Ding Z, Verbaan FJ, Bivas-Benita M, Bungener L, Huckriede A, van den Berg DJ, Kersten G, Bouwstra JA. 2009. Microneedle Arrays for the Transcutaneous Immunization of Diphtheria and Influenza in BALB/c Mice. Journal of Controlled Release 136:71-78.

Diridollou S, Patat F, Gens F, Vaillant L, Black D, Lagarde JM, Gall Y, Berson M. 2000. In Vivo Model of The Mechanical Properties of Human Skin Under Suction. Skin and Research Technology 6:214-221.

Donnelly RF, Garland MJ, Morrow DIJ, Migalska K, Singh TRR, Majithiya R, Woolfson AD. 2010. Optical Coherence Tomography is a Valuable Tool in the Study of the

Effects of Microneedle Geometry on Skin Penetration Characteristics and In-Skin Dissolution. Journal of Controlled Release 147:333-341.

Donnelly RF, Majithiya R, Singh TRR, Morrow DIJ, Garland MJ, Demir YK, Migalska K, Ryan E, Gillen D, Scott CJ, Woolfson AD. 2011. Design, Optimization and Characterisation of Polymeric Microneedle Arrays Prepared by a Novel Laser-Based Micromoulding Technique. Pharmaceutical Research 28:41-57.

Dunn MG, Silver FH. 1983. Viscoelastic Behaviour of Human Connective Tissue: Relative Contribution of Viscous and Elastic Components. Connective Tissue Research 12:59-70.

Ebah LM. 2012. Extraction and Analysis of Interstitial Fluid and Characterisation of the Interstitial Compartment in Kidney Disease. In: School of Biomedicine. Manchester: University of Manchester. p 1 - 274.

Ebenstein DM, Pruitt LA. 2004. Nanoindentation of Soft Hydrated Materials for Application to Vascular Tissues. Journal of Biomedical Materials Research Part A 69:222-232.

Ebenstein DM, Pruitt LA. 2006. Nanoindentation of Biological Materials. Nano Today 1:26-33.

Edwards C, Marks R. 1995. Evaluation of Biomechanical Properties of Human Skin. Clinics in Dermatology 13:375-380.

Elias PM. 1983. Epidermal Lipids, Barrier Function and Desquamation. The Journal of Investigative Dermatology 80:44s-49s.

Ely JW, Osheroff JA, Chambliss ML, Ebell MH. 2006. Approach to Leg Edema of Unclear Etiology. Journal of the American Board of Family Medicine 19:148-160.

Feest TG, Rajamahesh J, Byrne C, Ahmad A, Ansell D, Burden R, Roderick PJ. 2004. Trends in Adult Renal Replacement Therapy in the UK: 1982-2002. QJM 98:21-28.

Fenske NA, Lober CW. 1986. Structural and Functional Changes of Normal Aging Skin. Journal of the American Academy of Dermatology 15:571-585.

Fercher AF. 2010. Optical Coherence Tomography – Development, Principles, Applications. Zeitschrift für Medizinische Physik 20:251-276.

Fercher AF, Mengedoht K, Werner W. 1988. Eye-length Measurement by Interferometry with Partially Coherent Light. Optics Letters 13:186-188.

Ferrario M, Moissl U, Garzotto F, Cruz DN, Clementi A, Brendolan A, Tetta C, Gatti E, Signorini MG, Cerutti S, Ronco C. 2014. Effects of Fluid Overload on Heart Rate Variability in Chronic Kidney Disease Patients on Hemodialysis. BMC Nephrology 15:1-11.

Fischer AH, Jacobson KA, Rose J, Zeller R. 2008. Hematoxylin and Eosin Staining of Tissue and Cell Sections. CSH Protocols 3:1-2.

Flores S, Rider AC. 2016. Mesoamerican Nephropathy: A Novel Case of Kidney Failure in a US ED. American Journal of Emergency Medicine 34:1323.e1325-1323.e1326.

Fourtanier A, Berrebi C. 1989. Miniature Pig as an Animal Model to Study Photoaging. Photochemistry and Photobiology 50:771 - 784.

Frank Peacock W, Soto KM. 2010. Current Technique of Fluid Status Assessment. Congestive Heart Failure 16 Suppl 1:S45-S51.

Fung YC. 1993. Biomechanics: Mechanical Properties of Living Tissues, 2nd ed. New York: Springer-Verlag.

Garner L. 2004. Contact Dermatitis To Metals. Dermatologic Therapy 17:321-327.

Geerligs M, Peters GW, Ackermans PA, Oomens CW, Baaijens FP. 2010b. Does Subcutaneous Adipose Tissue Behave as an (Anti-)Thixotropic Material? Journal of Biomechanics 43:1153-1159.

Geerligs M, Peters GWM, Ackermans PAJ, Oomens CWJ, Baaijens FPT. 2008. Linear Viscoelastic Behavior of Subcutaneous Adipose Tissue. Biorheology 45:677-688.

Geerligs M, van Breemen L, Peters G, Ackermans P, Baaijens F, Oomens C. 2011. In vitro Indentation to Determine the Mechanical Properties of Epidermis. Journal of Biomechanics 44:1176-1181.

Gerstel MS, Place VA. 1976. Drug Delivery Device. In. United States: Alza Corporation.

Gibbs LME, Addington-Hall J, Gibbs JSR. 1998. Dying from Heart Failure: Lessons from Palliative Care. British Medical Journal 317:961-962.

Gibson T, Stark H, Evans JH. 1968. Directional Variational in Extensibility of Human Skin In Vivo. Journal of Biomechanics 2:201-204.

Gill HS, Denson DD, Burris BA, Prausnitz MR. 2008. Effect of Microneedle Design on Pain in Human Volunteers. Clinical Journal of Pain 24:585-594.

Glaister DH. 1975. Human Tolerance to Impact Acceleration. Injury: The British Journal of Accident Surgery 9:191-198.

Gniadecka M. 1996. Localisation of Edema in Lipodermasclerosis, Lymphedema and Cardiac Insufficency. Journal of American Academy of Dermatology 35:37-41.

Gniadecka M, Serup J, Sondergaard J. 1994. Age-Related DIurnal Changes of Dermal Oedema: Evaluation by High-Frequency Ultrasound. British Journal of Dermatology 131:849-855.

Graham HK, Akhtar R, Kridiotis C, Derby B, Kundu T, Trafford AW, Sherratt MJ. 2011. Localised Micro-Mechanical Stiffening in the Ageing Aorta. Mechanisms of Ageing and Development 132:459-467.

Granta LD. 2003. Material Data Book. In. Cambridge University Engineering Department. p 1-37.

Grassmann A, Gioberge S, Moeller S, Brown G. 2005. ESRD Patients in 2004: Global Overview of Patient Numbers, Treatment Modalities and Associated Trends. Nephrology Dialysis Transplantation 20:2587-2593.

Groves RB. 2011. Quantifying the Mechanical Properties of Skin In Vivo and Ex Vivo to Optimise Microneedle Device Design. In: Cardiff University.

Groves RB, Coulman SA, Birchall JC, Evans SL. 2012. Quantifying the Mechanical Properties of Human Skin to Optimise Future Microneedle Device Design. Computer Methods in Biomechanics and Biomedical Engineering 15:73-82.

Groves RB, Coulman SA, Birchall JC, Evans SL. 2013. An Anisotropic, Hyperelastic Model for Skin: Experimental Measurements, Finite Element Modelling and Identification of Parameters for Human and Murine Skin. Journal of Mechanical Behaviour of Biomedical Materials 18:167-180.

Gupta J, Gill HS, Andrews SN, Prausnitz MR. 2011. Kinetics of Skin Resealing after Insertion of Microneedles in Human Subjects. Journal of Controlled Release 154:148-155.

Guyton AC, Granger HJ, Taylor AE. 1971. Interstitial Fluid Pressure. Physiological Reviews 51:527 - 563.

Hamer RA, El-Nahas AM. 2006. The Burden of Chronic Kidney Disease. British Medical Journal 332:563-564.

Haq MI, Smith E, John DN, Kalavala M, Edwards C, Anstey A, Morrissey A, Birchall JC. 2009. Clinical Administration of Microneedles: Skin Puncture, Pain and Sensation. Biomedical Microdevices 11:35-47.

Hay J. 2011. Complex Shear Modulus of Commerical Gelatin by Instrumented Indentation. In: Agilent Technologies, Inc.

Hay J. 2012. Rapid Characterisation of Elastic Modulus and Hardness via Express Test. In: Agilent Technologies, Inc.

Hay J, Cherneva S. 2013. In Vitro Complex Shear Modulus of Bovine Muscle Tissue (Steak). In: Agilent Technologies, Inc.

Heilbronner R, Barrett S. 2014. Image Analysis in Earth Sciences. Springer Berlin Heidelberg.

Hendriks FM. 2001. Mechanical Behaviour of Human Skin In Vivo - A Literature Review. Koninklijke Philips Electronics NV.

Hendriks FM. 2005. Mechanical Behaviour of Human Epidermal and Dermal Layers In Vivo. In. Eindhoven: Eindhoven University of Technology.

Henry S, McAllister DV, Allen MG, Prausnitz MR. 1998. Microfabricated Microneedles a Novel Approach to Transdermal Drug Delivery. Journal of Pharmaceutical Sciences 87.

Holme MN, Schulz G, Deyhle H, Weitkamp T, Beckmann F, Lobrinus JA, Rikhtegar F, Kurtcuoglu V, Zanette I, Saxer T, Muller B. 2014. Complementary X-ray Tomography Techniques for Histology-Validated 3D Imaging of Soft and Hard Tissues using Plaque-Containing Blood Vessels as Examples. Nature protocols 9:1401-1415.

Holt CA, Evans SL. 2009. Measuring the Mechanical Properties of Human Skin In Vivo using Digital Image Correlation and Finite Element Modelling. The Journal of Strain Analysis for Engineering Design 44:337-345.

Huang D, Swanson EA, Lin CP, Schuman JS, Stinson WG, Chang W, Hee MR, Flotte T, Gregory K, Piuliafito CA, Fujimoto JG. 1991. Optical Coherence Tomography. Science, New Series 254:1178-1181.

Huang H, Fu C. 2007. Different Fabrication Methods of Out-of-Plane Polymer Hollow Needle Arrays and their Variations. Journal of Micromechanics and Microengineering 17:393-402.

Hung SC, Kuo KL, Peng CH, Wu CH, Lien YC, Wang YC, Tarng DC. 2014. Volume Overload Correlates with Cardiovascular Risk Factors in Patients with Chronic Kidney Disease. Kidney International 85:703-709.

Ianches M. 2015. PMMA Microneedles Specifications. In: 10x Technology.

Indermun S, Luttge R, Choonara YE, Kumar P, du Toit LC, Modi G, Pillay V. 2014. Current Advances in the Fabrication of Microneedles for Transdermal Delivery. Journal of Controlled Release 185:130-138.

Jacquemoud C, Bruyere-Garnier K, Coret M. 2007. Methodology to Determine Failure Characteristics of Planar Soft Tissues using a Dynamic Tensile Test. Journal of Biomechanics 40:468-475.

James W, Berger T, Elston D. 2006. Andrew's Diseases of the Skin: Clinical Dermatology. In, Eleventh ed: Saunders.

Jones ML, Bancroft JD, Gamble M. 2008. Theory and Practice of Histological Techniques. In: Elsevier, editor. Connective Tissue and Stains, 6th ed: Elsevier.

Kalantar-Zadeh K, Regidor DL, Kovesdy CP, Van Wyck D, Bunnapradist S, Horwich TB, Fonarow GC. 2009. Fluid Retention is Associated with Cardiovascular Mortality in Patients Undergoing Long-Term Hemodialysis. Circulation 119:671-679.

Kalluri H, Kolli CS, Banga AK. 2011. Characterization of Microchannels Created by Metal Microneedles: Formation and Closure. AAPS Journal 13:473-481.

Kelchen MN, Siefers KJ, Converse CC, Farley MJ, Holdren GO, Brogden NK. 2016. Micropore Closure Kinetics are Delayed following Microneedle Insertion in Elderly Subjects. Journal of Controlled Release 225:294-300.

Kendall MA, Chong YF, Cock A. 2007. The Mechanical Properties of the Skin Epidermis in Relation to Targeted Gene and Drug Delivery. Biomaterials 28:4968-4977.

Kerr M. 2012. Chronic Kidney Disease in England: The Human Financial Cost. NHS Kidney Care.

Kerr M, Bray B, Medcalf J, O'Donoghue DJ, Matthews B. 2012. Estimating the Financial Cost of Chronic Kidney Disease to the NHS in England. Nephrology Dialysis Transplantation 0:1-8.

Khanna P, Strom JA, Malone JI, Bhansali S. 2008. Microneedle-Based Automated Therapy for Diabetes Mellitus. Journal of Diabetes Science and Technology 2:1122-1129.

Khatyr F, Imberdis C, Vescovo P, Varchon D, Lagarde J. 2004. Model of the Viscoelastic Behaviour of Skin In Vivo and Study of Anisotropy. Skin and Research Technology 10:96-103.

Kim YC, Park JH, Prausnitz MR. 2012. Microneedles for Drug and Vaccine Delivery. Advanced Drug Delivery Reviews 64:1547-1568.

Kirk E, Kvorning SA. 1949. Quantitative Measurements of the Elastic Properties of the Skin and Subcutaneous Tissue in Young and Old Individuals. Journal of Gerontology 4:273-284.

Kitzman DW, Rich MW. 2010. Age Disparities in Heart Failure Research. Journal of American Medical Association 304:1950-1951.

Kochhar JS, Goh WJ, Chan SY, Kang L. 2013a. A Simple Method of Microneedle Array Fabrication for Transdermal Drug Delivery. Drug Development and Industrial Pharmacy 39:299-309.

Kochhar JS, Quek TC, Soon WJ, Choi J, Zou S, Kang L. 2013b. Effect of Microneedle Geometry and Supporting Substrate on Microneedle Array Penetration into Skin. Journal of Pharmaceutical Sciences 102:4100-4108.

Kolli CS, Banga AK. 2008. Characterization of Solid Maltose Microneedles and their Use for Transdermal Delivery. Pharmaceutical Research 25:104-113.

Kong XQ, Zhou P, Wu CW. 2011. Numerical Simulation of Microneedles' Insertion into Skin. Computer Methods in Biomechanics and Biomedical Engineering 14:827-835.

Kramer BK, Schweda F, Riegger GAJ. 1999. Diuretic Treatment and Diuretic Resistance in Heart Failure. The American Journal of Medicine 106:90-96.

Kwon J, Subhash G. 2010. Compressive Strain Rate Sensitivity of Ballistic Gelatin. Journal of Biomechanics 43:420-425.

Lanir Y, Fung YC. 1974. Two-Dimensional Mechanical Properties of Rabbit Skin - Experimental System II. Journal of Biomechanics 7:171-184.

Lara MF, Gonzalez-Gonzalez E, Speaker TJ, Hickerson RP, Leake D, Milstone LM, Contag CH, Kaspar RL. 2012. Inhibition of CD44 Gene Expression in Human Skin Models, using Self-Delivery Short Interfering RNA Administered by Dissolvable Microneedle Arrays. Human gene therapy 23:816-823.

Larson K, Ho HH, Anumolu PL, Chen TM. 2011. Hematoxylin and Eosin Tissue Stain in Mohs Micrographic Surgery: A Review. Dermatological Surgery 37:1089-1099.

Lasagni C, Seidenari S. 1995. Echographic Assessment of Age-Dependent Variations of Skin Thickness. Skin and Research Technology 1:81-85.

Lee JW, Choi SO, Felner EI, Prausnitz MR. 2011. Dissolving Microneedle Patch for Transdermal Delivery of Human Growth Hormone. Small 7:531-539.

Lee KY, Mooney DJ. 2001. Hydrogels for Tissue Engineering. Chemical Reviews 101:1869-1879.

Lee Y, Hwang K. 2002. Skin Thickness of Korean Adults. Surgical and Radiologic Anatomy 24:183-189.

Leveque JL, de Rigal J, Agache PG, Monneur C. 1980. Influence of Ageing on the In Vivo Extensibility of Human Skin at a Low Stress. Archives of Dermatological Research 269:127-135.

Levick JR. 1987. Flow Through Interstitium and Other Fibrous Matrices. Quarterly Journal of Experimental Physiology 72:409-438.

Li G, Badkar A, Nema S, Kolli CS, Banga AK. 2009. In Vitro Transdermal Delivery of Therapeutic Antibodies using Maltose Microneedles. International Journal of Pharmaceutics 368:109-115.

Li H, Low YS, Chong HP, Zin MT, Lee CY, Li B, Leolukman M, Kang L. 2015. Microneedle-Mediated Delivery of Copper Peptide Through Skin. Pharmaceutical Research 32:2678-2689.

Liu R, Zhang M, Jin C. 2016. In Vivo and In Situ Imaging of Controlled-Release Dissolving Silk Microneedles into the Skin by Optical Coherence Tomography. Journal of Biophotonics.

Liu X, Lu Z, Lewis R, Carré MJ, Matcher SJ. 2013. Feasibility of using Optical Coherence Tomography to Study the Influence of Skin Structure on Finger Friction. Tribology International 63:34-44.

Lo Gullo R, Mishra S, Lira DA, Padole A, Otrakji A, Khawaja RD, Pourjabbar S, Singh S, Shepard JA, Digumarthy SR, Kalra MK, Stone JR. 2015. Quantification of Interstitial Fluid on Whole Body CT: Comparison with Whole Body Autopsy. Forensic Science Medicine and Pathology 11:488-496.

Lo Presti D, Ingegnosi C, Strauss K. 2012. Skin and Subcutaneous Thickness at Injecting Sites in Children with Diabetes: Ultrasound Findings and Recommendations for Giving Injection. Pediatric diabetes 13:525-533.

Loizidou EZ, Inoue NT, Ashton-Barnett J, Barrow DA, Allender CJ. 2016. Evaluation of Geometrical Effects of Microneedles on Skin Penetration by CT Scan and Finite Element Analysis. European Journal of Pharmaceutics and Biopharmaceutics 107:1-6.

Manschot JFM, Brakkee AJM. 1986. The Measurement and Modelling of the Mechanical Properties of Human Skin In Vivo - Part I Journal of Biomechanics 19:511-515.

Markidou A, Shih WY, Shih WH. 2005. Soft-Materials Elastic and Shear Moduli Measurement using Piezoelectric Cantilevers. Review of Scientific Instruments 76:064302-064301 - 064302-064307.

Markman B, Barton FE. 1987. Anatomy of the Subcutaneous Tissue of the Trunk and Lower Extremity. Plastic and Reconstructive Surgery 80:248-254.

Martanto W, Davis SP, Holiday NR, Wang J, Gill HS, Prausnitz MR. 2004. Transdermal Delivery Of Insulin Using Microneedles In Vivo. Pharmaceutical Research 21:947-952.

McAllister DV. 2003. From the Cover: Microfabricated Needles for Transdermal Delivery of Macromolecules and Nanoparticles: Fabrication Methods and Transport Studies. Proceedings of the National Academy of Sciences 100:13755-13760.

McMurray JJ, Stewart W. 2000. Epidemiology, Aetiology, and Prognosis of Heart Failure. Heart 83:596-602.

Meijer R, Douven LF, Oomens CWJ. 1999. Characterisation of Anisotropic and Non-linear Behaviour of Human Skin In Vivo. Computer Methods in Biomechanics and Biomedical Engineering 2:13-27.

Mendez GF, Cowie MR. 2001. The Epidemiological Features of Heart Failure in Developing Countries: A Review of the Literature. International Journal of Cardiology 80:213-219.

Moffatt CJ, Franks PJ, Doherty DC, Williams AF, Badger C, Jeffs E, Bosanquet N, Mortimer PS. 2003. Lymphoedema: An Underestimated Health Problem. Quarterly Journal of Medicine 96:731-738.

Moissl UM, Wabel P, Chamney PW, Bosaeus I, Levin NW, Bosy-Westphal A, Korth O, Muller MJ, Ellegard L, Malmros V, Kaitwatcharachai C, Kuhlmann MK, Zhu F, Fuller NJ. 2006. Body Fluid Volume Determination via Body Composition Spectroscopy in Health and Disease. Physiological Measurement 27:921-933.

Moronkeji K, Akhtar R. 2015. Mechanical Properties of Aging Human Skin. In: Derby B, Akhtar R, editors. Mechanical Properties of Aging Soft Tissues: Springer International Publishing. p 237-263.

Morton RL, Tong A, Howard K, Snelling P, Webster AC. 2010. The Views of Patients and Carers in Treatment Decision Making for Chronic Kidney Disease: Systematic Review and Thematic Synthesis of Qualitative Studies. British Medical Journal 340:c112-c112.

Moy P, Foster M, Gunnarsson CA, Weerasooriya T. 2011. Loading Rate Effect on Tensile Failure Behavior of Gelatins under Mode I.15-23.

Mridha M, Odman S. 1985. Characterisation of Subcutaneous Oedema by Mechanical Impedance Measurements. Journal of Investigative Dermatology 85:575-578.

Mridha M, Odman S, Oberg PA. 1992. Mechanical Pulse Wave Propagation in Gel, Normal and Oedematous Tissues. Journal of Biomechanics 25:1213-1218.

Mukerjee EV, Collins SD, Isseroff RR, Smith RL. 2004. Microneedle Array for Transdermal Biological Fluid Extraction and In Situ Analysis. Sensors and Actuators A: Physical 114:267-275.

Mukerjee EV, Isseroff RR, Collins SD, Smith RL. 2003. Microneedle Array with Integrated Microchannels for Transdermal Sample Extraction and In Situ Analysis. In: 12th

International Conference on Solid State Sensors, Actuators and Mircosystems. Boston. p 1439-1441.

Nachman M, Franklin SE. 2016. Artificial Skin Model Simulating Dry and Moist In Vivo Human Skin Friction and Deformation Behaviour. Tribology International 97:431-439.

Nesto RW, Bell D, Bonow RO, Fonseca V, Grundy SM, Horton ES, Le Winter M, Porte D, Semenkovich CF, Smith S, Young LH, Kahn R. 2003. Thiazolidinedione Use, Fluid Retention, and Congestive Heart Failure: A Consensus Statement from the American Heart Association and American Diabetes Association. Circulation 108:2941-2948.

Newton VL, McConnell JC, Hibbert SA, Graham HK, Watson REB. 2015. Skin Aging: Molecular Pathology, Dermal Remodelling and the Imaging Revolution. Giornale Italiano Di Dermatologia E Venereologia 150:665-674.

Nguyen HX, Banga AK. 2015. Enhanced Skin Delivery of Vismodegib by Microneedle Treatment. Drug delivery and translational research 5:407-423.

Ni Annaidh A, Bruyere K, Destrade M, Gilchrist MD, Ottenio M. 2012. Characterization of the Anisotropic Mechanical Properties of Excised Human Skin. Journal of the Mechanical Behavior of Biomedical Materials 5:139-148.

Odegard GM, Gates TS, Herring HM. 2005. Characterisation of Viscoelastic Properties of Polymeric Materials through Nanoindentation. Experimental Mechanics 45:130-136.

Ogden RW. 2009. Anisotropy and Nonlinear Elasticity in Arterial Wall Mechanics. In: Gerhard A. Holzapfel RWO, editor. Biomechanical Modelling at the Molecular, Cellular and Tissue Levels: Springer Vienna. p 179-258.

Olatunji O, Das DB, Al-Qallaf B. 2009. Simulation Based Optimisation of Microneedle Geometry to Improve Drug Permeability in Skin. In: The European Multidisciplinary Society for Modelling and Simulation Technology. Loughborough, UK. p 1-8.

Olatunji O, Das DB, Garland MJ, Belaid L, Donnelly RF. 2013. Influence of Array Interspacing on the Force Required for Successful Microneedle Skin Penetration: Theoretical and Practical Approaches. Journal of Pharmaceutical Sciences 102:1209-1221.

Oliver WC, Pharr GM. 1992. An Improved Technique for Determining Hardness and Elastic Modulus using Load and Displacement Sensing Indentation Experiments. Journal of Materials Research 7:1564-1583.

Onofriescu M, Hogas S, Voroneanu L, Apetrii M, Nistor I, Kanbay M, Covic AC. 2014. Bioimpedance-Guided Fluid Management in Maintenance Hemodialysis: A Pilot Randomized Controlled Trial. American Journal of Kidney Diseases 64:111-118.

Oomens CWJ, Van Campen DH, Grootenboer HJ. 1987. A Mixture Approach to the Mechanics of Skin. Journal of Biomechanics 20:877-885.

Pailler-Mattei C, Bec S, Zahouani H. 2008. In Vivo Measurements of the Elastic Mechanical Properties of Human Skin by Indentation Tests. Medical Engineering and Physics 30:599-606.

Pailler-Mattei C, Pavan S, Vargiolu R, Pirot F, Falson F, Zahouani H. 2007a. Contribution of Stratum Corneum in Determining Bio-Tribological Properties of the Human Skin. Wear 263:1038-1043.

Pailler-Mattei C, Pavan S, Vargiolu R, Pirot F, Falson F, Zahouani H. 2007b. Contribution of Stratum Corneum in Determining Bio-Tribological Properties of the Human Skin. In: 16th International Conference on Wear of Materials. p 1038-1043.

Pailler-Mattéi C, Zahouani H. 2006. Analysis of Adhesive Behaviour of Human Skin In Vivo by an Indentation Test. Tribology International 39:12-21.

Park JH, Allen MG, Prausnitz MR. 2005. Biodegradable Polymer Microneedles: Fabrication, Mechanics and Transdermal Drug Delivery. Journal of Controlled Release 104:51-66.

Parker ER, Rao MP, Turner KL, Meinhart CD, C. MN. 2007. Bulk Micromachined Titanium Microneedles. Journal of Microelectromechanical Systems 16:289-295.

Parker KP. 2003. Sleep Disturbances in Dialysis Patients. Sleep Medicine Reviews 7:131-143.

Pauwels E, Van Loo D, Cornillie P, Brabant L, Van Hoorebeke L. 2013. An Exploratory Study of Contrast Agents for Soft Tissue Visualization by Means of High Resolution X-ray Computed Tomography Imaging. Journal of Microscopy 250:21-31.

Peacock WF, Costanzo MR, De Marco T, Lopatin M, Wynne J, Mills RM, Emerman CL. 2009. Impact of Intravenous Loop Diuretics on Outcomes of Patients Hospitalized with Acute Decompensated Heart Failure: Insights from the ADHERE Registry. Cardiology 113:12-19.

Pegoraro C, MacNeil S, Battaglia G. 2012. Transdermal Drug Delivery: From Micro to Nano. Nanoscale 4:1881-1894.

Pierard GE, Lapiere CM. 1977. Physiopathological Variations in the Mechanical Properties of Skin. Archives of Dermatological Research 260:231-239.

Prausnitz MR. 2001. Overcoming the Skin's Barrier: The Search for Effective and User-Friendly Drug Delivery. Diabetes Technology and Therapeutics 3:233-236.

Prausnitz MR, Langer R. 2008. Transdermal Drug Delivery. Nature Biotechnology 26:1261-1268.

Qiu Y, Guo L, Zhang S, Xu B, Gao Y, Hu Y, Hou J, Bai B, Shen H, Mao P. 2015. DNA-Based Vaccination against Hepatitis B Virus using Dissolving Microneedle Arrays Adjuvanted by Cationic Liposomes and CpG ODN. Drug Delivery:1-8.

Radhakrishnan RS, Radhakrishnan HR, Xue H, Moore-Olufemi SD, Mathur AB, Weisbrodt NW, Moore FA, Allen SJ, Laine GA, Cox CS, Jr. 2007. Hypertonic Saline Reverses

Stiffness in a Sprague-Dawley Rat Model of Acute Intestinal Oedema, Leading to Improved Intestinal Function. Critical Care Medicine 35:538-543.

Renephra. 2012. Transdermal Fluid Removal Part I (Microneedle Technology). In.

Renephra. 2015. Transdermal Fluid Removal Part II (MicroneedleTechnology). In.

Rich MW, Chyun DA, Skolnick AH, Alexander KP, Forman DE, Kitzman DW, Maurer MS, McClurken JB, Resnick BM, Shen WK, Tirschwell DL. 2016. Knowledge Gaps in Cardiovascular Care of the Older Adult Population. Journal of the American College of Cardiology 67:2419-2440.

Ridge MD, Wright V. 1966. Mechanical Properties of Skin: A Bioengineering Study of Skin Structure. Journal of Applied Physiology 21:1602-1606.

Romgens AM, Bader DL, Bouwstra JA, Baaijens FP, Oomens CW. 2014. Monitoring the Penetration Process of Single Microneedles with Varying Tip Diameters. Journal of the Mechanical Behavior of Biomedical Materials 40:397-405.

Rosado C, Pinto P, Rodrigues LM. 2005. Modelling TEWL-Desorption Curves: A New Practical Approach for the Quantitative In Vivo Assessment of Skin Barrier. Experimental Dermatology 14:386-390.

Ryan TJ. 1995. Lymphatics and Adipose Tissue. Clinics in Dermatology 13:493-498.

Ryckman RA, Powell DA, Lew A. 2012. Ballistic Penetration of Perma-Gel. In: AIP Conference Proceedings. p 143-148.

Samant P, Prausnitz MR. 2016. Microneedle Patches for Point-of-Care Diagnostics. In: The 4th International Conference on Microneedles. GSK House, London: Microneedles 2016.

Sandby-Moller J, Poulsen T, Wulf HC. 2003. Epidermal Thickness at Different Body Sites: Relationship to Age, Gender, Pigmentation, Blood Content, Skin Type and Smoking Habits. Acta Dermatological Venereol 83:410-413.

Sawicka KM, Roemer EJ, Simon SR. 2007. Enzyme Composite Nanofibers as Novel Transdermal Delivery Coating. IEEE Xplore:232-233.

Schade H. 1912. Studies on the Organ Function of Connective Tissue I. Communication of: The Elastic Function of the Connective Tissue and the Intravital Measurement of their Disorders. Journal of Experimental Pathology and Therapy 11:369-399.

Schambach SJ, Bag S, Schilling L, Groden C, Brockmann MA. 2010. Application of Micro-CT in Small Animal Imaging. Methods 50:2-13.

Seibert E, Muller SG, Fries P, Pattmoller J, Kuss O, Heine GH, Girndt M, Schneider G, Kotanko P, Zhu F, Levin NW, Kuhlmann MK. 2013. Calf Bioimpedance Spectroscopy for Determination of Dry Weight in Hemodialysis Patients: Effects on Hypertension and Left Ventricular Hypertrophy. Kidney and Blood Pressure Research 37:58-67.

Shergold OA, Fleck NA, Radford D. 2006. The Uniaxial Stress versus Strain Response of Pig Skin and Silicone Rubber at Low and High Strain Rates. International Journal of Impact Engineering 32:1384-1402.

Singh S, Loke YK, Furberg CD. 2007. Thiazolidinediones and Heart Failure: A Teleo-Analysis. Diabetes care 30:2148-2153.

Stewart S, Jenkins A, Buchan S, McGuire A, Capewell S, McMurray JJ. 2002. The Current Cost of Heart Failure to the National Health Service in the UK. European Journal of Heart Failure 4:361-371.

Strober W. 2001. Trypan Blue Exclusion Test of Viability. Current Protocols in Immunology:21:23B:A.23B.21–A.23B.22.

Sutton GC. 1990. Epidemiologic Aspects of Heart Failure. American Heart Journal 120:1538-1540.

Tagami H, Ohi M, Iwatsuki K, Kanamaru Y, Yamada M, Ichijo B. 1980. Evaluation of the Skin Surface Hydration In Vivo by Electrical Measurement. Journal of Investigative Dermatology 75:500-507.

Thali MJ, Kneubuehl BP, Zollinger U, Dirnhofer R. 2002. The ‘‘Skin–Skull–Brain Model’’: A New Instrument for the Study of Gunshot Effects. Forensic Science International 125:178-189.

Treffel P, Panisset F, Faivre B, Agache P. 1994. Hydration, Transepidermal Water Loss, pH and Skin Surface Parameters: Correlations and Variations between Dominant and Non-Dominant Forearms. British Journal of Dermatology 130:325-328.

Tsai YC, Chiu YW, Tsai JC, Kuo HT, Hung CC, Hwang SJ, Chen TH, Kuo MC, Chen HC. 2015. Association of Fluid Overload with Cardiovascular Morbidity and All-cause Mortality in Stages 4 and 5 CKD. Clinical Journal of the American Society of Nephrology 10:39-46.

Tsaturyan AK, Izacov VJ, Zhelamsky SV, Bykov BL. 1984. Extracellular Fluid Filtration as the Reason for the Viscoelastic Behaviour of the Passive Myocardium. Journal of Biomechanics 17:749-755.

Valente MAE, Voors AA, Damman K, Van Veldhuisen DJ, Massie BM, O’Connor CM, Metra M, Ponikowski P, Teerlink JR, Cotter G, Davison B, Cleland JGF, Givertz MM, Bloomfield DM, Fiuzat M, Dittrich HC, Hillege HL. 2014. Diuretic Response in Acute Heart Failure: Clinical Characteristics and Prognostic Significance. European Heart Journal 35:1284-1293.

van der Maaden K, Luttge R, Vos PJ, Bouwstra J, Kersten G, Ploemen I. 2015. Microneedle-Based Drug and Vaccine Delivery via Nanoporous Microneedle Arrays. Drug Delivery and Translational Research 5:397-406.

van der Maaden K, Sekerdag E, Jiskoot W, Bouwstra J. 2014. Impact-Insertion Applicator Improves Reliability of Skin Penetration by Solid Microneedle Arrays. AAPS Journal 16:681-684.

Verbaan FJ, Bal SM, van dB, Dijksman JA, van Hecke M, Verpoorten H, Luttge R, Bouwstra JA. 2008. Improved Piercing of Microneedle Arrays in Dermatomed Human Skin by an Impact Insertion Method. Journal of Controlled Release 128:80-88.

Verbaan FJ, Bal SM, van dB, Groenink WHH, Verpoorten H, Luttge R, Bouwstra JA. 2007. Assembled Microneedle Arrays Enhance the Transport of Compounds Varying over a Large Range of Molecular Weight across Human Dermatomed Skin. Journal of Controlled Release 117:238-245.

Veronda DR, Westmann RA. 1970. Mechanical Charcterisation of Skin - Finite Deformations. Journal of Biomechanics 3:111-124.

Victrex. 2014. Victrex® High Performance PEEK Polymers. In: Victrex plc.

Walton LA, Bradley RS, Withers PJ, Newton VL, Watson RE, Austin C, Sherratt MJ. 2015. Morphological Characterisation of Unstained and Intact Tissue Micro-Architecture by X-ray Computed Micro- and Nano-Tomography. Scientific Reports 5:1-14.

Wang PM, Cornwell M, Prausnitz MR. 2005. Minimally Invasive Extraction of Dermal Interstitial Fluid for Glucose Monitoring using Microneedles. Diabetes Technology and Therapeutics 7:131-141.

Watson REB. 2013. Histology Protocol. In.

Wilkes GL, Brown IA, Wildnauer RH. 1973. The Biomechanical Properties of Skin. CRC Critical Reviews in Bioengineering 1:453-495.

Wilkes GL, Wildnauer RH. 1973. Structure-Property Relationships of the Stratum Corneum of Human and Neonatal Rat II. Dynamic Mechanical Studies. Biochimica et Biophysica Acta 304:276-289.

Williams AC. 2004. Structure and Function of Human Skin. In: Transdermal and Topical Drug Delivery: From Theory to Clinical Practice: Pharmaceutical Press. p 1-25.

Wu KS, van Osdol WW, Dauskardt RH. 2006. Mechanical Properties of Human Stratum Corneum: Effects of Temperature, Hydration and Chemical Treatment. Biomaterials 27:785-795.

Xiang Z, Wang H, Murugappan SK, Yen S-C, Pastorin G, Lee CY. 2015. Dense Vertical SU-8 Microneedles Drawn from a Heated Mold with Precisely Controlled Volume. Journal of Micromechanics and Microengineering 25:1-10.

Yan G, Warner KS, Zhang J, Sharma S, Gale BK. 2010. Evaluation Needle Length and Density of Microneedle Arrays in the Pretreatment of Skin for Transdermal Drug Delivery. International Journal of Pharmaceutics 391:7-12.

Yuan Y, Verma R. 2006. Measuring Microelastic Properties of Stratum Corneum. Colloids and Surfaces B: Biointerfaces 48:6-12.

Zahn JD, Talbot D, Liepmann D, Pisano AP. 2000. Microfabricated Polysilicon Microneedles For Minimally Invasive Biomedical Devices. Biomedical Microdevices 2:295-303.

Zahouani H, Pailler-Mattei C, Sohm B, Vargiolu R, Cenizo V, Debret R. 2009. Characterization of the Mechanical Properties of a Dermal Equivalent Compared with Human Skin In Vivo by Indentation and Static Friction Tests. Skin Research and Technology 15:68-76.

Zak M, Kropka P, Kobielarz M, Dudek A, Kaleta-Kuratewicz K, Szotek S. 2011. Determination of the Mechanical Properties of the Skin of Pig Foetuses with Respect to its Structure. Acta of Bioengineering and Biomechanics 13:37-43.

Zheng Y, Mak FT, Lue B. 1999. Objective Assessment of Limb Tissue Elasticity: Development of a Manual Indentation Procedure. Journal of Rehabilitation Research and Development 36:71-85.

Chapter 8

8. Appendix

8.1 3D Image Analysis using XMT

XMT imaging was performed on skin Model 3A. The staining and wax embedding protocol is summarised as follows: full thickness microneedle treated skin was soaked in paraformaldehyde for 4 hours and then rehydrated in PBS solution for 5 mins. The tissue was then subsequently stained with Lugol's contrasting agent for 21 hours. After staining, the sample was washed three times in water and placed in 70% ethanol for 15 mins, then in 90% IMS for 15 mins, followed by 15 mins in 100% ethanol and then 3 xylene washes of 30 mins. Finally, it was placed on the processor for wax embedding for 30 mins.

The skin was then imaged on a Carl Zeiss Xradia MicroXMT-500 system using 4× objective, with a source voltage of 45 kV, a source current of 78 μA and a power source of 3.5 W. The sample was positioned 8 mm from the source and 45 mm from the detector.

The size of the sample was approximately 2 × 2 mm, 1015 TIFF images were obtained using Avizo 8 imaging software (FEI™, Oregon, USA). The image stacks were opened in ImageJ using the orthogonal selection. The XY view showed the vertical cross-section of the skin through the stratum corneum, epidermis and dermis, whilst the XZ view showed the planar cross-section of the skin through the dermis. In the case where the XY view showed that there was no breach of skin's layers, no disruption was seen in XZ view. When there was a breach, this was observed in the XY view and confirmed by the disruption in the XZ view. A single image was analysed following confirmation of the breach in skin as shown in the region shaded red in Fig. 94.

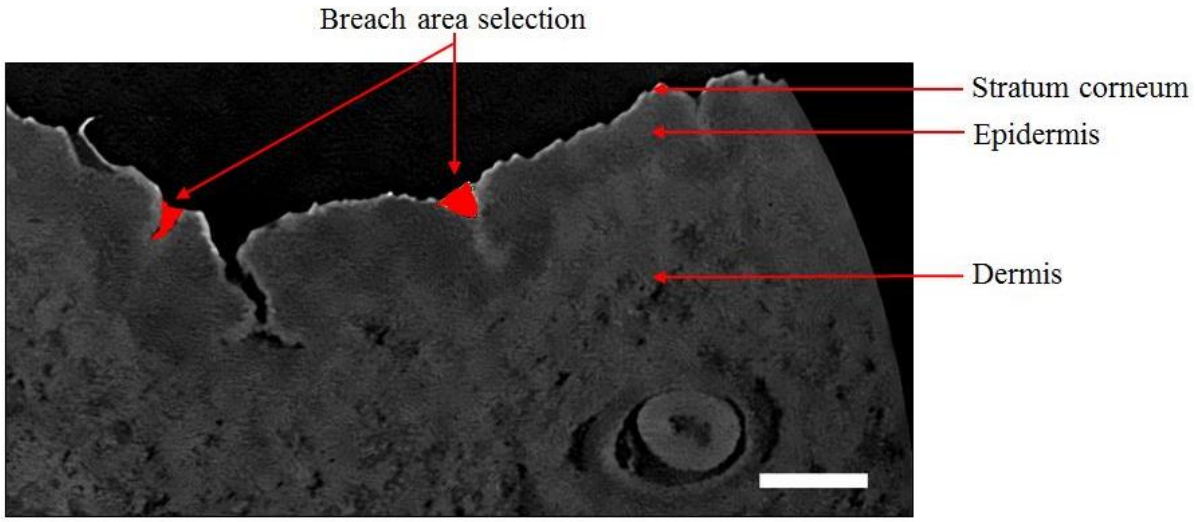

Figure 94 Breach area selection on XMT image of microneedle treated skin. Scale bar represents 100 μm.

3D reconstruction of the image stacks was carried out using Avizo 8 and prior to segmentation, noise in the data was reduced by applying a non local means filter. In some areas of the images the contrast was poor and therefore, manual adjustments to the segmentation were necessary. This process was labour intensive and improved staining techniques is required to ensure that there is better contrast between the layers of skin so as to reduce the time spent in manual segmentation of the data.

Skin Model 3A was used for the 3D image analysis because of the thinner, less stiff abdominal skin and the high volume of water content, compliant gelatine gel as determined from micromechanical tests. The volume rendered image of Model 3A presented in Fig. 95 shows the irregular surface topography of the stratum corneum. The lines in the skin are highlighted; however, it is challenging to detect any perforations caused by the application of microneedles using the impact applicator in the reconstructed image.

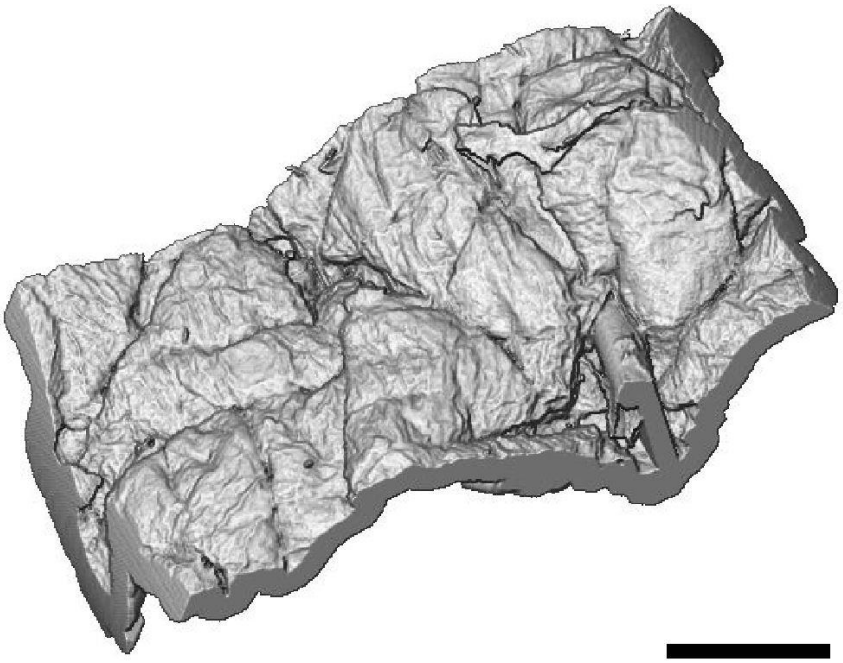

Figure 95 Volume rendering showing the output of the segmentation process on microneedle treated Model 3A, showing the stratum corneum and epidermal layers only. Scale bar represents 100 μm.

In addition, Fig. 96 shows the various orthogonal views of the reconstructed image. The different views show that skin is not a flat surface, but consists of many undulations. These undulations vary in size and depth.

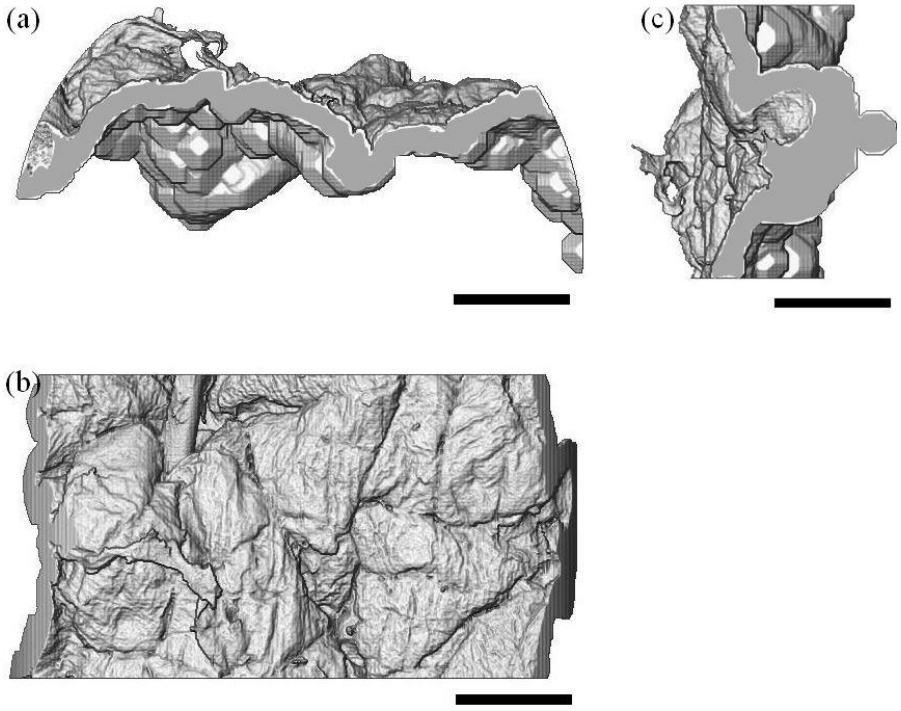

Figure 96 Volume rendering showing the various orthogonal layouts of the 3D image of the skin, where (a) XY, (b) XZ and (c) YZ. Scale bar represents 100 μm.

Furthermore, a comparison of the breach area for the XMT image analysis and H&E staining is shown in Fig. 97. The stratum corneum, epidermis and dermis are well defined for the H&E images (Fig. 97a) and are comparable to the XMT images (Fig. 97b). The H&E stained skin appears to be prone to sectioning induced artefacts (Fig 97a), which does not appear to be the case for the XMT image (Fig. 97b). The microneedle induced disruption through the layers in the XMT image visually appears to be similar to what is observed in the H&E images. The delamination to the stratum corneum seen in the H&E images is also observed in the XMT images. 7 images were analysed for the XMT and H&E images. The breach area for the XMT images was 1921 ± 1682 μm^2 compared to that of the H&E images, which was 3417 ± 2178 μm^2. The breach profiles observed with the two techniques appear comparable hence providing validation of the measurements from the H&E images.

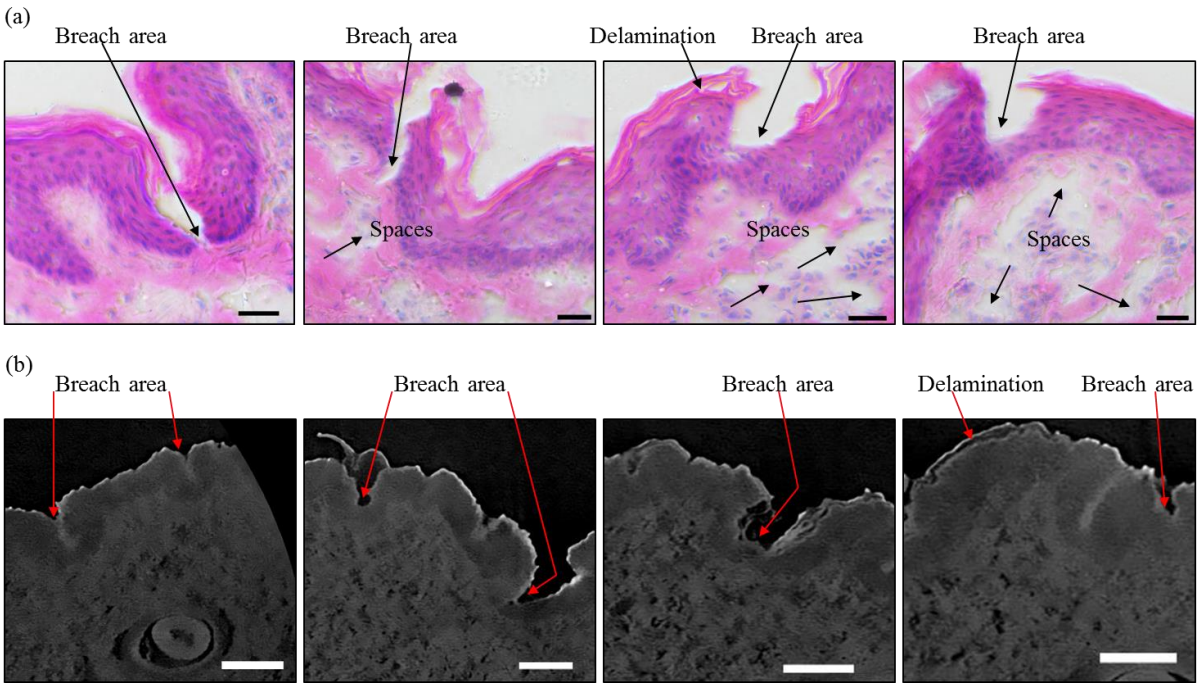

Figure 97 Comparison of imaging techniques on Model 3A, where (a) XMT images and (b) H&E images. Scale bar represents 100 μm.

This pilot study demonstrates the feasibility of utilising XMT for 3D analysis of microneedle perforation of skin.

8.2 ImageSXM Software Code

/Volumes/Home/Image SXM dev/SXM 198 CW 2 Sep/Source files/MIASMA src files/Microneedles.pas Page: 1Thursday, September 24, 2015 / 15:34

```
{ = = =
```

```
begin
GetMNAver := MNAver; { make version available to other routines }
end;
{ ——————————————————————————————————————————————————————————————————————————
——— }
procedure PreambleMNA;
begin
DoingMIASMA := true;
DoingMNA := true;
SuppressLog := true; { keep Session Log clear of clutter }
SuppressMessages := true; { neater to not update Info window }
SXMwindow := true;
AbortAnalysis := false;
OpeningCellRGBimage := true;
Measurements := [XYLocM, AreaM];
TempHistoMag := HistoMag;
HistoMag := 1;
end;
{ ——————————————————————————————————————————————————————————————————————————
——— }
procedure FilePreambleMNA (Folder: integer);
begin
SLogArrayOnReset;
DiagnosticLog(stringOf('Microneedle Analysis v', MNAver : 1));
DiagnosticLog('+');
DiagnosticLog('+Load: ' + AbbrevPathName(CellsLoadFolder, true, 50));
DiagnosticLog('+Save: ' + AbbrevPathName(CellsSaveFolder, true, 50));
DiagnosticLog('+');
DiagnosticLog('+'); { spreadsheet tabs }
DiagnosticLog(stringOf('+', tab, 'Area in sq.µm'));
DiagnosticLog(stringOf('+', tab, '----------'));
RefreshSessionLog; { dummy call to update SLog window }
SuppressLog := true; { keep Session Log clear of clutter }
SuppressMessages := true; { neater to not update Info window }
SXMwindow := true;
end;
{ ——————————————————————————————————————————————————————————————————————————
——— }
procedure UpdateMNAinfoWindow (MessageText: GPCstr);
var
FilesDoneInThisFolder, FilesDone, FilesToDo: longint;
begin
FilesDoneInThisFolder := FileIndexInThisFolder - 1; { index = number in this folder }
FilesDone := FilesDoneInPrevFolders + FilesDoneInThisFolder;
FilesToDo := NumFilesInBatch - FilesDone;
```

```
MNAstr := stringOf('Microneedle Analysis', cr, cr);
MNAstr := stringOf(MNAstr, 'Analysing image ', FilesDone + 1 : 1, ' of ', NumFilesInBatch : 1, cr);
MNAstr := MNAstr + cr + MessageText + cr;
ShowInInfo(MNAstr);
end;
{ ——————————————————————————————————————————————————————————————————————————————— }
procedure MNAdiagnostics;
begin
end;
{ ——————————————————————————————————————————————————————————————————————————————— }
procedure AnalyseMicroneedles (ImageNum: integer);
var
InfoR, InfoB: InfoPtr;
ScaleBarPixels: integer;
WinLeftEdge, WinBotEdge, WinRightEdge, dX, dY: integer;
Bin, LocalMin, FirstMax, FirstMin, LastMax: integer; { SDB 25 Jun 15 }
SaveSliceStart: integer; { SDB 25 Jun 15 }
NumFound, xClick4, yClick4: integer;
DistToClick4, MinDistSoFar: extended;
i, Damage: integer;
{ ————————————————————————————————— }
procedure MakeLineInScaleBar (x1, x2, y: integer);
begin
with Info^ do begin
KillRoi;
LX1 := PixelsPerLine + x1;
LY1 := nLines + y;
LX2 := PixelsPerLine + x2;
LY2 := nLines + y;
RoiType := LineRoi;
MakeRegion;
RoiShowing := true;
end;
end;
{ ————————————————————————————————— }
procedure SetScaleFromBar;
const
SmallxScaleBox = 200; { rectangle in bottom right that contains scale bar }
SmallyScaleBox = 125;
LargexScaleBox = 300; { rectangle in bottom right that contains scale bar }
LargeyScaleBox = 150;
var
xScaleBox, yScaleBox: integer;
y, i, LeftEdge, RightEdge, ScaleBarWidth, ScaleBarSum, ScaleBarNum: integer;
MNApixPerMicron: real;
begin
```

```
RemoveZcalib; { otherwise PlotLineProfile gives odd z values }
ScaleBarPixels := 100; { default scale 100 pix = 100 µm }
ScaleBarSum := 0;
ScaleBarNum := 0;
if Info^.PixelsPerLine < 800 then begin
xScaleBox := SmallxScaleBox;
yScaleBox := SmallyScaleBox;
end
else begin
xScaleBox := LargexScaleBox; { make search region for scale bar a bit bigger }
yScaleBox := LargeyScaleBox;
end;
for y := -yScaleBox to -yScaleBox div 3 do begin
MakeLineInScaleBar(-xScaleBox, -5, y); { take profile close to bottom right corner }
ShowPlot := false;
PlotLineProfile;
ShowPlot := true;
RightEdge := 0;
for i := 1 to xScaleBox - 10 do
if PlotData^[i] > 250 then { scale bar is usually black = 255 }
RightEdge := i;
LeftEdge := xScaleBox;
for i := xScaleBox - 10 downto 1 do
if PlotData^[i] > 250 then { scale bar is usually black = 255 }
LeftEdge := i;
ScaleBarWidth := RightEdge - LeftEdge;
if (ScaleBarWidth > 25) and (ScaleBarWidth < 125) then begin
ScaleBarSum := ScaleBarSum + ScaleBarWidth;
ScaleBarNum := ScaleBarNum + 1;
end;
if ScaleBarNum > 4 then begin
ScaleBarPixels := round(ScaleBarSum / ScaleBarNum);
leave;
end;
end;
MNApixPerMicron := ScaleBarPixels / 100; { scale bar always = 100 µm? }
with Info^ do begin
xScale := MNApixPerMicron; yScale := xScale;
xInc := 1 / xScale; yInc := 1 / yScale;
xSize := PixelsPerLine / xScale; ySize := nLines / yScale;
xUnit := 'µm'; yUnit := 'µm';
SpatiallyCalibrated := true;
end;
KillRoi;
end;
```

```
{ ———————————————————————————— }
function Get2clicks (var Click: ClickArray): boolean;
var
i: integer;
{ ———————————————————————————— }
procedure DrawCross (mouseLoc: point); { draw cross at mouse loc }
const
box = 5;
begin
with mouseLoc do begin
MoveTo(h - box, v);
LineTo(h + box, v);
MoveTo(h, v - box);
LineTo(h, v + box);
end;
end;
{ ———————————————————————————— }
procedure GetClickPos (i: integer);
var
mouseLoc: point;
begin
WaitForMouse;
GetMouse(mouseLoc);
DrawCross(mouseLoc);
ScreenToOffscreen(mouseLoc);
Click[i].pt := mouseLoc;
end;
{ ———————————————————————————— }
begin
Get2clicks := false;
SetPortWindowPort(Info^.wRef); { ensures that click coords are local, ie relative to window }
SetCursor(ToolCursor[SelectionTool]); { make sure cursor is a cross }
for i := 1 to 2 do begin
SuppressMessages := false;
ClearInfoWindow;
ShowMessage(stringOf(MNAstr, cr, 'Waiting for click ', i : 1, '...'));
GetClickPos(i);
ShowMessage(' ');
SuppressMessages := true;
if not PtInRect(Click[i].pt, Info^.PicRect) then begin
FlushEvents(EveryEvent, 0); { don't act on this click }
exit;
end;
end;
FlushEvents(EveryEvent, 0); { discard mouse clicks from event buffer }
```

```
dX := Click[2].pt.h - Click[1].pt.h;
dY := Click[2].pt.v - Click[1].pt.v;
Click[4].pt.h := (Click[1].pt.h + Click[2].pt.h) div 2; { centre of line }
Click[4].pt.v := (Click[1].pt.v + Click[2].pt.v) div 2;
SuppressBeachBall; { allows cosses to show }
Get2clicks := true;
end;
{ ———————————————————————— }
procedure TakeOutBaseline;
{ ———————————————————————— }
procedure MakeBaseline;
begin
with Info^ do begin
KillRoi;
LX1 := Click[1].pt.h;
LY1 := Click[1].pt.v;
LX2 := Click[2].pt.h;
LY2 := Click[2].pt.v;
RoiType := LineRoi;
MakeRegion;
RoiShowing := true;
end;
end;
{ ———————————————————————— }
begin
Click[1].pt.h := Click[1].pt.h - dX div 2; { extend line from click 1 to click 2 }
Click[1].pt.v := Click[1].pt.v - dY div 2;
Click[2].pt.h := Click[2].pt.h + dX div 2;
Click[2].pt.v := Click[2].pt.v + dY div 2;
MakeBaseline;
DoClear; { draw white line to separate damaged tissue from background }
Click[1].pt.v := Click[1].pt.v - 1; { nudge up and do again }
Click[2].pt.v := Click[2].pt.v - 1;
MakeBaseline;
DoClear; { draw white line to separate damaged tissue from background }
KillRoi;
SuppressBeachBall; { allows cosses to show }
end;
{ ———————————————————————— }
begin
```

```
OrigInfo := Info;
ResetToColour(R);
SetScaleFromBar;
if MNAbreach then begin { SDB 25 Jun 15 }
ResetToColourBlind(G);
UseThisInfo := Info;
end
else begin
Info := OrigInfo;
ResetToColourBlind(R); MedianFilter; Smooth; { prep R channel }
SOK := DuplicateOffscreen(''); InfoR := Info;
Info := OrigInfo;
ResetToColourBlind(B); MedianFilter; Smooth; { prep B channel }
SOK := DuplicateOffscreen(''); InfoB := Info;
SOK := DuplicateOffscreen(RemoveSuffix(OrigInfo^.Title)); { use orig title (without suffix) }
UseThisInfo := Info; { to ensure log displays correctly }
CurrentMathOp := MinMath;
RealImageMath := false;
MathGain := 1.0;
MathOffset := 0.0;
DoMath(InfoR^.PicNum, InfoB^.PicNum, UseThisInfo, Info^.PicRect); { min of R and B ch }
GetRidOfWindow(OrigInfo);
GetRidOfWindow(InfoR);
GetRidOfWindow(InfoB);
Info := UseThisInfo;
end;
with Info^ do
if nLines < ScreenHeight div 2 then ResizeSXMwindow(0) { 200% }
else if nLines < ScreenHeight then ResizeSXMwindow(1) { 100% }
else if nLines < ScreenHeight * 2 then ResizeSXMwindow(2) { 50% }
else ResizeSXMwindow(3); { 33% }
with Info^ do begin { reposition image }
WinLeftEdge := rleft + rwidth + 16;
MoveWindow(wRef, WinLeftEdge, PicBaseTop, false);
WinBotEdge := PicBaseTop + round(nLines * magnification);
WinRightEdge := WinLeftEdge + round(PixelsPerLine * magnification);
DoHistogram; { generate histogram before smoothing it }
GetSmoothHistogram;
if PixelsPerLine > nLines then { put Histogram below image }
MoveWindow(HistoWindow, WinLeftEdge, WinBotEdge + 32, true)
else { or to right of image if image is 'portrait' }
MoveWindow(HistoWindow, WinRightEdge + 32, PicBaseTop, true);
DrawHistogram;
end;
if MNAbreach then begin { SDB 25 Jun 15 }
FirstMax := 0;
for Bin := 80 downto 1 do { find first local max in smoothed histogram }
if (Histogram[Bin] > 2000) and (Histogram[Bin] >= Histogram[Bin - 1])
```

```
and (Histogram[Bin] >= Histogram[Bin + 1]) then
FirstMax := Bin;
for Bin := FirstMax to 250 do { find last local maximum in smoothed histogram }
if (Histogram[Bin] > 2000) and (Histogram[Bin] >= Histogram[Bin - 1])
and (Histogram[Bin] >= Histogram[Bin + 1]) then
LastMax := Bin;
for Bin := 250 downto FirstMax do { find first local minimum in smoothed histogram }
if (Histogram[Bin] <= Histogram[Bin - 1]) and (Histogram[Bin] <= Histogram[Bin + 1]) then
FirstMin := Bin;
SliceStart := FirstMin + (LastMax - FirstMin) div 3 - 10; { colour epidermal layer in red }
end
else begin
LocalMin := 0;
for Bin := 240 downto 80 do { find last local minimum in smoothed histogram }
if (Histogram[Bin] > 2000) and (Histogram[Bin] <= Histogram[Bin - 1])
and (Histogram[Bin] <= Histogram[Bin + 1]) then begin
LocalMin := Bin;
end;
if LocalMin = 0 then begin { if that didn't work because of the smoothing then... }
GetRectHistogram; { find last local minimum in unsmoothed histogram }
for Bin := 240 downto 80 do
if (Histogram[Bin] > 2000) and (Histogram[Bin] <= Histogram[Bin - 1])
and (Histogram[Bin] <= Histogram[Bin + 1]) then begin
LocalMin := Bin;
end;
end;
if LocalMin = 0 then begin
LocalMin := 150; { histogram had no valley so }
Beep; { set to something sensible }
end;
SliceStart := LocalMin; { colour epidermal layer in red }
end;
SliceEnd := 255;
EnableDensitySlice;
if not Get2clicks(Click) then begin
ShowMessage('Microneedle analysis aborted');
exit;
end;
SaveSliceStart := SliceStart;
SliceStart := 0; { colour everything but epidermal layer in red }
SliceEnd := SaveSliceStart;
ThresholdToForeground := true; { density slice red -> black }
NonThresholdToBackground := true; { everything else -> white }
Macro := true;
ApplyLookupTable; { apply without dlog box }
Macro := false;
```

```
TakeOutBaseline;
DoOpeningWithCount(3); { tidy rough edges of damage }
CellsIncEdges := false; { ensure objects at edge are ignored }
DoParticleAnalysisXY(-1, 999, 999999, NumFound);
Measurements := [AreaM, xyLocM, LengthM]; { make sure Area is displayed in Results }
if InvertYCoordinates then
Click[4].pt.v := Info^.nLines - 1 - Click[4].pt.v; { for comparison with xyCenter values }
xClick4 := round(Click[4].pt.h / OrigInfo^.xScale);
yClick4 := round(Click[4].pt.v / OrigInfo^.yScale);
MinDistSoFar := 999999; { find object closest to click 4 }
for i := 1 to NumFound do begin
DistToClick4 := (xCenter^[i] - xClick4) * (xCenter^[i] - xClick4) +
(yCenter^[i] - yClick4) * (yCenter^[i] - yClick4);
PerimLen^[i] := round(sqrt(DistToClick4)); { for diagnostics }
if DistToClick4 < MinDistSoFar then begin
Damage := i;
MinDistSoFar := DistToClick4;
end;
end;
{ padding gives neater }
DiagnosticLog(stringOf(tab, mArea^[Damage] : 6 : 0, tab, ' ', tab)); { spreadsheet output }
RefreshSessionLog; { dummy call to update SLog window }
Wait(60); { pause to allow user to see result }
end;
{ ——————————————————————————————————————————————————————————————————————
——— }
procedure FilePostambleMNA (Folder: integer);
begin
if DoingMNAbatch then
GetRidOfWindow(UseThisInfo)
else
ResetGrayMap; { ensures next image loads with default greyscale LUT }
end;
{ ——————————————————————————————————————————————————————————————————————
——— }
procedure PostambleMNA;
var
SLogTitleStr: GPCstr;
begin
if DoingMNAbatch then
CloseSessionLog;
err := CloseAWindow(HistoWindow);
HistoMag := TempHistoMag;
RestoreCompensation;
DoingMNA := false;
DoingMNAbatch := false;
```

```
DoingMIASMA := false;
OpeningCellRGBimage := false;
SuppressLog := false;
SuppressMessages := false;
SXMwindow := false;
if AbortAnalysis then
MNAstr := stringOf('Microneedle Analysis', cr, cr, 'Analysis aborted')
else
MNAstr := stringOf('Microneedle Analysis', cr, cr, 'Analysis complete');
SLogTitleStr := 'MNA-' {+ NaToStr(CellsLoadFolder.name)} + MakeDateTimeSuffix;
SLogArrayFSpec := MakeFSpecInFolder(SLogTitleStr, CellsSaveFolder);
SaveSLogToArray := false;
SaveSLogArray; { save SLog Array to same folder as folder of images }
ShowMessage(MNAstr);
end;
{ ——————————————————————————————————————————————————————————————————————
——— }
procedure MicroneedleSingle; { open and analyse a single image }
begin { for diagnostics and calibration }
PreambleMNA;
MNAsingle := true;
NavServWinTitle := 'Open One Image For MNA';
SOK := DoOpenNavServ; { open single image }
if not SOK then exit;
CellsTotalNumImages := 1;
CellsLoadFolder := GetFolderSpec(FileSpec);
CellsSaveFolder := CellsLoadFolder;
FilePreambleMNA(-1);
DoingMNAbatch := false;
NumFilesInBatch := 1; { set for single-image analysis }
FileIndexInThisFolder := 1;
AnalyseMicroneedles(1);
FilePostambleMNA(-1);
PostambleMNA;
end;
{ ——————————————————————————————————————————————————————————————————————
——— }
procedure MicroneedleAnalysis;
var
Folder, NumFiles, ImageNum: integer;
```

```
begin
PreambleMNA;
MNAsingle := false;
if not NavServChooseFolder(FolderSpec) then exit;
CellsLoadFolder := GetFolderSpec(FolderSpec);
CellsSaveFolder := GetFolderSpec(CellsLoadFolder);
{ get specs of files in selected folder and }
if not GetAllCellsFSpecs then exit; { files in folders within selected folder }
DoingMNAbatch := true;
NumFilesInBatch := CellsTotalNumImages; { set global var for other routines }
for Folder := 0 to CellsNumFolders do begin { for each folder... }
NumFiles := CellsNumFilesInFolder[Folder];
FilesDoneInPrevFolders := CellsNumFilesInPrev[Folder]; { set global var }
FilePreambleMNA(Folder);
if (NumFiles > 0) and not AbortAnalysis then
for ImageNum := 1 to NumFiles do begin { for each image in folder... }
FileIndexInThisFolder := ImageNum; { set global var }
MNAstr := NaToStr(CellsSortDirRec[Folder, ImageNum].RecFileSpec.name);
UpdateMNAinfoWindow(MNAstr);
with CellsSortDirRec[Folder, ImageNum] do begin
FileSpec := RecFileSpec;
SOK := DoOpen(FileSpec);
end;
AnalyseMicroneedles(ImageNum);
FilePostambleMNA(Folder);
if AbortMIASMA then leave; { pressing 'esc' will abort }
end;
if AbortMIASMA then leave; { pressing 'esc' will abort }
end;
PostambleMNA;
end;
{ ——————————————————————————————————————————————————————————————————————
——— }
end.
```